Metabolic Alterations Associated with Hemorrhagic Shock and Traumatic Injury as Measured in the Urine

A DISSERTATION
SUBMITTED TO THE FACULTY OF THE GRADUATE SCHOOL
OF THE UNIVERSITY OF MINNESOTA
BY

Elizabeth Rose Lusczek

IN PARTIAL FULFILLMENT OF THE REQUIREMENTS
FOR THE DEGREE OF
DOCTOR OF PHILOSOPHY or EDUCATION

E. Russel Ritenour and Bruce Hammer

December 2011

Acknowledgements

First and foremost, I wish to extend my warmest thanks for the mentorship and support of Dr. Greg Beilman. Without his support, I would be pursuing a very different path in life. This work is a reflection of his outstanding character, scholarship and trust. I hope I can live up to it. I also extend many special thanks to my colleagues and coworkers in Dr. Beilman's lab. In particular, I wish to thank Nancy Witowski and Dan Lexcen, my co-conspirators in the study of metabolomics in hemorrhagic shock. I would have been lost without your expertise and knowledge. I also wish to thank Kristine Mulier, whose tireless efforts in performing the pig experiments and managing the lab are vital to my work and to every research project in the lab. I wish to thank the University of Minnesota's Nuclear Magnetic Resonance Facility for their valuable expertise and assistance in running experiments.

To Sharon Jones and Devora Shapiro, I thank your for your friendship and support. Both of you have more intelligence and strength of character than anyone I've ever met. I am humbled and uplifted by our friendship. I am so grateful for your care and support, and hope that I return it in kind. To Eric Knight, I love you. Your steadiness has been and will ever be a rock for me. I am so lucky to have you in my corner. To Don Smith, Katie Cadwell, Jesse Bond and the Raccoonbear City: yours is a second home to me. You welcomed me when life was very bleak. I shall never be able to say how important you are to me.

I would also like to thank Barbara Schwartz, Jill Gettings, Nancy Kukulka, and Erin Olson for keeping me healthy. The past few years have been a challenge, and I am lucky to have found such competent and caring women.

I also wish to extend deepest love and thanks to my family, Stan and Linda Lusczek, and Jasmin, Chris, and Sam Hodzic. Though I've been far from you these past several years, you were never far from my thoughts. Now that my career as a graduate student is ending, I hope to spend more time with you and to watch my nephew grow up. I'm so pleased you'll be able to join me for the defense of this work. I hope you will be proud.

Finally, I wish to thank my committee: Greg Beilman, Bruce Hammer, Russ Ritenour, Jie Zhang, and Ramesh Harjani. There is potential for collaboration with many you in this work, and I hope we can continue to work together. I look forward to your honest assessment of this dissertation. I sincerely thank you for the time and consideration you give to this body of work.

Funding was provided by the Office of Naval Research (grants N00014-09-1-0323 and N000-05-1-0344), the University of Minnesota Medical School, and the Minnesota Medical Foundation.

Dedication

With love and respect, I dedicate this dissertation to my parents, Stan and Linda Lusczek. Your dedication in providing me with the best education possible put me on the path of discovery.

Abstract

Introduction: This dissertation focuses on profiling the changes in metabolism that occur as a result of hemorrhagic shock and traumatic injury as observed in urine obtained from a porcine model. Hemorrhagic shock and traumatic injury are responsible for the majority of deaths under the age of 44. A porcine model of hemorrhagic shock and traumatic injury was used to examine changes in metabolism due to hemorrhagic shock and traumatic injury. Changes in metabolism were hypothesized to be dependent upon the metabolic state the animal occupies upon injury (fed or fasted). It was also hypothesized that a metabolite or metabolites could serve as a marker of mortality.

Materials and Methods: Nuclear magnetic resonance (NMR) spectroscopy and Chenomx software were used to generate individual profiles of metabolite concentrations (the metabolome) for each urine sample obtained. Because hemorrhagic shock produces drastic changes in urine concentration and large fluctuations in the concentrations of endogenous metabolites in the urine, urine must be normalized to urine output to allow for accurate comparisons between urine samples. The urinary metabolome was analyzed with partial least squares discriminant analysis (PLS-DA) and with a scale-free network.

Results: PLS-DA models showed that metabolites associated with respiration, ischemia/reperfusion injury, and cell membrane damage were observed in the urine two hours after the initiation of resuscitation. Other metabolites which may be associated with injury sustained from surgical preparation were observed at 20 hours after the initiation of resuscitation. The metabolites 1,6-Anhydro β-D-glucose and mannose were associated with the metabolome of fed animals. The network analysis of the metabolome

is reflective of the scale-invariant nature of metabolism. Respiratory metabolites were separated by whether they are involved in aerobic or anaerobic respiration. Anaerobic metabolites were also associated with markers of cell membrane rupture. Lactate, pyruvate, 2-oxoglutarate, succinate, taurine, glycine, dimethylamine, and creatinine were identified as well-connected hub metabolites in the network. No metabolites were associated with survival alone.

Conclusions: The pathophysiology associated with hemorrhagic shock can be treated as a scale invariant process particularly with respect to metabolism. Results from a traditional metabolomics treatment of the data with PLS-DA models were congruent with results from a scale-invariant, weakly modular network of the urinary metabolome. Other samples obtained from these experiments (muscle, liver, and serum) could benefit from a similar treatment. Additional work in (a) integrating the metabolomes of all four biological samples and (b) creating a physics-based theory of hemorrhagic shock may provide important information about mortality and the propagation of injury.

Table of Contents

List of Tables

List of Figures

Chapter 1: Introduction

Hemorrhagic shock and traumatic injury are the most common causes of death for American civilians aged 1-44 years. An estimated 29.6 million injuries occur per year, resulting in approximately 179,000 deaths [1]. The problem is more complicated in combat settings, particularly when patient care is applied in the field with limited resources and under non-optimal conditions. This is highlighted by the statistic that 87% of patients have no documentation of pre-hospital treatment. It is estimated that 17% of deaths due to battlefield trauma are preventable. More than 80% of these deaths are related to hemorrhage [2]. Over the past 50 years, marked advances in resuscitation and post-injury care have reduced mortality rates by nearly 80% in the civilian sector and by about 50% in the military sector [1,3].

Historically, D.P. Cuthbertson's definition of the "ebb" and "flow" phases of hemorrhagic shock was an early attempt to characterize the metabolic response. The ebb period is defined by "depression" of metabolism, increased permeability of the capillaries, and loss of vascular tone, particularly when hemorrhage is accompanied by trauma. The flow period which follows is defined by an increase in metabolism, apparently driven by an inflammatory response which "precedes actual repair." With respect to urine production, Cuthbertson notes widespread irregularities among experimental subjects, from the prevalence of anuria during the ebb phase to the restoration of urine output during the flow phase [4]. In general, the ebb period lasts for less than 24 hours. The flow period can last for many days.

A comprehensive understanding of the mechanisms that underlie hemorrhagic shock is still lacking. Conditions of reduced perfusion and oxygen delivery are key to defining the pathophysiology associated with hemorrhagic shock. These conditions induce a complex system of interrelated responses and compensatory actions. Among these are a switch from aerobic respiration to anaerobic metabolism, increased production of reactive oxygen species, an inflammatory response, an immune response, and a hormonal response. Many of these responses lead to cell death. Left unchecked, this can progress to multiple organ dysfunction (MODS), though the mechanisms linking cell death to MODS are unclear.

The metabolic component of the response to hemorrhagic shock and traumatic injury is examined here in a porcine model that is designed to (1) assess the effect of feeding status on hemorrhagic shock, traumatic injury, and resuscitation, and (2) to reflect battlefield conditions with limited resources for the first hour of resuscitation. The experiment includes 40 animals: negative controls (n=5), positive controls (n=3), fasted animals subjected to the hemorrhagic shock and traumatic injury protocol (n=16), and sucrose-fed animals subjected to the hemorrhagic shock and traumatic injury protocol (n=16). A pulmonary contusion, a 35% hemorrhage, and a liver crush injury are all administered to experimental animals and positive controls. For the first hour after injury, resuscitation measures are limited to maintaining blood pressure at 80 mmHg with administration of lactated Ringer's. This is followed by full resuscitation measures (shed blood and lactated Ringers to 90 mmHg by algorithm) for experimental animals. This period is maintained for 20 hours. Experimental measures obtained during this time

include timed serum, urine, liver, and muscle biopsies. The tissue and biofluid samples are frozen at -80°C, and are later processed with metabolomics techniques to identify and quantify the metabolites present in each sample. Additionally, several measures of vitals and clinical laboratory variables are taken. A list of these variables is presented in Appendix A.

This dissertation focuses specifically on the metabolic information contained in the urine samples. Urine samples are analyzed with standard techniques used in metabolomics, a field of study devoted to systematically profiling the collection of metabolites contained in a particular biological sample. It is assumed that a given physiologic or pathophysiologic state is associated with a characteristic metabolic profile or metabolome. Generally, metabolites are identified with either NMR or mass spectroscopy, and quantified with software. The set of metabolite concentrations are analyzed with chemometric techniques to identify patterns and relationships between metabolites. Here, ^{1}H NMR spectra are collected of each urine sample, and the spectra are profiled using Chenomx software [5] to identify and quantify 62 metabolites. Partial least squares discriminant analysis (PLS-DA) models are built to establish links between the metabolic profile and observable quantities in Chapter 6.

Metabolomics has several shortcomings. The metabolic profile associated with a given pathophysiology does little to address causality or provide context for what is observed. Without experiments such as ^{13}C tracing, it is impossible to state whether an implicated metabolic pathway is upregulated or downregulated. Many metabolites are involved in several interconnected pathways, and traditional metabolomics is also unable

to pinpoint which pathway or pathways are altered by the associated pathophysiology. Additionally, like the other –omics disciplines (genomics, proteomics), metabolomics is an attempt to solve an inverse problem. There is no existing model or theory that can be fit to the data; instead, models are constructed from the data itself, which is likely incomplete, noisy, and composed of interdependent or confounded variables. The lack of a theory to fit to observed data means that there is little context to describe observed behavior.

Biofluids are far more common in metabolomics studies than tissue samples because they are easy to obtain and process for high-throughput studies, but interpretation of the resulting metabolomes can be difficult. Interpretation of the urinary metabolome is particularly difficult because it is composed of filtered blood that has been subjected to the absorbing, secreting and reabsorbing mechanisms of the kidney. This process is largely a black box, particularly with respect to hemorrhage.

Some things can be done to address these shortcomings within the confines of these experiments, which do not include ^{13}C tracing. First, some context is provided from West et al's theory of allometric scaling with respect to metabolic rate [6]. The authors present metabolic rate as a scale-invariant quantity that spans all levels of an organism, from chemical processes in the mitochondrial membrane to the organism as a whole. Known sub-mitochondrial, sub-cellular, and cellular processes that are implicated in hemorrhagic shock are discussed in light of scale invariance, and are tied together in Chapter 2 to highlight the interdependence of certain physiological processes over scales of several orders of magnitude. The treatment of this topic begins with a discussion of

the loss of molecular oxygen in redox reactions and the electron transport chain (~10^{-10} m), and scales up to discuss the effects of this on the mitochondrial scale (~10^{-6} m), the cellular scale (~10^{-5} m), and the organ scale (~10^{-1} m). Treatment of the pathophysiology of metabolism with respect to hemorrhage is particularly appropriate since cellular metabolism is known to be a scale-invariant process [7]. Scale-invariant networks can be used to model cellular metabolism. These networks establish functional relationships between metabolites, a feature lacking in traditional metabolomics analyses. This kind of analysis is carried out in Chapter 7.

Though this dissertation focuses only on the urinary metabolome, it must be understood that little can be said about a truly systemic pathophysiology such as shock with information from only one type of biological sample. Integration of the muscle, liver, and serum metabolomics data, though outside the scope of this dissertation, will be key to understanding the metabolic adaptations that occur as a result of hemorrhagic shock, which is the ultimate goal of these experiments. However, integration of this data will require that the urinary metabolome is well-understood in its own right. To that end, this dissertation is composed of three chapters of background material and three chapters of analysis. Chapter 2 gives a treatment of known metabolic alterations associated with hemorrhagic shock and the consequences of these alterations. This information is presented as occurring over several scales, extending from the sub-mitochonrial scale to the whole-body scale. Because the urine is presented here, some knowledge of the kidney is required for context; this is presented in Chapter 3. A treatment of the discipline of metabolomics is given in Chapter 4, including history, common analysis

practices, and long-term goals of the field. Chapter 5 begins the analysis portion of this dissertation, with a treatment of normalization of the urinary metabolome. Because of drastic changes in fluid volume associated with hemorrhage and the administration of resuscitation fluids, urine concentration varies widely throughout the experiment. These changes must be accounted for if the metabolite concentrations in each urine sample are to be accurately compared. Chapter 6 uses PLS-DA models to associate metabolites with experimental timepoint (roughly pre-shock, shock, early resuscitation, and late resuscitation), experimental group, and survival. In Chapter 7, a network analysis of the urinary metabolome is discussed. This work concludes with a comparison of the results of Chapters 6 and 7, and future directions for data analysis of these experiments will be explored.

Chapter 2: Hemorrhagic Shock

Often a result of traumatic injury, hemorrhagic shock is a condition of reduced perfusion that results in diminished delivery of oxygen to tissues. In the United States, trauma is responsible for an estimated 179,000 deaths annually and 61% of deaths of people under the age of 44 [1]. The physiological state that accompanies hemorrhagic shock is caused by loss of the circulating blood volume to the system, and the compensatory actions such as vasoconstriction, inflammatory response, and immune response that are undertaken by the organism as a whole can result in further injury on a systemic level. The mechanism or mechanisms that lead from the organism's initial response to trauma and hemorrhage to the development of multiple organ failure is unknown, though thousands of original research articles on mechanisms of injury associated with hemorrhagic shock have been written over the past 50 years. A host of cytokines and markers of inflammation play a role in the propagation and sustainment of injury. Reactive nitrogen species play a role in addition to their oxygen counterparts. Disruptions and alterations in calcium, an important component of cell signaling, have also been studied [8,9].

While other biological systems such as the endocrine system are involved in the compensatory actions that occur as a result of shock, this thesis will demonstrate that alterations in metabolism are important to understanding the organism's response to hemorrhage. It is a goal of this work to suggest that, while many mechanisms are important in the progression of hemorrhagic shock, a unified picture of the organism's response as a whole is lacking. Study of individual mechanisms via evaluation of individual components of a particular pathway provide useful supporting information

about the physiological consequences of hemorrhagic shock, but even taken as a whole, they do not provide a global picture of the progression of the pathology from insult to death. Current cutting-edge research on biological networks, fractal analyses, and nonlinear dynamics may all have a place in filling this gap.

Fractals, scale invariance, and self-similarity provide structure to the understanding of hemorrhagic shock and its consequences in terms of metabolism on multiple levels within an organism. The cardiovascular system can be considered to be a space-filling network composed of terminal end units (capillaries) which are the same size. Assuming this network has evolved to minimize energy expenditure while delivering oxygen to the entire system, West et al. have derived a universal quarter-law scaling law for biological systems which covers 21 orders of magnitude [10]. This scaling law has important implications for metabolism, as the model predicts that metabolic rate scales as $M^{3/4}$, where M is body mass. Such a law allows one to extrapolate the metabolic rate of mammals from the shrew (M~0.001 kg) to the elephant (M~5000 kg). The scale invariance in metabolic rate was found to extend to all levels of organization for a given organism, extending from the organism itself down to the cellular level, the mitochondrial level, and to the level of the respiratory complex within the mitochondrial cristae [6].

The metabolic consequences of oxygen loss via hemorrhagic shock will be discussed on various scale levels starting at the respiratory complex. The consequences of the loss of oxygen to the coupled reactions of electron transport through the respiratory complex and oxidative phosphorlyation will come first. The discussion will then scale up

to the mitochondrial level, where alterations in the tricarboxylic acid (TCA) cycle will be discussed. At the cellular level, mechanisms of cellular death arising from the conditions at the lower levels will be discussed. Finally, the consequences of hemorrhagic shock at the organ level in the form of multiple organ failure will be discussed. While outside the scope of this thesis, the framework of scale invariance may shed new light on the implications of the development of late, system-wide complications such as multiple organ failure.

Level 0: The respiratory complex and aerobic respiration

Disruptions to normal physiological function as a result of hemorrhage can be considered to begin with the absence of molecular oxygen. The respiratory complex, located inside the mitochondrial inner membrane, is responsible for the transfer of electrons along the electron transport chain, a process which is coupled to the transfer of protons across the mitochondrial membrane. The resulting energy is captured in the form of ATP, the basic unit of energy in eukaryotic metabolism. Oxygen is a vital component of this process, as it is the terminal end unit of the electron transport chain. It is the energetically preferred electron acceptor, and its presence is required to couple electron transport to oxidative phosphorylation, the process that stores energy in the form of ATP. When oxygen is lacking, these processes (collectively termed aerobic respiration) cannot function, and anaerobic respiration becomes the primary source of ATP generation. The ATP yield from anaerobic respiration is 2 molecules of ATP, whereas aerobic respiration yields 31 molecules of ATP.

Oxidation corresponds to loss of an electron, and reduction to the gain of an electron. An oxidizing agent will oxidize other substances, and become reduced in the process. Reducing agents reduce other substances, and will become oxidized themselves. For example, NADH is oxidized to NAD+. This process can also be thought of as the removal of hydrogen (oxidation) or the addition of hydrogen (reduction). The transfer of electrons between oxidizing and reducing agents occurs in the respiratory complex and is the cornerstone of respiration (see Figure 2.1). However, such reactions can also be pathological. These types of reactions are highly implicated in hemorrhagic shock.

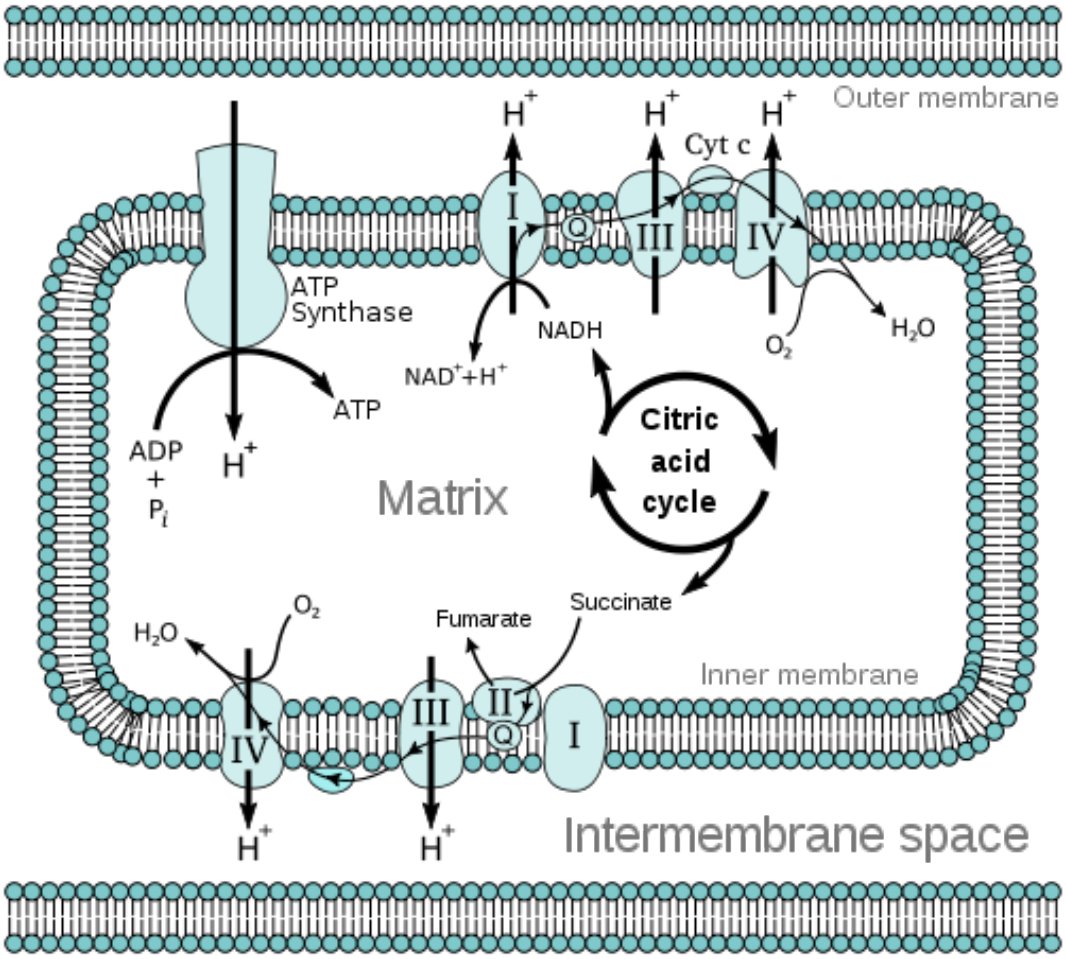

Figure 2.1: Diagram of the respiratory complex embedded in the inner membrane of the mitochondria. The complex is composed of four enzymes shown as Complex I, Complex II, Complex III, and Complex IV. The diagram illustrates the coupling of electron transport through the chain to the production of ATP. The implications of the loss of oxygen via hemorrhagic shock to the citric acid cycle will be discussed in the next section. Figure from http://en.wikipedia.org/wiki/Oxidative_phosphorylation.

Oxidative stress, a state characterized by an overabundance of reactive species, occurs in small amounts within normal physiologic function of mitochondrial oxidative phosphorylation as a consequence of the reactions that occur in the respiratory chain.

Under normal conditions, some electrons leak out of the respiratory complex prematurely and lead to the formation of a partially reduced form of oxygen, superoxide anion O_2^-. This leads to the formation of additional highly reactive compounds such as hydrogen peroxide and the hydroxyl radical. These compounds are known as free radicals, or molecules with unpaired electrons that are highly reactive. Free radicals that contain oxygen such as hydrogen peroxide are collectively known as reactive oxygen species (ROS). Electron leakage from the respiratory chain is known to increase under ischemic conditions, to a level significant enough to cause damage. The re-introduction of oxygen to the system does not remedy the situation; rather, it is made worse. This type of pathophysiology, called reperfusion injury, generates more free radicals than does ischemia [11,12]. Left unchecked, the resulting imbalance in free radicals can disrupt the homeostasis of the cell as a whole, and cause damage to lipids, proteins, and DNA [13]. To begin to understand how this occurs, we scale the discussion up to the level of the mitochondria.

Level 1: The mitochondria and the TCA cycle: The hub of the metabolic network and aerobic respiration

If one imagines scaling upward from the redox reactions that are implicated in ischemia/reperfusion injury, the next logical step is to look at the mitochondrion. As discussed, the mitochondrial membrane contains the respiratory complexes of the electron transport chain. The tricarboxylic acid (TCA) cycle precedes the electron transport chain via the TCA intermediate succinate, and it is linked to vital

extramitochondrial processes such as glycolysis. Through the steps of glycolysis, the TCA cycle, electron transport, and oxidative phosphorylation, the cell is able to break down one molecule of glucose and store the energy in 31 molecules of ATP. Collectively, these steps make up aerobic respiration, a process that is wholly reliant upon the mitochondria. This makes the TCA cycle the cornerstone of cellular metabolism.

The process of glycolysis, which occurs in the cytosol of the cell, is a breakdown of glucose molecules that culminates in the formation of pyruvate. Pyruvate is then transported from the cytosol to the mitochondria, where it is oxidized into acetyl CoA. This molecule marks the first step in the TCA cycle, shown below in Figure 2.2.

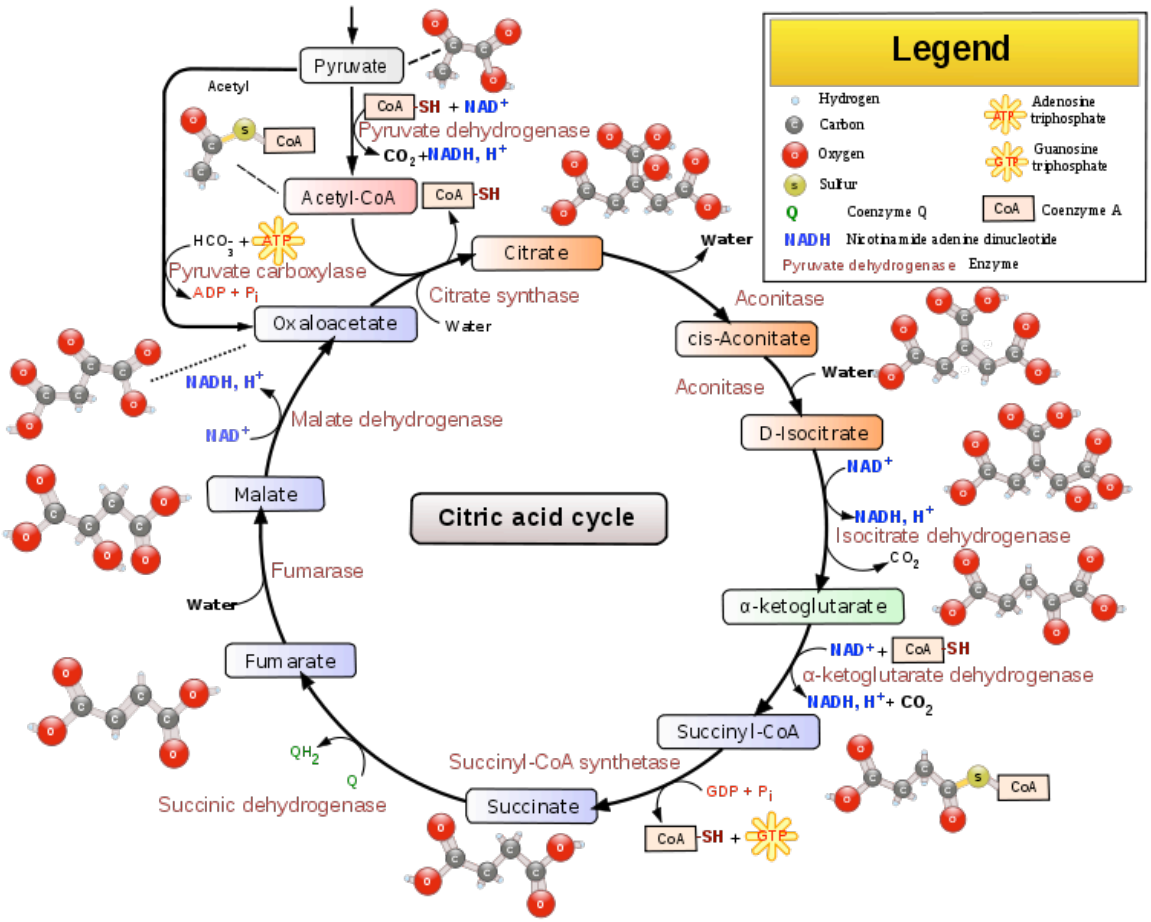

Figure 2.2: The tricarboxylic acid (TCA), or Citric acid, cycle. Metabolites citrate, cis-Aconitate, 2-oxoglutarate (α-ketoglutarate), succinate, and fumarate are quantified in the urine of pigs subjected to hemorrhagic shock, and will be discussed in Chapter 6. This metabolic pathway is the cornerstone of catabolism in eukaryotic cells. Figure taken from http://en.wikipedia.org/wiki/TCA_cycle.

The TCA cycle is linked to the electron transport chain via the metabolite succinate (see Figure 2.1). Through its intermediate metabolites and its products, the TCA cycle has connections to almost all other anabolic and catabolic pathways of metabolism, as shown in Figure 2.3.

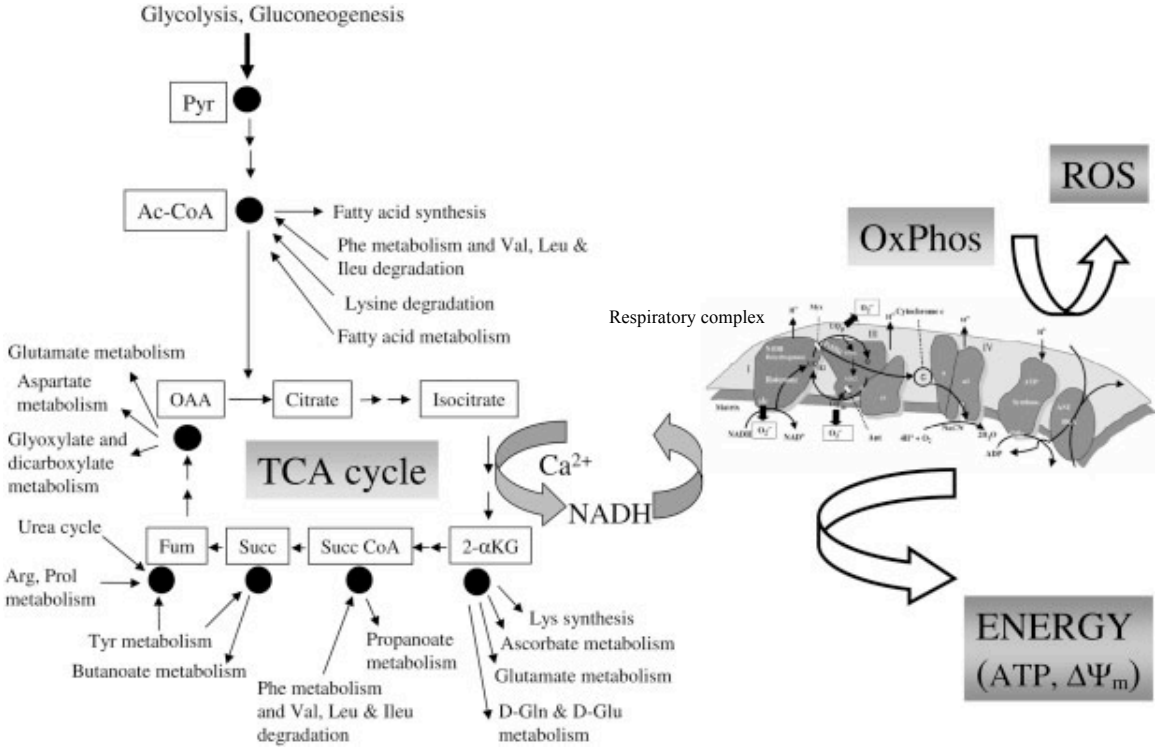

Figure 2.3 The figure shows the connection between the TCA cycle, the electron transport chain and the respiratory complexes, and oxidative phosphorylation (OxPhos), the site of the lion's share of ATP generation. The processes outlined here show the links between the steps of aerobic respiration. Through the TCA cycle and its intermediates, the mitochondria is connected to most other metabolic processes in the cell. Figure taken from [14].

As the name implies, aerobic respiration can only occur in the presence of oxygen. We will see that anaerobic respiration, the alternative respiratory mechanism that is given preference in hypoxic conditions, operates wholly outside the mitochondria. The exclusion of mitochondria from cellular respiration is not the end of the consequences for mitochondria in hypoxic conditions. Mitochondria can suffer disruptions in membrane potentials and increased production of ROS [8,15]. Depolarization of the inner mitochondrial membrane and excessive ROS production in a fraction of the

mitochondria within a cell can trigger oscillations in mitochondrial membrane potential, ROS production, and a change in redox state of mitochondria throughout the cell [16]. This demonstrates the interconnectedness of mitochondrial function within a cell and we will see that this connectedness forms a network that links many mitochondria, extending beyond the confines of the cell.

Level 2: Outside the mitochondria: Anaerobic respiration and ROS, revisited

In hypoxic conditions, pyruvate does not enter the mitochondria; instead, it is broken down to lactate in the cytosol. This mechanism, anaerobic respiration, is favored under conditions of low oxygen when the production of pyruvate in the cytosol exceeds the usage of pyruvate in the mitochondria. The mitochondria are essentially excluded from respiration at a substantial cost. Anaerobic respiration yields only two molecules of ATP as compared to the 31 given up by aerobic respiration. One would expect abnormal ATP levels to be observed as a consequence of hemorrhagic shock, and they are [8]. Additionally, the breakdown of pyruvate to lactate yields large amounts of lactate that must be metabolized by the liver or the kidney. High lactate levels in the blood are a standard clinical marker of shock. Increases in lactate in the urine and serum are observed after hemorrhage and trauma in the porcine experiments discussed in Chapters 5-7.

Free radicals are also part of regulating normal cellular processes outside of the mitochondria. ROS production via neutrophils and catecholamines are important mechanisms for maintaining normal functionality under environmental stress. Nitric

oxide (NO) is important in maintaining vascular tone. Superoxide is important in the maintenance of redox homeostasis in the presence of low levels of oxidative stress that occur due to electron leakage as discussed above. These molecules are sensitive to the levels of oxygen in the system—as oxygen tension falls, the system becomes more reduced and compensatory mechanisms are upregulated. A cohort of compensatory mechanisms for maintaining redox homeostasis on the cellular level exists, as shown in Figure 2.4.

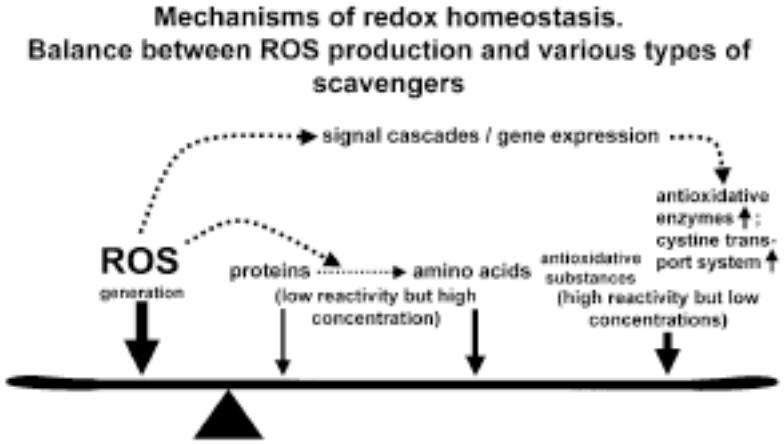

Figure 2.4: Redox homeostasis mechanisms. Excessive ROS production is balanced by the production of oxygen radical scavengers, or compounds that counteract the effect of reactive oxygen species. Antioxidants such as glutathione and superoxide dismutase are powerful neutralizers of free radicals, but exist at relatively low abundances in biological systems. Amino acids such as tyrosine, tryptophan, and cysteine are less reactive than antioxidants, and have weak scavenging properties. However, these compounds help maintain redox homeostasis by their sheer abundance. (Figure taken from [17]).

When this balance is disturbed, the compensatory mechanisms described above are used to bring the physiological system back into balance. In certain cases, the mechanisms that are protective become detrimental to the cell and lead to death. It is unclear how to define the transition between normal physiology and pathophysiology that occurs in this context. However, the duality of the protective and harmful aspects of free radicals and ROS is well accepted in modern physiological research.

Several mechanisms of cellular ROS production are appropriate to the discussion of the pathophysiology relevant to trauma and ischemia/reperfusion injury [18,19]. Neutrophils, which rely on ROS as part of the mechanism used to clear diseased tissue, can infiltrate tissues. This is a hallmark of acute inflammation in trauma. Catecholamines, particularly epinephrine, are an important part of the hormonal response to injury, and are responsible for the initiation of such physiological responses as vasoconstriction. However, catecholamines become a source of ROS when oxidized. Finally, a well-studied mechanism of I/R injury in epithelial cells is via the enzyme xanthine dehydrogenase, the enzyme xanthine oxidase (XO), and its substrates hypoxanthine and xanthine. In ischemic conditions, xanthine dehydrogenase is converted to xanthine oxidase, and the metabolite ATP degrades to the substrates xanthine and hypoxanthine in the following manner:

ATP ➔ADP ➔Adenosine➔ Inosine ➔Hypoxanthine ➔Xanthine ➔ Uric Acid➔Allantoin

Upon reperfusion and the reintroduction of oxygen to the system, hypoxathine and xanthine react with XO to form superoxide [20] Increases in urinary excretion of hypoxanthine and xanthine are indicative of ATP depletion [21].

Level 3: Cell death and the mitochondrial network

The previous sections have highlighted how the lack of oxygen causes pathological alterations to sub-cellular processes and depletion of ATP stores. The culmination of these processes can result in cellular death [14,22]. The signal for cell death can be given by the mitochondria, for example, when mitochondrial ROS production increases. Under these conditions, the outer mitochondrial membrane is depolarized and becomes permeable. This initiates a cascade of reactions which culminate at the cellular level in apoptosis [13]. One such proposed mechanism, the mitochondrial permeability transition pore, is illustrated in Figure 2.5.

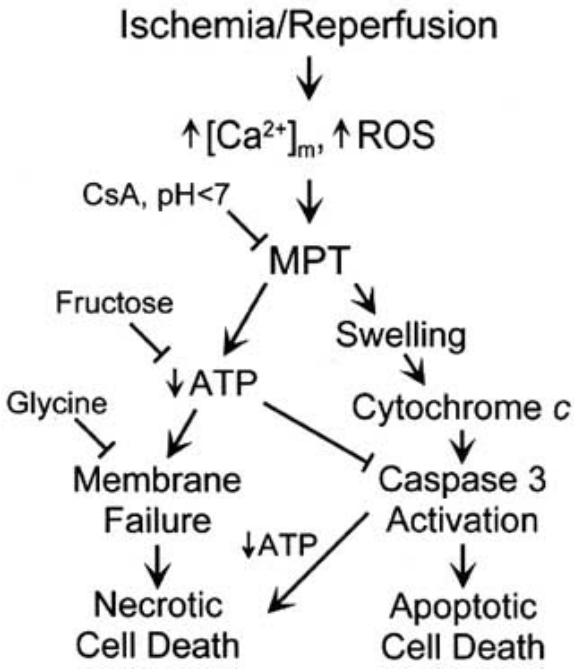

Figure 2.5: The cascade of events linking ischemia/reperfusion injury with cell death as described in the mitochondrial permeability transition pore mechanism (MPT=mitochondrial permeability transition). Note that this mechanism links reactive oxygen species, mitochondrial membrane depolarization, and decreased ATP levels. The pore is thought to remain closed during ischemia, and opens upon reperfusion. The opening of the pore allows Figure taken from the Center for Cell Death, Injury, and Regeneration at the Medical University of South Carolina (http://academicdepartments.musc.edu/ccdir/research_projects/MPT)

An increase in lactate production after loss of mitochondrial membrane potential due to induced apoptosis has been observed [23]. This suggests a link between mitochondrial membrane function and compensatory anaerobic glycolysis, a phenomenon which should occur as a result of severe hemorrhage.

Though the MPT mechanism links many of the pathophysiologies associated with hemorrhagic shock to cell death, it does not explain in and of itself how the injury

propagates from mitochondria to mitochondria, and from cell to cell. Such a propagation of injury and death must occur if it is to explain the systemic injury that can develop days after hemorrhage. As stated earlier in this chapter, the mitochondria themselves can be considered to form a network. Disruption of the mitochondria or its constituents via oxidative stress, for example, may result in a "transition to a critical pathophysiological state" [14], a disruption that is propagated throughout the network. These networks display power law behavior that implies scale invariance, a property that would allow for propagation of dysfunction over several orders of magnitude, linking mitochondrial and cellular dysfunction with systemic dysfunction.

Level 4: The organ

The discussions of the previous levels suggest that redox homeostasis becomes disrupted under conditions of reduced perfusion and ischemia, such as those that accompany hemorrhagic shock. When oxygen is unavailable, homeostasis is disrupted and the system is shifted toward a more reduced state. This has been quantified at the organ level in the form of redox potentials in ischemic dog hearts [24]. Before ischemia, the average redox potential of dog hearts from seven experiments was -239.6 mV. Under ischemic conditions induced by opening the thorax, the average redox potential was measured to be -263.1 mV. Gudbjarnason et al. calculated the redox potential of each state by measuring the concentrations of lactate and pyruvate in coronary sinus blood and arterial blood. Lactate and pyruvate serve as proxies for NAD+ and $NADH_2$, the oxidized and reduced substrates in muscle, respectively. These two metabolites play the

same role in liver cells [25]. Krebs notes that this relationship is valid for the cytoplasm; to assess the redox state of the mitochondria, the ratio of β-hydroxybutyrate to acetoacetate is appropriate. Redox homeostasis is not reestablished upon re-oxygenation; in fact, the opposite happens. Free radical generation can increase by 2 orders of magnitude upon reperfusion[20].

Redox states as assessed by the lactate to pyruvate ratio are shown in Figure 2.6 below. Lactate and pyruvate levels in liver and muscle samples were taken from the experiments discussed in chapters 6 and 7. Ratios were log-transformed to facilitate visualization. In the liver (left), pairwise t-tests showed that lactate to pyruvate ratios of E2 animals that died (magenta) are different from C1 animals (black), E1 animals that lived (green), and E2 animals that lived (turquoise). In the muscle, the lactate to pyruvate ratios for C1 animals (black) are different from both E1 animals that lived (green) and E2 animals that died (magenta). Means of statistically significant log-transformed lactate to pyruvate ratios are shown in Table 2.1 with p-values.

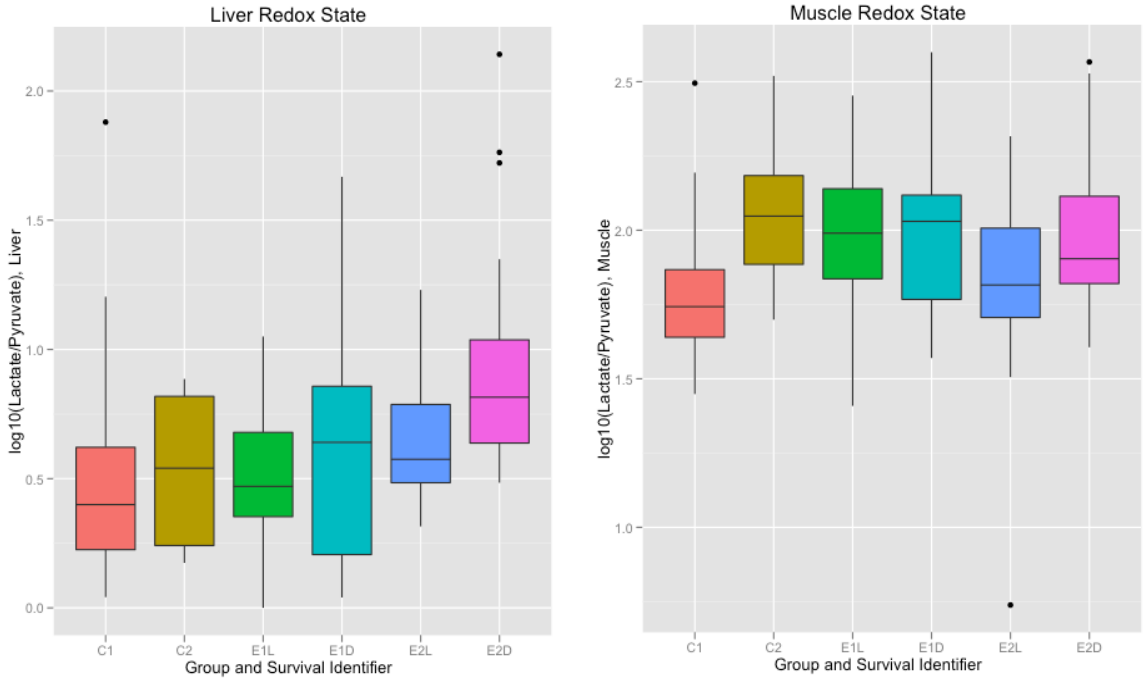

Figure 2.6: Redox state of liver (L) and muscle (R) tissue from the porcine hemorrhagic shock experiments discussed in Chapters 6 and 7. In each case, the ratio of Lactate:Pyruvate has been log-transformed for ease of visibility. Legend: C1= no hemorrhage; C2=hemorrhage, no resuscitation; E1=fasted, hemorrhaged, and resuscitated; E2=fed, hemorrhaged, and resuscitated. L=lived; D=died. Outliers were not assessed in this data.

Liver Log(Lactate/Pyruvate)			**Muscle Log(Lactate/Pyruvate)**	
C1: 0.47±0.23	E1L: 0.53±0.23	E2L: 0.64±0.23	C1: 1.78±0.23	C1: 1.78±0.23
E2D: 0.94±0.44	E2D: 0.94±0.44	E2D: 0.94±0.44	E1L: 1.98±0.23	E2D: 1.99±0.26
$p=1.6\times10^{-5}$	$p=1.3\times10^{-5}$	p=0.0071	p=0.01	p=0.045

Table 2.1: Means ± standard deviations and p-values for the statistically different redox states described above. Comparisons are organized by column; for instance, in the liver, C1 and E2 animals that died are shown to be different with a p-value of 1.6×10^{-5}. It is outside the scope of this chapter to interpret the results of organ redox state as measured in these experiments. This result is intended to illustrate that organ

redox state is indeed altered in the hemorrhagic shock and traumatic injury experiments that are the focus of this dissertation.

In some patients, the alterations in organ function progress to organ dysfunction or further, to multiple organ dysfunction syndrome (MODS). In the latter scenario, even organs that are not directly subjected to trauma are injured. As Aon argues, "The strong interconnectedness among components (of the mitochondrial network) bestows scaling properties to these networks, implying that the result of an action in the subcellular realm, e.g., mitochondrial network, can escalate to the tissue and organ levels, such as under crises, like heart attack or disease, resulting in catastrophic arrhythmias" [26].

The transition from normal physiology to pathophysiology on the organ level is as ill-defined as on the cellular level. Only some trauma patients will develop MODS after a deficit of oxygen; whether or not a patient will progress to MODS seems dependent upon a host of factors including duration and severity of hypoxia, immune status, severity of injury, or underlying conditions such as diabetes [27,28]. Onset of MODS can occur as quickly as 24 hours, or may develop over days.

It may be possible to model the transition from normal physiology to pathophysiology as a phase transition, though little to no evidence of this is found in the literature. Consideration of the fractal properties of the organ system may be helpful. The vasculature, lungs, kidney, and folding of the intestines all demonstrate fractal organization [29], and though phase transitions as a mechanism for pathophysiology have not been studied, phase transitions in fractal media have [30]. Percolation and Ising models may also be relevant [31,32].

The difference between aerobic and anerobic respiration due to loss of oxygen is apparent on all four levels discussed in this chapter—at the level of electron transport, at the level of TCA metabolism inside the mitochondria, at the cellular level with enzyme-based generation of ROS and apoptosis, and at the organ level with lactic acidosis and a change in redox state. The author does not claim that the path traced in the above discussion, connecting the readily observed organism as a whole, the cell, and the mitochondria, and ending at the level of relevant redox reactions in the mitochondria is the only path from oxygen loss to death in hemorrhagic shock. However, it is a path with known, well-studied components, and it can be understood as occurring in a scale-free environment that provides a conceptual and mathematical link between individual components of a system that operates over 8 orders of magnitude. We see that conditions of redox homeostasis inside the mitochondria contribute to mechanisms of apoptosis, which in turn is linked to multiple organ failure. The interdependence of these mechanisms, linked across scales of several orders of magnitude, demonstrates the fundamental interconnectedness of biological systems.

Chapter 3: The Kidney

The previous chapter discussed the consequences of hemorrhagic shock and injury for cellular metabolism. Because the latter chapters of this dissertation focus on metabolites observed in the urine, a discussion of the major anatomical and physiological processes of the kidney is in order. In the course of this discussion, it will be demonstrated that some key characteristics of the kidney are in line with previously discussed notions of scale invariance and have certain properties shared by networks.

In addition to creating urine, the kidney is responsible for maintaining system-wide homeostasis in the organism. This involves maintaining adequate solute (mostly salt) concentrations in the blood, filtering waste for excretion, balancing acid/base and buffer levels, and maintaining blood pressure over long periods of time. Blood flow to the structures of the kidney and the rate at which it filters the blood must both be very tightly controlled. The average value of the blood pressure is fixed by the kidney, a feat it accomplishes by regulating the total fluid volume in the body via tubuloglomerular feedback (TGF) [33]. This mechanism will be discussed in the context of hemorrhage below.

For reference, the major structures of the kidney are shown in Figure 3.1. Blood flows in through the renal artery to be filtered by the kidney. The filtrate (urine) exits the kidney through the ureter, which leads to the bladder. Filtered blood eventually exits the kidney through the renal vein.

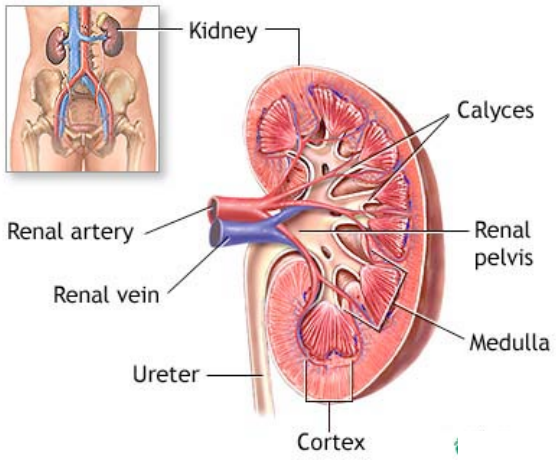

Figure 3.1: Cross-section of the human kidney, courtesy of the University of Maryland Medical Center (http://www.umm.edu/imagepages/1101.htm).

The workhorse of the kidney is a collection of filtering and urine-collecting structures known as nephrons (see Figure 3.2); each human kidney is estimated to contain about one million nephrons [33]. These structures are responsible for filtering waste from the blood and also play key roles in the regulation of acid/base homeostasis and blood pressure regulation. Any filtrate that is not taken back into the blood is eventually excreted in the urine via the ureter and the bladder.

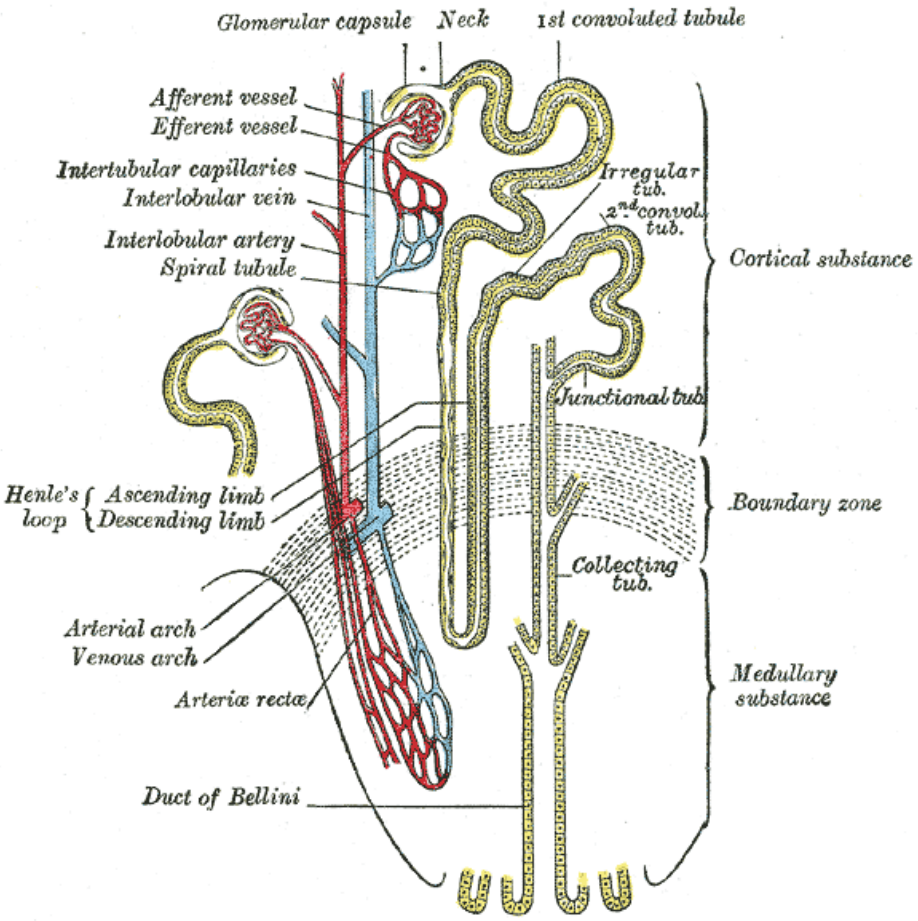

Figure 3.2: Nephron of a kidney. Blood flows into the kidney via the renal artery, where it eventually reaches the afferent arteriole at the glomerular capusle, the start of the nephron. Structurally, most nephrons span the cortex and medulla. Figure from Gray's Anatomy [34]. The glomerular capsule, the afferent and efferent vessels, the first convoluted tubule, and the Loop of Henle are discussed in the text below. The macula densa is not shown here.

The filtration process begins with the glomerulus. Here, capillary loops of the glomerulus are surrounded by a hollow space known as the glomerular capsule or Bowman's capsule. Blood enters and leaves the capsule via the afferent and efferent arterioles, respectively. Approximately 20% of the blood is filtered from the capsule; the

remainder flows out of the efferent arteriole. The efferent arterioles branch out to form the peritubular capillaries, which permeate the cortex before merging back together to exit the kidney via the renal vein. The rate at which blood is filtered at the glomerulus is known as the glomerular filtration rate, or GFR. In normal humans, the GRF is about 180 L per day [33]. This quantity is highly regulated through TGF to maintain homeostasis.

The composition of the filtrate at the beginning of the nephron is very similar to that of plasma, save the large proteins that are filtered out by passage of the fluid through Bowman's capsule. As the filtrate travels through the nephron from the cortex to the medulla, its composition changes via three major mechanisms: filtration, secretion, and reabsorbtion. Most organic molecules (lactate, glucose, amino acids, etc) are reabsorbed at the first convoluted tubule, or proximal tubule (Figure 3.2). This part of the nephron also secretes organic anions such as 4-aminohippurate, and organic cations such as choline and creatinine. The secretion of creatinine by the proximal tubule complicates the use of creatinine clearance as a measure of GFR [35]. The tubules also secrete osmolytes such as trimethylamine and trimethylamine N-oxide. These metabolites are known to protect the kidneys from an otherwise stressful environment with high concentrations of salt and urea [36,37].

The urine is concentrated as it passes through the Loop of Henle as shown in Figure 3.2. Though the mechanisms that conectrate the urine as it passes through the tubules are not completely understood, it is clear that a countercurrent exchange system is established between the vasa recta and the Loop of Henle in the medulla that allows concentration of the urine [38]. The common medical teaching is that the countercurrent

gradient is established via active transport of sodium chloride and urea absorbtion and secretion in various parts of the kidney. However, lactate and glucose concentrations in the inner medulla may also play a role [39].

After leaving the Loop of Henle, the nephron tubule winds back to the glomerulus. The macula densa sits at this juncture (see Figure 3.3), and is a key component in the regulation of renal blood flow and GFR. The relationship between the kidneys and the cardiovascular system is a prominent functional component of this location. Feedback mechanisms become important here, as intrarenal baroreceptors, renal sympathetic nerves, and the macula densa are all in communication with each other to regulate homeostasis via TGF. A portion of the filtrate that has passed through the concentrating mechanisms of the Loop of Henle will return to the glomerulus in its tubule. Here, the macula densa cells sense the concentration of the filtrate; the information is communicated back to glomerulus to decrease the GFR. The mechanism that accomplishes the decrease in GFR is unknown; however, it involves both hemodynamic coupling and vascular signaling [40]. TGF is affected by the presence of angiotensin II, a hormone that constricts the arterioles to maintain GFR.

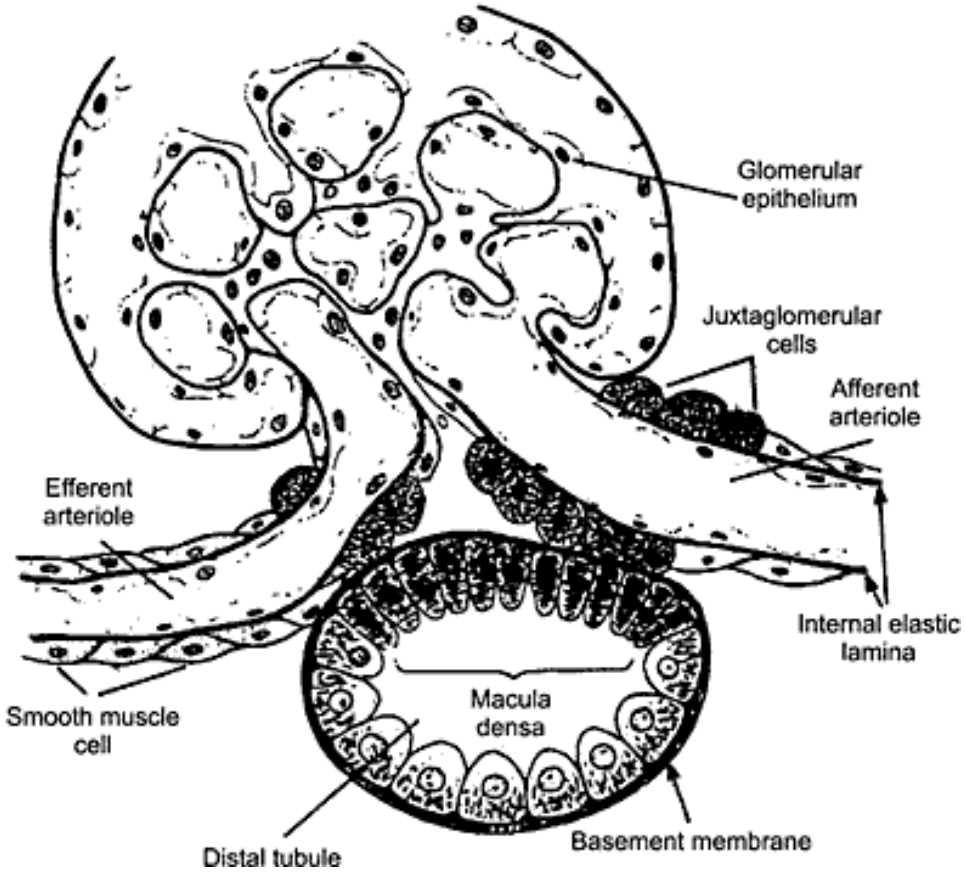

Figure 3.3: The juxtaglomerular apparatus that forms the beginning of the nephron. Renin-secreting mechanisms are located in the macula densa and in the juxaglomerular cells, or granular cells. Note that the macula densa is located on the other side of the loop of Henle from the glomerulus. The tubule winds back to the glomerulus and aids in TGF. Figure from Kaul et al [41].

During hemorrhage, the kidney attempts to maintain blood flow to the inner medulla while allowing flow to the cortex to remain reduced. Increased vascular resistance in both the afferent and efferent arterioles allows GFR to remain normal at this point unless the hemorrhage is severe. This environment is known to persist even after blood volume, blood pressure, cardiac output, and urine output are normalized [42]. The macula densa senses changes in fluid flow. In response, the juxtaglomerular cells secrete renin (see

Figure 3.4), a hormone that signals the production of angiotensin II in the liver. Angiotensin II is a potent vasoconstrictor, and it is responsible for maintaining GFR under conditions of reduced blood flow as described. Renin release can be stimulated by high glucose levels, high succinate levels, or high osmolyte levels [43]. This may explain the association between increased levels of trimethylamine N-oxide and ischemic injury to the kidney [44].

Cells of the proximal tubule are subject to mitochondrial dysfunction in response to ischemia/reperfusion injury in much the same manner as outlined in Chapter 2. Experiments demonstrate that MPT directly follows disruptions to the respiratory chain [45] in these cells. The cells of the glomerulus, on the other hand, are robust to hypoxic conditions because they require little oxygen to function under normal conditions. The opposite is true for cells in the cortex

[46]

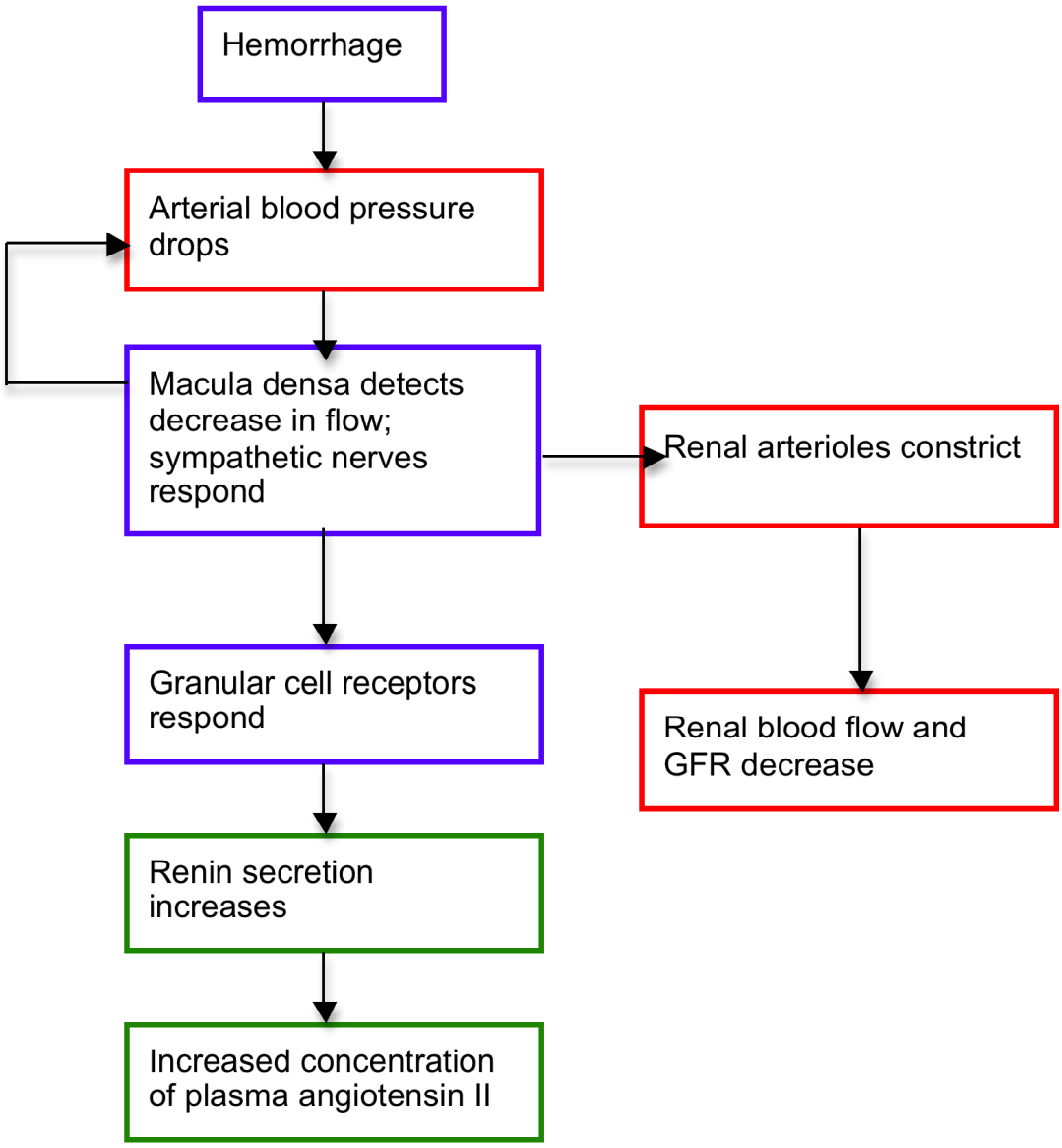

Figure 3.4: Flowchart of events from hemorrhage to the release of angiotensin II as described in the text. Red indicates a decrease in the quantity or effect described; green indicates an increase in the quantity or effect described; blue indicates an event. Reproduced from Vander's Renal Physiology [33].

As discussed in Chapter 2, blood lactate levels are an important clinical marker of hemorrhagic shock and traumatic injury. The large amounts of lactate generated by

injury must be cleared, and the kidney plays a significant role in the clearance of lactate according to Bellomo et al. The liver and the kidney metabolize most of the excess lactate. Less than 10% is excreted in the urine. The clearance of lactate appears to be handled via a feedback loop of glycolysis and gluconeogenesis between the cortex and medulla, respectively. Renal ability to clear lactate is steady through 30% blood loss. At 40%, renal lactate uptake decreases. At 50% hemorrhage, the kidney becomes a source of lactate. Reperfusion does not restore normal lactate clearance [47]. In the shock experiments discussed in the latter half of this thesis, average volume hemorrhaged was 36.09 ± 2.99% which implies that lactate clearance is largely normal.

Certain aspects of kidney structure and function are concomitant with notions of scale invariance and networks that were discussed previously. Kidney function may be modeled with networks of nephrons that are capable of modeling emergent behavior [40]. The venous and tubule systems that infiltrate the kidneys both have space-filling scale-invariant properties [29]. Kidney behavior shares important characteristics with metabolic networks and mitochondrial networks. While certain characteristic variables associated with nephron behavior can oscillate with time, the kidney as a whole is quite stable [48]. It is so stable that a human can survive with only a fraction of a kidney [40]. This may be a consequence of the kidney's structure, a complicated system of interdependent components whose behaviors are coupled. Tubuloglomerular feedback effectively regulates GFR on a timescale of seconds, while the consequences of this process leads to whole-body regulation of blood pressure after a few days.

Chapter 4: Metabolomics

It has been shown that powerful changes in metabolism accompany hemorrhagic shock and traumatic injury. The basic anatomy and physiology of the kidney has been discussed, with brief treatments of the urine-concentrating mechanisms and how the kidney participates in the global response to hemorrhage. In this chapter, it will be demonstrated that techniques used in the field of metabolomics can identify and quantify metabolites in a biological sample. This method will be applied to porcine hemorrhagic shock and traumatic injury in Chapters 5-7 of this dissertation

Born out of J.K. Nicholson's pharmaceutical research [49], metabolomics is part of the "omics" branch of molecular biology that performs large-scale profiling. In the study of drug toxicity, multiple organ function must often be assessed. Genomics and proteomics, the predecessors of metabolomics, were natural phenomena to examine since many drugs interact with genetic material or produce sets of enzymes that metabolize the drug. In general, however, pharmaceuticals can interact with organisms in ways that are not limited to interactions with genes and proteins. Additionally, genomics and proteomics do not provide real-time markers of multiple organ function *in vivo.* Metabolites in biofluids are in dynamic equilibrium with cellular metabolites. One can then assume that drug interactions with genes and proteins will leave their mark in the metabolites present in the organism's fluids, since metabolites can be considered as the collective end product of gene expression [50].

Metabolomics attempts to systematically identify and quantify the concentrations of a large portion of the metabolites of an organism in response to a given stimulus or

physiological state [51], allowing the concept to extend beyond drug toxicity studies to encompass a wide range of physiological states including disease, injury, and nutrition. Metabolomics studies are generally observation driven and hypothesis-generating. Tissues and biofluids have been examined in a variety of nutritional, drug, and disease states in an effort to characterize an organism's biochemical response to such stimuli [52-57]. Many studies espouse high-throughput technologies in conjunction with nuclear magnetic resonance or mass spectrometry to generate as many metabolic profiles in a given state as possible. Common goals are to identify biomarkers or sets of biomarkers of disease [58-60], to profile normal variation in metabolism, and to aid in pharmaceutical research [61-63]. Plants and bacteria are also the subject of metabolomics studies [64,65] but are outside the scope of this work.

Metabolomics relies upon the identification of varying amounts of metabolites in a complex matrix. Abundances can range from approximately 0.01 mM for trace metabolites to about 100 mM for abundant metabolites, such as urea in the urine. Nicholson proposed nuclear magnetic resonance as the detection technique of choice, as it allows quantification of metabolites simultaneously with little sample preparation and "without prejudice" [49]. Mass spectrometry has also become a primary detection tool [66-68]. In this body of work, NMR is used exclusively for quantification of metabolites.

Nuclear Magnetic Resonance Theory

Magnetization: The NMR signal arises from the bulk magnetization induced in a sample by a large static magnetic field, B_0. Each nuclear particle has an intrinsic magnetic

moment, $\vec{\mu}$. (For the sake of discussion, we will focus on the proton signal; the proton's magnetic moment is 1.41×10^{-26} J/T.) When placed in a magnetic field $\vec{B}$, each state has a potential energy of $\vec{\mu} \cdot \vec{B}$. In general, the magnetic moments in a sample are randomly aligned, leaving zero net magnetization in the sample as shown in figure 1.

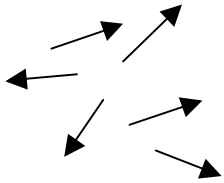

Figure 4.1: Randomly aligned magnetic moments

However, when the sample is placed in a large static magnetic field, the *z*-components of the moments align or anti-align with the field.

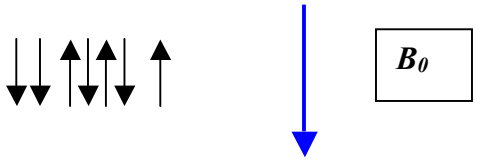

Figure 4.2: Magnetic moments in a static field

The spin system obeys Boltzmann statistics; the distribution is therefore given by

$$N_{up} = N_{down} e^{-2\mu B / kT} \qquad (4.1)$$

where 2μB is the energy difference between the up and down states, *k* is Boltzmann's constant, and *T* is the absolute temperature. This factor can be calculated easily since $\mu B = m\gamma\hbar B$, where *m* is the spin quantum number; γ is the gyromagnetic ratio, or 42.576 MHz/T for protons, and $\hbar$ is Planck's constant. At room temperature, the ratio of spins aligned to antialigned with the magnetic field is only on the order of one in $1x10^6$. This small asymmetry is the source of the bulk magnetization of the sample and thus the NMR signal.

To calculate the bulk magnetization of the sample, we must turn to the partition function, as this is a thermal system. To start, the bulk magnetization *M* is given by

$$\vec{M} = N\langle\vec{\mu}\rangle \qquad 4.2$$

where *N* is the spin density of the sample, in number of spins per unit volume and $\langle\vec{\mu}\rangle$ is the average magnetic moment of the sample. Because the spin states are quantized by the quantum number *m* along the *z* axis, we will calculate $\langle\vec{\mu}\rangle$ with a partition function, summing over the spin states *m*.

$$\langle \mu_z \rangle = \gamma\hbar \frac{\sum_{m=-I}^{I} m e^{\gamma m\hbar B / kT}}{\sum_{m=-I}^{I} e^{\gamma m\hbar B / kT}} \qquad (4.3)$$

We can approximate the exponential terms with their polynomial expansions. Because $m\gamma\hbar B/kT << 1$, we can use the approximation $e^x \approx 1 + x$. For protons, we sum over the spin states {-1/2, 1/2}, obtaining

$$\langle \mu_z \rangle = \frac{\gamma^2\hbar^2 I(I+1)}{3kT} B \qquad (4.4)$$

where *I* is the spin of the particle, e.g. ½ for protons. Thus, we see that the z-component of the average magnetization of the sample is given by

$$M_z = \frac{N\gamma^2\hbar^2 I(I+1)}{3kT} B \qquad (4.5)$$

In practice, the static magnetic field of an NMR spectrometer is directed along the *z* axis of the laboratory coordinate system.

The Bloch Equations: The expectation value of the magnetic moment obeys the classical behavior predicted by analyzing the torque on the magnetic moment:

$$\frac{d\mu}{dt} = \gamma(\vec{\mu} \times \vec{B}) \qquad (4.6)$$

becomes

$$\frac{d\langle\vec{\mu}\rangle}{dt} = \gamma(\langle\vec{\mu}\rangle \times \vec{B}) \qquad (4.7)$$

Because of this relationship, the spin system can be described classically, by only considering vector calculus, as is done here. The time-dependent behavior of the

magnetization vector can be obtained easily by multiplying $\langle \vec{\mu} \rangle$ on both sides by N so that

$$\frac{d\vec{M}}{dt} = \gamma(\vec{M} \times \vec{B}) \qquad (4.8)$$

In practice, $\vec{B}$ is aligned with the z axis as mentioned above. Imposing this condition allows us to examine the time dependence of each component of the magnetization, though care must be taken to use coordinate systems correctly, as the torque on the magnetic moments is best viewed in a rotating reference frame relative to the stationary laboratory frame.

The bulk magnetization $\vec{M}(t)$ precesses about the axis of the static magnetic field (the z axis in the laboratory frame) with frequency ω_0:

$$\omega_o = -\gamma B_o \qquad (4.9)$$

where ω_0 is the Larmor frequency, and γ and B_0 are the gyromagnetic ratio and the static magnetic field strength in Tesla, respectively.

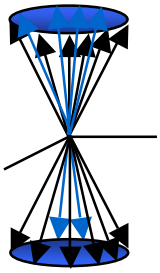

Figure 4.3: Spins precess about the laboratory z-axis with angular frequency ω_0.

Note that the Larmor frequency can be understood as the frequency of photon required to induce transitions between the Zeeman states of the protons in the static field.

The magnetic moment's precession constitutes a changing magnetic field, which will induce a voltage in a receiver coil according to Faraday's Law. However, no signal is detectable when the bulk magnetization is collinear with the *z* axis because of symmetry. In this case, $\frac{d\Phi}{dt} = 0$, where Φ is the magnetic flux; therefore, no signal is produced in accordance with Faraday's law. When an RF pulse is applied to perturb the sample from the *z*-axis, the magnetization precesses about the *z*-axis with angular frequency ω_0 in such a way as to break the symmetry. Now, $\frac{d\Phi}{dt} \neq 0$and the resulting voltage is picked up by the receiver coil. A specifically-calibrated pulse, called the 90° pulse, is applied in the *x*-*y* plane to bring the bulk magnetization vector from the *z*-axis down into the *x*-*y* plane, resulting in a maximized signal.

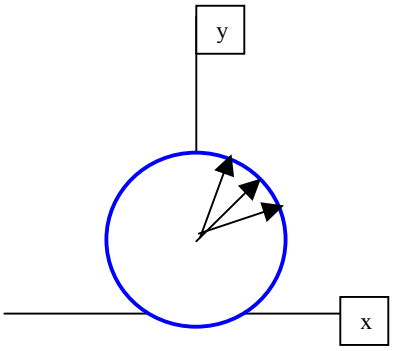

Figure 4.4: Spins are in the *x*-*y* plane after the application of a 90° pulse.

The signal decays exponentially as the spins relax from the *x*-*y* plane back to the *z*-axis; this is due to *spin-lattice relaxation* as the spin population returns to thermal equilibrium along the *z*-axis. However, the signal also decays as the spins dephase in the *x*-*y* plane due to *spin-spin relaxation*. Bloch assumed solutions to differential equations governing

the time-dependence of the magnetization vector to arrive at a set of equations describing the signal's behavior; these rely on the use of rotating frames of reference.

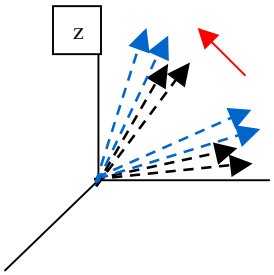

Figure 4.5a: Precessing spins return to thermal equilibrium due to spin-lattice interactions.

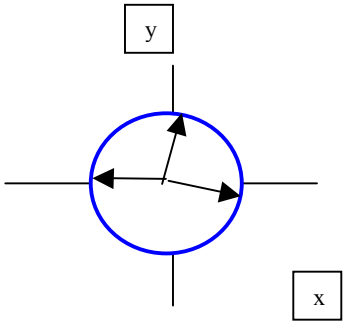

Figure 4.5b: Spins dephase in the x-y plane due to spin-spin interactions.

The equation governing spin-lattice interactions comes from the time-dependent behavior of the *z*-component of the magnetization. Bloch proposed that

$$\frac{dM_z}{dt} = R_1[M_o - M_z(t)] \qquad (4.10)$$

such that

$$M_z(t) = M_o - [M_o - M_z(0)]e^{-R_1 t} \qquad (4.11)$$

where R_1 is the relaxation rate constant; $T_1 = 1/R_1$. For the transverse magnetization components, Bloch proposed that

$$\frac{dM_x}{dt} = -R_2 M_x(t) \qquad (4.12\text{ a})$$
$$\frac{dM_y}{dt} = R_2 M_y(t) \qquad (4.12\text{ b})$$

such that

$$M_x(t) = M_x(0)e^{-R_2 t} \qquad (4.13\text{ a})$$
$$\mathrm{M_y}(t) = M_y(0)e^{-R_2 t} \qquad (4.13\text{ b})$$

Here, T_2=1/R_2 describes the transverse relaxation of the spins.

To express the Bloch equations in the laboratory frame, we must incorporate the original time dependence of the magnetization, $\frac{d\vec{M}}{dt} = \gamma(\vec{M} \times \vec{B})$. Thus, we have

$$\begin{aligned}
\frac{dM_z}{dt} &= \gamma[\vec{M}(t) \times \vec{B}(t)]_z - R_1(M_z(t) - M_o) \\
\frac{dM_x}{dt} &= \gamma[\vec{M}(t) \times \vec{B}(t)]_x - R_2 M_x(t) \qquad (4.14) \\
\frac{dM_y}{dt} &= \gamma[\vec{M}(t) \times \vec{B}(t)]_y - R_2 M_y(t)
\end{aligned}$$

These are the famous Bloch equations, describing the behavior of the bulk magnetization of a sample in an NMR experiment. The equations predict the exponential decay of the NMR signal according to two relaxation mechanisms: spin-lattice interactions, and spin-spin interactions. The time constant governing spin-lattice interactions is given by T_1; the time constant governing spin-spin interactions is T_2. Both properties are inherent to a particular sample.

Chemical Shift: The NMR signal is the result of bulk magnetization induced in a sample

of spins (e.g. protons), but it is the magnetic field that each proton in the sample "sees" that determines the spectral position of a particular resonant peak. A cursory examination of the equation governing the Larmor precession frequency above (eq. 4.9) indicates that each proton will have its own resonant frequency determined by *B*. An NMR spectrum is composed of these resonant peaks. Because of diamagnetic effects of electron shielding, each proton will be subject to a different net magnetic field; this then results in a slightly different resonant frequency for each proton. Anisotropies in the magnetic field can also affect proton resonance frequencies. These paramagnetic effects are due mainly to different orientations of the molecules in the magnetic field. The effective magnetic field *B* seen by a given proton in an external magnetic field B_0 is given by

$$B = (1 - \sigma)B_o \qquad (4.15)$$

where σ is a dimensionless shielding constant. In this way, different compounds will have different resonant frequencies.

The chemical shift of a given compound, then, is a way to reference the positions of the different proton resonances relative to a known internal standard, such as 4,4-dimethyl-4-silapentane-1-sulfonic acid (DSS) or 3-trimethylsilylpropionic acid (TSP). Chemical shift is defined in such a way as to be independent of the spectrometer frequency:

$$\delta = \frac{\text{resonant frequency - reference frequency}}{\text{spectrometer frequency}} \times 10^6 \qquad (4.17)$$

The chemical shift is given in units of parts per million to make a manageable scale. By definition, the chemical shift of the internal standard is 0 ppm. A resonant peak on the right end of the spectrum is subject to greater shielding effects than one at the left end;

therefore a resonant peak at 2 ppm is subject to greater shielding effects than one at 6 ppm.

In this way, different proton resonant frequencies form a "fingerprint" according to how the proton is shielded from the external field by neighboring electrons. The shielding varies from molecule to molecule, giving each compound a unique resonant signature. Identification of these resonant signatures translates directly to identification of different molecules present in a sample. This means hundreds of different molecules may be identified in one spectrum, making this technique very appropriate for identifying many small molecules in a biological sample. In this, NMR has a significant advantage over mass spectrometry techniques. To identify organic acids, one must use gas chromatography mass spectrometry; to identify amino acids, ion-exchange chromatography must be used; for purines and pyrimidines, high performance liquid chromatography must be used [69,70]. All of these groups of metabolites can be detected in one spectrum with NMR.

The NOESY Pulse Sequence: Urine is composed of approximately 95% water under normal conditions, making it the dominant proton signal. To accurately identify and quantify metabolites that are present in the 1-0.01 mM range, the water signal must be dealt with. This could be accomplished in two ways: lyophilization of the sample to remove the water, or manipulation of the NMR signal by pulse sequence. The latter was chosen for the experiments discussed in Chapters 5-7 to minimize manipulation of the sample itself, which could lead to sample loss. In the preparation scheme used here,

urine is simply buffered, centrifuged, and mixed with an internal standard. Presaturation of the water signal is the simplest and most straightforward way to remove the water signal from the spectrum. Here, the transmitter is set to the water resonance, and a long, low power pulse is applied to saturate the water signal. This is followed by a short 90° pulse to excite the remaining spins. The result is shown in the top panel of Figure 4.6, which shows a 1D proton NMR spectrum of a urine sample with presaturation of the water signal. For comparison, a spectrum without presaturation of the water signal was taken with the same urine sample.

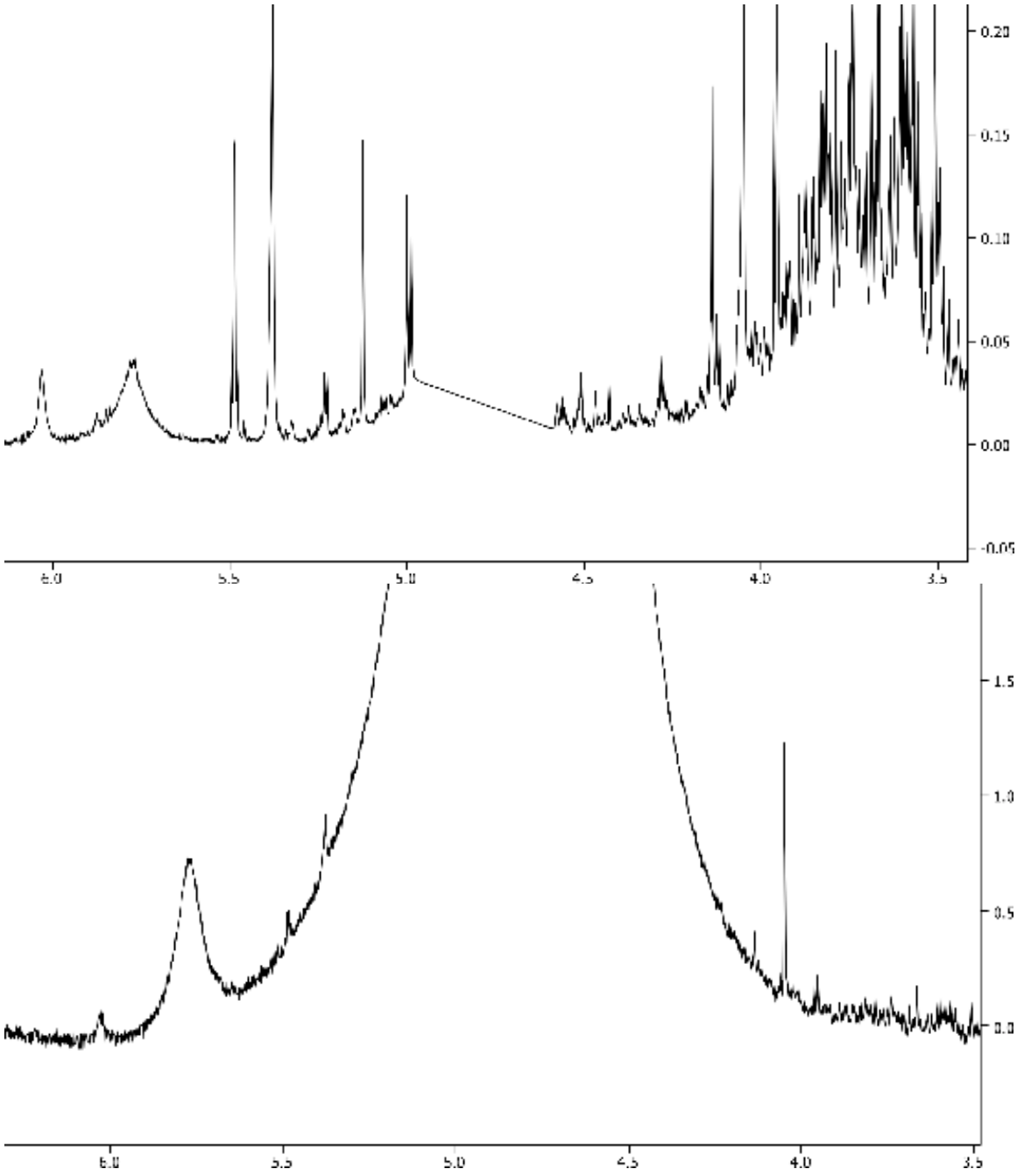

Figure 4.6: Example of a urine spectrum with presaturation of the water signal (top) and without (bottom). Presaturation increases signal to noise and allows for identification of peaks near the water resonance.

It is clear that the presaturation allows for proper identification of NMR spectral resonances that are otherwise overshadowed by the water peak. The signal-to-noise ratio is increased, as can be seen between 3.5 and 4.0 ppm in Figure 4.6.

NOESY presaturation is recommended for use with urinary metabolomics [51,71]. This technique allows for reliable quantification of signals that are close to the water resonance because of its fine control over chemical shift selectivity. However, resonances that have protons in exchange with water may be diminished by the suppression. In general, this is known for metabolites such as urea, and these resonances are usually not reported in the literature.

Experimental parameters used for metabolite quantification in the urine samples obtained from the model of hemorrhagic shock discussed in this dissertation are as follows: the 90° pulse width was calibrated for each sample, and was generally 12-13 μs. The relaxation time was defined by each sample's 90° pulse width. The relaxation delay was 2 s, the acquisition time was 3 s, the spectral width was 10 kHz, the total number of data points collected was 63,000, and the number of transients collected was 128, for a total experiment time of 11 minutes and 17 seconds. During the relaxation period, the water resonance was presaturated.

Analysis of Metabolomics Data

Standard analysis techniques: Once obtained, NMR spectral data can be dealt with in either a top-down or bottom-up fashion [72]. Traditional spectral methods rely on

comparisons of peak features, and individual metabolites are not quantified per se. Instead, a spectrum is divided into a set of bins of equal width and the spectral area contained in each bin is used for further analysis of the data. With targeted profiling, individual metabolites are identified and quantified with a library of known metabolite resonances that the user superimposes onto the spectrum. Concentrations are interpolated from the resonance of the internal standard, which is added to each sample at a known concentration. These concentrations are used in all further analyses of the data.

Targeted profiling methods are used in this analysis with Chenomx software [5]. The major advantage of targeted profiling over spectral binning occurs in regions of high spectral density, where one bin may contain resonances from several metabolites. In such cases, it is difficult to accurately assign the portion of spectral area contained in the bins to a particular chemical species. Additionally, changes in pH between samples will affect the chemical shift of spectral peaks. This means that bin content could change between samples. With Chenomx software, the spectral fits can be superimposed, allowing the user to accurately assign metabolite concentrations even in cases of significant metabolite overlap and variation in chemical shift.

Concentration data from both spectral binning and targeted profiling can be analyzed by standard chemometric methods [73,74]. It is assumed that these data sets are inherently incomplete and contain collinear structures. The most common method of extracting information from such a data set is principal components analysis [75], a method that performs a linear transformation of the data onto a set of orthogonal axes, or principal components. Each axis is defined in such a way as to define the largest portion

of variation in the data. The first principal component describes the largest portion of variance of the data set, the second principal component describes the second-largest portion of variance of the data set, and so on. Ideally, the first two or three components will describe most of the variance contained in the original data. The transformed data is expressed as scores and loadings. In this context, each point on a scores plot represents an individual experimental (urine) sample. Two or three-dimensional scores plots are used to visualize the orientation of samples with respect to each other in the principal component space. Samples that are closer together are more similar than samples that are farther apart. In this way, similar samples will cluster together, allowing visualizations of potentially meaningful clusters of data. The principal component loadings vectors are the eigenvectors of the covariance matrix, and express the weight of the original variables on the transformed data. The directions of the loadings correspond to the scores plots; in this way, it is possible to see which of the original variables contribute most to the position of a biological sample in the scores plot. Biplots allow efficient visualization of this by superimposing loadings onto a scores plot, as shown in Figure 2.7.

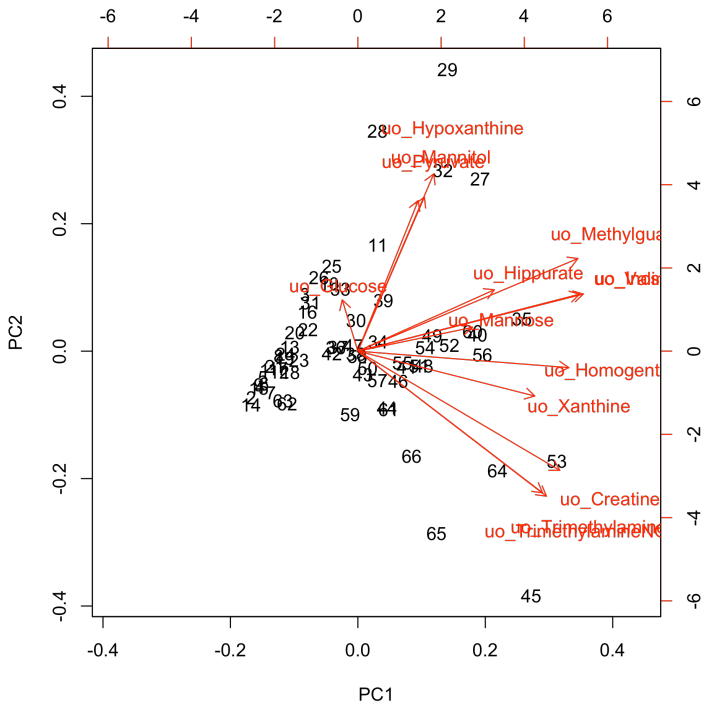

Figure 4.7: Biplot of the first two principal components in an analysis of urinary metabolome in hemorrhagic shock. Principal component 2 is plotted against principal component 1 to aid in visualization of the scores, which are identified as numbers. Each number corresponds to a urine sample in the data set. Loadings vectors are shown as red arrows, with the original variables (metabolite names) at the head. The orientations of the loadings vectors can be used to assess which of the original variables influence the position of the scores.

PCA can be useful for visualizing the variation in the data, identifying trends, and identifying outliers that lie far away from other data points. As such, it is often used as a first step in the analysis of metabolomic data. To build a model with classification or predictive power, other methods such as partial least squares discriminant analysis (PLS-DA) and orthogonal partial least squares discriminant analysis (OPLS-DA, a variation of PLS-DA), must be used. These methods treat the problem of how to model responses or

observables (ie survival) via a set of predictive variables (ie metabolite concentrations) [76]. These models can be used with metabolomics data to classify new samples and identify biomarkers. The relationship between the predictive variables (**X**) and the observables (**Y**) can be expressed as **Y=Tq+f**, where **Y** is the matrix of observables, **T** is the matrix of scores associated with the predictive variables, **q** is the matrix of loadings associated with **Y**, and **f** are the residuals, which should be small. Each element of **Y** is generally expressed as +1 if it is a member of the class, and -1 if not [76,77]. Both PCA and PLS-DA will be used in this analysis (see Chapter 6).

PLS-DA models are evaluated based on the value of Q^2, which is a measure of the goodness of fit or predictive power of the model. Specifically,

$$Q^2 = 1 - \frac{\sum_i (y_i - \hat{y}_i)^2}{\sum_i (y_i - \bar{y})^2}$$

where $\hat{y}_i$ is the predicted value of class membership for sample *i*, and $\bar{y}$ is the mean value of *y* for all samples [78]. Q^2 can take on values between 0 and 1, where 1 indicates perfect prediction. In practice, models with $Q^2 > 0.5$ are considered to have reasonable predictive power.

Correlations have also been used in metabolomic data analysis. Because metabolites are synthesized from other metabolites, there is a basic interdependence in metabolic systems. It is important to calculate correlations for systems in the same state, and sample sizes must be large enough (n>10) [79]. Log-log plots are often useful in this context.

Physiologies examined with metabolomics analysis techniques: Inborn errors of

metabolism are the obvious subset of physiologies to study with metabolomics. An early demonstration of the capabilities of NMR in this regard used urine to diagnose methylmalonic aciduria, canavan disease, cystinuria, glycerol kinase deficiency, 3-hydroxy-3-methylglutaryl-CoA lyase deficiency, alkaptonuria, and propionic aciduria [80]. In a book published only three years later, 58 inborn errors of metabolism were diagnosed with NMR of body fluids [70]. The standard model-building techniques used in metabolomics work well in this context. PCA and PLS-DA models were able to correctly discriminate between 47 normal urine samples obtained from newborns, 9 samples from newborns with PKU (phenylketonuria), and one sample from a child with maple syrup urine disease [81].

Many other physiologies have been examined with metabolomics techniques, including diabetes [82,83], various cancers [59,69,84-92], heart disease [93-96], neurological diseases [97-103], asthma [104], organ transplant [105], and celiac's disease [106]. The majority of these studies offer a handful of potential biomarkers culled from statistical analyses with PCA or PLS-DA models. Though most of the models can separate cases from controls, not all of them have been validated with a blinded set of data. It is often difficult to confirm biomarkers, and NMR studies with tracers such as ^{13}C are required to definitively prove which pathways are active and whether activity is upregulated, or downregulated. Metabolomics methods, even when they are not thoroughly utilized, often provide a reasonable starting place for further analysis of implicated pathways.

Some patient studies provide a first step on the road to clinical diagnosis with metabolomics. Models developed from large patient samples of Type 1 diabetics can

distinguish controls from case in serum, and can diagnose diabetic nephropathy with specificities and sensitivities that approach those of clinical techniques diabetes [107,108]. A study of Celiac's disease patients treated with a gluten-free diet [106] was able to separate treated patients from untreated patients with metabolomics techniques in both urine and serum. After one year on the diet, all but one Celiac's patient classified as healthy. A similar return to a healthy profile after treatment was observed in a study of cerebrospinal fluid of schizophrenic patients [99]. Finally, measurements of citrate in expressed prostate fluid and in semen were both better at identifying patients with prostate cancer than prostate-specific antigen measurements [109].

Metabolomics has underperformed in some studies of coronary heart disease. Conflicting results surround the validity of blood cholesterol content as a predictor of coronary disease. One study used proton NMR to demonstrate that differences in blood cholesterol could identify patients with coronary heart disease; these differences also apparently correlated with severity of disease [96]. Another group [94] claimed that the differences observed in these cholesterol profiles was due to patients' use of statins to manage cholesterol. A third study found that metabolomics techniques were no better at predicting cardiac events in diabetic patients than chance [110]. This collection of studies demonstrates the role that bias can play in confounding scientific results [73]. In this case, the bias is likely related to the perceived role of cholesterol in the development of heart disease. It has recently been suggested that the role of cholesterol in heart disease is anything but clear; however, the long history of cholesterol's association with heart disease has hindered research in understanding the impact of cholesterol on heart disease

[111]. This bias likely contributes to inconsistent results in metabolomics studies of heart disease that include cholesterol data.

Long-term goals: As evidenced by the above discussion, much of the current work in this field is focused on the identification and characterization of pathological states. A common goal of metabolomics studies is the characterization of pathology via biomarker discovery. While the concept of a biomarker under pathophysiological conditions is a useful one, it should not be expected that biological function or dysfunction could be completely characterized by one biomarker. Currently, metabolomics techniques can offer diagnostic capabilities that approach the accuracy of traditional clinical techniques, but ultimately, this is a step on the path toward the ultimate goal of personalized medicine [112]. Both systems biology and network analyses can pick up where metabolomics leaves off.

Systems biology is "the analysis of the relationships among the elements in a system in response to genetic or environmental perturbations, with the goal of understanding the system or the emergent properties of the system." [113] This definition certainly dovetails with that of metabolomics in general, but systems biology encompasses proteomics and genomics as well. Such a definition assumes that there is a molecular basis for pathophysiology in biological systems, and that pathophysiological states can be characterized as such. When viewed at a systems level, biological functions and states arise from a series of complex interactions between the nodes of a network. These interactions must be understood if personalized medicine is to be realized.

Biological networks [7] give a theoretical framework to the experimental maps that are constructed in metabolomics, genomics, and proteomics studies. These networks, which model the cellular control system as measured by the –omics disciplines, have certain attractive properties. They obey a power-law in degree distribution, and they show scale-invariance. Scale invariant networks have the characteristic that all nodes are closely connected—any two are connected by only a few links. This is accomplished by the presence of a handful of hub nodes, which are linked to many other nodes.

In terms of cellular metabolism, the nodes of such a network are metabolites. Metabolites are linked if they participate in an enzyme-catalyzed reaction. These links have a direction since most of these processes are irreversible. The number of "in" and "out" links to a metabolite dictates how well-connected it is to other metabolites, thus leading to the presence of well-connected hub metabolites such as pyruvate [7]. Metabolic networks constructed in this way demonstrate functional relationships between metabolites. This is potentially useful in any number of pathophysiological states. However, network analyses are not commonly performed with metabolomics data. Such an analysis will be performed on the urine metabolomics data presented in chapter 7.

Relevance to hemorrhagic shock: Evidence of injury and pathophysiology due to hemorrhagic shock should be present the metabolome associated with hemorrhagic shock and traumatic injury. The previous chapter's discussion of ischemia/reperfusion injury shows the role that metabolism plays in mediating the organism's response to hemorrhagic shock. However, to date, there has been only one proper metabolomics

study of hemorrhagic shock [114]. This study was done on serum samples obtained from 32 trauma patients, taken at an average of 28 minutes from trauma. A subset of the 43 profiled metabolites are associated with known pathologies such as metabolic acidosis, hyperglycemia, and decreased functionality of the urea cycle. Evidence of a decrease in lipid synthesis, which has not traditionally been studied with hemorrhagic shock, was also observed.

The above study was more limited in scope than the experiment that this thesis is part of. In the study outlined in chapters 6 and 7, 80 animals are subjected to a standardized hemorrhagic shock and traumatic injury model. Positive and negative controls are included. Serum, muscle, liver, and urine samples are all harvested multiple times over the course of each 72-hour experiment. This allows the progression of each animal's metabolic response to hemorrhagic shock, traumatic injury, and resuscitation to be followed under controlled conditions, instead of relying on a one-time sample. Biopsies from multiple sources also allow for a more complete picture of the organism's response as a whole. For instance, metabolites that are generally seen as markers of I/R injury such as hypoxanthine and xanthine indicate a depletion of ATP stores when observed in the urine [21]. A study of only serum would miss such information.

A network analysis of the hemorrhagic shock model described in this work could prove useful in elucidating the chain of events that drives the progression from hypoxia to cellular dysfunction to death. The presence of well-connected hubs allows perturbations in metabolism to rapidly propagate throughout the network, but it also makes the network vulnerable in a particular way. Scale-independent networks are robust to single-

component failure because of the type of connectedness they exhibit. If several randomly chosen metabolites are removed from the network, it will still function as a reasonable path can still connect the remaining metabolites. This robustness does not extend to hubs, however. If a hub is removed or altered, the network will split into a series of smaller, unconnected networks and the larger cellular network will fail [7]. Identification of failed metabolic hubs in the hemorrhagic shock and traumatic injury could be useful in elucidating mechanisms of pathophysiology.

The idea of "network medicine" [115] could also be useful. Systems biology and network biology assume that pathophysiologies are the result of a complex series of network interactions. Network medicine further hypothesizes that interdependencies of cellular networks lead to "deep functional, molecular, and causal relationships among apparently distinct phenotypes" [116]. In this vein, a longer version of the hemorrhagic shock study could potentially provide links to the development of complications such as acute respiratory distress syndrome or multiple organ dysfunction, which do not present until days after the insult. The experiments discussed in chapters 6 and 7 are not long enough to provide any information on the development of these pathophysiologies.

Chapter 5: Normalization of Urine

Hemorrhagic shock, defined by severe loss of an organism's fluid volume, is a leading cause of death in both military and civilian trauma victims [117,118]. When bleeding and coagulopathy are controlled, hemorrhagic shock can be reversed by restoring oxygen delivery to the organism using volume replacement intervention and supportive care to control bleeding. Despite these strategies, a number of patients still progress to irreversible hemorrhagic shock and death. The cellular mechanisms leading to complications from shock, such as acute respiratory distress syndrome, systemic inflammatory response syndrome, and multiple organ dysfunction syndrome are poorly understood. Even so, ischemia and dysoxia are known to greatly alter the metabolic rate, physiologic mechanisms, and biological mediators involved in the associated pathophysiology [118].

Metabolomics is a new field of study that proposes to outline the entire metabolome, or repertoire of small molecules, in an organism. Using proven analytical chemistry techniques such as Nuclear Magnetic Resonance (NMR) spectroscopy and mass spectrometry, metabolites are identified and quantified from a biological sample of an organism in a given physiological state [49]. The metabolome responds to changes in the physiological state of an organism, and certain metabolites in the metabolome may be indicative of the organism's response to stimuli, health or disease, or response to injury. Metabolomics has been used to investigate metabolic markers of ischemia/reperfusion injury in the kidney, heart, and intestine [44,105,119-122].

Biofluids such as urine and serum are gaining favor over tissue samples in metabolomic studies because they are easily obtained. However, data from biofluids, especially urine, must be accurately normalized to account for dilution effects. The issue of how to account for dilution changes has been studied extensively [123-127], and relative strengths and weaknesses of different methods have been described. Unfortunately, the most common normalization method, constant sum or integral normalization, may not be robust enough to handle samples with such widely changing individual metabolite concentrations as are known to arise from hemorrhagic shock [123]. Most importantly, the majority of evaluation of normalization techniques has been done with computer simulations of NMR data, or with spectra obtained from known chemical mixtures with known dilutions. There has not been an examination of the behavior of different normalization methods in hemorrhagic shock and resuscitation, a physiological state that encompasses large shifts in intravascular volume, drastic unknown changes in urine output and urine concentration, and systematic perturbations in the abundance of endogenous metabolites.

An understanding of changes in the urinary metabolome during hemorrhagic shock and resuscitation has the potential to illuminate the cellular adaptations taking place during this process. However, specific physiological alterations due to hemorrhagic shock complicate the analysis with respect to scaling and normalization. There are substantial changes in fluid volume and urine concentration due to blood loss, followed by dilution of the urine when resuscitation fluids are administered. As a result, urine output fluctuates throughout the course of shock and resuscitation [128]. Additionally,

large variations in metabolites associated with shock such as lactate, glucose, and urea means that application of integral normalization techniques are questionable in this setting.

The normalization methods examined here include five spectral post-processing normalization methods and two physiological estimates of urine concentration. The data set was comprised of 83 timed urine samples collected from 13 pigs subjected to hemorrhagic shock and resuscitation. Normalization constants for each sample were plotted against experimental timepoint to assess whether the normalization constants were reflective of expected changes in urine dilution. Urinary creatinine concentrations were compared with serum creatinine concentrations to test each normalization method's effect on the raw creatinine concentrations. Pairwise correlations of the normalization constants were compared with each other to highlight similarities and differences in their relative estimation of concentration. Finally, principal components analysis was used on a subset of the normalization methods to ensure that reasonable clustering of the data and reasonable proportions of variance were explained. In doing so, this paper examines the behavior of seven different normalization methods in the physiologically relevant setting of hemorrhagic shock described above in order to find an appropriate normalization method.

Materials and Methods: Data collection and animal protocols

Animal preparation and hemorrhagic shock protocol: A well-established model of porcine hemorrhagic shock, which has been previously described [129], was utilized. Male

Yorkshire pigs (Manthei Hog Farm, LLC, Elk River, MN) weighing between 15-20 kg were instrumented and splenectomized. A captive bolt device was used to create a blunt percussive injury to the chest. Hemorrhagic shock was then induced by withdrawal of blood from the inferior vena cava until a systolic pressure of the lower 50's was reached (typically 35-50 % of total blood volume). Shed blood was placed in an acid-citrate-dextrose bag for later use. A liver crush injury was induced using a Holcomb clamp technique [130], with two crush injuries created in the liver parenchyma. Animals received lactated Ringer's fluid given as 20 cc/kg intravenous (IV) boluses to maintain a systolic blood pressure of greater than 80 mmHg for one hour of limited resuscitation; then underwent full resuscitation by protocol (see Figure 5.1).

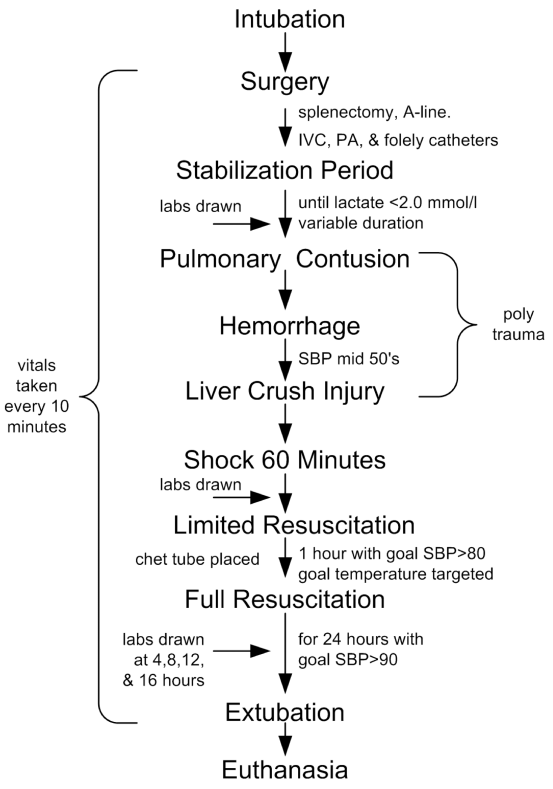

Figure 5.1: Graphical representation of the experimental protocol employed in both experiments, as discussed in the Materials and Methods.

Auto-transfused warmed blood was given at 10 cc/kg IV boluses for a target hemoglobin of greater than 6 g/dL, and, a urine output of greater than 1 cc/kg/hr was targeted using lactated Ringer's at 20 cc/kg IV boluses or blood at 10 cc/kg/hr. Serum creatinine levels were obtained at set timepoints from 1 mL aliquots of blood via rate reflectance spectrophotometry calibrated to isotope dilution mass spectrometry (Fairview Diagnostic Laboratories, Minneapolis, MN USA). After the resuscitation period, animals were

extubated and sent to recovery. At 24-48 hours after resuscitation, animals were re-intubated for endpoint sample harvesting and then euthanized.

Urine samples from seven animals were taken from a study performed in 2008, and samples from six animals were taken from a similar study (2009-2010). All experimental protocols and instrumentation were the same for the two experiments; the only difference was the experimental timepoints at which urine samples were obtained (see Table 1). A total of 83 urine samples were used in this study.

	Baseline	Shock 45	Time in hours after shock							End
			1	2	4	8	12	16	20	24/48
2008 (n=7)	X	X	X		X	X	X	X	X	X
2009-2010 (n=6)	X	X		X		X			X	X
Timepoint	1	2	3	4	5	6	7	8	9	10/11
Resuscitation phase			Early Resuscitation			Late Resuscitation				

Table 5.1: Experimental time points between the two experiments. Baseline/timepoint 1 samples were taken after instrumentation. Shock 45/timepoint 2 samples were taken after 45 minutes of hemorrhagic shock. LR1/timepoint 3 samples were taken after one hour of resuscitation; FR2/timepoint 4 samples were taken after 2 hours of resuscitation, etc. FR20/timepoint 9 samples indicate the end of resuscitation. Animals in the 2008 experiments had experimental endpoints at 24 or 48 hours after the end of resuscitation (PR24/timepoint 10 or PR48/timepoint 11). Animals in the 2009-2010 experiments had experimental endpoints of 48 hours after the end of resuscitation (PR48/timepoint 11).

Identification of metabolites from NMR: Urine samples were taken at the time intervals specified in Table 1 from the Foley catheter and were frozen and stored at -80° C.

Samples were thawed at the time of preparation for NMR analysis. One mL of thawed urine was mixed with 0.5 mL of 0.2 M sodium phosphate buffer prepared with D2O to control pH. The mixture was placed on ice for 10 minutes and then centrifuged at 7000g for 10 minutes. 500 μL of the supernatant was withdrawn and combined with 50 μL of the internal standard 3-(Trimethylsilyl)propionic acid (TSP, Sigma-Aldrich, USA) to a concentration of 1 mM [131]. The internal standard was prepared with D2O to provide a lock for the NMR signal. The pH of the final solution was recorded (mean 7.62, standard deviation 0.22) and the mixture was transferred to separate 5 mm NMR tubes (Wilmad, LabGlass, USA).

Proton NMR spectra were taken with a Bruker Avance spectrometer with autosampler and 5mm triple resonance 1H/13C/15N TXI CryoProbe with Z-gradient, running TopSpin v. 2.16 (Bruker BioSpin, Fremont, CA USA) at 700.13 MHz (Figure 5.2). A 1D NOESY (Nuclear Overhauser Effect Spectroscopy) pulse sequence was used. The 90° pulse width was calibrated for each sample, and was generally 12-13 μs. The relaxation time was defined by each sample's 90° pulse width. The relaxation delay was 2 s, the acquisition time was 3 s, the spectral width was 10 kHz, the total number of data points collected was 63,000, and the number of transients collected was 128, for a total experiment time of 11 minutes and 17 seconds. During the relaxation period, the water resonance was presaturated. All spectra were collected at a temperature of 298 K. Line broadening at 0.5 Hz was applied before FFT; autophasing and auto-baseline correction were applied by TopSpin.

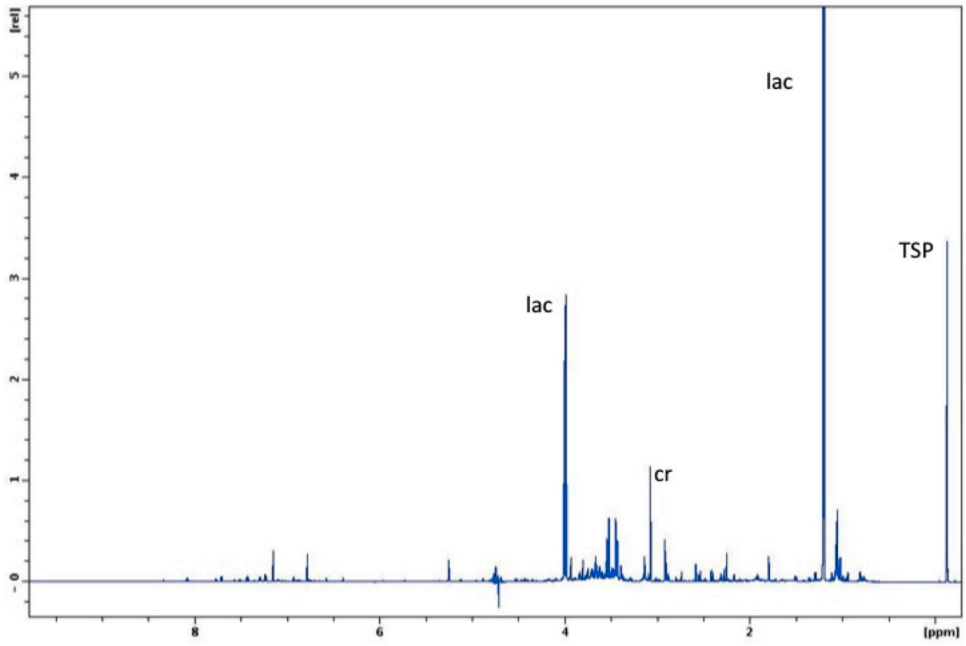

Figure 5.2: NMR spectrum of a representative urine sample taken on a 700 MHz Bruker Avance Spectrometer with NOESY pulse sequence.

Chenomx software [5] was used to identify and quantify a portion of the metabolites present in each urine sample. Fine manual phasing and baseline corrections and the software's Reference Deconvolution algorithm were applied to each spectrum before targeted profiling of the metabolites was performed. Fifty-seven metabolites were fit in each urine sample in this study, resulting in a profile containing the concentration of each identified metabolite in millimoles per liter (mM). The metabolomic profiles containing the urine concentrations were then normalized in seven different ways described below.

Normalization of urinary metabolites: Each urine sample has seven normalization constants associated with it, one for each method of normalization, with the exception of urine output as stated below.

Constant Sum (CS): This post-processing method controls for the varying concentration in the urine by dividing the concentration of each metabolite by the sum of the concentration for all the metabolites profiled with Chenomx in a given sample. This method assumes that each metabolite's concentration is increased by the same amount due to the increased concentration of the urine sample. The normalized metabolite abundances are expressed as a fraction of profiled metabolites.

Constant Sum, excluding lactate, glucose, and urea concentrations (CS-LGU): This post-processing method is the same as CS; however, lactate, glucose, and urea concentrations are left out of the calculation of the normalization constants because the concentrations of these metabolites are highly variable during the experiment. The units of the normalized metabolite abundances are the same as for CS normalization.

Total Spectral Intensity (TSI): The assumptions for this post-processing method are the same as for constant sum normalization. Each spectrum was divided into bins of width 0.04 ppm, and standardized to the spectral area under the TSP peak. Bins were summed over the entire spectral area between 0 and 10 ppm, excluding the spectral regions containing water and urea to approximate the total area covered by the spectrum. The raw metabolite concentrations are divided by this quantity and the normalized quantity is expressed as a fraction of spectral intensity.

Probabilistic Quotient (PQ1 and PQ2): In these two post-processing methods [124], a "reference sample" representing the median concentration of the urine is constructed and used to calculate the normalization constants for each sample. Two different methods were used to construct the reference sample. The first method (PQ1) used the metabolite concentrations from the baseline urine samples as the reference sample for the balance of that pig's experimental samples. The second method (PQ2) used each metabolite's median concentration across all pigs at baseline as the reference sample, i.e., a hypothetical pig at baseline. The hypothetical pig at baseline was used as the reference sample for all experimental samples. Both PQ1 and PQ2 normalization constants are unitless, so metabolite concentrations normalized to PQ1 and PQ2 also have units of millimoles per liter (mM).

Osmolality (OSM): Osmolality is a direct measure of the concentration of solute particles in the urine. Aliquots of urine were tested for osmolality using micro-osmometry by freezing point depression, with values reported as the number of solute particles in moles dissolved in a kilogram of urine. Metabolite concentrations were normalized by dividing by the osmolality of the appropriate sample. The value returned is a ratio of the abundance of a given metabolite relative to the total number of solute particles. To return a normalized metabolite concentration of nanomoles of metabolite per millimoles of solute, each urine sample's osmolality has been mulitplied by a factor of 1×10^{-6}.

Urine Output (UO): Urine output quantifies the volume of urine excreted per hour per kilogram of pig mass. Normalization to urine output is performed by multiplying raw

metabolite concentrations by urine output, whereas raw metabolite concentration is divided by the normalization constant for all other methods. For this reason, when modeling normalization constants, the inverse of urine output is used. Metabolite abundances normalized to urine output have units of nanomoles of metabolite per hour per kg of pig mass (nmol/hr/kg). Urine output data was not available at experimental endpoint (24/48 hours after the initiation of shock).

Materials and Methods: Data analysis

Seven of the physiological parameters (lactate, arterial pH, base excess, heart rate, mean arterial pressure, cardiac output, and hemoglobin) that are known to change with hemorrhagic shock were compared with repeated measures analysis of variance (rmANOVA) for both experiments to justify pooling the data.

Repeated measures ANOVA was used to estimate the average normalization constant for each timepoint collected. Covariance structures (auto-regressive, unspecified or compound symmetry) were used to account for the correlation expected among the samples collected for each pig when the model indicated a statistically significant fit. Variance components were used otherwise. Tukey's adjustment was used to correct for the multiple pairwise comparisons made to determine the reason for the statistical significance when found. Spearman rank correlation analysis was used to compare the normalization constants in a pairwise manner.

Urinary creatinine levels were compared to serum creatinine levels to test the behavior of the normalization methods. Appearance of creatinine in the urine should

follow that of serum levels because it is freely filtered by the kidneys. Creatinine levels, which correlate with renal blood flow in healthy kidneys, should accumulate in the blood as a result of decreased renal handling and reduced intravascular volume from hemorrhagic shock. A robust normalization technique should preserve this behavior. Estimated mean creatinine concentrations in the serum and urine for each normalization method plus raw concentrations were calculated by rmANOVA with error bars to indicate the 95% confidence interval.

Principal components analysis (PCA), a standard metabolomics analysis tool, was used to reduce data dimensionality and identify key metabolites responsible for variation in the physiology studied. The urinary metabolomic data sets were standardized in preparation for PCA. Singular value decomposition was used, and PCA was performed on the correlation matrix derived from the standardized metabolomic data. For each method of normalization, PCA with metabolite reduction was performed up to 4 times to identify influential observations and eliminate them from the dataset. The method used to reduce the number of metabolites included in the PCA was that recommended by Joliffe [75]. Influential observations were clearly identified on the PC1 (principal component 1) by PC2 (principal component 2) score plot; samples that were outliers were clearly separated from the rest of the observations. To confirm a sample's outlier status, the PC loadings and concentrations for the metabolites in a sample were reviewed. In each case, the samples in question contained metabolites that loaded strongly in PC1 or PC2. The metabolite concentrations in these samples were at least 1.5 interquartile ranges (IQR) beyond the IQR, a standard definition of a statistical outlier.

Results:

Normalization constants were analyzed by timepoint with rmANOVA. The results of Tukey's multiple range tests are shown as the estimated mean normalization constant and 95% confidence interval (Figure 5.3). The result shows a decrease in the magnitude of the normalization constants after resuscitation ($p \leq 0.0556$) in PQ1 and PQ2 (timepoints 7-9), OSM (timepoint 8), and UO (timepoints 7-8). Additionally, baseline UO was significantly higher than at timepoints 4 and 6-9. No significant pairwise comparisons between timepoints were observed in CS, CS-LGU, or TSI.

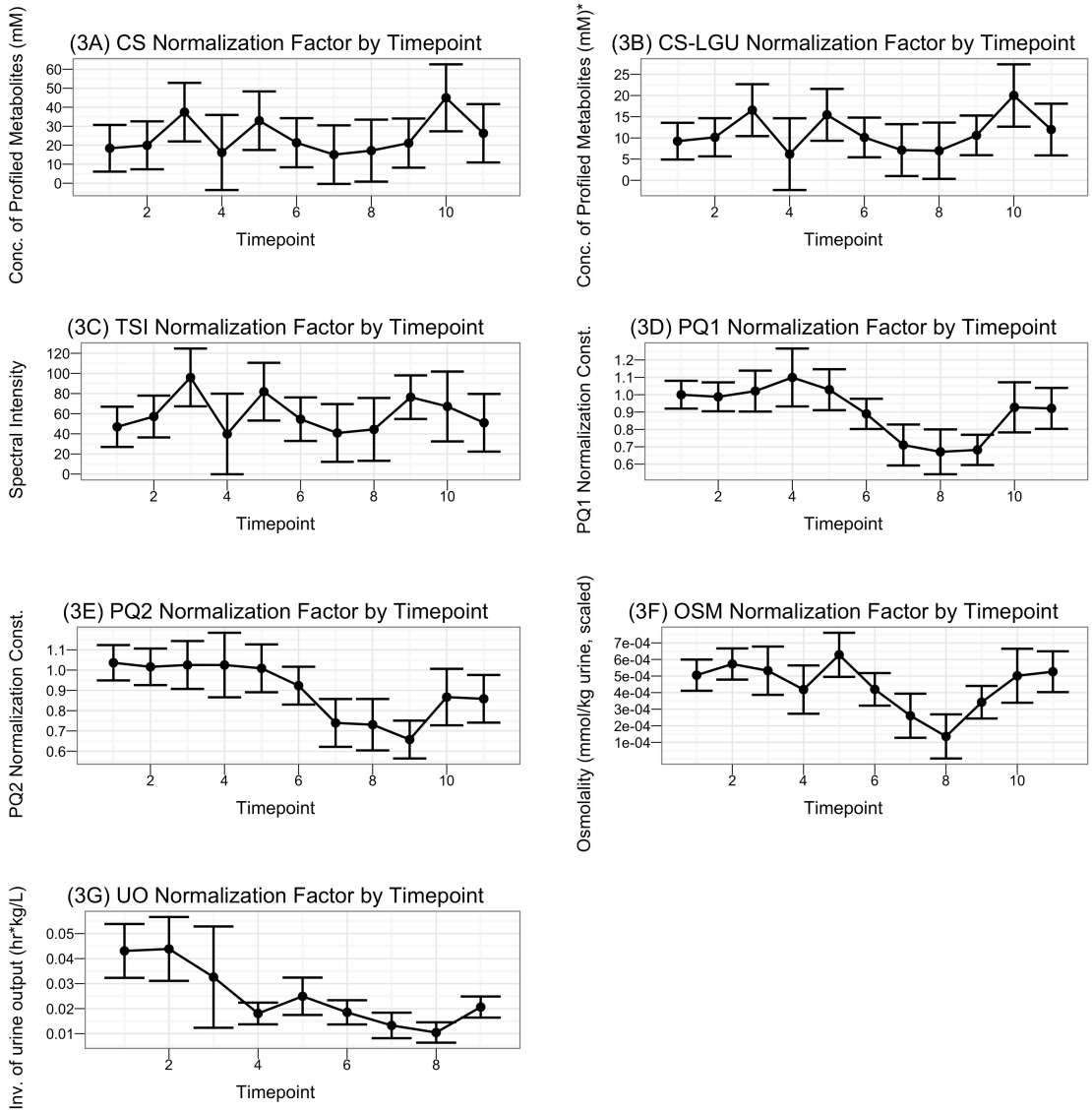

Figure 5.3 (A-G): The seven plots of the estimated mean normalization constant with error bars to indicate the 95% confidence interval for the mean as estimated by rmANOVA. (3A): Constant sum normalization constants (mM) plotted against experimental timepoint. (3B): Constant Sum, excluding lactate, glucose, and urea concentrations (mM, *: exclusive of lactate, glucose, and urea concentrations) normalization constants plotted against experimental timepoint. (3C): Total spectral intensity (arbitrary units, obtained by spectral binning) normalization constants plotted against experimental timepoint. (3D) and (3E): PQ1 and PQ2 normalization constants (unitless) plotted against experimental timepoint. (3F): OSM normalization constants (mmol of solvent per kg of urine, scaled by a factor of 1×10^{-6}), plotted against experimental

timepoint. (3G): Urine output normalization constants (hr kg/nmol) plotted against experimental timepoint. The UO normalization constant is the inverse of the animal's urine output.

Creatinine values for serum and urine under all normalization methods are shown in Figure 5.4. Serum creatinine levels were found to vary significantly between experiments, with a greater rise in creatinine levels between timepoints 3 and 10 for the 2009-10 experiments compared to 2008 (Figure 5.4A). The difference in average creatinine between experiments, while statistically significant, is not clinically relevant.

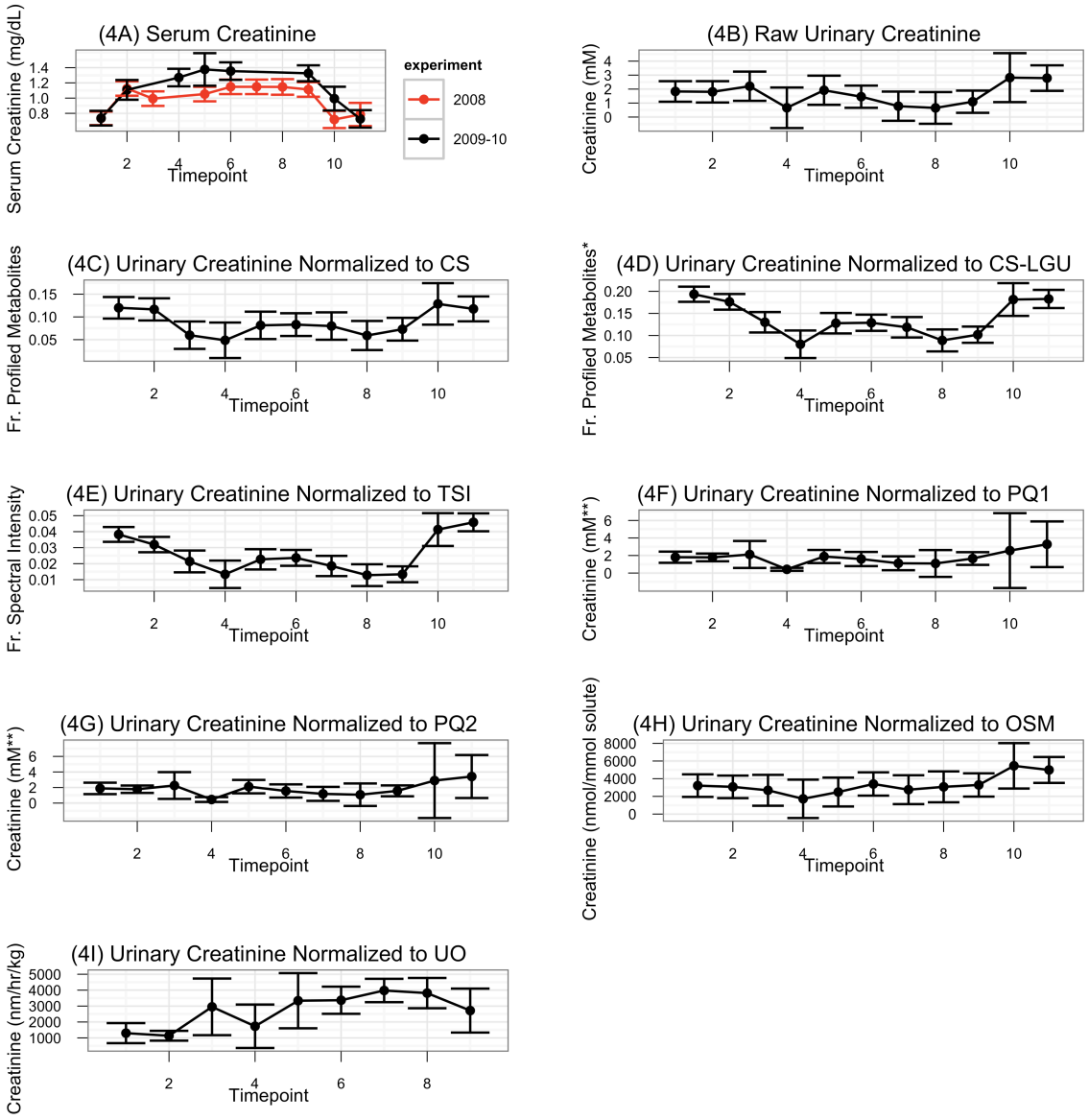

Figure 5.4 (A-I): The nine stacked plots illustrate the estimated mean creatinine concentration in the serum (A) and urine (B-I) for each normalization method plus raw. Error bars indicate the 95% confidence interval for the mean as estimated by rmANOVA. *: Profiled metabolites are exclusive of lactate, glucose, and urea. **: Units are mM but scaled by the appropriate PQ normalization constant.

Urinary creatinine levels did not vary between experiments; however, they did vary with normalization method (Figures 5.4 B-I). Urinary creatinine normalized to UO follows the same general pattern as serum creatinine though they are not the same ($p < 0.0001$). Urine normalized to CS, CS-LGU, and TSI suggest the opposite pattern ($p < 0.0001$), with a decrease in normalized creatinine abundance between baseline and endpoint. There is little change with time in the abundance of urinary creatinine normalized to PQ1 ($p < 0.0001$), PQ2 ($p < 0.0001$), and OSM ($p \leq 0.0779$). The statistical significance for PQ1 and PQ2 is due to the reduction in variability and decreased magnitude observed at timepoint 4.

Spearman rank correlation coefficients were calculated for each pair of normalization constants. Plots of the normalization constants against each other, r-values, and p-values are shown in Figure 5.5. The correlations indicate that CS, CS-LGU, and TSI are correlated ($r \geq 0.79$, $p < 0.0001$). The PQ methods are correlated with each other ($r=0.67$, $p < 0.0001$), but not with CS, CS-LGU, or TSI ($r \leq |0.18|$, $p > 0.11$). UO and OSM are also correlated with each other ($r=0.65$, $p < 0.001$). Thus, CS, CS-LGU, and TSI are related, PQ1 and PQ2 are related, and OSM and UO are related. UO has at least a moderate correlation to all other normalization methods, and is the only method to have a nearly significant p-value ($p < 0.051$) associated with every other normalization method. OSM is comparable in this regard, though there is no statistical significance with PQ2 ($p=0.12$).

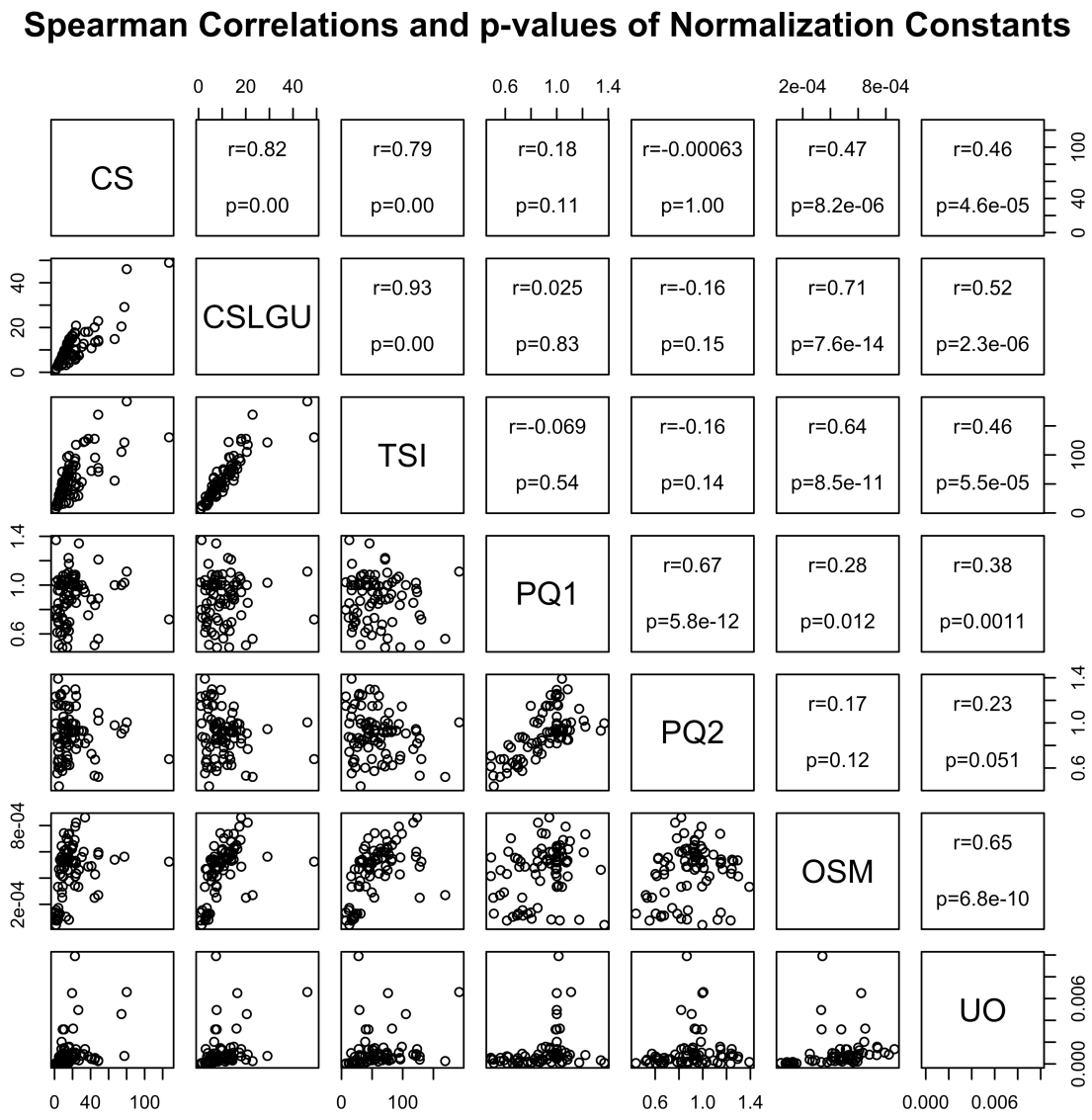

Figure 5.5: Scatter plots of each of the normalization constants against each other (below diagonal) with Spearman correlation r-values and p-values (above diagonal). Scales on the plots vary with the constants as described in Figure 5.2. The plotting convention is as follows: the graph in the second row of the figure plots the CS normalization constants on the x-axis and the CS-LGU normalization constants on the y-axis.

Given the similarities observed in calculation and findings between CS/CS-LGU/TSI, PQ1/PQ2, and OSM/UO, it was decided that principal components analysis would not be completed on urinary metabolomic data normalized to CS, TSI, and PQ1. Only CS-LGU, PQ2, OSM, UO, and the raw data would be analyzed by PCA. The number of samples removed due to influential status via up to four rounds of PCA with metabolite reduction varied from method to method. These samples were clear statistical outliers for the metabolites loading heavily on the relevant PC (PC1 or PC2; see Table 5.2). Experimental notes were reviewed to find a non-statistical justification for removal of the outliers, and none was found.

Pig	Timepoint	RAW	CS-LGU	PQ2	OSM	INV UO	# methods that removed sample
30209	Baseline			X			1
50508	LR 1	X		X		X	3
	FR 4	X		X	X		3
	FR 8				X	X	2
	FR 12					X	1
	FR 16			X	X		2
	FR 20			X	X	X	3
	PR 48	X		X	X		3
51109	S 45			X			1
	FR 8			X			1
	FR 20			X			1
	PR 48	X	X				2
51408	LR 1			X			1
	FR 4			X			1
	FR 8			X			1
	PR 24			X	X		2
62208	FR 8			X			1
62209	Baseline		X				1
	FR 2	X	X			X	3
	FR 8					X	1
	FR 20			X			1
	PR 48		X				1
101209	PR 48	X		X			2
101909	FR 2	X	X				2
Total Number of Samples Removed from PCA as Influential		7	5	16	6	6	

Table 5.2: Urine samples removed from PCA due to influential status. Samples are indicated by identifiers "Pig " (date of experiment) and "Timepoint".

Table 5.3 shows the metabolites and number of PCs retained by each method, the eigenvalues, the cumulative eigenvectors/loadings, and the proportion of variation explained for each PC. Thirteen metabolites were not retained by any of the normalization methods or in the raw data. The number of metabolites retained varied

from 12-20 and the proportion of variation explained ranged from 35% to 66%. Of the four normalization methods, UO described the most variation, at 54% in two principal components.

Metabolites Retained by at Least One Method	Loadings (Multiplied by 100, rounded to nearest integer) Black indicates metabolite not retained by method.											
	Raw			CS-LGU			PQ2		OSM		UO	
	PC1	PC2	PC3	PC1	PC2	PC3	PC1	PC2	PC1	PC2	PC1	PC2
1-Methylnicotinamide							7	45	-12	52		
2-Methylglutarate	35	0	-4									
2-Oxoglutarate				13	-4	49			7	5		
4-Hydroyxbenzoate	29	-4	-23									
Acetate							19	29				
Alanine	33	9	21	-2	35	28						
Allantoin	26	-17	-36									
Ascorbate	33	1	-24				30	13	42	13		
Betaine				-18	38	-11						
Citrate				26	-4	44	7	26				
Creatine	7	45	14	-28	7	7	29	-43			38	-25
Creatinine				36	-25	-25						
Formate							28	-34	6	-40		
Glucitol				-2	36	-2						
Glucose				11	36	-32					-5	11
Glutamate				23	11	23						
Glutamine												
Glycerol				3	13	28			33	-19		
Glycine				-22	14	6	36	-22				
Hippurate							20	4			23	19
Homogentisate				-15	27	3					37	2
Hypoxanthine											11	51
Inosine							35	6			37	19
Isoleucine	36	5	7				37	18	36	0		
Lactate	10	-28	57									
Mannitol											9	41
Mannose				14	32	-29			14	17		
Methylguanidine				39	16	-14						
N-Isovaleroylglycine							32	28				
N,N-Dimethylglycine									22	38		
Niacinamide	14	-38	-1	28	20	5						
Oxypurinol									12	-1		
Phenylacetylglycine				25	0	-9			22	4		
Pyruvate	20	-33	40						0	27	9	45
Quinolinate	30	10	-6									
Taurine									34	-23		
Trigonelline				37	-3	-4						
Trimethylamine	14	44	14				29	-33			36	-29
Trimethylamin N-oxide	15	44	9						12	-42	36	-30
Tyrosine				11	25	22						
Urea	22	-11	-35						28	1		
Valine	33	-4	21				29	23			36	20
Xanthine				3	-19	0			19	2	33	-5
Xanthosine				25	13	1						
Eigenvalue	5.4	2.6	1.9	3.6	2.5	1.8	4.6	2.4	3.4	2.2	4.5	2.0
Cumulative Variance Explained	36%	54%	66%	19%	32%	41%	35%	53%	21%	35%	37%	54%
Number of Metabolites Retained	15			20			13		16		12	

Table 5.3: Results of PCA analysis including metabolites retained for raw and normalized urine samples, eigenvectors/loadings, eigenvalues, and proportion of variation explained. The metabolites not retained by

any method include 1-6-Anhydro-β-D-glucose, Adenosine, Choline, cis-Aconitate, Dimethylamine, Fumarate, Glutathione, Glycoproline, Lysine, Proline, Succinate, Tryptophan, and Tyramine.

Two and three-dimensional (2 retained PCs and 3 retained PCs, respectively) scores plots were reviewed for clustering (see Figure 5.6). All four normalization methods appeared to cluster the late resuscitation timepoints separately from the other timepoints, with slight differences between the normalization methods. Little meaningful clustering of the raw urine data was observed.

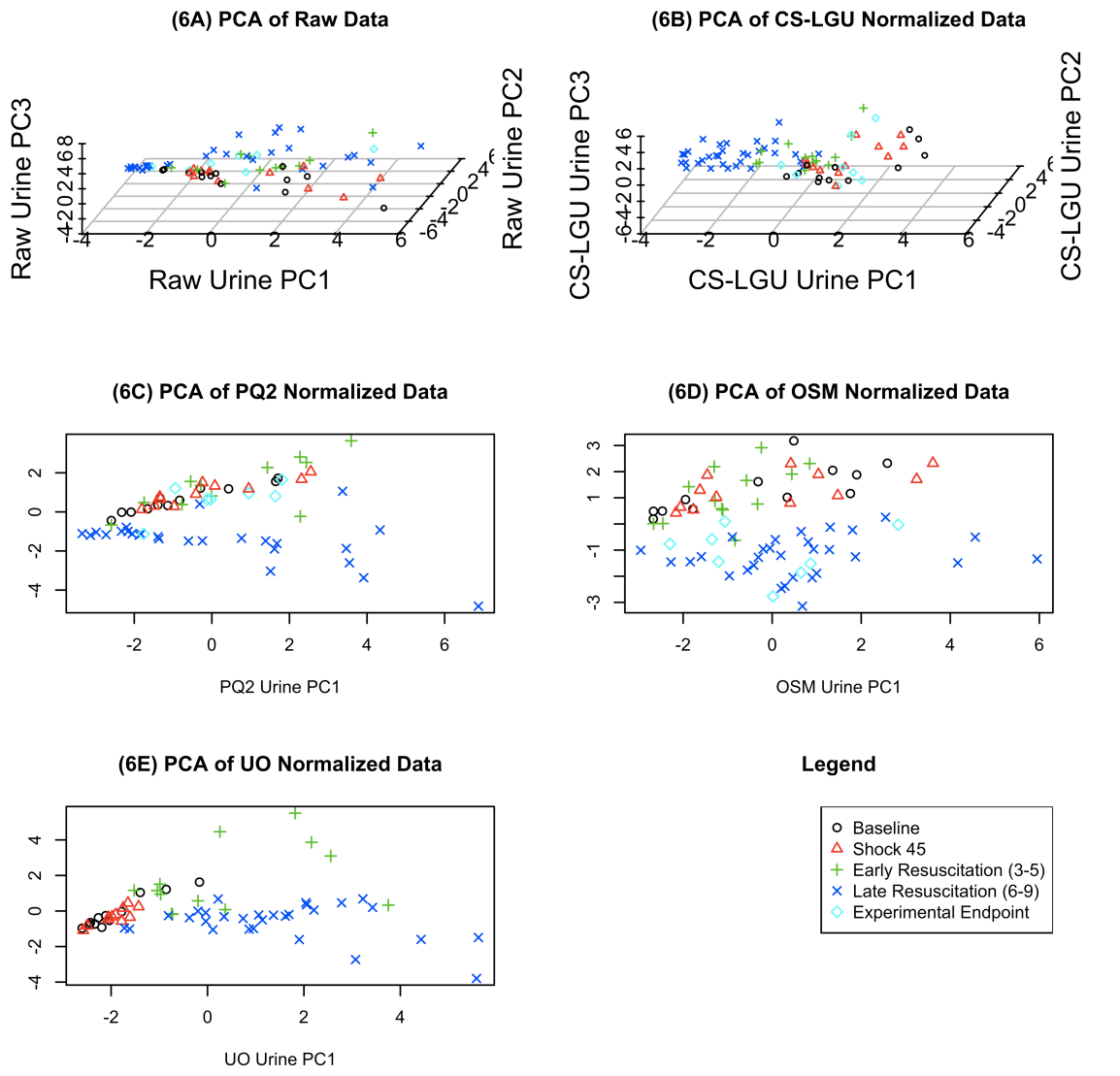

Figure 5.6 (A-E): Scores Plots in 3D (3 PCs retained) or 2D (2 PCs retained) for the 4 normalization methods promoted to principal components analysis plus the raw data. The timepoints of the experiment were grouped into phases: timepoint 1 (baseline; black circles), timepoint 2 (Shock 45; red triangles), early resuscitation (timepoints 3-5; green crosses), late resuscitation (timepoints 6-9; blue x), and experimental endpoint (timepoints 10-11; cyan diamonds). (6A): Raw urine metabolomics data expressed in 3 PC variables, retaining 15 metabolites and 66% of the variation. (6B) Urine metabolomics data normalized to CS-LGU expressed in 3 PC variables. Twenty metabolites and 41% of the variation are retained. (6C) Urine metabolomics data normalized to PQ2 expressed in 2 PC variables. Thirteen metabolites and 53% of

the variation are retained. (6D) Urine metabolomics data normalized to OSM expressed in 2 PC variables. Sixteen metabolites and 35% of the variation are retained. (6E) Urine metabolomics data normalized to UO expressed in 2 PC variables. Twelve metabolites and 54% of the variation are retained.

Discussion

Urine is often used in metabolomics studies because it is readily available. However, changes in dilution confound the quantification of metabolite concentrations in urine samples. This problem is exacerbated in hemorrhagic shock, where urine concentrations are known to vary widely. Additionally, large variations in endogenous metabolites are often involved in the systemic response to hemorrhagic shock. These variations can further confound some of the normalization methods that are commonly used.

Seven methods for normalizing urine metabolomics data were examined in a porcine model of hemorrhagic shock and resuscitation. Evaluation criteria were that the normalization constants reflect expected increases and decreases in urine concentration and that normalized urinary creatinine levels reflect serum creatinine levels. Normalization methods were also compared for similarities in urine concentration estimation using Spearman correlation. Unrelated methods were analyzed by PCA and scores plots were compared with those of the raw data to check for meaningful separation of the data.

Analysis of the normalization constants by timepoint with rmANOVA indicates that the constants associated with each urine sample are reflective of the sample's concentration. While there was no indication of a significant increase in urine concentration as a consequence of hemorrhage, there was a trend toward decrease in

urine concentration after resuscitation for all normalization methods and a significant decrease in urine concentration in all methods except CS, CS-LGU, and TSI. This is at least partially due to the administration of resuscitation fluids after timepoint 2, and the subsequent increase of intravascular fluid volume. The decrease in urine concentration is generally observed during later time points in the hemorrhagic shock model (Timeponts 6-9).

Serum creatinine levels varied between the two experiments pooled in this study. Serum creatinine levels are known to be variable even in healthy individuals [132]. Both groups present a consistent pattern with lower serum creatinine levels at baseline and at timepoint 11 with elevated levels after shock. Normal serum creatinine values for weaner pigs (< 40 lbs) range from 0.75-1.95 mg/dL and values for feeder pigs (40-80 lbs) range from 0.79-1.87 mg/dL [133]. Ultimately, the differences observed here between experiments are small (0.2-0.3 mg/dL) relative to the width of the normal range. Such differences are considered clinically insignificant.

Urinary creatinine normalized to UO most closely tracks serum creatinine. There is a slight depression of urinary creatinine levels relative to serum creatinine during shock, which is likely reflective of reduced blood flow to the kidney after shock and reduced filtration capabilities of the nephron [35]. When compared to UO-normalized creatinine, urinary creatinine under the other normalizations displays little change over the course of the experiment (PQ1, PQ2, OSM), or displays the opposite behavior (CS, CS-LGU, TSI; see Figure 5.4).

The discrepancy between UO and the other normalization methods arises from the resulting time-dependence of normalization by urine output, which expresses urinary creatinine levels as nanomoles per hour per kilogram of pig mass. This is reflective of the clearance of creatinine from the blood, a decidedly time-dependent phenomenon. No other normalization method returns a time-dependent value of metabolite abundance in the urine; therefore, no other method can yield a result that is concordant with renal clearance. The clear relationship between serum creatinine levels and creatinine clearance as indicated by the urinary creatinine values normalized to UO distinguishes it from all other normalization methods. This observation should not lead to outright rejection of other methods, however. The urinary creatinine levels returned by the remaining normalization methods are reflective of creatinine levels at a given timepoint. Serum creatinine is assumed to rise in the blood as a result of reduced filtering capabilities of the nephron from ischemic kidney damage. Because of this, the total amount of creatinine excreted in the urine will be diminished. This is observed in CS, CS-LGU, and TSI-normalized urine (Figure 5.4 C-E).

Each normalization method estimates the urine concentration differently, and the correlation analysis of the normalization constants (Figure 5.5) highlights these differences. The two physiological measures of urine dilution, OSM and UO, are well-correlated with each other. These two methods are at best moderately correlated with the post-processing methods, save OSM with CS-LGU and TSI. Still, UO and OSM have the strongest correlations with the other methods, indicating an underlying physiological mechanism to the estimation of concentration.

It is observed that CS, CS-LGU, and TSI are highly correlated with each other because these normalization constants are all reflective of NMR spectral intensity. PQ1 and PQ2 are well-correlated with each other because both methods are dependent on median estimates of concentration at baseline. However, the normalization constants for PQ1 and PQ2 are only moderately correlated with UO and OSM, and are not correlated with CS, CS-LGU, and TSI. The PQ methods and the integral methods (CS, CS-LGU, TSI) should be well correlated unless there is some systematic variation in the metabolite abundances across the samples [124,127]. This is the case in a hemorrhagic shock state.

The three major contributors to endogenous metabolite variation in this data set are urinary lactate, glucose, and urea. Contributions from each of these metabolites were removed from the CS-LGU normalization constant. The urea signal was also removed from the TSI normalization constant because of complications from the water suppression, as is standard practice with spectral binning [134].

There are both physiological and experimental sources of metabolite variation in this model that must be considered. Lactate is a well-studied marker of traumatic injury [135,136]. Lactate levels are seen to vary from 0.004 mM to 15.33 mM in the raw data, with the highest concentrations occurring at timepoints 3 and 4 (1-2 hours after shock). It is also known that hemorrhagic shock produces alterations in energy metabolism [137] that make additional contributions to systematic metabolite variation. In this case, glucose is observed to fluctuate over a range of 0.014-18.93 mM in the raw data. The kidney's handling of lactate may also be involved in glucose variation [47]. Finally, urea, which can build up in the blood under conditions of decreased perfusion, ranges from 0.22-76.8 mM

in the raw data. This, too, has a physiological basis, as blood urea levels are known to increase in trauma patients. Blood urea levels are used as a nonspecific indicator of renal function if the kidneys are unable to clear it [47,138]. As a consequence, low fractional excretion of urea is often observed in patients with impaired kidney function [139,140]. The urea signal is further compromised because urea protons are in exchange with water. From an experimental standpoint, suppression of the water signal in proton NMR will render the urea signal unreliable. All three of these metabolites were removed from the CS-LGU normalization constant in an attempt to control for variation and address the known shortcomings of the CS method. Given the lack of correlation with this method and PQ1/PQ2 and the retained correlation with CS and TSI, it was not sufficient. Other metabolites could very well be contributing to the lack of agreement between the CS methods and the PQ methods. One likely candidate is creatine, which is present in very small amounts in timepoints 1-4, and increases steadily through the experimental endpoint, covering a range of 0.006 mM to 2.9 mM in the raw data. Creatinuria is documented as an indication of traumatic injury [141].

When PCA was applied to the metabolomic data under different normalizations as described, it was found that different methods retained different metabolites. Several metabolites were rejected by all normalization methods (see Table 2). This phenomenon has not been discussed in metabolomics normalization literature.

As discussed, PCA for all of the normalized metabolomic data elevated to this part of the analysis shows some separation of the urine samples by timepoint (Figure 5.6). Early timepoints, corresponding to baseline (black circles), shock (red triangles), and

early resuscitation (green crosses) are separated from late timepoints (blue x's), corresponding to post-resuscitation. The separation of late resuscitation timepoints (6-9) is reflective the decrease in concentration under rmANOVA analysis of the normalization constants. No separation of the data is seen in principal components analysis of the raw data. The similar clustering of the normalized data into pre-resuscitation and post-resuscitation states suggests that 1) some normalization is required to obtain useful clustering of urine metabolomics data, 2) metabolomics may be useful in differentiating between states of pre-resuscitation and post-resuscitation, and 3) changes occurring in the physiological state of the animals between hemorrhage and post-resuscitation can be differentiated by urine alone.

Of the post-processing methods, none stands out as better or worse than another. The CS methods (CS, CS-LGU, TSI) are fairly well-correlated to physiological measures of dilution but it is known that they are not robust to the large shifts in metabolite abundances that are seen in this setting. Additionally, these three methods did not show statistical significance in dilution of the urine at late timepoints (Figure 5.3). On the other hand, the PQ methods are more robust to drastic systematic changes in metabolism by design. They show a statistically significant decrease in urine concentration at late resuscitation timepoints. However, correlations of normalization constants in Figure 5.4 indicate that they are different from every other normalization method save each other.

This study demonstrates that UO stands out as being different from the other normalization methods under the examination of creatinine concentrations with time. Creatinine normalized to urine output is reflective of renal clearance; other

normalizations of creatinine are not. The inherent time-dependence of renal clearance has been demonstrated. The concentration of solute into urine by the kidneys has been modeled by time-dependent partial differential equations [142,143].

It has been argued that urine output is the only way to obtain concentrations suitable for absolute comparisons of urine metabolite abundance [123]. Therefore, when relationships between urine metabolomic profiles and serum metabolomic profiles are studied, it is suggested that urine must be normalized to UO if meaningful comparisons are to be made. UO also had at least moderate correlations with all other normalization methods, and it is the only normalization method to have a nearly significant p-value associated with all other normalization methods. The principal components analysis provides some small additional support for urine output, as it describes the next highest percent of variation in the data set after the raw data.

Not all experimental situations allow for collection of urine output data. In these cases, OSM is preferable, as it is reflective of the physiological metabolite-concentrating mechanisms of the kidney. If osmolality data is not available, one of the post-processing methods would suffice, though care must be taken to apply these methods judiciously. The literature discusses the known issue with Constant Sum and TSI methods—namely, that large perturbations in single metabolite variations can artificially alter normalized metabolite concentrations [123,124,127]. If this is not the case, the computationally light CS/TSI methods could be used. However, if there is large systematic variation in metabolite abundances, one of the PQ methods should be used.

It is recognized that the relatively small sample size used (n=13 across both experiments) is not ideal. However, the entire sample set is composed of 83 samples. Additionally, urine output data was not available for experimental endpoint (timepoints 10/11). The strength of UO as a normalization method was apparent despite the lack of endpoint data because of its time dependence.

Conclusions

A major challenge in metabolomics is the normalization of urine to account for dilution. Hemorrhagic shock exacerbates the problem by inducing severe changes in intravascular volume and urine output, accompanied by large fluctuations in metabolite abundances as a response to injury. To accurately analyze urine metabolomic data, changes in concentration must be accounted for. Seven normalization methods were examined under these conditions to see which would be most appropriate to use in analysis of urine metabolomics data with a porcine model of hemorrhagic shock and resuscitation. While no statistically significant increase in concentration is observed after hemorrhage, all methods show a trend toward dilution of the urine after resuscitation fluids are administered. PCA of the normalized metabolite concentrations shows that the normalized data clusters according to experimental timepoint, and consequently by dilution.

Based on this analysis of normalization constants for each sample, serum and urine values of creatinine, correlations between normalization constants, and principal components analysis of the metabolite concentrations, it is concluded that urine output

normalization is the most appropriate method to use, especially when comparing urine and serum metabolomics data. If urine is being analyzed independently for biomarkers, a different normalization method could be used.

Chapter 6: Standard Metabolomics Analysis of Hemorrhagic Shock and Traumatic Injury in the Urine

Previous chapters have outlined what is known about the pathophysiology of traumatic injury and hemorrhagic shock with respect to metabolism. In Chapter 4, analysis techniques used in metabolomics were introduced. This chapter details the analysis of urine metabolomics data obtained from animals subjected to a standardized protocol of hemorrhagic shock, pulmonary contusion, and liver crush injury. The animal model is the same as that discussed in Chapter 5; however, this analysis includes four experimental groups and a total of forty animals. All 40 animals are instrumented and sedated in the same manner. The experimental groups are outlined in Table 6.1.

Group	*n* (died)	Type	Description
C1	5 (0)	Negative Control	Not injured, hemorrhaged, or resuscitated
C2	3 (3)	Positive Control	Injured and hemorrhaged, but not resuscitated
E1	16 (5)	Experiment-Fasted	Injured, hemorrhaged, and resuscitated (fasted for 24 hours beforehand)
E2	16 (8)	Experiment-Fed	Injured, hemorrhaged, and resuscitated (fed with a bolus of 140 mL of sucrose and 140 mL of water before the procedure)

Table 6.1: Experimental groups and sample sizes in the analysis performed in this chapter.

This chapter uses standard metabolomics analysis techniques to evaluate the metabolic changes that accompany hemorrhagic shock and traumatic injury as seen in the urine. A mixed models analysis is done to assess dependence of urinary metabolite levels on survival, experimental group, and experimental timepoint. Principal components analysis is used to identify outliers in the data set, and partial least squares discriminant

analysis (PLS-DA) is used to associate metabolites with the observable quantities associated with experimental timepoint, experimental group, and survival.

It is hypothesized that the urinary metabolome is related to these observable quantities. Association of urinary metabolites with experimental timepoint has the potential to identify the shock state and to follow phase of care during resuscitation. Association of urinary metabolites with experimental group is used to distinguish between injured animals and non-injured control animals, and is used in conjunction with the experimental timepoints to examine how feeding state influences the metabolic response to injury and hemorrhage. Finally, metabolites associated with survival status have the potential to predict mortality from hemorrhagic shock and traumatic injury. These results will be compared to a network analysis of the same data set, which is performed in Chapter 7.

Materials and Methods: Data collection and animal protocols

Animal preparation and hemorrhagic shock protocol: The experimental protocol was approved by the University of Minnesota Animal Use Committee and was conducted in accordance with established guidelines for the treatment of laboratory animals. A well-established model of porcine hemorrhagic shock, which has been previously described [129], was utilized. Male Yorkshire pigs (Manthei Hog Farm, LLC, Elk River, MN) weighing between 15-20 kg were randomized to experimental group. E2 animals were fed boluses of 140 mL of sucrose with 140 mL water. All other animals were fasted for 24 hours prior to the experiment. Animals were anesthetized with an intramuscular dose

of telazol (Wyeth Animal Health, Madison, NJ). Anesthesia was maintained by an IV infusion of propofol (2-9 mg/kg, AstraZeneca Pharmaceuticals, Wilmington, England) and 60% inhaled nitrous oxide. Upon sedation, the pigs were orally intubated and ventilated to maintain a PO_2 of 70-120 torr and a PCO_2 of 35-45 torr (SERVO Ventilator 900C, Siemens, Malvern, PA). Peripheral intravenous lines were placed in the surgically exposed right femoral artery and right jugular vein. A catheter was placed in the right femoral artery for continuous measurement of blood pressure and blood sampling. An introducer (7 French Avanti, Cordis Corporation, Miami Lakes, FL) was placed into the right jugular vein and a Swan-Ganz catheter (5 French, Edwards Lifesciences, Irvine, CA) was placed for measurements of pulmonary artery pressure, pulmonary wedge pressure, cardiac output, and mixed venous blood sampling. Animals then underwent a midline laparotomy and splenectomy. A Foley catheter was placed in the urinary bladder via stab cystostomy for collection of urine. The inferior vena cava (IVC) was cannulated for blood removal. After surgical preparation, animals were allowed to stabilize until plasma lactate levels reach a value of 2.0 mmol/L or less.

C1 animals were monitored for the duration of the experiment, and were not subjected to injury, hemorrhage, or resuscitation. A captive bolt device was used to create a blunt percussive injury to the chest of C2, E1, and E2 animals. Hemorrhagic shock was then induced in these animals by withdrawal of blood from the IVC until a systolic pressure of the lower 50's was reached (typically 35% of total blood volume). Shed blood was placed in an acid-citrate-dextrose bag for later use. A liver crush injury

was induced using a Holcomb clamp technique [130], with two crush injuries created in the liver parenchyma.

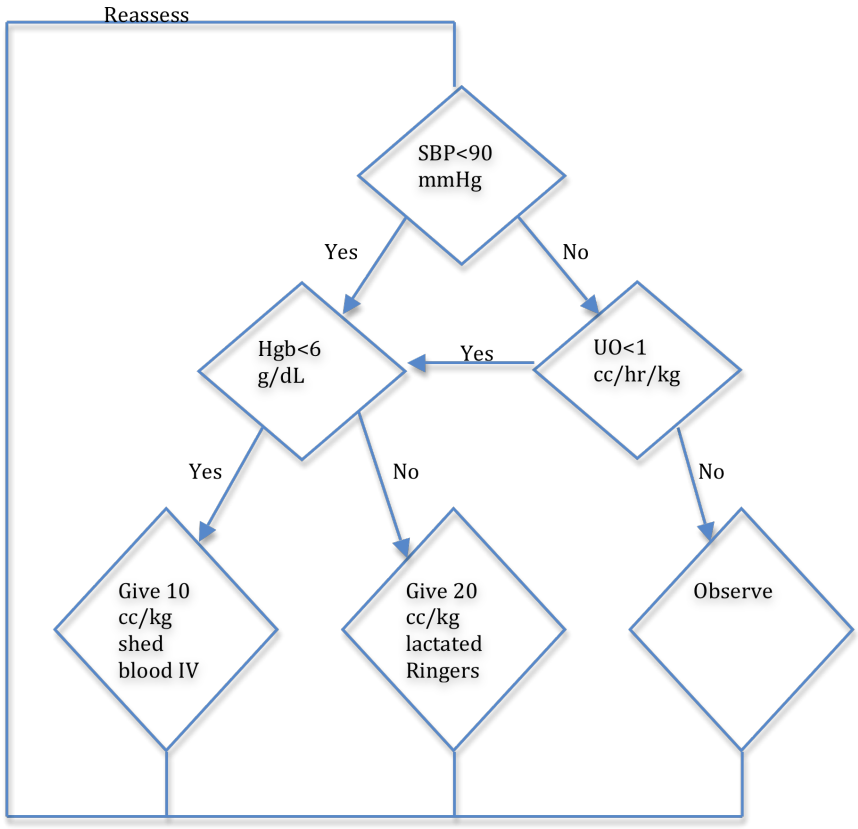

Figure 6.1: Resuscitation algorithm used for shocked, resuscitated animals (groups E1 and E2).

Animals in the E1 and E2 groups were resuscitated with lactated Ringer's fluid given as 20 cc/kg intravenous (IV) boluses to maintain a systolic blood pressure of greater than 80 mmHg for one hour of limited resuscitation, then underwent full resuscitation by protocol. Auto-transfused warmed blood was given at 10 cc/kg IV boluses for a target hemoglobin of greater than 6 g/dL, and, a urine output of greater than 1 cc/kg/hr was targeted. Lactated Ringer's at 20 cc/kg IV boluses or blood at 10 cc/kg/hr

were given as needed (see Figure 6.1). After a resuscitation period of 20 hours, animals were extubated and sent to recovery. At 48 hours after resuscitation, animals were re-intubated for endpoint sample harvesting and then euthanized with Beuthanasia D (1 ml/10kg IV). Urine samples from all forty animals were taken at set timepoints throughout the experiment (see Table 6.2). A total of 165 samples were obtained.

	Baseline	Shock 45	**Time in hours after shock**			
			2	8	20	48
Timepoint	B	S45	FR2	FR8	FR20	PR48
Phase of care	Pre-shock	Shock	Early resuscitation	Late resuscitation		End

Table 6.2: Experimental timeline of urine sample collection and classification into phase of care. Timepoint designations are used in labeling graphics throughout this chapter.

Identification of urinary metabolites from NMR: Urine samples were taken at the time intervals specified in Table 6.2 from the Foley catheter and were frozen and stored at -80° C. Samples were thawed at the time of preparation for NMR analysis. One mL of thawed urine was mixed with 0.5 mL of 0.2 M sodium phosphate buffer prepared with D2O to control pH. The mixture was placed on ice for 10 minutes and then centrifuged at 7000g for 10 minutes. 500 μL of the supernatant was withdrawn and combined with 50 μL of the internal standard 3-(Trimethylsilyl)propionic acid (TSP, Sigma-Aldrich, USA) to a concentration of 1 mM [131]. The internal standard and the buffer were prepared with D_2O to provide a lock for the NMR signal. The pH of the final solution was

recorded and the mixture was transferred to separate 5 mm NMR tubes (Wilmad, LabGlass, USA).

Proton NMR spectra were taken with a Bruker Avance spectrometer with autosampler and 5mm triple resonance 1H/13C/15N TXI CryoProbe with Z-gradient, running TopSpin v. 2.16 (Bruker BioSpin, Fremont, CA USA) at 700.13 MHz (Figure 6.2). A 1D NOESY (Nuclear Overhauser Effect Spectroscopy) pulse sequence was used to collect spectra of each sample. The 90° pulse width was calibrated for each sample, and was generally 12-13 μs. The relaxation time was defined by each sample's 90° pulse width. The relaxation delay was 2 s, the acquisition time was 3 s, the spectral width was 10 kHz, the total number of data points collected was 63,000, and the number of transients collected was 128, for a total experiment time of 11 minutes and 17 seconds. During the relaxation period, the water resonance was presaturated. All spectra were collected at a temperature of 298 K. Line broadening at 0.5 Hz was applied before FFT;

autophasing and auto-baseline correction were applied by TopSpin.

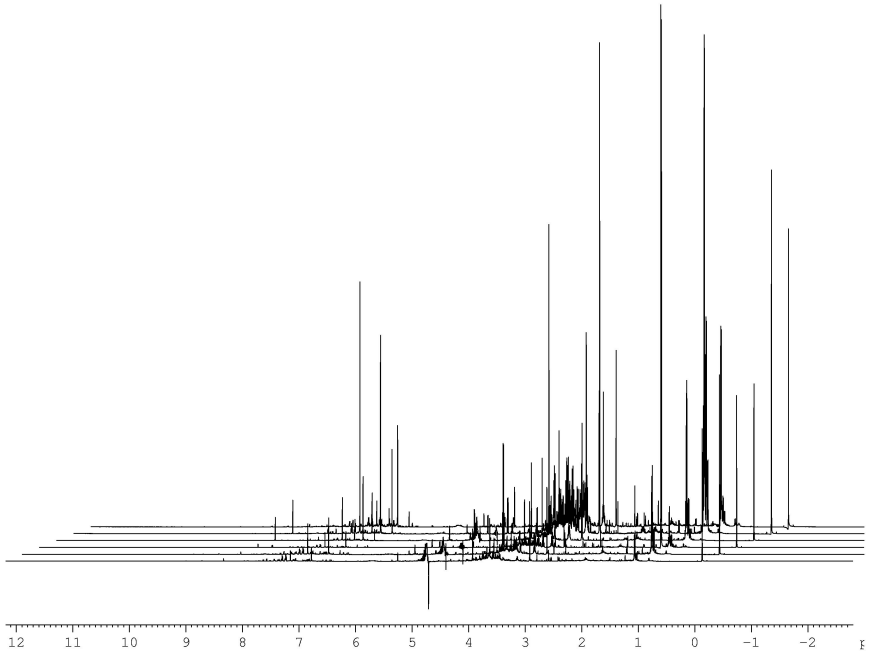

Figure 6.2: Stacked plots of an E1 animal. Spectra are (from front to back): Baseline, S45, FR2, FR8, FR20, PR48. The lactate peak at 1.4 ppm is most prominent at FR2. Other prominent peaks at 1.2 ppm are metabolites of propofol, the anesthetic used. Note that the data from PR48 is omitted from this analysis because there is no measurement of urine output at this timepoint.

Chenomx software [5] was used to identify and quantify a portion of the metabolites present in each urine sample. Fine manual phasing, baseline corrections, and the software's Reference Deconvolution algorithm were applied to each spectrum before targeted profiling of the metabolites was performed. Sixty-two metabolites were fit in each urine sample in this study, resulting in a profile containing the concentration of each identified metabolite in millimoles per liter (mM).

Preparation of data for analysis: Metabolite concentrations were multiplied by urine output (cc/hour) to correct for changes in the concentration of urine throughout the experiment. Urine output data was not available at experimental endpoint (48 hours after the initiation of shock) and this data was omitted from the analysis. The final metabolite abundances (nmol/hr/kg) were log-transformed (base 10) to allow for comparisons between metabolites over several orders of magnitude (range: 0-5.9x10^5 nmol/hr/kg). To deal with taking the logarithm of zero, 0.1 was added to the normalized data. The range of the log-transformed, normalized data is [-1, 5.77]. Urea was removed from the data set because its signal is compromised by the NOESY pulse sequence.

Materials and Methods: Data analysis

Mixed Models: Normalized metabolite concentrations for E1 and E2 animals were analyzed models by statistician Teresa Nelson with mixed linear models using the MIXED procedure in SAS software (version 9.2, SAS Institute Inc. Cary, NC, USA). This analysis was used to assess statistical significance with experimental timepoint, experimental group, and survival status. Two and three-way interactions of these parameters were also considered. The mixed modeling procedure is a generalization of the standard linear model that allows for correlation between variables and for nonconstant variance. The assumptions of this analysis are that the data are normally distributed, that the means of the data are linear in terms of some set of parameters, and that the variances and covariances of the data are linear in terms of a different set of parameters. In order to meet these assumptions, most of the metabolite variables had to

be log-transformed. The square root was used to transform metabolites 1-methylnicotinamide and nicotinamide because of zeros in the data. In the remainder of the analysis, all metabolites were log-transformed as discussed in the previous paragraph. The square root transformation was only used in the mixed models analysis at Ms. Nelson's discretion. Control animals were not treated in this analysis.

PCA: Principal components analysis (PCA) was carried out in R software (http://cran.r-project.org/), an open source and freely available statistical analysis software package. Briefly, the covariance matrix of the data is calculated; then the eigenvalues and eigenvectors (loadings) of the covariance matrix are calculated. PCA scores plots were used with a 95% Hotelling ellipse to identify outliers. Samples that lie outside of the ellipse were removed from analysis. PCA was run on again on the remaining samples and the 95% Hotelling ellipse was re-calculated for a second round of outlier removal.

PLS-DA: Partial least squares discriminant analysis (PLS-DA), a supervised analysis scheme [76], was performed on the normalized, log-transformed, auto-scaled data set. Outliers were also removed for this analysis. The software package SIMCA-P+ (Umetrics, Umea, Sweden) was used to generate PLS-DA models. As discussed in Chapter 4, PLS-DA allows associations to be made between the data (***X***) and observables (***Y***). Loadings vectors and observable class identifiers (eg experimental timepoint, group, or survival) were plotted to visualize associations between observables and metabolites.

Results:

Survival statistics: 100% of animals survived in the C1 group and 100% of the animals died in the C2 group. In the experimental groups, 31% of E1 animals died during the experiment and 50% of E2 animals died during the experiment. The difference between the number of deaths in the E1 and E2 groups was not statistically significant (p=0.3634, see Figure 6.3).

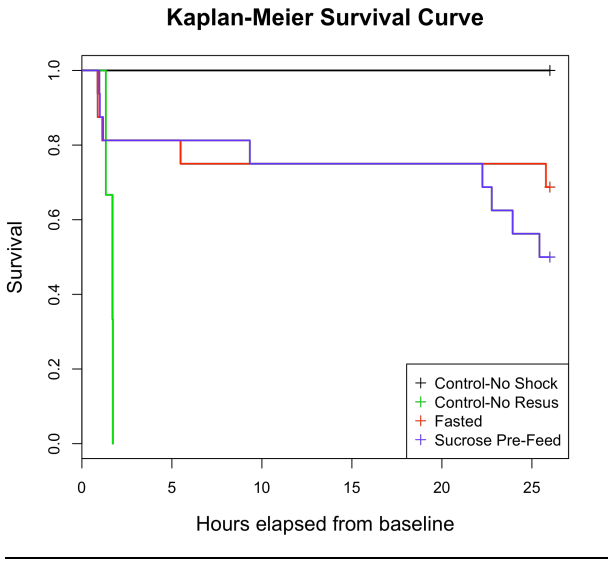

Figure 6.3: Kaplan-Meier curve of survival between the four study groups.

Profiled metabolites: Sixty-two metabolites were profiled in each urine sample with Chenomx software (see Table 6.3). Metabolite concentrations returned by Chemomx were multiplied by urine output (cc/hr) to correct for dilution effects. Urea was subsequently removed from the analysis because its signal is compromised by the NOESY pulse sequence.

1,6 Anhydro-β-D-glucose	Creatine	Lactate	Taurine
1-methylnicotinamide	Creatinine	Lactose	Malonate
2-Ethylacrylate	Cytosine	Malonate	Tiglylglycine
2-Methylglutarate	Dimethylamine	Mannitol	Trigonelline
2-Oxoglutarate	Ethanolamine	Mannose	Trimethylamine
3-Hydroxyisovalerate	Formate	Methylguanidine	Trimethylamine N-oxide
3-Methylxanthine	Fumarate	N,N-Dimethylglycine	Tryptophan
4-Aminohippurate	Glucose	N-Methylhydantoin	Tyramine
Acetate	Glycine	N-Phenylacetylglycine	Tyrosine
Acetoacetate	Hippurate	Nicotinamide	Urea
Acetone	Histamine	Phenylacetylglycine	Urocanate
Alanine	Histidine	Phenylalanine	Xanthine
Allantoin	Homogentisate	Pyruvate	cis-Aconitate
Betaine	Hypoxanthine	Quinolinate	π-Methylhistidine
Choline	Inosine	Ribose	
Citrate	Isovalerate	Succinate	

Table 6.3: List of 62 metabolites profiled with Chenomx software in each of the 165 urine samples.

Mixed Models Result: The metabolites profiled in Table 6.3 were characterized as having significant behavior ($p<0.05$) with experimental timepoint, with experimental group, with experimental time, and two and three-way interactions of these parameters. No metabolites were found to vary significantly with survival status alone, or with survival status and experimental group. One metabolite, cytosine, was found to not change significantly with any parameter. The results are summarized in table 6.4.

Varies significantly with experimental timepoint		
1-Methylnicotinamide	Formate	Ribose
2-Ethylacrylate	Glycine	Taurine
2-Methylguanidine	Hippurate	Thymine
3-Hydroxyisovalerate	Histamine	Tiglylglycine
3-Methylxanthine	Hypoxanthine	Trimethylamine
Acetate	Lactose	Trimethylamine N-oxide
Alanine	Malonate	Tryptophan
Acetoacetate	Mannitol	Tyramine
Acetone	N,N-Dimethylglycine	Tyrosine
Choline	Nicotinamide	Urocanate
Creatinine	Phenylacetylglycine	cis-Aconitate
Dimethylamine	Quinolinate	

Varies significantly with experimental group
1,6-Anhydro β-D-glucose

Varies significantly with experimental group and timepoint
Citrate
Glucose
Histidine
Lactate
Succinate

Varies significantly with survival and timepoint		
4-Aminohippurate	Homogentisate	Phenylalanine
Allantoin	Isovalerate	Xanthine
Creatine	Methylguanidine	
Ethanolamine	N-Phenylacetylglycine	

Varies significantly with survival, experimental group, and experimental timepoint		
2-Oxoglutarate	Mannose	π-Methylhistidine
Betaine	N-Methylhydantoin	
Fumarate	Pyruvate	
Inosine	Trigonelline	

Table 6.4: Results of the mixed modeling analysis for effects of experimental timepoint, experimental group, and survival status, as well as two and three-way interactions of these parameters. Only E1 and E2 urine samples were analyzed here. "Significant" indicates $p<0.05$ for the independent variables and two or three way interactions.

Principal components analysis: Principal components analysis was applied twice to the urinary metabolomics data. Each round of PCA was used to identify outliers. These were defined as scores that lie outside of a 95% confidence interval as shown by Hotelling's ellipse on a scores plot of principal component 1 by principal component 2 (see Figure 6.4). Seven samples were removed in the first round of outlier removal, shown in the left panel.

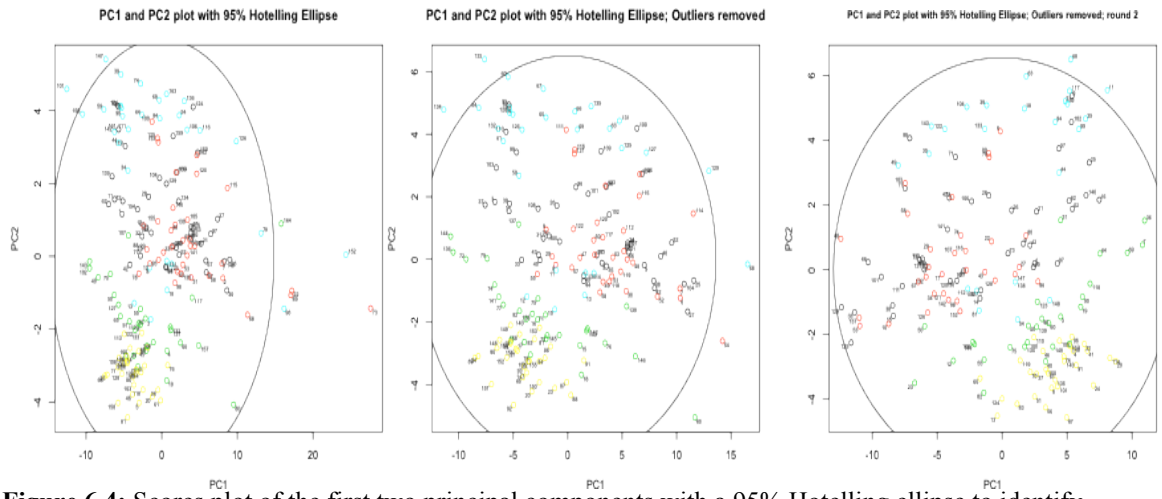

Figure 6.4: Scores plot of the first two principal components with a 95% Hotelling ellipse to identify outliers. Two rounds of outlier removal were completed. Panel (a) shows the full data set; panel (b) shows

the PCA scores and 95% Hotelling ellipse after the first round of outlier removal; panel (c) shows the PCA scores and 95% Hotelling ellipse after the second round of outlier removal. A total of thirteen samples were identified as outliers and removed from the analysis.

The process was repeated, and an additional six samples were identified and removed in the second round (middle panel of 6.4). Of the outliers identified, four samples were taken at the S45 timepoint, eight samples were taken at FR2, and two were taken at FR8. Three-dimensional scores plots showing the difference between the analysis with outliers and without outliers is shown in Figure 6.5. Removal of outliers caused the proportion of variance explained by the first three principal components to drop from 74% to 64%.

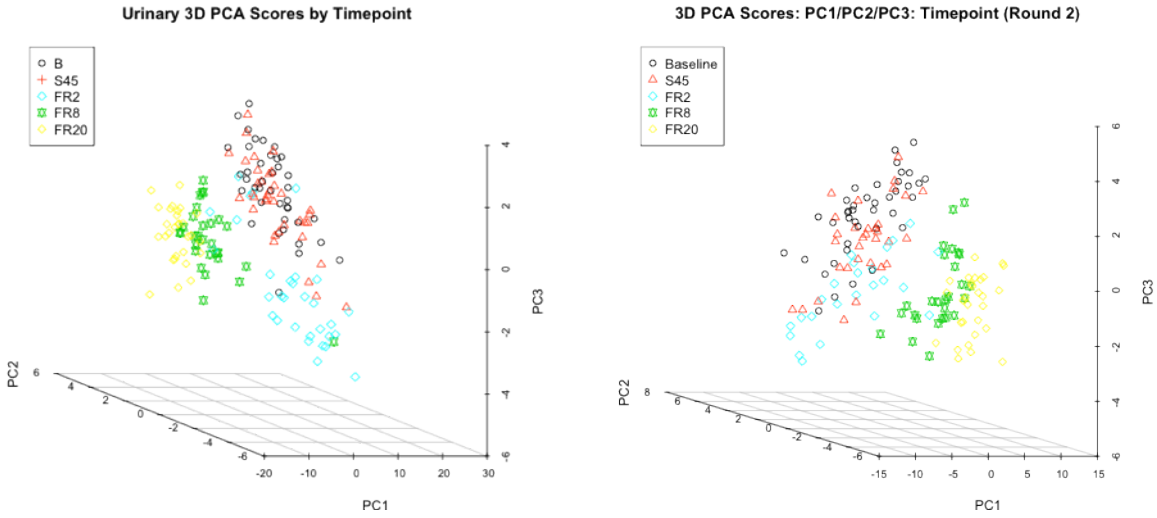

Figure 6.5: Side-by-side comparison of PCA scores plots before outlier removal (L) and after two rounds of outlier removal (R). The PCA with outliers explains a higher proportion of variance (74%) than that with outliers removed (64%).

Additionally, it was observed that PCA shows sample clustering by experimental timepoint only. There is little to no clustering by group or survival status, as shown in Figure 6.6.

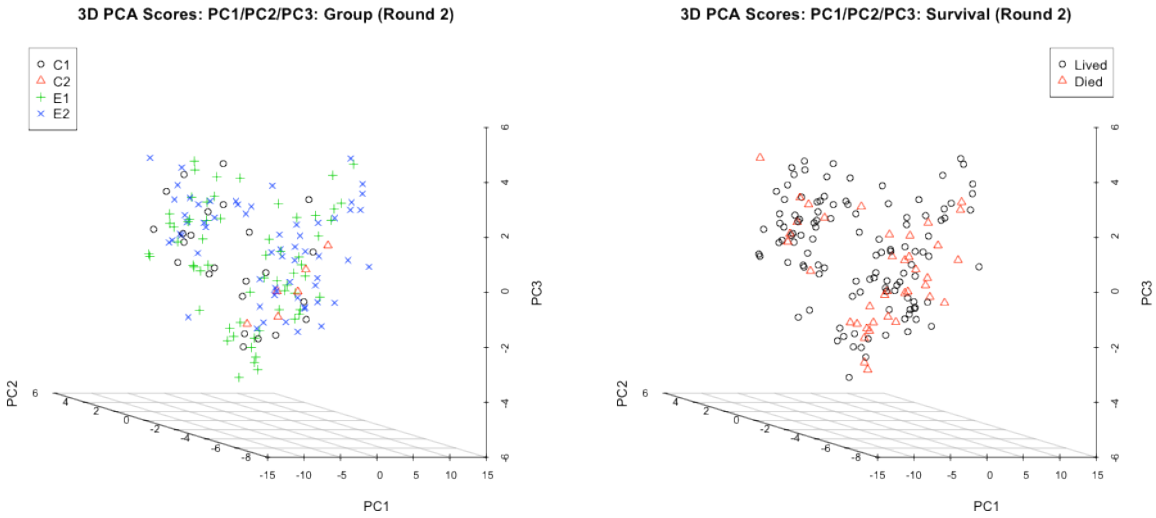

Figure 6.6: Three-dimensional scores plots of the data with outliers removed. This is the same data as in Figure 6.5 but the scores are colored by group (left) or survival (right). Comparison of these plots with the scores colored by experimental timepoint indicate that PCA of the urinary metabolome is best suited to highlighting the differences according to experimental timepoint.

Partial least squares discriminant analysis: A PLS-DA model was constructed with SIMCA-P+ software (v. 12.0) on the normalized, log-transformed data with outliers removed. Models were constructed of the full data set and of various subsets of the data. Models were judged based upon the fraction of data explained by the model (R^2) and the model's ability to accurately assign samples to a class (Q^2) as discussed in Materials and Methods.

Model	Data subset/Class	R^2	Q^2
A	E2 (by survival)	0.74	0.09
B	Full (by survival)	0.55	0.22
C	E1 vs C1	0.49	0.30
D	Full (by group)	0.46	0.32
E	E2 (by timepoint)	0.58	0.47
F	Full (by timepoint)	0.57	0.48
G	E1 (by timepoint)	0.64	0.55
H	E2 FR8 vs C1 FR 8*	0.97	0.62
I	E2 FR2 vs C1 FR2*	0.96	0.63
J	E2 vs C1*	0.77	0.68
K	E1 Baseline vs E2 Baseline*	0.92	0.69
L	E1 vs E2*	0.90	0.77
M	E1 FR2 vs C1 FR2*	0.98	0.78
N	B vs FR2 (full data set)*	0.88	0.81
O	E1 FR8 vs E2 FR8*	0.98	0.86
P	FR2 vs FR20 (full data set)*	0.95	0.90
Q	E1 B vs E1FR2 vs E1FR20*	0.96	0.92

Table 6.5: Model parameters for various PLS-DA models built using the specified data subsets with SIMCA-P+ software. R^2 estimates the fraction of the data explained, and Q^2 estimates the model's ability to accurately classify a new sample. (*) indicates that the model has good predictive value; $Q^2>0.5$. All models built to discriminate by survival had poor predictive value ($Q^2<0.5$, data not shown).

PLS-DA analysis was used to examine subsets of the data as outlined in Table 6.5. Though discrimination of urine samples by survival is poor, several of these models are able to discriminate urine samples by experimental group as well as timepoint. Models of the same subset of data by different class identifiers produced different R^2 and Q^2 values (models B, D, and F). The models with the highest predictive power are labeled (*) in Table 6.5. Scores and loadings plots of all models in Table 6.5 are reported in Appendix B; some are reproduced here.

A PLS-DA model of the full data set that discriminates urine samples by experimental timepoint is shown in Figure 6.7 (model F). This model has moderate

predictive power (R^2=0.57, Q^2=0.48). Examination of the loadings plot in Figure 6.7 (bottom) identifies associations between metabolites and experimental timepoints. For example, baseline and S45 are loosely associated with trigonelline, mannitol, and N,N-dimethylglycine. FR2 is associated with succinate and choline. FR20 is loosely associated with taurine, glycine, formate, homogentisate, creatine, and trimethylamine N-oxide.

In general, models of the full urine data set have poor to moderate predictive power. The predictive power was increased by selectively choosing physiological states to model, as is often the case in supervised analysis schemes. Many of the relationships observed in Model F are preserved in subsequent models with better predictive power. For example, respiratory metabolites are common to FR2 models, and creatine and trimethylamine N-oxide are common to FR20 models.

F: Full data set differentiated by timepoint. R^2=0.57, Q^2=0.48

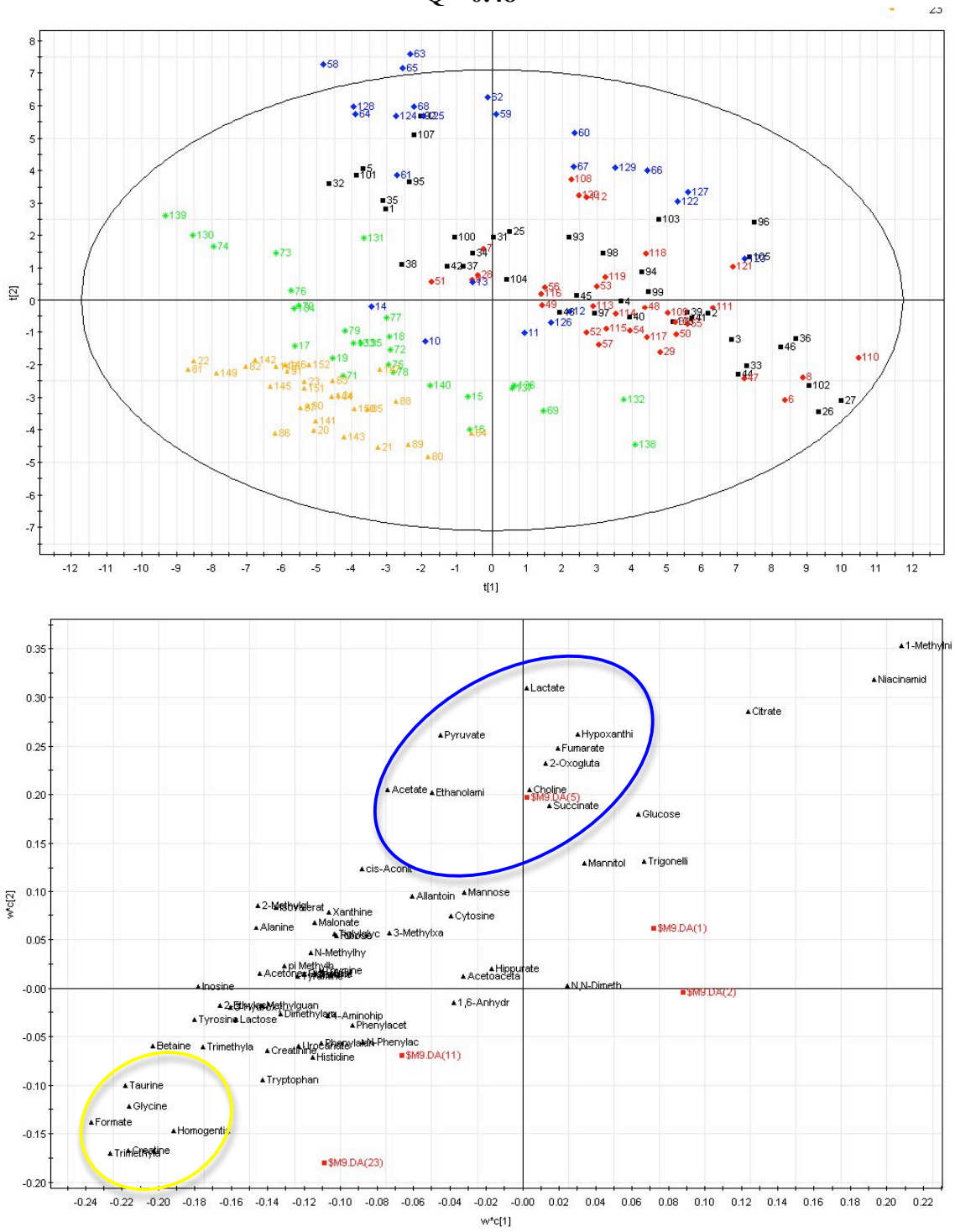

Figure 6.7: Scores plot (top) and loadings plot (bottom) for PLS-DA model of the full urine data set by timepoint. There is moderate separation between B/S45 data (black/red), FR2 data (blue), and FR8/FR20

data (green/yellow). Examination of the loadings plot shows that FR2 (blue) is strongly associated with choline and succinate. FR20 samples (yellow) are somewhat associated with taurine, glycine, formate, homogentisate, creatine, and trimethylamine N-oxide.

Explicitly stated, the major results that are obtained from examining the models presented in Table 6.5 are as follows:

1. The urine metabolome does not discriminate by survival. The only survival information is obtained indirectly by modeling C1 and C2.

2. FR2 is a distinguishing timepoint that is generally associated with metabolites of both aerobic and anaerobic respiration, as well as markers of hypoxia and cellular membrane breakdown.

3. FR20 is a distinguishing timepoint, though levels of the metabolites commonly associated with this timepoint do not differ between experimental and control animals.

4. The urine metabolome reflects phase-of-care.

5. The urine metabolome separates experimental animals from controls, though E1 is similar to C1 at all timepoints but FR2.

6. E1 and E2 animals differ before shock and injury, and the response to hemorrhage is different.

To illustrate these results, six models (A, N, P, Q, C, and K) are presented.

1. The urine metabolome does not discriminate by survival.

All PLS-DA models that were built to discriminate by survival had $Q^2<0.5$ (data not shown). Urine does not give direct information about mortality from trauma or

hemorrhagic shock. All models that were constructed to discriminate urine samples by survival had Q^2 values less than 0.5; several of these had negative Q^2 values (data not shown). This indicates that urine is not a good biofluid for assessing or predicting survival in a hemorrhagic shock and traumatic injury model.

Model A: E2 by survival. R^2=0.74, Q^2=0.09

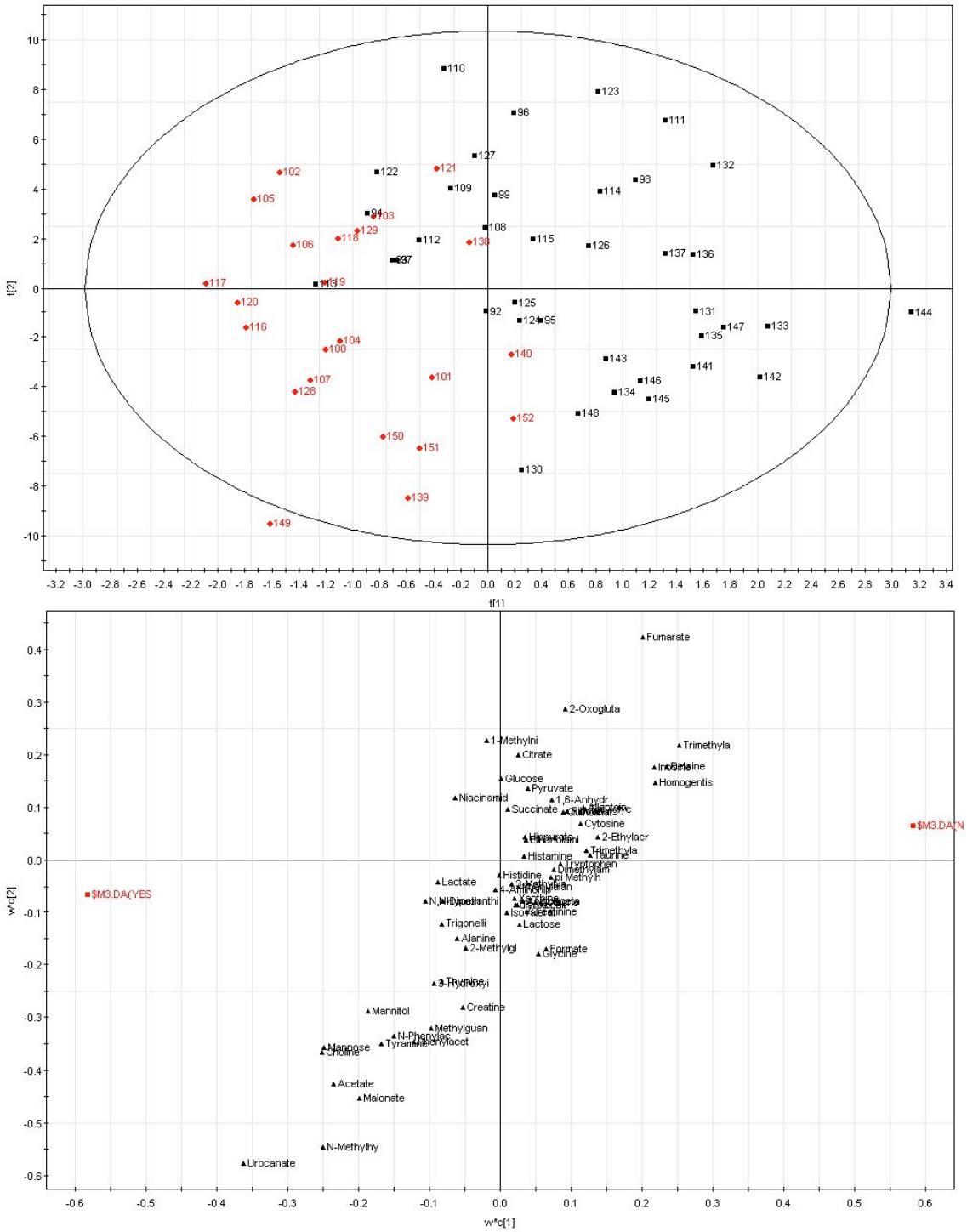

Figure 6.8: PLS-DA model discriminating between urine samples of E2 animals that lived (black) and those that died (red).

2. The FR2 timepoint is commonly associated with metabolites of aerobic and anaerobic respiration.

In models I, M, N, P, and Q (see Appendix B), we see that FR2 is a distinguishing timepoint in the experiment. Model N is shown in Figure 6.9. The metabolites associated with this timepoint are involved in respiration, components of cellular membranes, and known markers of ischemia/reperfusion injury. In model N, anaerobic metabolism is highlighted via lactate and pyruvate, I/R injury is highlighted by hypoxanthine, choline is a common component of phospholipids and thus of cellular membranes, osmotic stress is highlighted by betaine, and catabolism is highlighted by formate.

Model N: Baseline vs. FR2. R^2=0.88, Q^2=0.81

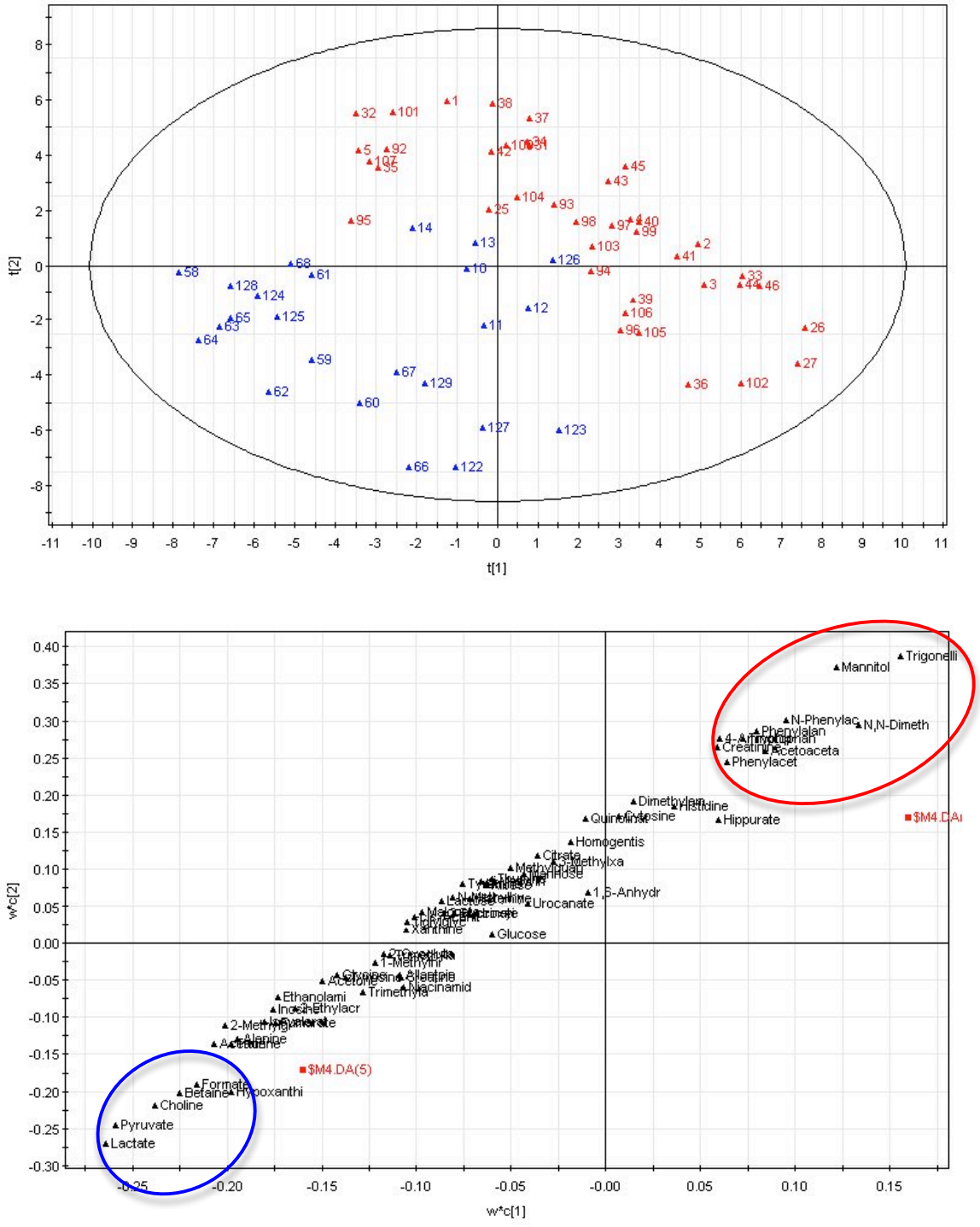

Figure 6.9: PLS-DA model of Baseline (red) and FR2 (blue). Loadings associate metabolites with the observation of experimental timepoint. Metabolites associated with baseline are ringed in red and those associated with FR2 are ringed in blue. Metabolites grouped with FR2 are associated with anaerobic

respiration (lactate, pyruvate), ischemia/reperfusion injury (hypoxanthine), cellular damage (choline), osmotic stress (betaine) and catabolism (formate).

Other metabolites that are commonly highlighted by FR2 models (E, F, G, M, N, P, and Q) are glucose, acetate, citrate, 2-oxoglutarate, succinate, formate, ethanolamine, 1-methylnicotinamide, and nicotinamide. All of these metabolites are observed to increase at the FR2 timepoint (see Appendix C for plots). These metabolites can all be associated with the mechanisms discussed in Chapter 2.

3. The FR20 timepoint can be distinguished from other timepoints. However, the metabolites associated with FR20 cannot be distinguished between C1, E1, and E2 animals.

Models E, F, G, P and Q show that FR20 is a distinguishing timepoint. Metabolites associated with this timepoint have been linked to organ injury. Amino acids and osmolytes are also associated with this timepoint. Model P is shown in Figure 6.10.

Model P: FR2 vs. FR20. R^2=0.95, Q^2=0.90

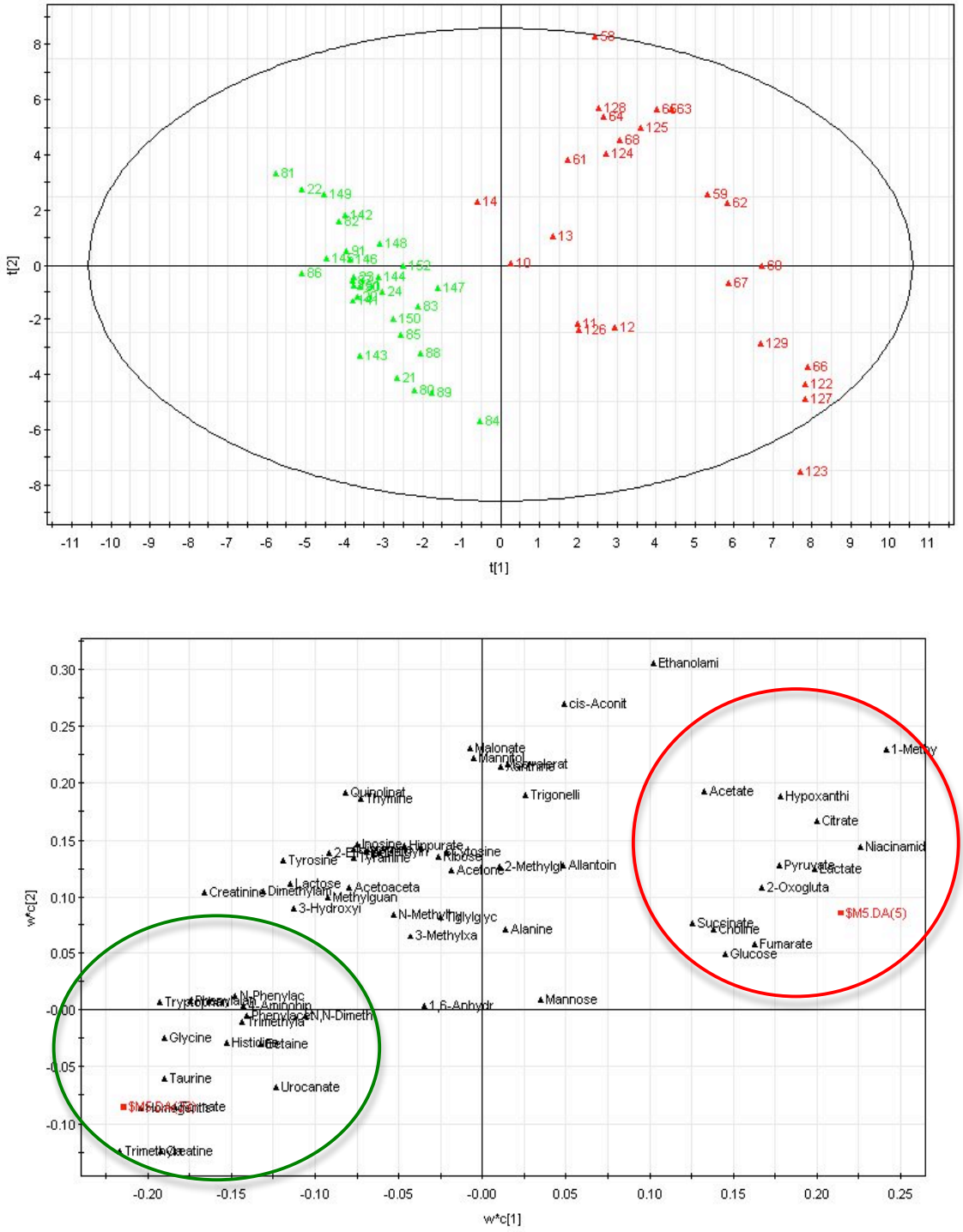

Figure 6.10: PLS-DA model of FR2 (red) and FR20 (green) timepoints. Metabolites associated with FR2 are largely associated with respiration, ischemia/reperfusion injury, and cell damage. Metabolites

associated with FR20 are N-phenylacetylglycine, phenylalanine, tryptophan, 4-aminohippurate, phenylacetylglycine, N,N-dimethylglycine, trimethylamine, glycine, histidine, betaine, taurine, urocanate, homogentisate, formate, trimethylamine N-oxide, and creatine.

Among the PLS-DA models that can discriminate the FR20 timepoint as presented in Appendix B, the most commonly identified metabolites were creatine, formate, glycine, homogentisate, taurine, and trimethylamine N-oxide. In general, the metabolites associated with FR20 are all elevated at that timepoint. However, none of these metabolites are distinguishable by experimental group. Levels of these metabolites are similar for experimental animals and non-injured control animals (see boxplots in Appendix C).

4. The urinary metabolome can discriminate phase of care: pre-shock, early resuscitation, and late resuscitation.

That the urine metabolome can distinguish certain timepoints leads to the next result. The experimental timepoints can be roughly categorized as pre-shock (baseline), shock (S45), early resuscitation (FR2) and late resuscitation (FR8/FR20) as seen in Model F, though B/S45 and FR8/FR20 timepoints are not well-separated here. The urine metabolome is not an ideal medium to assess the shock state because vasoconstriction and other fluid-compensating measures mean that little to no urine is produced during shock. According to the mixed models analysis performed by Ms. Nelson, there was a significant decrease ($p<0.05$) in urine output from baseline to S45 in E1 and E2 animals. Urine output is significantly lower at S45 than at FR8 or FR20 ($p<7.2x10^{-6}$ via pairwise t-

tests); therefore, urine output, not the urine metabolome, is useful for assessing the shock state. A boxplot of urine output for the experimental timepoints is shown in Figure 6.11.

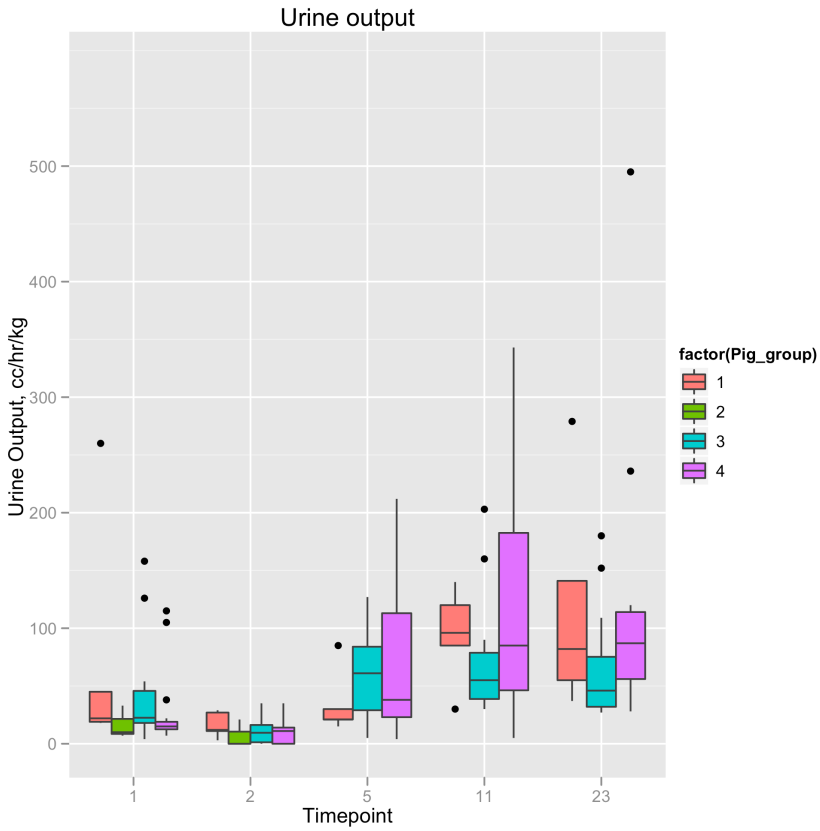

Figure 6.11: Boxplot of urine output shows that urine output is depressed at S45 in hemorrhaged animals (green, turquoise, and purple). The mixed models result for urine output for E1 and E2 animals shows that the average urine output drops significantly due to hemorrhage ($p<0.05$), rises after hemorrhage and then drops at FR20 to an average value significantly higher than baseline. The box covers the first (Q1) and third (Q3) quartile of the data. The line in the box represents the median value. The whiskers extend to ± 1.5*IQR, where IQR=Q3-Q1. Outliers are shown as points.

The urine metabolome is more useful for assessing resuscitation. Here, we can differentiate phase-of-care as pre-shock, early resuscitation, and late resuscitation. This

is illustrated by models N, P, Q, and to a lesser extent, F and G. Model Q is shown in Figure 6.12.

Model Q: E1 B vs E1 FR2 vs E1 FR20. R^2=0.96, Q=0.92

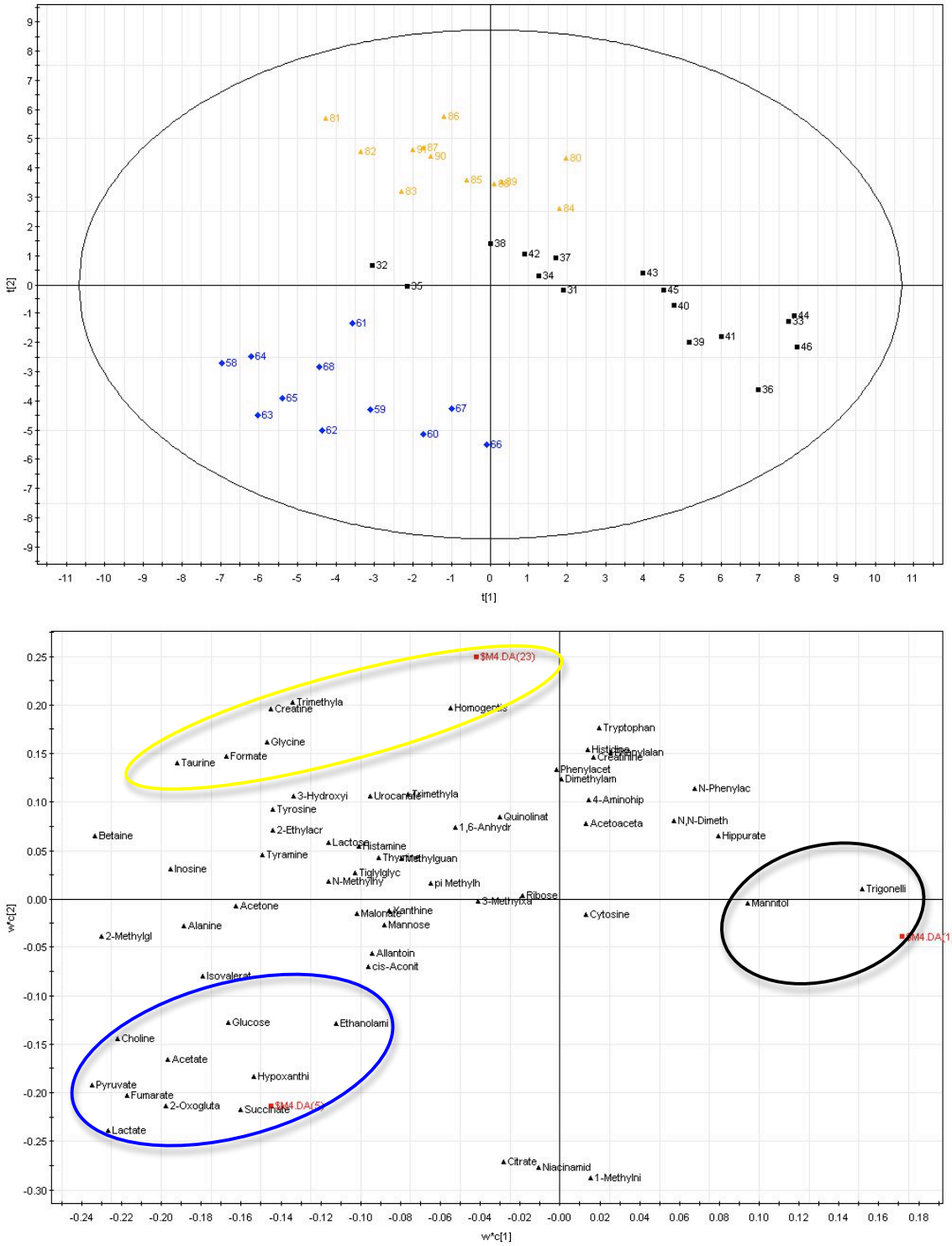

Figure 6.12: PLS-DA model of E1 urine samples at baseline (black), FR2 (blue), and FR20 (green). The high Q^2 of this model indicates the predictive value of urine with respect to phase-of-care. Exogenous

metabolite mannitol and trigonelline are associated with baseline samples. The respiratory metabolites, choline, ethanolamine (cell damage), and hypoxanthine (I/R injury) are associated with FR2, and markers of injury and catabolism are associated with FR20 (creatine, trimethylamine N-oxide, glycine, formate, and taurine).

For E1 animals, phase-of-care as defined above is well-classified. The primary metabolites that were commonly identified with FR2 were also defined in this model. The same is true for the metabolites identified at FR20. The cluster of metabolites at the bottom of the plot (citrate, 1-methylnictinamide, and niacinamide) are normally associated with FR2.

5. The metabolome is able to distinguish experimental animals from control animals in certain models.

PLS-DA models of the urinary metabolome were generally able to distinguish shocked animals from non-shocked animals. In E1 animals, this was only true at the FR2 timepoint (R^2=0.98, Q^2=0.78). Model C was not able to discriminate between E1 and C1 when all timepoints were considered. When separate models were made for E1 and C1 at each timepoint, all had R^2>0.9, but only S45 and FR2 had Q^2>0.5.

Model M: E1 at FR2 vs. C1 at FR2. R^2=0.98, Q^2=0.78

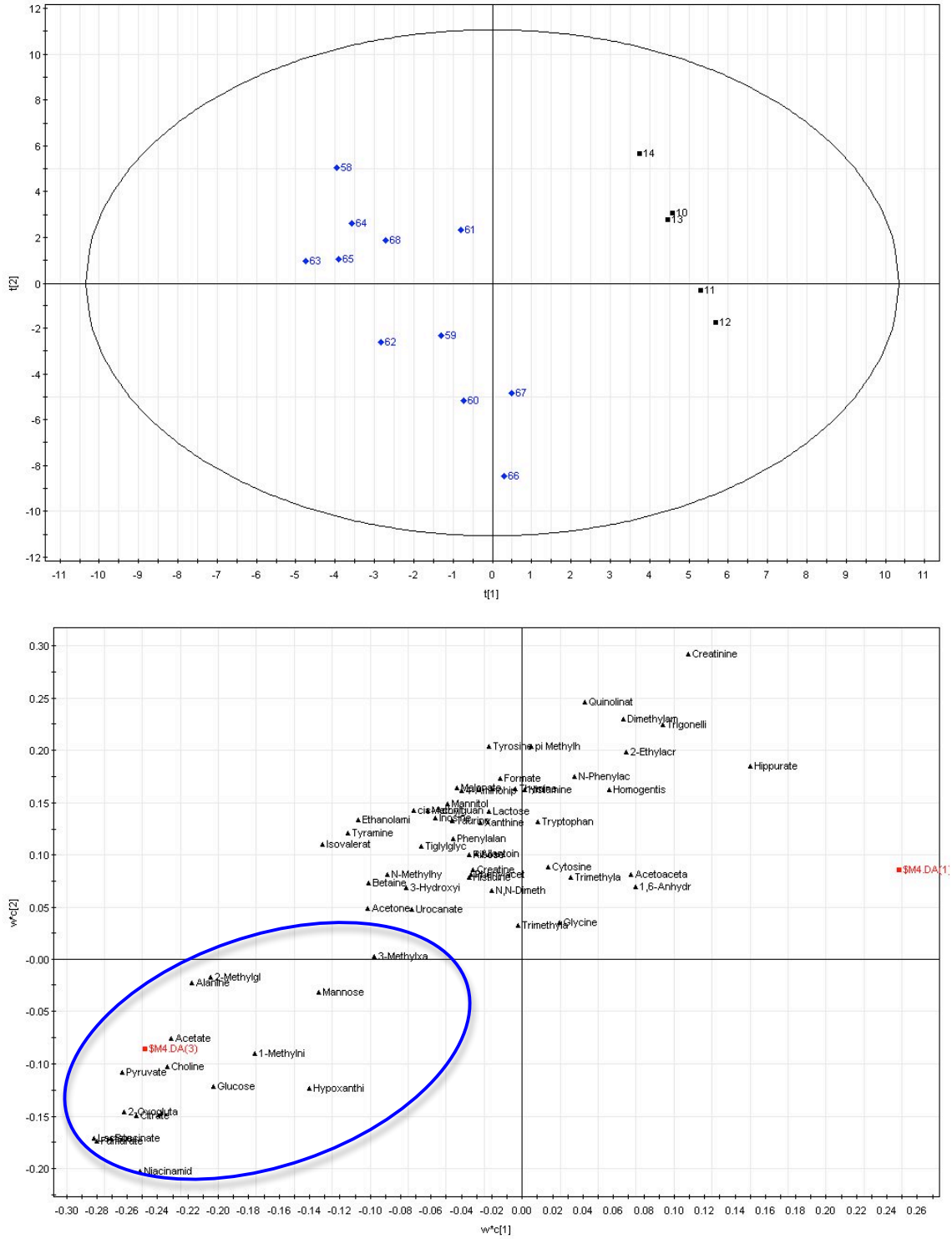

Figure 6.13: PLS-DA model of E1 urine samples at FR2 (blue) vs. C1 urine samples at FR2 (black). This

model and the model of S45 urine samples were the only models able to distinguish between E1 and C1 samples.

PLS-DA models that support the claim that shocked animals can be distinguished from non-shocked animals are models H, I, J, and M (see Appendix B).

6. E1 and E2 animals can be discriminated, both before and after hemorrhage.

Finally, PLS-DA model K (Figure 6.14) implies that fed and hemorrhaged animals enter trauma in a different state than fasted animals do. Models J, L, and O characterize the response of E2 animals to trauma. Models L and O also provide evidence that E2 animals respond to hemorrhage and trauma differently than E1 animals (see Appendix B for models).

Model K: E1 B vs. E2 B. R^2=0.92, Q^2=0.69

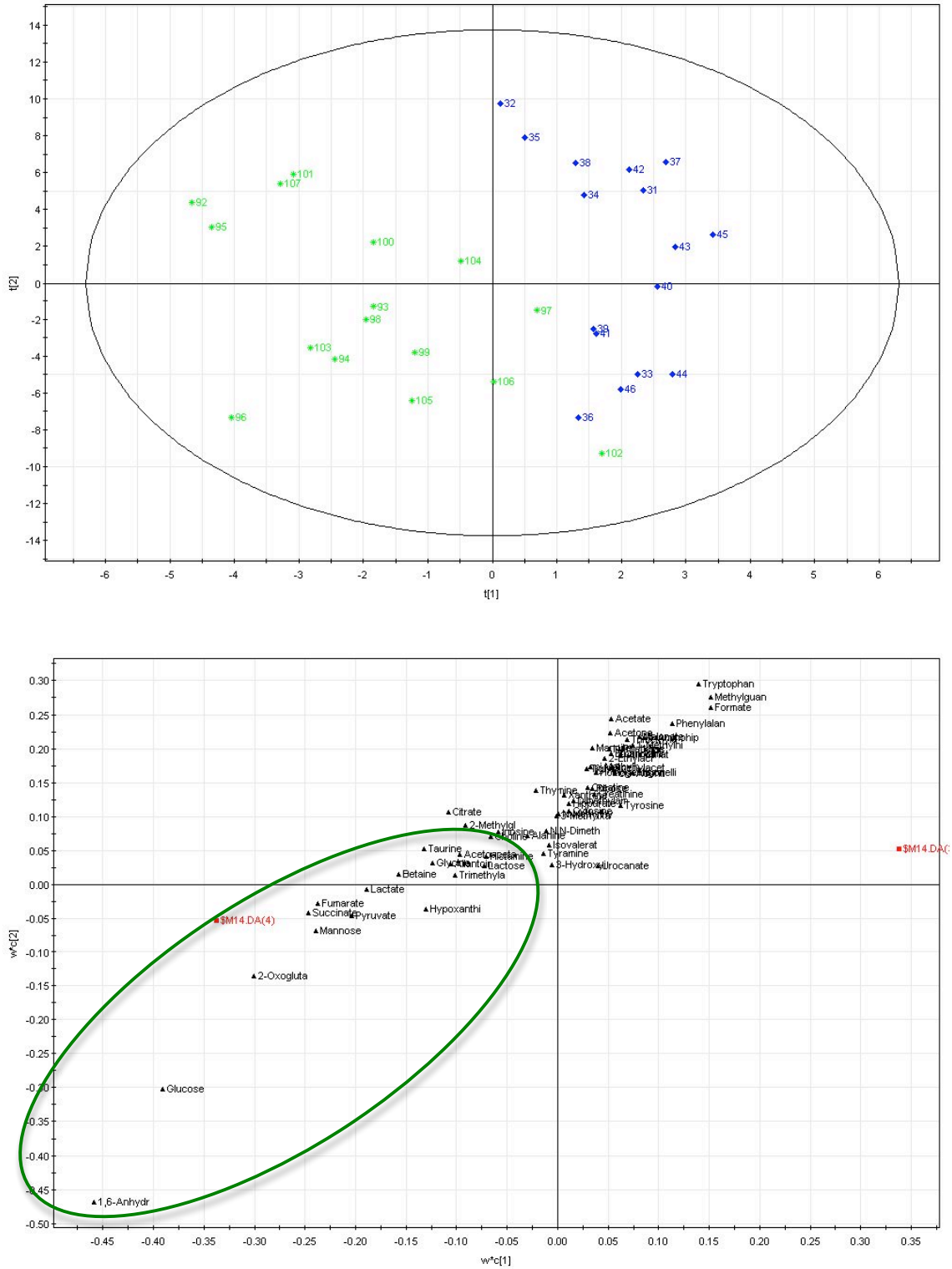

Figure 6.14: PLS-DA model of E1 baseline urine samples (blue) and E2 urine samples at baseline (green).

No metabolites are clearly associated with E1 samples, though E2 samples are associated with 1,6-Anhydro β-D-glucose, and metabolites associated with respiration. These samples are, to a lesser extent, also associated with taurine, mannose, hypoxanthine, acetoacetate, glycine, betaine, trimethylamine N-oxide, allantoin, acetoacetate, and lactose.

The metabolite 1,6-Anhydro β-D-glucose distinguishes all E2 urine samples; it is elevated in these samples relative to all others ($p<2e-16$ via student's t-test). This is confirmed by the mixed models result, where 1,6-Anhydro β-D-glucose was found to be significantly elevated in the urine of E2 animals.

Glucose is also responsible for this variation, particularly at early timepoints when the animal is presumably clearing the fed sucrose. Urinary glucose values in these animals become similar to fasted animals by FR8. Values of urinary glucose between the fasted (E1) and fed (E2) animals are significantly higher in E2 animals at both baseline and S45 (see Table 6.6).

Timepoint	Group	Average Glucose +/- standard deviation	p-value
Baseline	E1	1,100±1,510 nmol/hr/kg	1.287e-06
	E2	59,600±106,000 nmol/hr/kg	
S45	E1	247±358 nmol/hr/kg	2.765e-05
	E2	23,500±25,000 nmol/hr/kg	

Table 6.6: Table comparing urinary glucose values at baseline and S45 between experimental groups. Glucose values were significantly higher for E2 (fed) animals as compared to E1 (fasted) animals. The p-values comparing the groups were obtained with a Student's t-test.

Model L (Appendix B) shows that mannose also distinguishes fed (E2) animals from non-resuscitated (C1) and fasted (E1) animals. This metabolite was commonly identified

in addition to 1,6-Anhydro β-D-glucose among models that can discriminate E2 urine samples.

Discussion:

Mixed models analysis: This analysis was performed by statistician Teresa Nelson on the urinary metabolome. Metabolites were analyzed for variation with experimental timepoint, experimental group, and survival as well as two and three-way interactions of these parameters. Only E1 and E2 animals were considered in this analysis. Most of the metabolites analyzed changed with timepoint only. Levels of twenty metabolites had some dependence on survival, but all were coupled with either timepoint or timepoint and group. No direct association with survival was observed, and this lack of survival information proved to be a defining characteristic of the urine metabolome under PLS-DA analysis. Only one metabolite, 1,6-Anhydro β-D-glucose, was observed to change significantly by experimental group alone. This metabolite was subsequently observed to drive separation between E2 animals and other animals in all PLS-DA models that were constructed to discriminate E2 urine samples. A boxplot of this metabolite is shown in Figure 6.15.

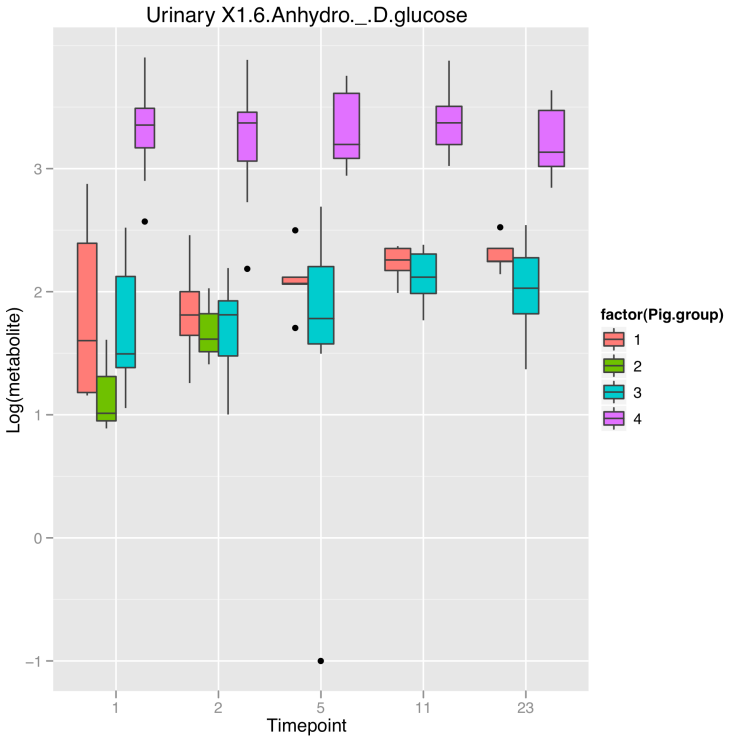

Figure 6.15: Boxplot of urinary 1,6-Anhydro β-D-glucose. Orange=C1, green=C2, turquoise=C3, and purple=C4. 1,6-Anhydro β-D-glucose was observed at roughly constant levels throughout the experiment, and is significantly elevated in the urine of E2 (fed) animals. This implies that the metabolite arises from glucose, though the mechanism is unknown.

Principal components analysis: Of the 13 samples identified as outliers with a 95% Hotelling ellipse, the majority of them were taken at the FR2 timepoint. A three-dimensional plot of the PCA scores demonstrated that urine is prone to group by experimental timepoint. To further examine relationships between the urinary metabolites and observable quantities, the supervised analysis technique of partial least squares discriminant analysis was used on the urinary metabolome to link experimental timepoint, experimental group, and survival status with specific metabolites.

PLS-DA models: These models demonstrate that urine has little predictive power to discriminate urine samples by survival status. They also show that models can discriminate by group in certain cases.

Urine samples can be discriminated by timepoint (Model F, Appendix B, Q^2=0.55). The predictive power was greatly improved when only baseline, FR2, and FR20 samples are included in the model (Model Q, Figure 6.13, Q^2=0.92). Baseline samples are associated with trigonelline and mannitol, both of which may be exogenous compounds. FR2 samples were associated with lactate, pyruvate, glucose, acetate, fumarate, succinate, 2-oxoglutarate, hypoxanthine, choline and ethanolamine. FR20 samples were associated with taurine, glycine, creatine, trimethylamine N-oxide, formate, and homogentisate.

When urine samples from all groups were discriminated by timepoint alone, many of the same metabolites were identified. When baseline samples were compared to FR2 samples (Model N, Figure 6.9, Q^2=0.81), hypoxanthine, choline, lactate and pyruvate are among the metabolites associated with FR2. In the model of FR2 vs. FR20 (Model P, Figure 6.11, Q^2=0.90), acetate, lactate, glucose, pyruvate, citrate, 2-oxoglutarate, succinate, fumarate, choline, hypoxanthine, 1-methylnicotinamide, and nicotinamide are associated with FR2. Taurine, glycine, homogentisate, creatine, formate, and trimethylamine N-oxide are among the metabolites associated with FR20.

E1 and C1 urine samples can be separated, but only at FR2 and S45 (model M, see Figure 6.13. Data not shown for S45 model). E2 urine samples can generally be

separated from controls; this is true when the full set of urine samples from each group are compared (model J), as well as when the data is limited to samples taken at FR2 or FR8 (models H and I). Both E1 and E2 urine samples are largely discriminated via the metabolites glucose, lactate, pyruvate, citrate, 2-oxoglutarate, succinate, and fumarate. E2 samples are also commonly identified by 1,6-Anhydro β-D-glucose and mannose. Few metabolites were observed to be strongly associated with C1 samples.

Discrimination between E1 and E2 urine samples implies the presence of differences in metabolism due to pre-feeding. E2 urine can often be properly discriminated from that of non-hemorrhaged pigs because of elevated 1,6-Anhydro β-D-glucose levels ($Q^2 \geq 0.62$). Discrimination between E1 and E2 urine can be improved by examining urine taken at FR8 (model O, $Q^2 = 0.86$). This implies that there are differences in response to hemorrhage and traumatic injury based upon feeding state. Metabolites associated with E1 urine samples at FR8 are betaine, acetate, quinolinate, 4-aminohippurate, creatine, tyrosine, N,N-dimethylglycine, and urocanate. Metabolites associated with E2 urine at FR8 are 1,6-Anhydro β-D-glucose, glucose, N-methylhydantoin, fumarate, 2-oxoglutarate, formate, histamine, ribose, and 3-methylxanthine. Most of the metabolites highlighted by this model are not indicative of the general behavior of the urinary metabolome, and warrant further investigation. It should also be noted that comparison of E1 and E2 urine at timepoints other than baseline and FR8 have poor predictive value (data not shown).

When all metabolites from all PLS-DA analyses are taken together, a portion of metabolites were repeatedly associated with certain observables. These metabolites are

compiled in Table 6.7 with associated physiological roles. Boxplots of these metabolites are shown in Appendix C. These metabolites provide an overview of the properties of the urinary metabolome associated with hemorrhagic shock and traumatic injury.

Metabolite	Associated observables	Observation and role in physiology
1,6-Anhydro β-D-glucose	E2	Elevated in E2 animals; normal component of urine; distinguishes between fed and fasted animals.
Mannose	E2	Elevated in E2 animals through FR20; anti-inflammatory properties, particularly with respect to acute lung injury
1-Methylnicotinamide	FR2	Increased at FR2, particularly in E1 animals; falls to 0 nm/hr/kg in some animals by FR8 or FR20; metabolite of nicotinamide (see below); has anti-inflammatory and ROS-scavenging properties; may be involved in regulation of thrombosis
2-oxoglutarate	FR2, E2	Elevated in E2 animals at B-FR2; elevated in E1 and E2 animals at FR2; TCA metabolite; involved in aerobic metabolism
Acetate	FR2, E1	Increased in E1 animals at FR2; wide variability in E2 animals at FR2; byproduct of anaerobic respiration
Choline	FR2	Elevated in E1 animals at FR2; drops in all animals at FR8; major component of phospholipids and membranes; may indicate cell membrane damage
Citrate	FR2, E2	Elevated in E1 and E2 animals FR2-FR8; TCA metabolite; involved in aerobic metabolism
Ethanolamine	FR2	Slightly elevated in E1 animals at FR2; component of phospholipids and membranes and may be indicative of cell membrane damage
Fumarate	FR2, E2	Elevated in E1 and E2 animals at FR2; TCA metabolite formed by oxidation of succinate (see succinate below); involved in aerobic respiration
Glucose	FR2, E2	Elevated in E2 animals B-FR2; elevated in E1 animals at FR2; major energy source via glycolysis
Hypoxanthine	FR2	Slightly elevated in E1 and E2 animals at FR2; purine metabolism; increases in hypoxanthine are indicative of oxidative stress
Lactate	FR2, E2	Elevated in E1 and E2 animals at FR2; involved in anaerobic metabolism; clinical marker of injury
Nicotinamide	FR2	Elevated in E1 and E2 animals at FR2; drops to 0 nm//kg/hr in many animals by FR8/FR20; component of NAD; has anti-inflammatory properties; also referred to as niacinamide
Pyruvate	FR2, E2	Elevated in E1 and E2 animals at FR2; intermediate between glycolysis and the TCA cycle (aerobic conditions); converts to lactate (anaerobic conditions)
Succinate	FR2, E2	Elevated in E1 and E2 animals at FR2; elevated in E2 animals B-FR2; TCA metabolite; can donate electrons to the electron transport chain via succinate + FAD → fumarate + $FADH_2$

Creatine	FR20	Elevated in all animals at FR20; creatinuria is a known marker of trauma but may also be present in normal individuals
Formate	FR20	Elevated in all animals at FR20; slightly more elevated in E1 and E2 animals than in C1 animals; involved in metabolism of one-carbon compounds. Can also inhibit the electron transport chain
Glycine	FR20	Elevated in all animals at FR20; slightly more elevated in E1 and E2 animals; amino acid; protein precursor
Homogentisate	FR20	Elevated in all animals at FR20; generated in breakdown of phenylalanine and tyrosine. These metabolites are precursors of catecholamines, such as epinephrine.
Taurine	FR20	Elevated in all animals at FR20; amino acid stored in muscle cells. Presence in urine may indicate damage to muscle.
Trimethylamine N-oxide	FR20	Elevated in all animals at FR20; oxidized from choline via trimethylamine; osmolyte; contributes to protein stability in the presence of high urea concentrations; known marker of kidney injury

Table 6.7: Summary of all metabolites retained in the major categorical comparisons that the urinary metabolome can discriminate between in PLS-DA analyses. Physiological properties and associations are also summarized.

The FR2 timepoint is associated with the physiological mechanisms associated with hemorrhagic shock that were discussed in Chapter 2. In the cohort of models that discriminate FR2 samples specifically (models H, M, N, P, and Q), the urinary metabolites associated with respiration were commonly identified. The TCA metabolites citrate, 2-oxoglutarate, succinate, and fumarate were associated with this timepoint. All were observed to increase in E1 and E2 animals at FR2 (see boxplots in Appendix C). Glucose, lactate, pyruvate, and acetate were also increased at this timepoint in E1 and E2 animals (see Appendix C). It is interesting that metabolites of both aerobic and anaerobic metabolism are increased at this timepoint. Because they are measured in the urine, these metabolites are subject to the filtering, secreting, and reabsorbing mechanisms of the kidney, which is a black box. It is unclear exactly what the observed pattern in

respiratory metabolite levels means. By FR2, the animal has been subjected to full resuscitation measures for two hours. It could be that respiration is upregulated in response to hemorrhage and resuscitation. It could also be that aerobic respiration was shut down during and just after hemorrhage, and that TCA metabolites and a certain amount of pyruvate were regarded as waste and excreted. Anaerobic metabolism would be upregulated here, generating large amounts of lactate that need to be handled by the kidney. Proof of this would require knowledge of the time course of urine creation and ^{13}C tracing experiments, which is not available. Another potential explanation is the kidney itself, whose metabolism is not well understood. It could be that the respiratory metabolites are reflective of the kidney's metabolism. However, knowledge of kidney metabolism would require kidney tissue samples and profiling of the kidney metabolome. While it is unclear how to explain the observed pattern of respiratory metabolites in the urine at FR2, it is clear that both aerobic and anaerobic cellular respiration are altered by the processes of trauma, hemorrhage, and resuscitation. The urinary metabolome confirms the central role of respiration to metabolism and homeostasis in the organism, and that regulation of these processes are altered in hemorrhagic shock.

Hypoxanthine, choline, and ethanolamine were also both reflective of the FR2 timepoint and of the physiology discussed in Chapter 2. The generation of hypoxanthine under conditions of ischemia and reperfusion was discussed with respect to level 2 (processes that occur outside the mitochondria). Increased excretion of hypoxanthine is reflective of diminished ATP levels [21]. Choline and ethanolamine are common components of phospholipids, which are components of cellular membranes. Presence of

these metabolites in the urine may be suggestive of cellular membrane rupture and cellular death [144]. Mechanisms of cell death associated with shock were discussed in level 3 of Chapter 2.

Two other metabolites, nicotinamide and 1-methylnicotinamide, were consistently identified with the FR2 timepoint. Both metabolites were elevated at FR2 in E1 and E2 animals (see Appendix C). This pattern (ie elevated at FR2) is shared with the other metabolites identified at this timepoint. However, nicotinamide and 1-methylnicotinamide are distinguished by the fact that both metabolites are observed to disappear in many animals at FR8 and FR20. Both metabolites have exhibited anti-inflammatory properties [145,146]. 1-methylnicotinamide may also mediate thrombosis [147].

The metabolites commonly observed at FR20 were all observed at increased levels at FR20 with respect to previous timepoints. The metabolites creatine, trimethylamine N-oxide, and taurine are related to injury—creatinuria is a known marker of trauma [141] and trimethylamine N-oxide is a known marker of ischemic kidney injury [44]. The presence of elevated taurine levels may indicate damage to muscle, as taurine is abundant in muscle cells. However, these metabolites are observed in C1 animals at comparable levels (see boxplots in Appendix C). Glycine, homogentisate, and taurine are also observed at roughly the same levels in C1, E1, and E2 animals at FR20. Of the metabolites commonly identified at FR20, formate is the only metabolite that indicates any difference between experimental groups at this timepoint. It is observed to be elevated in both E1 and E2 animals with respect to C1 animals. This metabolite is the

simplest carboxyl group, and is an intermediate in many reactions. It may be argued that it is indicative of catabolism in general.

It must be concluded that the mechanisms driving these observations are not due to traumatic injury or ischemic injury to the kidney. These observations may be due to splenectomy and laparotomy, which are a source of trauma in and of themselves. Another possible explanation is that these observations are due to sedation. Two animals were sedated but not subject to splenectomy or laparotomy in a different set of hemorrhagic shock experiments done in this lab. These animals had creatine values similar to those in the current study. The same is true for trimethylamine N-oxide, taurine, glycine, and formate. Homogentisate was not profiled in the urine in this study. See Appendix C for scatterplots of these metabolites.

Fed, hemorrhaged animals were primarily distinguished by the presence of elevated 1,6-Anhydro β-D-glucose. This metabolite, also known as glucosan, was found to be manufactured from sugars under conditions similar to that in the rumen of sheep [148]. The metabolite is also found in human urine, though its origins are not known [149]. Regardless, the presence of 1,6-Anhydro β-D-glucose here is linked to sucrose pre-feed. It was detected at nearly constant levels in all animals over the course of the experiment, but is significantly elevated in E2 animals, as shown in Figure 6.15. Elevated mannose levels are also present in E2 animals. This metabolite has demonstrated anti-inflammatory properties, particularly with respect to acute lung injury [150]. Fed animals had a tendency to die at extubation and exhibited evidence of third-spacing intravascular

fluid, though this has no statistical significance. It is possible that mannose plays a role in this pathophysiology, but it is unclear how elevated mannose in the urine reflects this.

Conclusions

The urinary metabolome highlights the basic metabolic alterations due to hemorrhagic shock that were discussed in Chapter 2. Specifically, the metabolites associated with respiration, ischemia/reperfusion injury, and cell death are all associated with the FR2 timepoint via PLS-DA models. Though the cause of the observed levels of these metabolites in the urine cannot be determined by these experiments, their collective association with the FR2 timepoint demonstrates that respiration, hypoxic injury, and cell death are indeed central to the metabolic alterations caused by hemorrhage. Other metabolites associated with FR2 are nicotinamide, a component of NAD, and 1-methylnicotinamide, a metabolite with anti-inflammatory properties that may be involved with regulation of thrombosis.

Other metabolites are associated with the FR20 timepoint, though in general metabolite levels are observed to be the same between E1, E2, and C1 animals. This implies that whatever mechanism drives the observed metabolite quantities is not related to hemorrhage. Creatine and trimethylamine N-oxide are known to be associated with damage from trauma, ischemia, and increased urea levels, and taurine in the urine may imply damage to muscle cells. However, that these metabolites levels are the same in non-injured, non-hemorrhaged controls as they are in experimental animals invalidates

these associations. It is possible that the laparotomy and splenectomy that is performed on all animals contributes to these markers of injury, or that this is a function of sedation.

E2 animals can be discriminated from other animals primarily through elevated levels of the metabolite 1,6-Anhydro β-D-glucose. This is likely due to pre-feeding of sucrose; however, it is unknown how 1,6-Anhydro β-D-glucose is produced in the body. Mannose levels are also somewhat elevated in these animals; this metabolite may have protective properties particularly with respect to acute lung injury.

These results imply that the urinary metabolome is capable of discriminating phase of care, particularly with respect to pre-shock, early resuscitation, and late resuscitation phases. Additionally, animals fed sucrose before trauma can also be discriminated from fasted, injured animals and from non-hemorrhaged controls. Fasted, injured animals can only be discriminated from non-hemorrhaged controls at the FR2 timepoint. Though the urinary metabolome can discriminate by experimental group and experimental timepoint, it cannot discriminate by survival. This is reflected in the mixed models analysis in that several metabolites are found to vary significantly by time alone and that 1,6-Anhydro β-D-glucose varies by experimental group alone. No metabolites were found to vary by survival alone, though several of the metabolites were found to vary by experimental timepoint and survival or by experimental timepoint, experimental group, and survival.

The results presented here will be compared to those of Chapter 7 as obtained with a network analysis of the urinary metabolome.

Ch. 7: Network analysis of Hemorrhagic Shock and Traumatic Injury in the Urine

This chapter details the network analysis of urine metabolomics data obtained from animals subjected to a standardized protocol of hemorrhagic shock, pulmonary contusion, and liver crush injury. The section Materials and Methods: Data collection and animal protocols is reproduced verbaitm from Chapter 6. The experimental groups are outlined again for reference in Table 7.1.

Group	*n* (died)	Type	Description
C1	5 (0)	Negative Control	Not injured, hemorrhaged, or resuscitated
C2	3 (3)	Positive Control	Injured and hemorrhaged, but not resuscitated
E1	16 (5)	Experiment-Fasted	Injured, hemorrhaged, and resuscitated (fasted for 24 hours beforehand)
E2	16 (8)	Experiment-Fed	Injured, hemorrhaged, and resuscitated (fed with a bolus of 140 mL of sucrose and 140 mL of water before the procedure)

Table 7.1: Experimental groups and sample sizes in the analysis performed in this chapter.

In this chapter, a network analysis of the urinary metabolome will be performed. This analysis, which is not generally seen with metabolomics data, relies on notions of connectedness as understood by graph theory and topology. Additional information is supplied, as the network can identify functional relationships between the metabolites.

It is hypothesized that the urinary metabolome reflects modular, scale-invariant structure that is characteristic of metabolism in general. This structure allows the identification of hub metabolites, which are highly connected metabolites that contribute to the robustness of the metabolic network. Association of these metabolites with pathophysiology may be helpful in determining mortality. Modules of functionally-

related metabolites are also identified. The metabolites and relationships identified here will be compared to those identified as being associated with observables highlighted in Chapter 6 (see Table 6.7 and Appendix C).

Materials and Methods: Data collection and animal protocols

Animal preparation and hemorrhagic shock protocol: The experimental protocol was approved by the University of Minnesota Animal Use Committee and was conducted in accordance with established guidelines for the treatment of laboratory animals. A well-established model of porcine hemorrhagic shock, which has been previously described [129], was utilized. Male Yorkshire pigs (Manthei Hog Farm, LLC, Elk River, MN) weighing between 15-20 kg were randomized to experimental group. E2 animals were fed boluses of 140 mL of sucrose with 140 mL water. All other animals were fasted for 24 hours prior to the experiment. Animals were anesthetized with an intramuscular dose of telazol (Wyeth Animal Health, Madison, NJ). Anesthesia was maintained by an IV infusion of propofol (2-9 mg/kg, AstraZeneca Pharmaceuticals, Wilmington, England) and 60% inhaled nitrous oxide. Upon sedation, the pigs were orally intubated and ventilated to maintain a PO_2 of 70-120 torr and a PCO_2 of 35-45 torr (SERVO Ventilator 900C, Siemens, Malvern, PA). Peripheral intravenous lines were placed in the surgically exposed right femoral artery and right jugular vein. A catheter was placed in the right femoral artery for continuous measurement of blood pressure and blood sampling. An introducer (7 French Avanti, Cordis Corporation, Miami Lakes, FL) was placed into the right jugular vein and a Swan-Ganz catheter (5 French, Edwards Lifesciences, Irvine,

CA) was placed for measurements of pulmonary artery pressure, pulmonary wedge pressure, cardiac output, and mixed venous blood sampling. Animals then underwent a midline laparotomy and splenectomy. A Foley catheter was placed in the urinary bladder via stab cystostomy for collection of urine. The inferior vena cava (IVC) was cannulated for blood removal. After surgical preparation, animals were allowed to stabilize until plasma lactate levels reach a value of 2.0 mmol/L or less.

C1 animals were monitored for the duration of the experiment, and were not subjected to injury, hemorrhage, or resuscitation. A captive bolt device was used to create a blunt percussive injury to the chest of C2, E1, and E2 animals. Hemorrhagic shock was then induced in these animals by withdrawal of blood from the IVC until a systolic pressure of the lower 50's was reached (typically 35% of total blood volume). Shed blood was placed in an acid-citrate-dextrose bag for later use. A liver crush injury was induced using a Holcomb clamp technique [130], with two crush injuries created in the liver parenchyma.

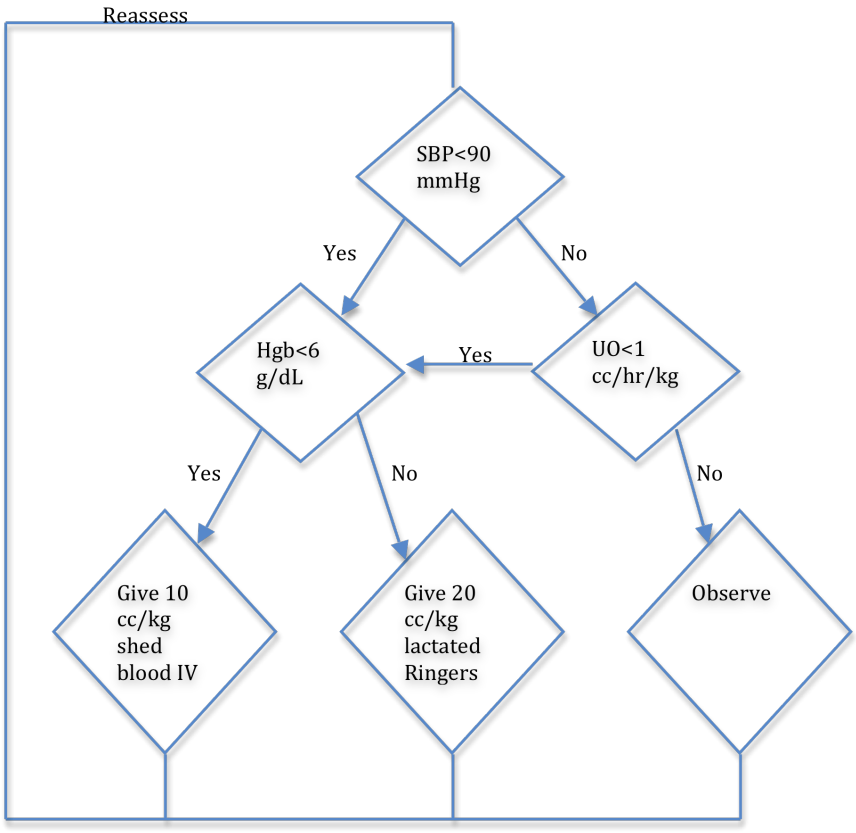

Figure 7.1: Resuscitation algorithm used for shocked, resuscitated animals (groups E1 and E2).

Animals in the E1 and E2 groups were resuscitated with lactated Ringer's fluid given as 20 cc/kg intravenous (IV) boluses to maintain a systolic blood pressure of greater than 80 mmHg for one hour of limited resuscitation, then underwent full resuscitation by protocol. Auto-transfused warmed blood was given at 10 cc/kg IV boluses for a target hemoglobin of greater than 6 g/dL, and, a urine output of greater than 1 cc/kg/hr was targeted. Lactated Ringer's at 20 cc/kg IV boluses or blood at 10 cc/kg/hr were given as needed (see Figure 7.1). After a resuscitation period of 20 hours, animals were extubated and sent to recovery. At 48 hours after resuscitation, animals were re-

intubated for endpoint sample harvesting and then euthanized with Beuthanasia D (1 ml/10kg IV). Urine samples from all forty animals were taken at set timepoints throughout the experiment (see Table 7.2). A total of 165 samples were obtained.

	Baseline	Shock 45	**Time in hours after shock**			
			2	8	20	48
Timepoint	B	S45	FR2	FR8	FR20	PR48
Phase of care	Pre-shock	Shock	Early resuscitation	Late resuscitation		End

Table 7.2: Experimental timeline of urine sample collection and classification into phase of care. Timepoint designations are used in labeling graphics throughout this chapter.

Identification of urinary metabolites from NMR: Urine samples were taken at the time intervals specified in Table 7.2 from the Foley catheter and were frozen and stored at -80° C. Samples were thawed at the time of preparation for NMR analysis. One mL of thawed urine was mixed with 0.5 mL of 0.2 M sodium phosphate buffer prepared with D2O to control pH. The mixture was placed on ice for 10 minutes and then centrifuged at 7000g for 10 minutes. 500 μL of the supernatant was withdrawn and combined with 50 μL of the internal standard 3-(Trimethylsilyl)propionic acid (TSP, Sigma-Aldrich, USA) to a concentration of 1 mM [131]. The internal standard and the buffer were prepared with D_2O to provide a lock for the NMR signal. The pH of the final solution was recorded and the mixture was transferred to separate 5 mm NMR tubes (Wilmad, LabGlass, USA).

Proton NMR spectra were taken with a Bruker Avance spectrometer with autosampler and 5mm triple resonance 1H/13C/15N TXI CryoProbe with Z-gradient, running TopSpin v. 2.16 (Bruker BioSpin, Fremont, CA USA) at 700.13 MHz (Figure 7.2). A 1D NOESY (Nuclear Overhauser Effect Spectroscopy) pulse sequence was used to collect spectra of each sample. The 90° pulse width was calibrated for each sample, and was generally 12-13 μs. The relaxation time was defined by each sample's 90° pulse width. The relaxation delay was 2 s, the acquisition time was 3 s, the spectral width was 10 kHz, the total number of data points collected was 63,000, and the number of transients collected was 128, for a total experiment time of 11 minutes and 17 seconds. During the relaxation period, the water resonance was presaturated. All spectra were collected at a temperature of 298 K. Line broadening at 0.5 Hz was applied before FFT; autophasing and auto-baseline correction were applied by TopSpin.

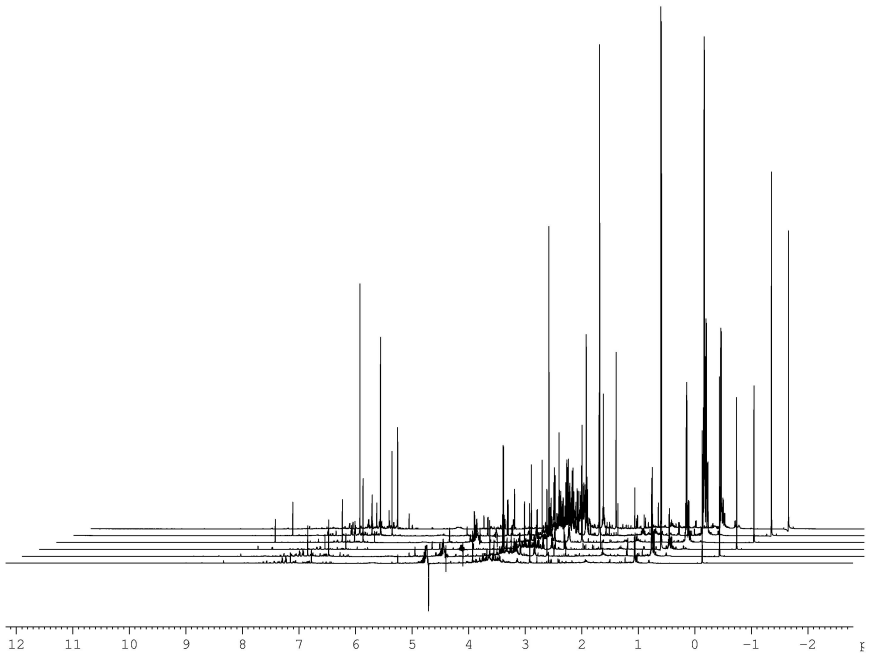

Figure 7.2: Stacked plots of an E1 animal. Spectra are (from front to back): Baseline, S45, FR2, FR8, FR20, PR48. The lactate peak at 1.4 ppm is most prominent at FR2. Other prominent peaks at 1.2 ppm are metabolites of propofol, the anesthetic used. Note that the data from PR48 is omitted from this analysis because there is no measurement of urine output at this timepoint.

Chenomx software [5] was used to identify and quantify a portion of the metabolites present in each urine sample. Fine manual phasing and baseline corrections and the software's Reference Deconvolution algorithm were applied to each spectrum before targeted profiling of the metabolites was performed. Sixty-two metabolites were fit in each urine sample in this study, resulting in a profile containing the concentration of each identified metabolite in millimoles per liter (mM).

Preparation of data for analysis: Metabolite concentrations were multiplied by urine output (cc/hour) to correct for changes in the concentration of urine throughout the experiment. Urine output data was not available at experimental endpoint (48 hours after the initiation of shock) and this data was omitted from the analysis. The final metabolite abundances (nmol/hr/kg) were log-transformed (base 10) to allow for comparisons between metabolites over several orders of magnitude (range: 0-5.9x10^5 nmol/hr/kg). To deal with taking the logarithm of zero, 0.1 was added to the normalized data. The range of the log-transformed, normalized data is [-1, 5.77]. Urea was removed from the data set because its signal is compromised by the NOESY pulse sequence.

Materials and Methods: Data analysis

Network Analysis: A network analysis using the WCGNA software package for R was carried out on the normalized, log-transformed metabolite data. Network distribution was modeled for both the data set with outliers included and the data set with outliers removed. Network connectivity was also modeled. Dissimilarity of metabolites was calculated using the topological overlap matrix (TOM) [151,152]. This is related to the correlation between metabolite pairs, as it is dependent on the adjacency *a* of a pair of metabolites, defined as $a = |s_{ij}|^{\beta}$, where s_{ij} is the correlation between metabolites *i* and *j*, and β is a power that is set to achieve scale-free topology (β=10 in this case). The elements of the TOM are defined as follows:

$$w_{ij} = \frac{l_{ij} + a_{ij}}{min[k_i, k_j] + 1 - a_{ij}}$$

where $l_{ij} = \sum_u a_{iu} a_{uj}$. Dissimilarity is calculated as 1-w_{ij}. This returns a measure of interaction between pairs of metabolites that is weighted by the strength of their correlation. A hierarchical clustering algorithm is applied to the TOM-based dissimilarity measure and a dendrogram is created. Metabolites are assigned to modules based on a dynamic branch height cutting algorithm in which a cutoff height is is determined for each branch based on the shape of the branch [153]. The authors claim that this algorithm is better at identifying biologically relevant clusters than static cutting algorithms which are generally employed in gene chip analysis.

To verify correlations between metabolites, log-log plots of normalized, log-transformed metabolite abundances are plotted against each other. A basic linear model was fit to each metabolite pair and slopes, *r* values, and p-values were all returned.

Results

The network analysis was carried out on the log-transformed, urine output-normalized data. The network distribution *P(k)* was evaluated for both the entire data set and for the data set with outliers removed. As seen in Figure 7.3, the data set with outliers removed gives a better fit, and it also yields a slope between -2 and -3, which is a characteristic of scale-invariant networks. Thus, the data set with outliers removed will be used to construct the networks.

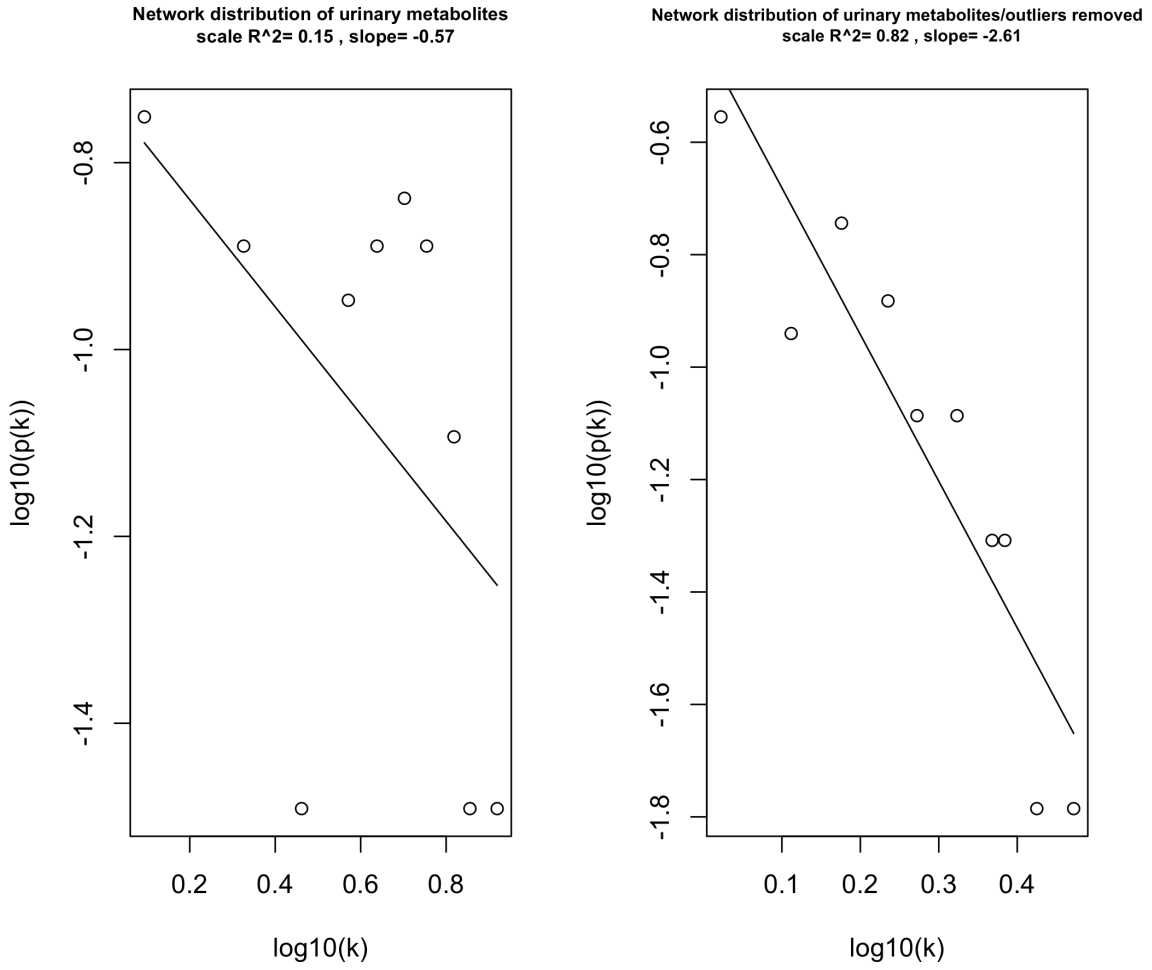

Figure 7.3: Degree distribution plots for the data with outliers (L) and without outliers (R). The distribution function $P(k) = ck^{-\gamma}$ predicts the number of links k of a node (metabolite). Small-world, scale-invariant networks obey the inequality $2<\gamma<3$, which gives the network the property that some metabolites are well-connected hubs that impart robustness to the network. Here, analysis of the data set with outliers removed results in $\gamma=2.61$ in accordance with a small-world, scale-free network, and also improves R^2 as compared to the full data set.

The clustering coefficient was also calculated as a function of connectivity and plotted on a logarithmic scale (Figure 7.4). Here, the clustering coefficient does not obey

a power law; it is independent of connectivity. According to the theory set forth by Ravasz and Barabasi [152], this implies that the network of urinary metabolites shows scale-free, but not modular structure. A hierarchical network (scale-free and modular) would show a power law distribution in both *P(k)* and *C(k)*. The mean clustering coefficient <*C*> of this network is 0.04. For hierarchical networks, <*C*> ~ 0.6.

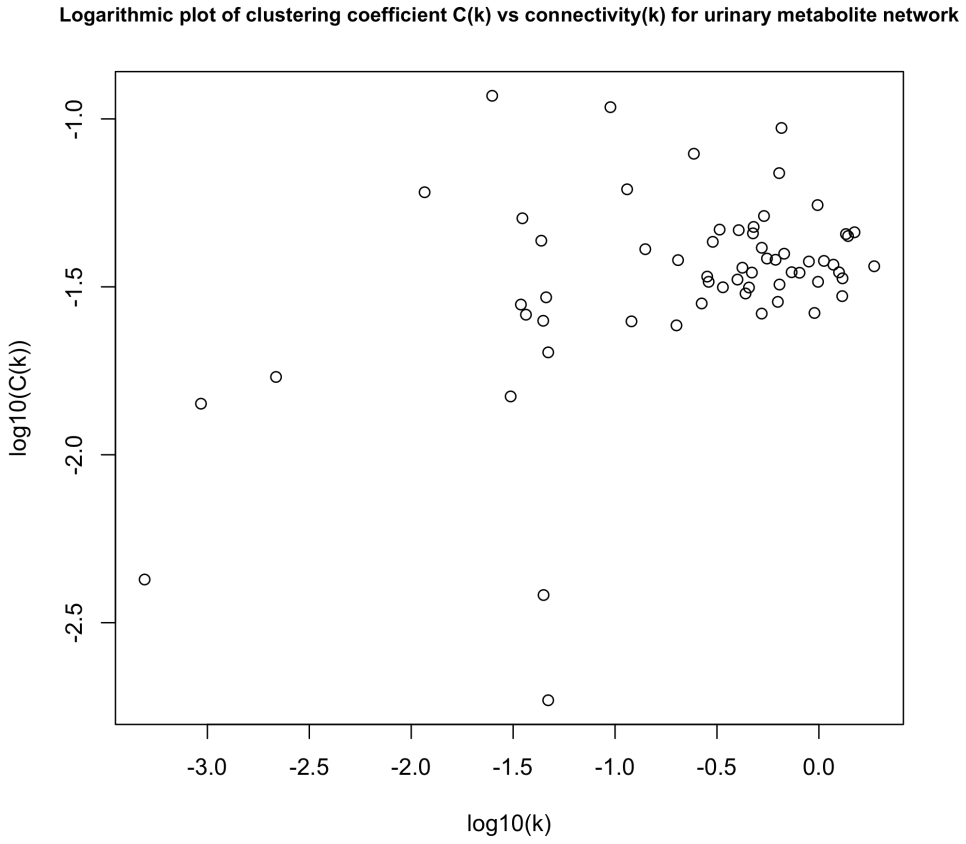

Figure 7.4: Network clustering coefficient *C(k)* as a function of the connectivity of the network nodes. Hierarchical networks should obey $C(k)=k^{-\gamma}$. The plot of *C(k)* here shows that *C(k)* is independent of *k*.

A scale-invariant network of the metabolomics data set with outliers removed was constructed, yielding information about functional relationships between metabolites in

the data. The TOM-based measure of dissimilarity (see Figure 7.5) was used to construct a dendrogram of metabolites, and metabolite modules were constructed with WGCNA's dynamic branch cutting algorithm. Though the network constructed here is not truly hierarchical, modules were still identified by the analysis.

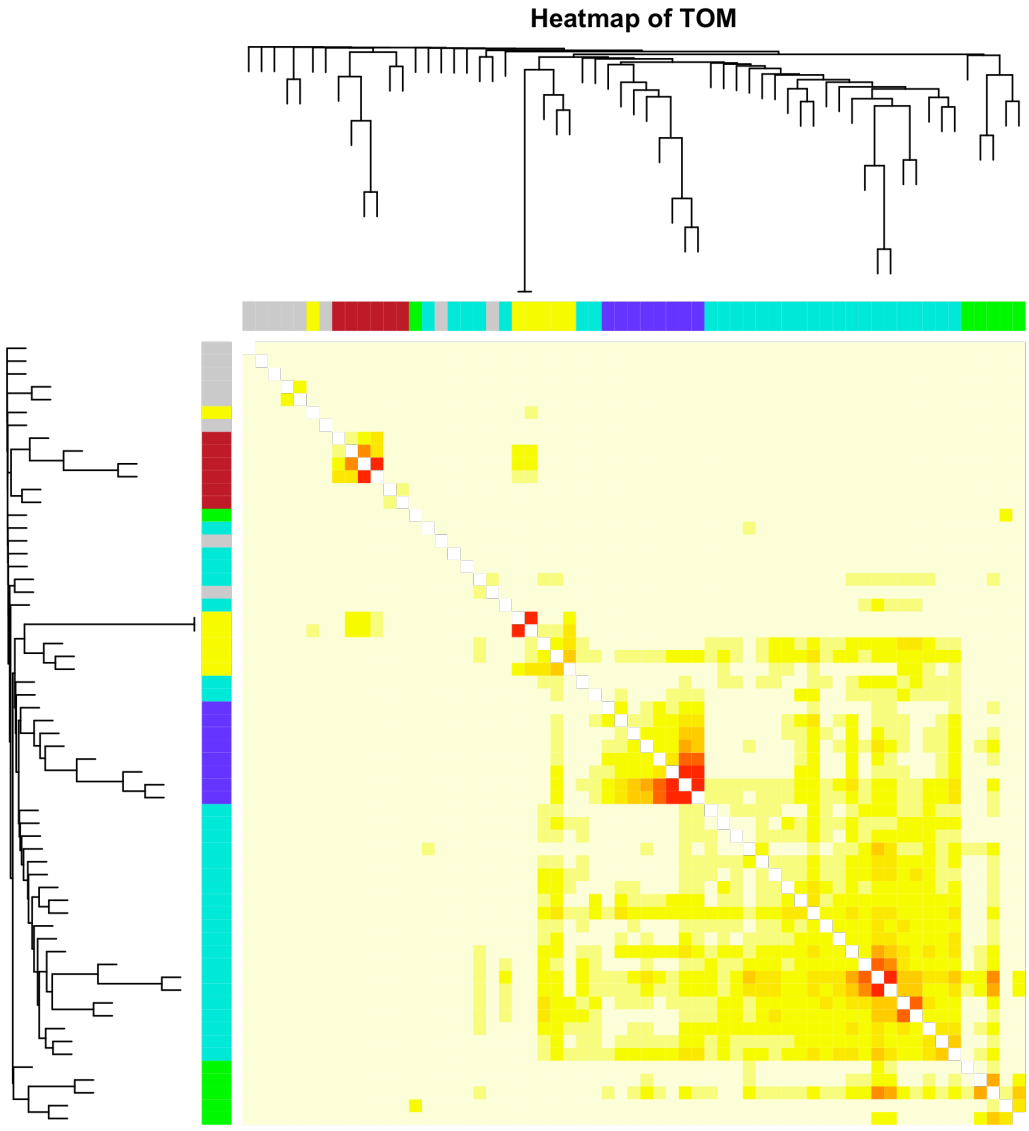

Figure 7.5: Heatmap visualization of the metabolite dissimilarity as calculated with the toplogical overlap matrix (TOM). Bright red corresponds to high topological overlap; yellow and cream correspond to areas

of progressively lower topological overlap. The modular structure can be seen along the diagonal. The dendrogram and modules shown on the axes are discussed in more detail in Figure 7.6.

In Figure 7.6, the dendrogram is shown with colors corresponding to different modules of metabolites. These modules correspond to functionally-related metabolites. Note that the TCA metabolites have been grouped in the red module. Six different modules of functionally-related metabolites were identified with a dynamic branch cutting algorithm; each color corresponds to a module. The grey module contains unlinked metabolites. Metabolites at the tips of the branches (lactate, pyruvate, creatinine, dimethylamine, glycine, taurine, succinate, 2-oxoglutarate) are hub metabolites.

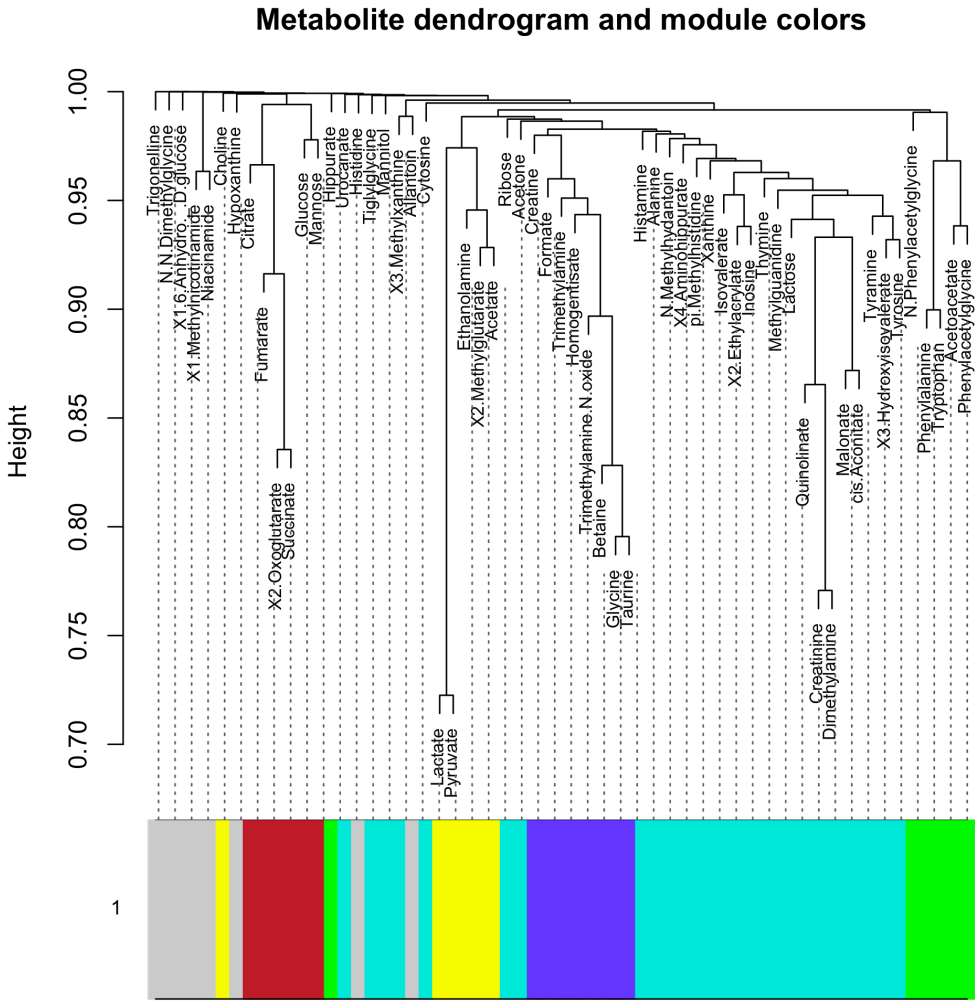

Figure 7.6: Urinary metabolite dendrogram and module assignment as modeled by the WGCNA package for R. The dendrogram was created with a toplogical overlap-based measure of dissimilarity.

Log-log plots of respiratory metabolites: Metabolites associated with the red module (citrate, fumarate, 2-oxoglutarate, succinate, glucose, and mannose) are largely involved in aerobic respiration, and metabolites associated with the yellow module (lactate, pyruvate, acetate, choline, ethanolamine, and 2-methylglutarate) are largely associated

with anaerobic respiration and cell membrane components[1]. The respiratory metabolites (lactate, pyruvate, acetate, glucose, citrate, 2-oxoglutarate, succinate, and fumarate) in these modules were analyzed for correlations; log-transformed concentrations with outliers removed were used. Pearson correlations and p-values were obtained for each pair of metabolites. Metabolite pairs with strong correlations ($r>0.8$) are lactate and pyruvate ($r=0.896$), 2-oxoglutarate and succinate ($r=0.859$), and 2-oxoglutarate and fumarate ($r=0.816$); the highest of these correspond to the hub metabolites identified in Figure 7.6. The metabolites of the TCA cycle (citrate, 2-oxoglutarate, succinate, and fumarate) were all correlated at $r>0.64$. In general, metabolites of the same module had higher correlation coefficients than those of different modules.

[1] These metabolites are all associated with the FR2 timepoint. See Chapter 6.

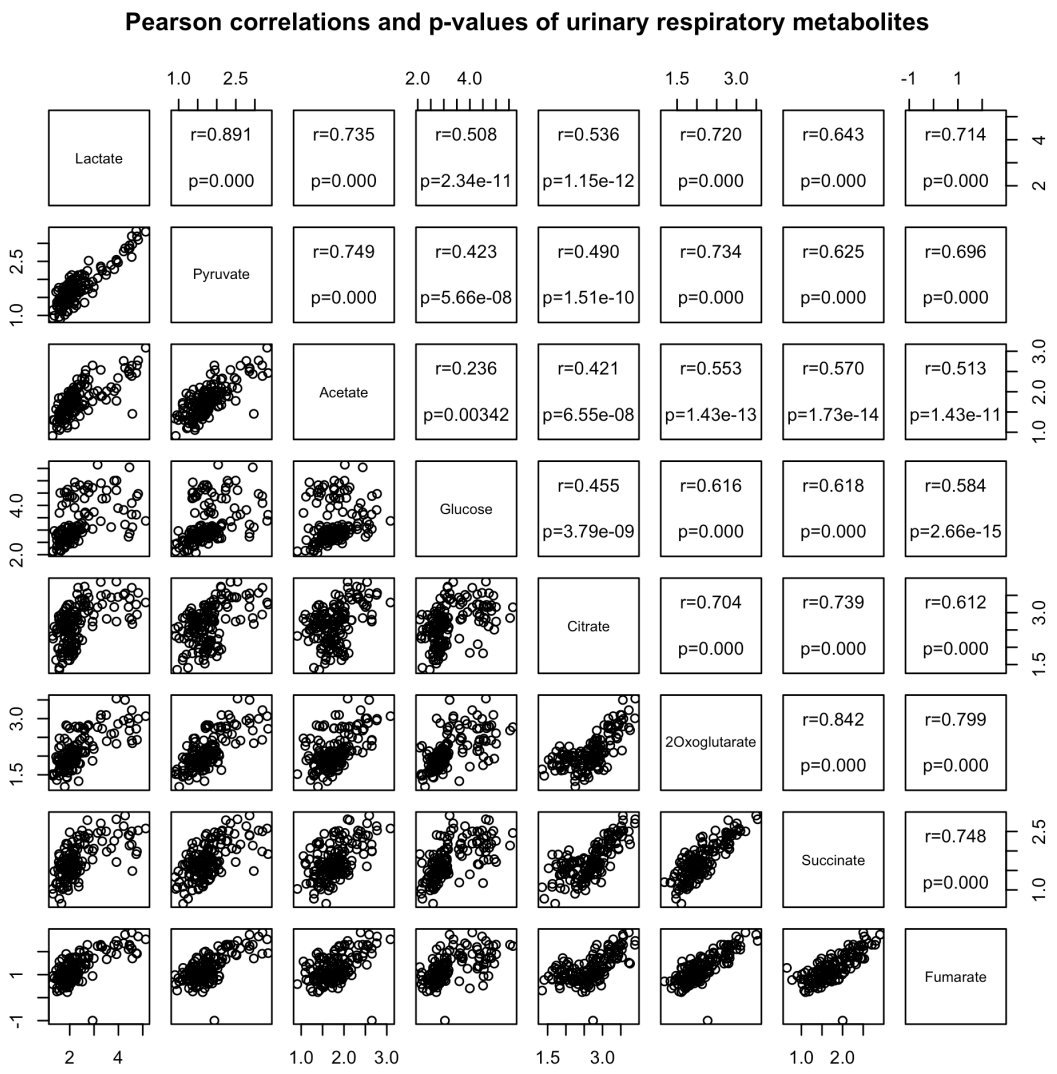

Figure 7.7: Pairs plots of urinary metabolites relevant to cellular respiration. These metabolites are associated with the yellow module and anaerobic respiration (lactate, pyruvate, acetate) or the red module and aerobic respiration (glucose, citrate, 2-oxoglutarate, succinate, fumarate). Plots appear below the diagonal, and Pearson correlation coefficients and uncorrected p-values for the relevant comparison are shown above the diagonal. Note that p=0.000 actually indicates $p<2x10^{-16}$.

The metabolites taurine, glycine, betaine, trimethylamine, and trimethylamine N-oxide were identified as part of the blue module. Glycine and taurine were identified as

hub metabolites. Pearson correlation coefficients in Figure 7.8 also show high linearity in log-log plots of these metabolites, confirming the functional relationship between these metabolites. All metabolites in Figure 7.8 have been associated with the FR20 timepoint in the PLS-DA models discussed in Chapter 6.

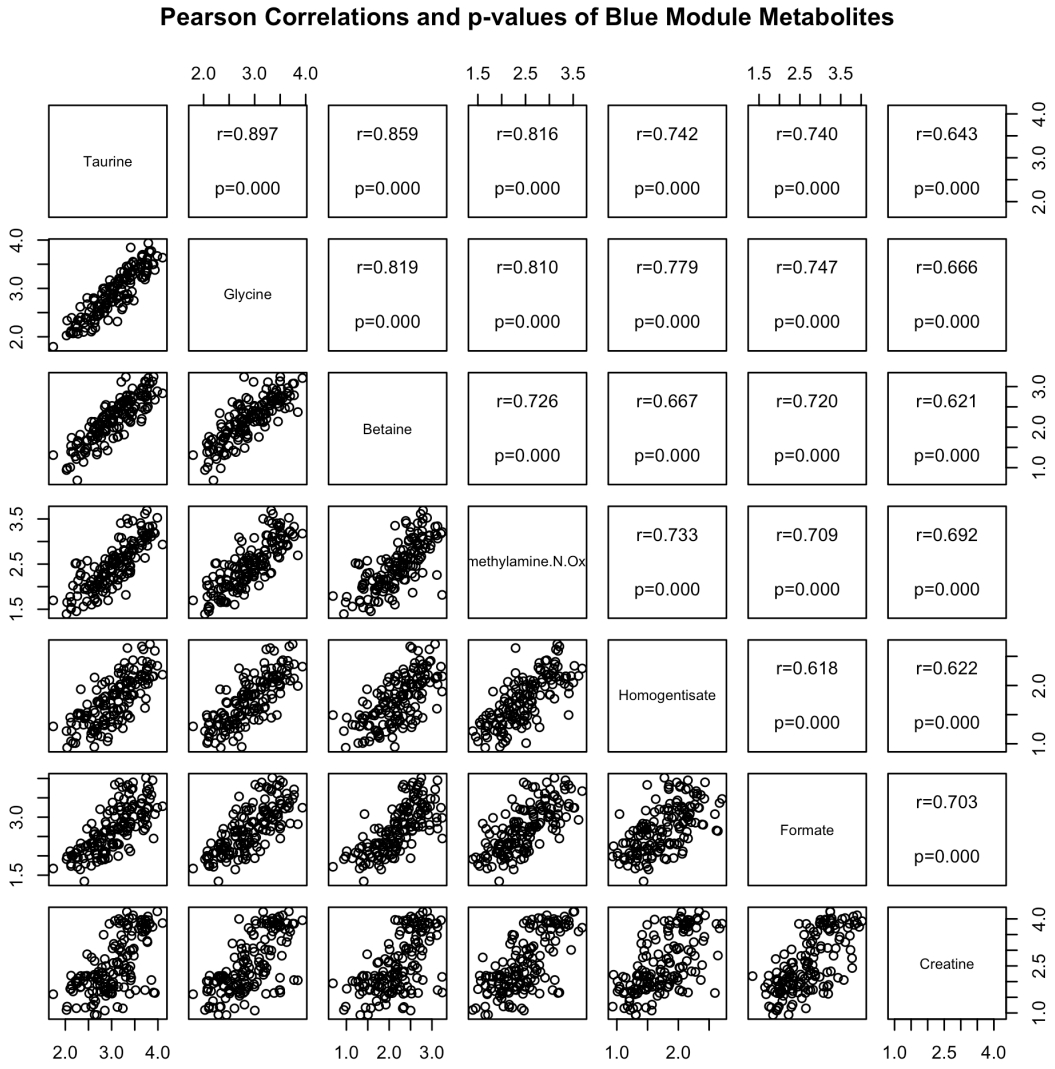

Figure 7.8: Log-log plots of urinary amines and amino acids. These metabolites were identified as being functionally related via network analysis (in the blue module). All metabolites were identified as

associated with the FR20 timepoint in Chapter 6. Log-log plots show high linearity among all pairs. Note that p=0.0 indicates $p < 2x10^{-16}$.

VisANT software [154] was used to visualize the network as constructed by WGCNA (see Figure 7.9). A list of nodes (metabolites) and edges (strength of correlation between metabolite pairs) are exported from R and displayed by the Java-based application. Because this is a weighted network, the thickness of the edge corresponds to the strength of the interaction. The network can be filtered by setting a threshold to hide edges less than the specified cutoff value. Figure 7.9 shows a visualization of the network of urinary metabolites with a threshold of 0.05. Unconnected metabolites have edges with weights contained in [0-0.05]. The threshold of 0.05 was chosen here because this is the cutoff at which the TCA metabolites become linked to the rest of the network via 2-oxoglutarate, lactate, and pyruvate. Above this value, the TCA metabolites are unlinked to the rest of the network. The maximum edge has a weight of 0.277 and links lactate and pyruvate. This value is quite low, as weights are defined in general to be contained in the interval [0,1]. This indicates weak modularity in the urinary network, which corresponds to the mean clustering coefficient of 0.04 observed in Figure 7.4.

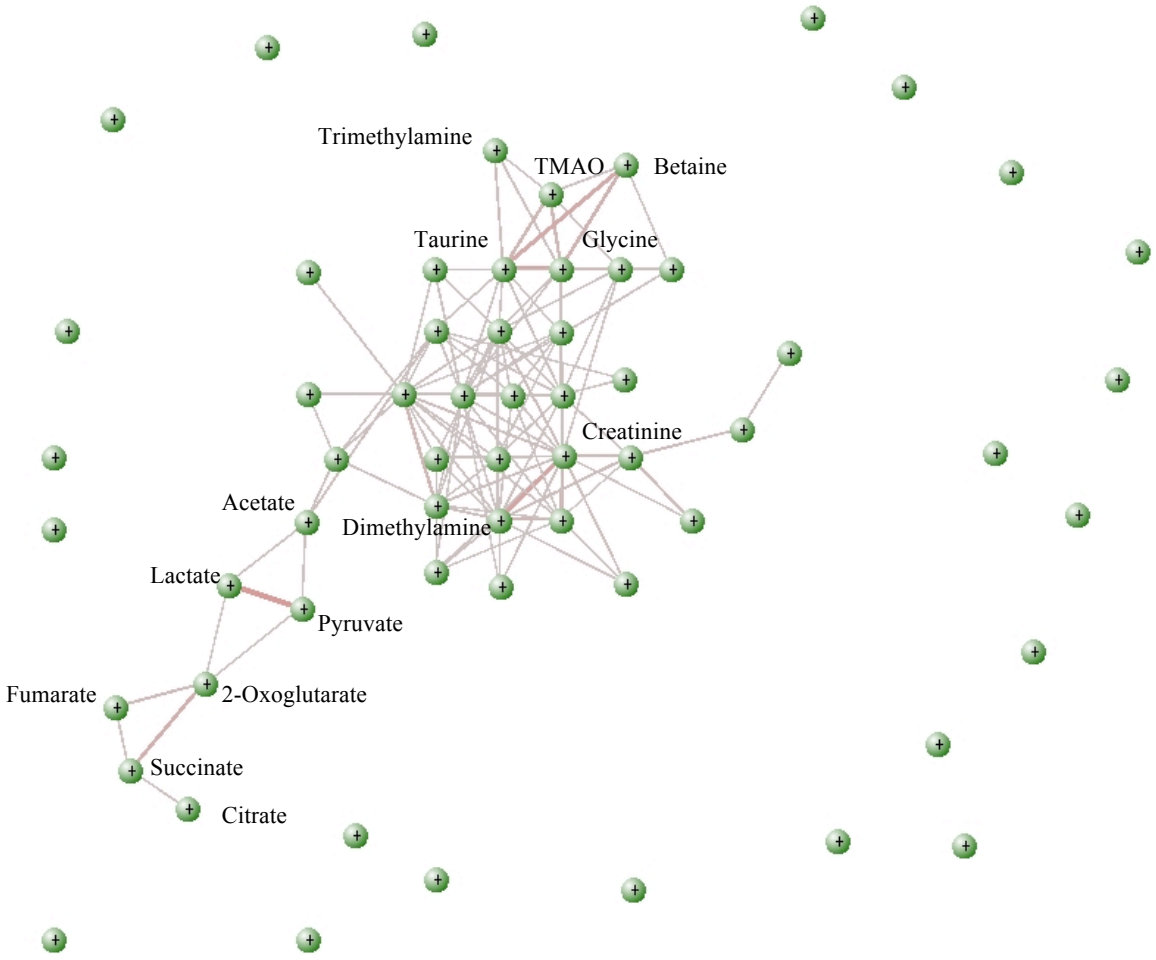

Figure 7.9: A visualization of the network created with the WGCNA software package and VisANT. The edge cutoff was set at 0.05. The weights of the interactions are illustrated by the weight and color of the lines. The heaviest line links the metabolites pyruvate and lactate at a weight of 0.277. Unlinked metabolites may be functionally related, but have interaction weights of less than 0.05. TCA-associated metabolites are strongly connected, as are tauine, glycine, and betaine and creatinine and dimethylamine. TMAO=Trimethylamine N-oxide.

Discussion:

It has been demonstrated [152] that the probability that a given metabolite can react with k other metabolites follows a power law $P(k)=ck^{-\gamma}$, with γ=2.2 for "nearly all organisms."

Additionally, these types of networks are found to have an average clustering coefficient of about 0.6. This quantity is indicative of the modularity of a network. In the urinary metabolic network constructed here, γ=2.61, in good agreement with Ravasz's result. The average clustering coefficient of the urinary metabolic network is 0.04, which is far below what a truly modular network could be expected to have. Thus, the network of urinary metabolites is shown to be scale-free but only weakly modular. It is unclear if this would be remedied by a more complete metabolome, as only 62 metabolites were identified in each sample, or if this is simply a property of the urine. Only six modules were identified with the WGCNA analysis, and most of the metabolites within the modules are not strongly connected. The strongest connectivity, present between the metabolites lactate and pyruvate, is at 0.27. The bulk of connections between urinary metabolites are quite weak at ~0.01 or less. The two most plausible explanations for this are (1) that the urinary metabolite network identified here is incomplete, and (2) that the urinary metabolome is composed of waste products, and no active metabolism occurs once the urine has left the kidney.

The network constructed here did not exhibit the combination of modular and scale-free properties that metabolic networks are known to possess. Despite this, six weak modules were identified in the urine. These modules appear to cluster according to functionality of the metabolites. In particular, many metabolites of the red (citrate, fumarate, 2-oxoglutatarate, succinate, mannose, glucose), yellow (choline, lactate, pyruvate, ethanolamine, 2-methylglutarate, acetate), and blue modules (creatine, formate, trimethylamine, homogentisate, trimethylanime N-oxide, betaine, glycine, taurine) were

identified as commonly associated with FR2 and FR20 timepoints (see Chapter 6). In the PLS-DA analysis, the respiratory metabolites were not separated. The network analysis separates metabolites associated with aerobic respiration in the red module from those associated with anaerobic metabolism in the yellow module. Further, the two metabolites that were associated with cell membrane rupture, choline and ethanolamine, are grouped in the yellow module with the anaerobic metabolites. This grouping supports the relationship between a pathological switch from aerobic metabolism to anaerobic metabolism and apoptosis.

When the network interaction threshold is increased to 0.05 in VisANT, the TCA metabolites break away from the rest of the network. At 0.06, lactate and pyruvate separate from the larger network as well, and citrate separates from the rest of the TCA metabolites. Several other connections are lost as well (see Figure 7.10). In general, the threshold for modeling interactions is quite low in the urine. At a threshold of 0.20, only creatinine and dimethylamine and lactate and pyruvate remain connected. It is possible that the liver, muscle, or serum networks are more modular in nature and thus have higher connectivity between metabolites. This deserves to be pursued at a later date.

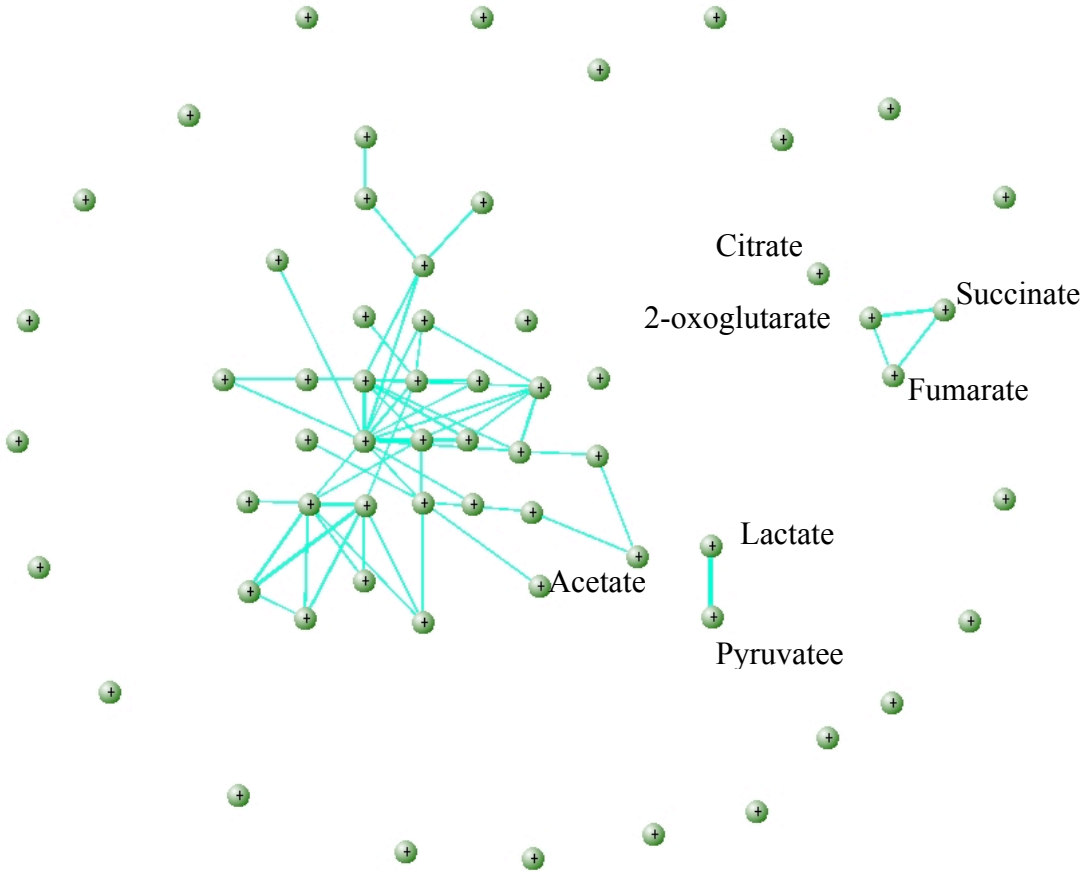

Figure 7.10: Network model of the urinary metabolome with a decreased threshold of 0.06. The respiratory metabolites separate from the rest of the network as the threshold of interaction is increased.

A fundamental property of scale-free networks is the existence of a small number of well-connected metabolites that interact with a large number of metabolites in the network. This property allows the system to remain robust to random failures; however, if the connectivity of the nodes is compromised, the network will fail. One of the goals of network analysis is identification of the hub metabolites that contribute to the robustness of the network. Here, the hub metabolites are identified as the "tips" of the dendrogram branches in Figure 7.6: lactate, pyurvate, creatinine, dimethylamine, and to a

lesser extent, 2-oxogluratare, succinate, glycine, and taurine. Half of the hub metabolites are related to respiration, highlighting its fundamental role in the pathophysiology of hemorrhagic shock. The importance of creatinine and dimethylamine was missed by the PLS-DA analysis. Thirty years ago, it was shown that creatinine is a precursor of dimethylamine in uremic patients with chronic kidney failure [155]. Though the pathophysiology studied here is certainly not related to chronic kidney disease, it may be that uremia (the accumulation of urea) may be the culprit, and not chronic kidney disease per se. Uremia is also implicated in the accumulation of trimethylamine N-oxide; it has been shown that methylamines are protective against protein denaturing and other deleterious effects due to excess urea as mentioned in Table 6.6 [36,156]. Like trimethylamine N-oxide, dimethylamine is observed at similar levels between non-hemorrhaged controls and hemorrhaged, injured animals (see Figure 7.11).

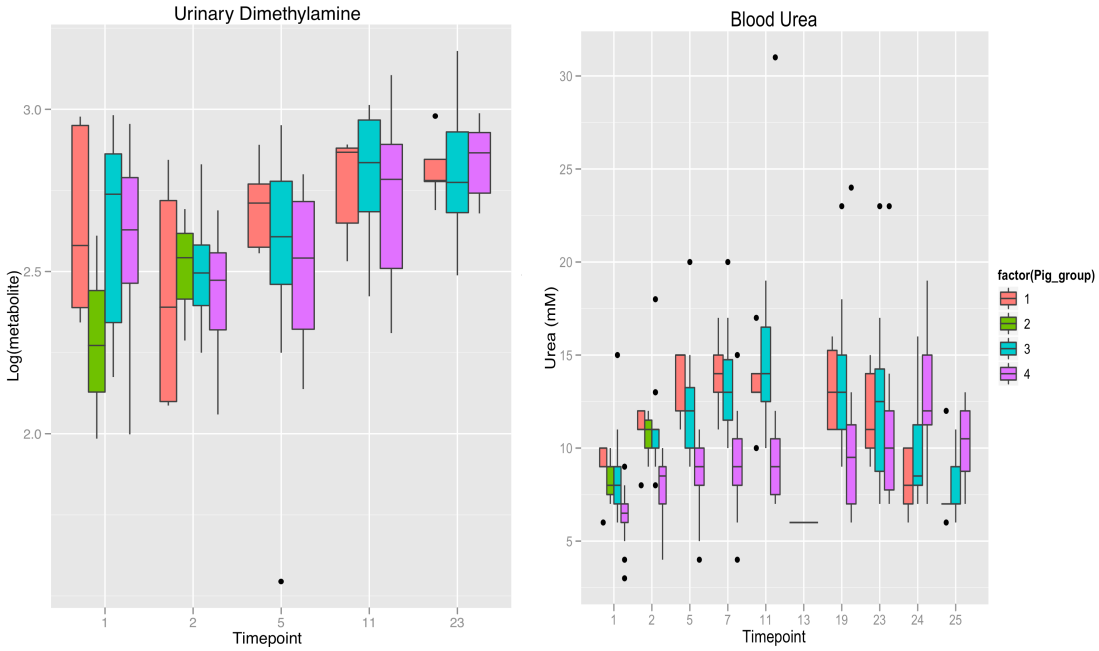

Figure 7.11: Boxplots of urinary dimethylamine (L) and blood urea (R) levels by experimental group. Orange=C1, green=C2, turquoise=E1, and purple=E2. Little difference in urinary dimethylamine is observed between experimental groups. For urea, little difference is observed between non-injured, non-hemorrhaged controls (C1) and fasted, injured, hemorrhaged controls (E1). E2 animals showed somewhat depressed blood urea levels at earlier timepoints.

While urea levels are observed to increase over the course of the experiment, similar levels are observed between C1 and E1 animals. E2 animals show slightly lower levels of urea. It is unclear why these patterns are observed in urea. If the kidneys were being damaged from reduced blood flow via hemorrhage, one would expect decreased handling and therefore higher levels of urea in the blood of shocked animals as compared to C1 animals. However, the mechanism in question (ie levels of trimethylamine n-oxide and dimethylamine increase in response to uremia) may still be at play since C1 animals do

suffer an increase in urea. It could be useful to examine serum levels of the methylamines to see if they follow the same pattern. It may be that the splenectomy and laparotomy are traumatic enough in and of themselves to cause urea buildup in the blood. Creatinine and dimethylamine may simply be related to the C1 urine, as these metabolites were observed in two PLS-DA models constructed to discriminate urine samples taken from C1 animals at FR2 (models I and M, Chapter 6). In both models, these metabolites were associated with C1 urine samples. It could be that the metabolites of the turquoise module are related to C1 urine samples as a whole; however, few of the PLS-DA models generated in Chapter 6 strongly associate metabolites with C1 samples. This assertion cannot be verified with the data at hand due to weaknesses on the part of both models.

The weakness of the modularity of the urinary metabolome as identified here must be considered. The blue, red, and yellow modules have clear counterparts in the PLS-DA models at FR2 and FR20. These modules have a clear context that has been verified with a different analysis, which strengthens the results surrounding these metabolites in both analyses. None of the metabolites in the turquoise and green modules were reliably identified with an observable quantity via PLS-DA. These modules may have been assigned erroneously. Additional weaknesses in the PLS-DA analysis must be considered as well. The most robust models generated involved small subsets of the data. The FR2 and FR20 timepoints and the E2 animals were the observables most reliably associated with urinary metabolites. The PLS-DA models constructed here have little to say about the other timepoints and experimental groups. As discussed in Chapter 6, there

is also little to no information about survival contained here, though this may be characteristic of the urine in general.

It would be useful to build a network for each experimental group or even each physiological state in this data set, where each animal's state is defined by experimental group, experimental timepoint, and the animal's survival status. With four experimental groups, five experimental timepoints, and survival status, there are forty possible states. However, since all C1 animals live and all C2 animals died before FR2, the data set is reduced to 28 possible states. Of these, an additional three states are associated with E1 animals that died at FR2, FR8, and FR20 and contain two urine samples or less. Additionally, only three animals comprise the C2 group.

Ideally, the network analysis would be done on a state-by-state basis. One metabolic network would be constructed from the metabolomics data associated with each state. These networks could then be compared for differences in hub metabolites, modules, and interaction strength. Such an analysis could shed light on how functional relationships between metabolites change with the progression of shock and resuscitation, with survival status, and with feeding status. This analysis cannot be done at interim with only 40 animals total; however at the end of the experiment, there should be enough urine samples in each state to construct networks for each one.

Conclusions

The network formed by the urinary metabolome associated with hemorrhagic shock and traumatic injury displays scale invariance but is only weakly modular. Three of six

modules identify metabolites associated with aerobic respiration, metabolites associated with anaerobic respiration and cell membrane components, and amines and amino acids. A fourth module is associated with unlinked metabolites. The significance of the two remaining modules is unknown, but one of them contains the hub metabolites creatinine and dimethylamine, two metabolites unidentified by PLS-DA. The hub metabolites lactate, pyruvate, succinate, and 2-oxoglutarate are associated with respiration and the FR2 timepoint. The hub metabolites glycine and taurine are associated with FR20.

PLS-DA models discussed in Chapter 6 identified the respiratory metabolites and cell membrane components with the FR2 timepoint, and the amines and amino acids with the FR20 timepoint. The respiratory metabolites, choline, and ethanolamine are elevated in injured animals relative to negative controls. These metabolites reflect the mechanisms discussed in Chapter 2. The amines and amino acids are at the same level in injured animals as negative controls. This is also true of dimethylamine and creatinine.

Chapter 8: Conclusions

The focus of this dissertation has been the construction and analysis of the urinary metabolome associated with hemorrhagic shock. Several background chapters discuss known metabolic alterations associated with hemorrhage in light of scale invariance, basic kidney function, and metabolomics in general. The urinary metabolome was constructed from ^{1}H proton NMR spectra of urine samples taken from a porcine model of hemorrhagic shock/traumatic injury and resuscitation. Urinary metabolite concentrations as profiled with Chenomx software were normalized to urine output to account for drastic changes in urine concentration as a result of hemorrhagic shock. The normalized metabolome was used to construct PLS-DA models that associate metabolites with phase of care and experimental group in Chapter 6. It was observed that the urinary metabolome does not directly contain survival information. This was reflected in the mixed models analysis of E1 (fasted) and E2 (fed) animals, in which all metabolites that were observed to change with survival also changed with experimental timepoint or with survival, experimental timepoint, and experimental group. Additionally, PLS-DA models constructed to discriminate by survival had very low predictive power.

Metabolites highlighted by this analysis are associated with the FR2 timepoint, the FR20 timepoint, and with discriminating E2 animals from other animals. Metabolites associated with FR2 are all involved in the physiological processes discussed in Chapter 2. Glucose, lactate, pyruvate, and acetate are all involved in anaerobic respiration; glucose, pyruvate, citrate, 2-oxogluratare, succinate, and fumarate are all involved in aerobic respiration. There is no distinction between types of respiration in these models.

Urinary hypoxanthine (which is increased at FR2 relative to other timepoints) is a known indicator of ATP depletion [21]. Choline and ethanolamine are two common phospholipid components; they are also components of cellular membranes. Their presence at increased levels at FR2 may indicate rupture of cellular membranes, a component of cell death. [144]. This cohort of metabolites is indicative of processes discussed at levels 0-2 in Chapter 2. Two other metabolites are associated with FR2, niacinamide and 1-methylnicotinamide. Niacinamide may still be part of the cohort that is clearly associated with cellular respiration during shock in that it is a component of NAD, a key component in aerobic respiration and electron transport. However, niacinamide and 1-methylnicotinamide have also been shown to inhibit inflammatory processes, and 1-methylnicotinamide may also have anti-thrombotic characteristics [145,147]. The metabolic pathways that are associated with these metabolites are unclear.

Metabolites associated with the FR20 timepoint include amines and amino acids: taurine, glycine, formate, homogentisate, creatine[2], and trimethylamine n-oxide. While it is tempting to attribute the presence of creatine and trimethylamine N-oxide to injury [44,141], this cannot be done. All metabolites associated with FR20 are observed at the same levels in C1, E1, and E2 animals. It is possible that the laparotomy and splenectomy that is performed on all animals is traumatic enough to elevate creatine and trimethylamine n-oxide in the urine. It is also possible that this is due to sedation. Two animals that were sedated and minimally instrumented (no laparotomy, no splenectomy) in a previous study support this claim with respect to formate, glycine, taurine, creatine, and trimethylamine

[2] Creatine is derived from amino acids.

N-oxide. Normalized, log-transformed values of these metabolites all fall in the same range for all animals regardless of treatment. (Homogentisate was not profiled in this study.) However, data from more than two animals is necessary to substantiate this claim.

The metabolite 1,6-Anhydro β-D-glucose is significantly elevated in the urine of E2 animals with respect to all others. Though the source of this metabolite is unknown, the experimental procedures common to all animals dictate that it is a product of the sucrose pre-feed. This metabolite is primarily responsible for discriminating E2 urine samples in all PLS-DA models built. Mannose also distinguishes these samples, and may be linked to some of the respiratory issues that animals from this group experience. Though the effect is not statistically significant, it has been observed that E2 animals die at extubation more often than E1 animals. Another portion of these animals (also not statistically significant) experience third-spacing of intravascular fluid and have required large amounts of resuscitation fluid. Several of the respiratory metabolites are also associated with E2 animals in models that discriminate between E2 and C1 animals. This effect is also observed in E1 animals, but it is unique to the FR2 timepoint.

The scale-invariant network analysis performed in Chapter 7 provides additional information through functional relationships between metabolites. Though the network was only weakly modular, three of the six modules formed in the analysis correspond to patterns identified in the PLS-DA analysis. Here, metabolites associated with anaerobic respiration were assigned to a different module than metabolites of aerobic metabolism. Additionally, ethanolamine and choline were identified in the same module as the

anaerobic metabolites. This provides a link between anaerobic respiration and cell membrane rupture. The metabolites associated with the FR20 timepoint were assigned to their own module; this module also includes betaine and trimethylamine. Both metabolites are osmolytes and may therefore be related to the movement of fluid associated with hemorrhage and resuscitation. Of the metabolites primarily associated with E2 animals, mannose was assigned to the same module as the aerobic metabolies, and 1,6-Anhydro β-D-glucose was placed in the module of unrelated metabolites. Hypoxanthine, niacinamide, and 1-methylnicotinamide are also in this module.

The analyses of Chapters 6 and 7 proved to provide complimentary information. Both analyses highlighted the same groups of metabolites. The PLS-DA analysis associated these metabolites with distinct experimental timepoints (FR2 and FR20), and the network analysis discriminated between metabolites of aerobic and anaerobic metabolism. The network analysis also associated markers of cell membrane rupture with the anaerobic metabolites. The network analysis failed to identify the importance of 1,6-Anhydro β-D-glucose in discriminating E2 animals. This metabolite was placed in the grey module, which is reserved for metabolites that have no functional relationships with any other.

Both analysis schemes have a place in metabolomics. This analysis will be improved upon when an additional 40 animals is completed next year. This will allow for the construction of better PLS-DA models, and it will allow for construction of networks for each state. Different physiologies can also be studied in this manner. Preliminary work on the creation of a urinary metabolome associated with both chronic

and acute pancreatitis will be presented at the 2011 meeting of the American Pancreatic Association. This work was done in collaboration with a group that has already done significant proteomics work with pancreatitis [157]. Future collaboration with this group provides an opportunity to integrate the metabolome and the proteome associated with pancreatitis.

Though this dissertation focuses only on the urinary metabolome, it must be understood that little can be said about a systemic pathophysiology such as shock with information from only one type of biological sample. Integration of the urinary metabolome with the liver, muscle, and serum metabolomes will be crucial to understanding the metabolic alterations that accompany hemorrhagic shock. It is possible that when taken together, the urine and serum metabolomes contain information about kidney function. Correlations and networks will be particularly useful when evaluating this.

Correlations will also be useful when tying physiological data with metabolomics data. If biomarkers are to be found in any of the metabolomics data, correlation of these metabolites with known indicators of shock (mean arterial pressure, cardiac output, hemoglobin, base excess, lactate, pH) will be an important early step in the process. Any biomarkers that are discovered, particularly in serum or the skin[3], may be used in conjunction with new technology to identify shock in trauma victims in the battlefield [158,159].

[3] Skin samples were also taken from animals in this study; they have not been analyzed yet. There is potential for a grant in conjunction with Dr. Harjani or Dr. Erickson (Cornell University).

Still, without a theory associated with a given pathophysiology, contextualization of metabolomics data remains difficult. Geoffrey West's work [6] provides a starting point for hemorrhagic shock, but the experimental application of these ideas to hemorrhagic shock is unclear to the author of this dissertation. This theory suggests that fractal geometry underlies the organization and function of biological systems [160]. The first place to look, then, for a theory of biological function and dysfunction is to the study of fractals. Many systems with fractal geometries obey power law distributions with non-integer exponents. As illustrated by the network analysis of Chapter 7, such power law distributions are important to the study of metabolism. Further investigation of the nature of the power law associated with metabolism, particularly with respect to hemorrhagic shock, is certainly warranted. Additionally, as was suggested in Chapter 2, consideration of the fractal structure of organs in the body may be important to understanding the propagation of pathophysiology such as multiple organ dysfunction. If the propagation of pathophysiology in an organ or any fractal system can be modeled by a phase transition, the application of statistical mechanics could shed light on this process. This has not been studied much, though Aon refers to phase transitions with respect to dysfunction in mitochondrial networks [161]. Finally, coupled oscillators can give rise to synchronous behavior observed in biological systems [162,163]. Aon has shown that the mitochondrial network in the heart can be modeled as a system of coupled oscillators [161]. A similar treatment of mitochondria with respect to hemorrhage should be pursued.

There is ample opportunity for further investigation into the metabolic adaptations that accompany hemorrhagic shock and resuscitation. There is much work to be done

with existing data with respect to the experiment discussed here. Metabolomics data from serum, muscle, and liver and physiological data must all be integrated with the urine data discussed here. Current collaborations with respect to pancreatitis allow the study of a new pathophysiology and an opportunity to integrate proteomics and metabolomics data. If strong biomarkers of hemorrhagic shock are identified in this study, they may be used in conjunction with new technologies for identifying shock in low-resource settings such as the battlefield. Finally, there is an array of fascinating theory to be studied that may have implications for the propagation of injury in hemorrhagic shock. The application of fractal geometry, power laws, phase transitions, and coupled oscillators to hemorrhagic shock will require the formation of new collaborations with physicists and/or mathematicians.

Bibliography

1. Cohn S. Military and civilian joint research gaps. . 2011.

2. Dubick MA. Current concepts in fluid resuscitation for prehospital care of combat casualties. *PREHOSPITAL COMBAT CASUALTY CARE*. 2011:18.

3. Holcomb JB, Stansbury LG, Champion HR, Wade C, Bellamy RF. Understanding combat casualty care statistics. *J Trauma*. 2006;60(2):397.

4. Cuthbertson D. POST-SHOCK METABOLIC RESPONSE* 1. *The Lancet*. 1942;239(6189):433-437.

5. Weljie AM, Newton J, Mercier P, Carlson E, Slupsky CM. Targeted profiling: Quantitative analysis of 1H NMR metabolomics data. *Anal Chem*. 2006;78(13):4430-4442.

6. West GB, Woodruff WH, Brown JH. Allometric scaling of metabolic rate from molecules and mitochondria to cells and mammals. *Proc Natl Acad Sci U S A*. 2002;99(Suppl 1):2473.

7. Barabási AL, Oltvai ZN. Network biology: Understanding the cell's functional organization. *Nature Reviews Genetics*. 2004;5(2):101-113.

8. Peitzman AB, Harbrecht BG, Udekwu AO, Billiar TR, Kelly E, Simmons RL. Hemorrhagic shock. *Curr Probl Surg*. 1995;32(11):925-1002.

9. Angele MK, Schneider CP, Chaudry IH. Bench-to-bedside review: Latest results in hemorrhagic shock. *Crit Care*. 2008;12(4):218. doi: 10.1186/cc6919.

10. West GB, Brown JH, Enquist BJ. A general model for the origin of allometric scaling laws in biology. *Science*. 1997;276(5309):122.

11. Zweier JL, Talukder M. The role of oxidants and free radicals in reperfusion injury. *Cardiovasc Res*. 2006;70(2):181.

12. Zweier JL, Flaherty JT, Weisfeldt ML. Direct measurement of free radical generation following reperfusion of ischemic myocardium. *Proceedings of the National Academy of Sciences*. 1987;84(5):1404.

13. Turrens JF. Mitochondrial formation of reactive oxygen species. *J Physiol (Lond)*. 2003;552(2):335-344.

14. Aon MA, Cortassa S, O'Rourke B. On the network properties of mitochondria. . 2007.

15. van Breukelen F, Krumschnabel G, Podrabsky JE. Vertebrate cell death in energy-limited conditions and how to avoid it: What we might learn from mammalian hibernators and other stress-tolerant vertebrates. *Apoptosis*. 2010;15(3):386-399.

16. Aon MA, Cortassa S, Marbán E, O'Rourke B. Synchronized whole cell oscillations in mitochondrial metabolism triggered by a local release of reactive oxygen species in cardiac myocytes. *J Biol Chem*. 2003;278(45):44735.

17. Dröge W. Free radicals in the physiological control of cell function. *Physiol Rev*. 2002;82(1):47.

18. Fink MP. Reactive oxygen species as mediators of organ dysfunction caused by sepsis, acute respiratory distress syndrome, or hemorrhagic shock: Potential benefits of resuscitation with ringer's ethyl pyruvate solution. *Current Opinion in Clinical Nutrition & Metabolic Care*. 2002;5(2):167.

19. SACK M. Mitochondrial depolarization and the role of uncoupling proteins in ischemia tolerance *Cardiovasc Res*. 2006;72(2):210 <last_page> 219. doi: 10.1016/j.cardiores.2006.07.010.

20. Zweier JL, Talukder M. The role of oxidants and free radicals in reperfusion injury. *Cardiovasc Res*. 2006;70(2):181.

21. Harkness R. Hypoxanthine, xanthine and uridine in body fluids, indicators of ATP depletion. *Journal of Chromatography B: Biomedical Sciences and Applications*. 1988;429:255-278.

22. Lipton P. Ischemic cell death in brain neurons. *Physiol Rev*. 1999;79(4):1431.

23. Tiefenthaler M, Amberger A, Bacher N, et al. Increased lactate production follows loss of mitochondrial membrane potential during apoptosis of human leukaemia cells. *Br J Haematol*. 2001;114(3):574-580.

24. Gudbjarnason S, Bing RJ. The redox-potential of the lactate-pyruvate system in blood as an indicator of the functional state of cellular oxidation. *Biochim Biophys Acta*. 1962;60(1):158-162.

25. Krebs H. The redox state of nicotinamide adenine dinucleotide in the cytoplasm and mitochondria of rat liver. *Adv Enzyme Regul*. 1967;5:409-434.

26. Aon MA. From isolated to networked: A paradigmatic shift in mitochondrial physiology. *Frontiers in physiology*. 2010;1.

27. Shoemaker W, Appel P, Kram H. Role of oxygen debt in the development of organ failure sepsis, and death in high-risk surgical patients. *Chest*. 1992;102(1):208.

28. Bone RC. Immunologic dissonance: A continuing evolution in our understanding of the systemic inflammatory response syndrome (SIRS) and the multiple organ dysfunction syndrome (MODS). *Ann Intern Med*. 1996;125(8):680.

29. Bassingthwaighte JB. *Fractal physiology.* New York: New York : Published for the American Physiological Society by Oxford University Press; 1994.

30. Stinchcombe R, Courtens E. Fractal, phase transitions and criticality [and discussion]. *Proceedings of the Royal Society of London.A.Mathematical and Physical Sciences*. 1989;423(1864):17.

31. Albert R, Barabási AL. Statistical mechanics of complex networks. *Reviews of modern physics*. 2002;74(1):47.

32. Bianconi G. Mean field solution of the ising model on a barabási-albert network. *Physics Letters A*. 2002;303(2-3):166-168.

33. Eaton DC. *Vander's renal physiology.* New York: New York : McGraw-Hill Medical; 2009.

34. Gray H, 1825-1861. *Gray's anatomy.* Edinburgh ; New York: Edinburgh ; New York : C. Livingstone; 1989.

35. Perrone RD, Madias NE, Levey AS. Serum creatinine as an index of renal function: New insights into old concepts. *Clin Chem*. 1992;38(10):1933.

36. Somero GN. From dogfish to dogs: Trimethylamines protect proteins from urea. *Physiology*. 1986;1(1):9.

37. Neuhofer W, Beck FX. Cell survival in the hostile environment of the renal medulla. *Annu Rev Physiol*. 2005;67:531-555.

38. Layton AT, Layton HE, Dantzler WH, Pannabecker TL. The mammalian urine concentrating mechanism: Hypotheses and uncertainties. *Physiology*. 2009;24(4):250.

39. Hervy S, Thomas SR. Inner medullary lactate production and urine-concentrating mechanism: A flat medullary model. *American Journal of Physiology-Renal Physiology*. 2003;284(1):F65.

40. Moss R, Kazmierczak E, Kirley M, Harris P. A computational model for emergent dynamics in the kidney. *Philosophical Transactions of the Royal Society A: Mathematical, Physical and Engineering Sciences*. 2009;367(1896):2125.

41. Kaul CL, Ramarao P. Renin release and the sympathetic nervous system. *Drugs Today*. 2000;36(10):699.

42. Hayes DF, Werner MH, Rosenberg IK, Lucas CE, Westreich M, Bradley V. Effects of traumatic hypovolemic shock on renal function. *J Surg Res*. 1974;16(5):490-497.

43. Toma I, Kang JJ, Sipos A, et al. Succinate receptor GPR91 provides a direct link between high glucose levels and renin release in murine and rabbit kidney. *J Clin Invest*. 2008;118(7):2526.

44. Serkova N, T FLORIAN F, Klawitter J, Freise CE, Niemann CU. 1H-NMR–based metabolic signatures of mild and severe ischemia/reperfusion injury in rat kidney transplants. *Kidney Int*. 2005;67(3):1142-1151.

45. Weinberg JM, Venkatachalam MA, Roeser NF, Nissim I. Mitochondrial dysfunction during hypoxia/reoxygenation and its correction by anaerobic metabolism of citric acid cycle intermediates. *Proceedings of the National Academy of Sciences*. 2000;97(6):2826.

46. Gregoire F. Oxidative metabolism of the normal rat glomerulus. *Kidney Int*. 1975;7:86-93.

47. Bellomo R. Bench-to-bedside review: Lactate and the kidney. *Crit Care*. 2002;6(4):322-326.

48. Marsh DJ, Sosnovtseva OV, Pavlov AN, Yip KP, Holstein-Rathlou NH. Frequency encoding in renal blood flow regulation. *American Journal of Physiology-Regulatory, Integrative and Comparative Physiology*. 2005;288(5):R1160.

49. Nicholson JK, Lindon JC, Holmes E. 'Metabonomics': Understanding the metabolic responses of living systems to pathophysiological stimuli via multivariate statistical analysis of biological NMR spectroscopic data. *Xenobiotica*. 1999;29(11):1181-1189.

50. Oliver SG, Winson MK, Kell DB, Baganz F. Systematic functional analysis of the yeast genome. *Trends Biotechnol*. 1998;16(9):373-378.

51. Beckonert O, Keun HC, Ebbels TMD, et al. Metabolic profiling, metabolomic and metabonomic procedures for NMR spectroscopy of urine, plasma, serum and tissue extracts. *Nature protocols*. 2007;2(11):2692-2703.

52. Bertram HC, Bach Knudsen KE, Serena A, et al. NMR-based metabonomic studies reveal changes in the biochemical profile of plasma and urine from pigs fed high-fibre rye bread. *Br J Nutr*. 2006;95(5):955-962.

53. Kemsley EK, Le Gall G, Dainty JR, et al. Multivariate techniques and their application in nutrition: A metabolomics case study. *Br J Nutr*. 2007;98(01):1-14.

54. Allen J, Davey HM, Broadhurst D, Rowland JJ, Oliver SG, Kell DB. Discrimination of modes of action of antifungal substances by use of metabolic footprinting. *Appl Environ Microbiol*. 2004;70(10):6157.

55. Sun J, Schnackenberg LK, Holland RD, et al. Metabonomics evaluation of urine from rats given acute and chronic doses of acetaminophen using NMR and UPLC/MS. *Journal of Chromatography B*. 2008;871(2):328-340.

56. Cassiday L. Diagnosing pneumonia with urinary metabolomics. *Journal of Proteome Research*. 2009;8(12):5409-5410.

57. Enea C, Seguin F, Petitpas-Mulliez J, et al. 1 H NMR-based metabolomics approach for exploring urinary metabolome modifications after acute and chronic physical exercise. *Analytical and Bioanalytical Chemistry*. 2010;396(3):1167-1176.

58. Sreekumar A, Poisson LM, Rajendiran TM, et al. Metabolomic profiles delineate potential role for sarcosine in prostate cancer progression. *Nature*. 2009;457(7231):910-914.

59. Spratlin JL, Serkova NJ, Eckhardt SG. Clinical applications of metabolomics in oncology: A review. *Clinical Cancer Research*. 2009;15(2):431.

60. Carraro S, Rezzi S, Reniero F, et al. Metabolomics applied to exhaled breath condensate in childhood asthma. *American journal of respiratory and critical care medicine*. 2007:200606-769OCv1.

61. Nicholson JK, Wilson ID. Understanding'global'systems biology: Metabonomics and the continuum of metabolism. *Nature Reviews Drug Discovery*. 2003;2(8):668-676.

62. Clayton TA, Lindon JC, Cloarec O, et al. Pharmaco-metabonomic phenotyping and personalized drug treatment. *Nature*. 2006;440(7087):1073-1077.

63. Lindon JC, Holmes E, Nicholson JK. Metabonomics in pharmaceutical R & D. *Febs Journal*. 2007;274(5):1140-1151.

64. Weckwerth W, Loureiro ME, Wenzel K, Fiehn O. Differential metabolic networks unravel the effects of silent plant phenotypes. *Proc Natl Acad Sci U S A*. 2004;101(20):7809.

65. Mashego MR, Rumbold K, De Mey M, Vandamme E, Soetaert W, Heijnen JJ. Microbial metabolomics: Past, present and future methodologies. *Biotechnol Lett*. 2007;29(1):1-16.

66. Woo HM, Kim KM, Choi MH, et al. Mass spectrometry based metabolomic approaches in urinary biomarker study of women's cancers. *Clinica Chimica Acta*. 2009;400(1-2):63-69.

67. Baumgartner C, Baumgartner D. Biomarker discovery, disease classification, and similarity query processing on high-throughput MS/MS data of inborn errors of metabolism. *Journal of biomolecular screening*. 2006;11(1):90.

68. Dettmer K, Aronov PA, Hammock BD. Mass spectrometry-based metabolomics. *Mass Spectrom Rev*. 2007;26(1):51.

69. Kind T, Tolstikov V, Fiehn O, Weiss RH. A comprehensive urinary metabolomic approach for identifying kidney cancer. *Anal Biochem*. 2007;363(2):185-195.

70. Moolenaar SH. *Handbook of 1H-NMR-spectroscopy in inborn errors of metabolism.* SPS Publ.; 2002.

71. Lindon JC, Nicholson JK, Holmes E. *The handbook of metabonomics and metabolomics* Amsterdam ; Elsevier, 2007.:561.

72. Wishart DS. Current progress in computational metabolomics. *Briefings in bioinformatics*. 2007;8(5):279.

73. Madsen R, Lundstedt T, Trygg J. Chemometrics in metabolomics--A review in human disease diagnosis. *Anal Chim Acta*. 2010;659(1-2):23-33.

74. Trygg J, Holmes E, Lundstedt T. Chemometrics in metabonomics. *Journal of proteome research*. 2007;6(2):469-479.

75. Jolliffe IT. Discarding variables in a principal component analysis. I: Artificial data. *Applied Statistics*. 1972:160-173.

76. Wold S, Sjostrom M, Eriksson L. PLS-regression: A basic tool of chemometrics. *Chemometrics Intellig Lab Syst*. 2001;58(2):109-130.

77. Brereton RG, Ebrary I. *Chemometrics for pattern recognition.* Wiley Online Library; 2009.

78. Westerhuis JA, Hoefsloot HCJ, Smit S, et al. Assessment of PLSDA cross validation. *Metabolomics*. 2008;4(1):81-89.

79. Camacho D, de la Fuente A, Mendes P. The origin of correlations in metabolomics data. *Metabolomics*. 2005;1(1):53-63.

80. Bamforth F, Dorian V, Vallance H, Wishart D. Diagnosis of inborn errors of metabolism using 1H NMR spectroscopic analysis of urine. *J Inherit Metab Dis*. 1999;22(3):297-301.

81. Constantinou MA, Papakonstantinou E, Spraul M, et al. 1H NMR-based metabonomics for the diagnosis of inborn errors of metabolism in urine. *Anal Chim Acta*. 2005;542(2):169-177.

82. Wang C, Kong H, Guan Y, et al. Plasma phospholipid metabolic profiling and biomarkers of type 2 diabetes mellitus based on high-performance liquid chromatography/electrospray mass spectrometry and multivariate statistical analysis. *Anal Chem*. 2005;77(13):4108-4116.

83. Orešič M, Simell S, Sysi-Aho M, et al. Dysregulation of lipid and amino acid metabolism precedes islet autoimmunity in children who later progress to type 1 diabetes. *J Exp Med*. 2008;205(13):2975.

84. Yang J, Xu G, Zheng Y, et al. Diagnosis of liver cancer using HPLC-based metabonomics avoiding false-positive result from hepatitis and hepatocirrhosis diseases. *Journal of Chromatography B*. 2004;813(1-2):59-65.

85. Issaq HJ, Nativ O, Waybright T, et al. Detection of bladder cancer in human urine by metabolomic profiling using high performance liquid chromatography/mass spectrometry. *J Urol*. 2008;179(6):2422-2426.

86. Serkova NJ, Gamito EJ, Jones RH, et al. The metabolites citrate, myo‐inositol, and spermine are potential age‐independent markers of prostate cancer in human expressed prostatic secretions. *Prostate*. 2008;68(6):620-628.

87. Tiziani S, Lopes V, Günther UL. Early stage diagnosis of oral cancer using 1H NMR-based metabolomics. *Neoplasia (New York, NY)*. 2009;11(3):269.

88. Monleón D, Morales JM, Gonzalez-Darder J, et al. Benign and atypical meningioma metabolic signatures by high-resolution magic-angle spinning molecular profiling. *Journal of Proteome Research*. 2008;7(7):2882-2888.

89. Denkert C, Budczies J, Weichert W, et al. Metabolite profiling of human colon carcinoma–deregulation of TCA cycle and amino acid turnover. *Molecular cancer*. 2008;7(1):72.

90. Bullinger D, Frohlich H, Klaus F, et al. Bioinformatical evaluation of modified nucleosides as biomedical markers in diagnosis of breast cancer. *Anal Chim Acta*. 2008;618(1):29-34.

91. Odunsi K, Wollman RM, Ambrosone CB, et al. Detection of epithelial ovarian cancer using 1H‐NMR‐based metabonomics. *International journal of cancer*. 2005;113(5):782-788.

92. Nishiumi S, Shinohara M, Ikeda A, et al. Serum metabolomics as a novel diagnostic approach for pancreatic cancer. *Metabolomics*. 2010:1-11.

93. Sabatine MS, Liu E, Morrow DA, et al. Metabolomic identification of novel biomarkers of myocardial ischemia. *Circulation*. 2005;112(25):3868.

94. Kirschenlohr HL, Griffin JL, Clarke SC, et al. Proton NMR analysis of plasma is a weak predictor of coronary artery disease. *Nat Med*. 2006;12(6):705-710.

95. Barba I, de León G, Martín E, et al. Nuclear magnetic resonance‐based metabolomics predicts exercise‐induced ischemia in patients with suspected coronary artery disease. *Magnetic Resonance in Medicine*. 2008;60(1):27-32.

96. Brindle JT, Antti H, Holmes E, et al. Rapid and noninvasive diagnosis of the presence and severity of coronary heart disease using 1H-NMR-based metabonomics. *Nat Med*. 2002;8(12):1439-1445.

97. Rozen S, Cudkowicz ME, Bogdanov M, et al. Metabolomic analysis and signatures in motor neuron disease. *Metabolomics*. 2005;1(2):101-108.

98. Michell AW, Mosedale D, Grainger DJ, Barker RA. Metabolomic analysis of urine and serum in Parkinson's disease. *Metabolomics*. 2008;4(3):191-201.

99. Holmes E, Tsang TM, Tabrizi SJ. The application of NMR-based metabonomics in neurological disorders. *NeuroRx*. 2006;3(3):358-372.

100. Kaddurah-Daouk R. Metabolic profiling of patients with schizophrenia. *PLoS Medicine*. 2006;3(8):e363.

101. Kaddurah-Daouk R, McEvoy J, Baillie R, et al. Metabolomic mapping of atypical antipsychotic effects in schizophrenia. *Mol Psychiatry*. 2007;12(10):934-945.

102. Greenberg N, Grassano A, Thambisetty M, Lovestone S, Legido‐Quigley C. A proposed metabolic strategy for monitoring disease progression in alzheimer's disease. *Electrophoresis*. 2009;30(7):1235-1239.

103. Tukiainen T, Tynkkynen T, Makinen VP, et al. A multi-metabolite analysis of serum by 1H NMR spectroscopy: Early systemic signs of alzheimer's disease. *Biochem Biophys Res Commun*. 2008;375(3):356-361.

104. Saude EJ, Skappak CD, Regush S, et al. Metabolomic profiling of asthma: Diagnostic utility of urine nuclear magnetic resonance spectroscopy. *J Allergy Clin Immunol*. 2011;127(3):757-764.

105. Wishart DS. Metabolomics in monitoring kidney transplants. *Curr Opin Nephrol Hypertens*. 2006;15(6):637.

106. Bertini I, Calabrò A, De Carli V, et al. The metabonomic signature of celiac disease. *Journal of Proteome Research*. 2008;8(1):170-177.

107. Mäkinen VP, Soininen P, Forsblom C, et al. Diagnosing diabetic nephropathy by 1 H NMR metabonomics of serum. *Magnetic Resonance Materials in Physics, Biology and Medicine*. 2006;19(6):281-296.

108. Mäkinen VP, Forsblom C, Thorn LM, et al. Metabolic phenotypes, vascular complications, and premature deaths in a population of 4,197 patients with type 1 diabetes. *Diabetes*. 2008;57(9):2480.

109. Kline EE, Treat EG, Averna TA, Davis MS, Smith AY, Sillerud LO. Citrate concentrations in human seminal fluid and expressed prostatic fluid determined via 1H nuclear magnetic resonance spectroscopy outperform prostate specific antigen in prostate cancer detection. *J Urol*. 2006;176(5):2274-2279.

110. Roussel R, Mentré F, Bouchemal N, et al. NMR-based prediction of cardiovascular risk in diabetes. *Nat Med*. 2007;13(4):399-400.

111. Taubes G. *Good calories, bad calories: Challenging the conventional wisdom on diet, weight control, and disease.* Random House of Canada; 2007.

112. Nicholson JK. Global systems biology, personalized medicine and molecular epidemiology. *Molecular systems biology*. 2006;2(1).

113. Weston AD, Hood L. Systems biology, proteomics, and the future of health care: Toward predictive, preventative, and personalized medicine. *Journal of proteome research*. 2004;3(2):179-196.

114. Cohen MJ, Serkova NJ, Wiener-Kronish J, Pittet JF, Niemann CU. 1H-NMR-based metabolic signatures of clinical outcomes in trauma patients-beyond lactate and base deficit. *J Trauma*. 2010;69(1):31.

115. Lee DS, Park J, Kay K, Christakis N, Oltvai Z, Barabási AL. The implications of human metabolic network topology for disease comorbidity. *Proceedings of the National Academy of Sciences*. 2008;105(29):9880.

116. Barabási AL, Gulbahce N, Loscalzo J. Network medicine: A network-based approach to human disease. *Nature Reviews Genetics*. 2011;12(1):56-68.

117. Bellamy RF. The causes of death in conventional land warfare: Implications for combat casualty care research. *Mil Med*. 1984;149(2):55-62.

118. Heckbert SR, Vedder NB, Hoffman W, et al. Outcome after hemorrhagic shock in trauma patients. *J Trauma*. 1998;45(3):545.

119. Turer AT, Stevens RD, Bain JR, et al. Metabolomic profiling reveals distinct patterns of myocardial substrate use in humans with coronary artery disease or left ventricular dysfunction during surgical ischemia/reperfusion. *Circulation*. 2009.

120. Lv Y, Liu X, Yan S, et al. Metabolomic study of myocardial ischemia and intervention effects of compound danshen tablets in rats using ultra-performance liquid

chromatography/quadrupole time-of-flight mass spectrometry. *J Pharm Biomed Anal*. 2010;52(1):129-135.

121. Feala JD, Coquin L, Paternostro G, McCulloch AD. Integrating metabolomics and phenomics with systems models of cardiac hypoxia. *Prog Biophys Mol Biol*. 2008;96(1-3):209-225.

122. Kinross J, Warren O, Basson S, et al. Intestinal ischemia/reperfusion injury: Defining the role of the gut microbiome. *Biomarkers*. 2009;3(2):175-192.

123. Craig A, Cloarec O, Holmes E, Nicholson JK, Lindon JC. Scaling and normalization effects in NMR spectroscopic metabonomic data sets. *Anal Chem*. 2006;78(7):2262-2267.

124. Dieterle F, Ross A, Schlotterbeck G, Senn H. Probabilistic quotient normalization as robust method to account for dilution of complex biological mixtures. application in 1H NMR metabonomics. *Anal Chem*. 2006;78(13):4281-4290.

125. Warrack BM, Hnatyshyn S, Ott KH, et al. Normalization strategies for metabonomic analysis of urine samples. *Journal of Chromatography B*. 2009.

126. Webb-Robertson BJM, Lowry DF, Jarman KH, et al. A study of spectral integration and normalization in NMR-based metabonomic analyses. *J Pharm Biomed Anal*. 2005;39(3-4):830-836.

127. Torgrip RJO, Åberg K, Alm E, Schuppe-Koistinen I, Lindberg J. A note on normalization of biofluid 1D 1 H-NMR data. *Metabolomics*. 2008;4(2):114-121.

128. Gunnar WP, Merlotti GJ, Barrett J, Jonasson O. Resuscitation from hemorrhagic shock. alterations of the intracranial pressure after normal saline, 3% saline and dextran-40. *Ann Surg*. 1986;204(6):686.

129. Mulier KE, Beilman GJ, Conroy MJ, Taylor JH, Skarda DE, Hammer BE. Ringer's ethyl pyruvate in hemorrhagic shock and resuscitation does not improve early hemodynamics or tissue energetics. *Shock*. 2005;23(3):248.

130. Holcomb JB, Pusateri AE, Harris RA, et al. Effect of dry fibrin sealant dressings versus gauze packing on blood loss in grade V liver injuries in resuscitated swine. *J Trauma*. 1999;46(1):49.

131. Mortishire-Smith RJ, Skiles GL, Lawrence JW, et al. Use of metabonomics to identify impaired fatty acid metabolism as the mechanism of a drug-induced toxicity. *Chem Res Toxicol*. 2004;17(2):165-173.

132. Levey AS, Bosch JP, Lewis JB, Greene T, Rogers N, Roth D. A more accurate method to estimate glomerular filtration rate from serum creatinine: A new prediction equation. *Ann Intern Med*. 1999;130(6):461.

133. Friendship RM, Lumsden JH, McMillan I, Wilson MR. Hematology and biochemistry reference values for ontario swine. *Canadian journal of comparative medicine*. 1984;48(4):390.

134. Slupsky CM, Rankin KN, Wagner J, et al. Investigations of the effects of gender, diurnal variation, and age in human urinary metabolomic profiles. *Anal Chem*. 2007;79(18):6995-7004.

135. Blow O, Magliore L, Claridge JA, Butler K, Young JS. The golden hour and the silver day: Detection and correction of occult hypoperfusion within 24 hours improves outcome from major trauma. *J Trauma*. 1999;47(5):964.

136. Husain FA, Martin MJ, Mullenix PS, Steele SR, Elliott DC. Serum lactate and base deficit as predictors of mortality and morbidity. *The American Journal of Surgery*. 2003;185(5):485-491.

137. Taylor JH, Beilman GJ, Conroy MJ, et al. Tissue energetics as measured by nuclear magnetic resonance spectroscopy during hemorrhagic shock. *Shock*. 2004;21(1):58.

138. Long C, Birkhahn R, Geiger J, Blakemore W. Contribution of skeletal muscle protein in elevated rates of whole body protein catabolism in trauma patients. *Am J Clin Nutr*. 1981;34(6):1087.

139. Carvounis CP, Nisar S, Guro-Razuman S. Significance of the fractional excretion of urea in the differential diagnosis of acute renal failure. *Kidney Int*. 2002;62(6):2223-2229.

140. Vivino G, Antonelli M, Moro M, et al. Risk factors for acute renal failure in trauma patients. *Intensive Care Med*. 1998;24(8):808-814.

141. Threlfall CJ, Maxwell AR, Stoner HB. Post-traumatic creatinuria. *J Trauma*. 1984;24(6):516.

142. Layton HE, Pitman EB. A dynamic numerical method for models of renal tubules. *Bull Math Biol*. 1994;56(3):547-565.

143. Stephenson JL, Mejia R, Tewarson R. Model of solute and water movement in the kidney. *Proc Natl Acad Sci U S A*. 1976;73(1):252.

144. Klein J. Membrane breakdown in acute and chronic neurodegeneration: Focus on choline-containing phospholipids. *J Neural Transm*. 2000;107(8):1027-1063.

145. Biedroń R, Ciszek M, Tokarczyk M, et al. 1-methylnicotinamide and nicotinamide: Two related anti-inflammatory agents that differentially affect the functions of activated macrophages. *Arch Immunol Ther Exp (Warsz)*. 2008;56(2):127-134.

146. Sikora A, Szajerski P, Piotrowski L, et al. Radical scavenging properties of nicotinamide and its metabolites. *Radiat Phys Chem*. 2008;77(3):259-266.

147. Chlopicki S, Swies J, Mogielnicki A, et al. 1‐Methylnicotinamide (MNA), a primary metabolite of nicotinamide, exerts anti‐thrombotic activity mediated by a cyclooxygenase‐2/prostacyclin pathway. *Br J Pharmacol*. 2007;152(2):230-239.

148. Oxford A. The conversion of certain soluble sugars to a glucosan by holotrich ciliates in the rumen of sheep. *J Gen Microbiol*. 1951;5(1):83.

149. Dorland L, Wadman S, de Jonge HF, Ketting D. 1, 6-anhydro-[beta]-d-glucopyranose ([beta]-glucosan), a constituent of human urine. *Clinica chimica acta*. 1986;159(1):11-16.

150. Xu X, Xie Q, Shen Y, et al. Involvement of mannose receptor in the preventive effects of mannose in lipopolysaccharide-induced acute lung injury. *Eur J Pharmacol*. 2010.

151. Zhao W, Langfelder P, Fuller T, Dong J, Li A, Hovarth S. Weighted gene coexpression network analysis: State of the art. *J Biopharm Stat*. 2010;20(2):281-300.

152. Ravasz E, Somera AL, Mongru DA, Oltvai ZN, Barabási AL. Hierarchical organization of modularity in metabolic networks. *Science*. 2002;297(5586):1551.

153. Langfelder P, Zhang B, Horvath S. Defining clusters from a hierarchical cluster tree: The dynamic tree cut package for R. *Bioinformatics*. 2008;24(5):719.

154. Hu Z, Mellor J, Wu J, DeLisi C. VisANT: An online visualization and analysis tool for biological interaction data. *BMC Bioinformatics*. 2004;5(1):17.

155. Simenhoff ML, Saukkonen JJ, Burke JF, et al. Importance of aliphatic amines in uremia. *Kidney Int Suppl*. 1978;(8)(8):S16-9.

156. Lee J, Lee H, Sadler P. Uraemia: Is urea more important than we think? *The Lancet*. 1991;338(8780):1438-1440.

157. Paulo JA, Lee LS, Wu B, Banks PA, Steen H, Conwell DL. Mass spectrometry‐based proteomics of endoscopically collected pancreatic fluid in chronic pancreatitis research. *PROTEOMICS–Clinical Applications*.

158. Yang AHJ, Moore SD, Schmidt BS, Klug M, Lipson M, Erickson D. Optical manipulation of nanoparticles and biomolecules in sub-wavelength slot waveguides. *Nature*. 2009;457(7225):71-75.

159. Kim J, Hammer B, Harjani R. A low power CMOS receiver for a tissue monitoring NMR spectrometer. . :221-222.

160. West GB, Brown JH, Enquist BJ. The fourth dimension of life: Fractal geometry and allometric scaling of organisms. *Science*. 1999;284(5420):1677.

161. Aon MA, Cortassa S, O'Rourke B. The fundamental organization of cardiac mitochondria as a network of coupled oscillators. *Biophys J*. 2006;91(11):4317-4327.

162. Mirollo RE, Strogatz SH. Synchronization of pulse-coupled biological oscillators. *SIAM J Appl Math*. 1990:1645-1662.

163. Strogatz SH, Stewart I. Coupled oscillators and biological synchronization. *Sci Am*. 1993;269(6):102-109.

Appendix A: Physiological variables

Animals are monitored continuously from baseline through FR20. They are instrumented to measure a host of physiological variables including vitals and clinical laboratory measurements. These are listed below. Vitals are recorded in the OR every ten minutes. Labs are performed on individual blood samples sent to the Fairview Clinical Laboratory.

Vitals			
Blood given (mL)	Arterial pH	Blood glucose (mg/dL)	Tissue oxygen saturation (15 mm, %)
Blood removed (mL)	BIS	Hemoglobin (g/dL)	Tissue oxygen saturation (multidepth, %)
Lactated Ringer's given (mL)	Base deficit (mEq/L)	Heart rate (beats per min)	Tissue harmonic imaging probe (15 mm)
OR fluids given (mL)	Bladder pressure (mmHg)	Blood lactate (mM)	Tissue harmonic imaging probe (mulitdepth)
Total fluids given (mL)	Calcium (mM)	Mean arterial pressure (mmHg)	Temperature (°C)
Arterial diastolic pressure (mmHg)	Cardiac output (L/min)	Pulmonary artery pressure (diastolic, mmHg)	Urine output (cc/hr)
Arterial systolic pressure (mmHg)	Chest tube output (mL)	Pulmonary artery pressure (systolic, mmHg)	Oxygen consumption (mL/min/kg)
Arterial O2 saturation (%)	Oxygen delivery (mL/min)	Potassium (mM)	Venous O2 saturation (%)
Partial pressure of CO2 (arterial, mmHg)	Oxygen extraction ratio (%)	Propofol (cc/hr)	Partial pressure of oxygen (venous, mmHg)
Partial pressure of O2 (arterial, mmHg)	Fraction of inspired oxygen (%)	Sodium (mM)	Wedge pressure (mmHg)

Labs			
Alanine aminotransferase (U/L)	ALK phosphatase (U/L)	Creatinine (blood, mg/dL)	Total protein (g/dL)
Aspartate transanimase (U/L)	Bilirubin (mg/dL)	Lactate dehydrogenase (U/L)	Blood urea (mg/dL)
Albumin (g/dL)	Creatine kinase (U/L)	Platelet count (#/L)	Creatinine (urine, mg/dL)

Appendix B: PLS-DA models

The following table is reproduced from Chapter 6. The PLS-DA models demonstrate the following six properties of the urine data set:

1. The urine metabolome does not discriminate by survival. The only survival information is obtained indirectly by modeling C1 and C2.
2. FR2 is a distinguishing timepoint that is generally associated with metabolites of both aerobic and anaerobic respiration, as well as markers of hypoxia and cellular membrane breakdown.
3. FR20 is a distinguishing timepoint, though levels of the metabolites commonly associated with this timepoint do not differ between experimental and control animals.
4. The urine metabolome reflects phase-of-care.
5. The urine metabolome separates experimental animals from controls, though E1 is similar to C1 at all timepoints but FR2.
6. E1 and E2 animals differ before shock and injury, and the response to hemorrhage is different.

Model	Data subset/Class	R^2	Q^2
A	E2 (by survival)	0.74	0.09
B	Full (by survival)	0.55	0.22
C	E1 vs C1	0.49	0.30
D	Full (by group)	0.46	0.32
E	E2 (by timepoint)	0.58	0.47
F	Full (by timepoint)	0.57	0.48
G	E1 (by timepoint)	0.64	0.55
H	E2 FR8 vs C1 FR 8*	0.97	0.62
I	E2 FR2 vs C1 FR2*	0.96	0.63
J	E2 vs C1*	0.77	0.68
K	E1 Baseline vs E2 Baseline*	0.92	0.69
L	E1 vs E2*	0.90	0.77
M	E1 FR2 vs C1 FR2*	0.98	0.78
N	B vs FR2 (full data set)*	0.88	0.81
O	E1 FR8 vs E2 FR8*	0.98	0.86
P	FR2 vs FR20 (full data set)*	0.95	0.90
Q	E1 B vs E1FR2 vs E1FR20*	0.96	0.92

These models are arranged in order of increasing predictive power. Asterisks indicate models with good predictive power ($Q^2>0.5$). Each model presented in the table is shown below with brief commentary on observed differences in the metabolome according to the scores (top panel) and loadings (bottom panel).

Model A: E2 by survival

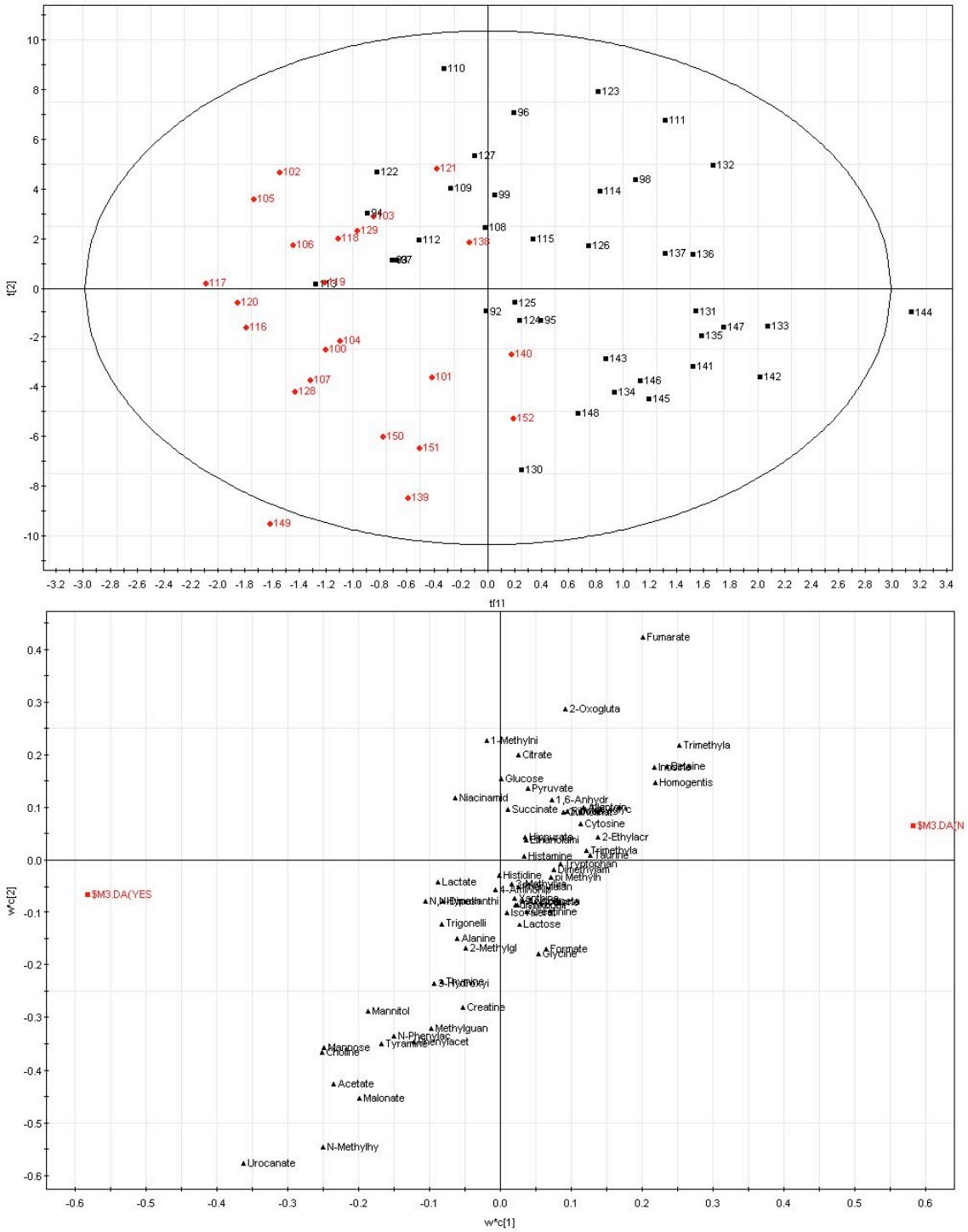

Model A: PLS-DA model discriminating between urine samples of E2 animals that lived (black) and those that died (red).

Model B: Full data set differentiated by survival

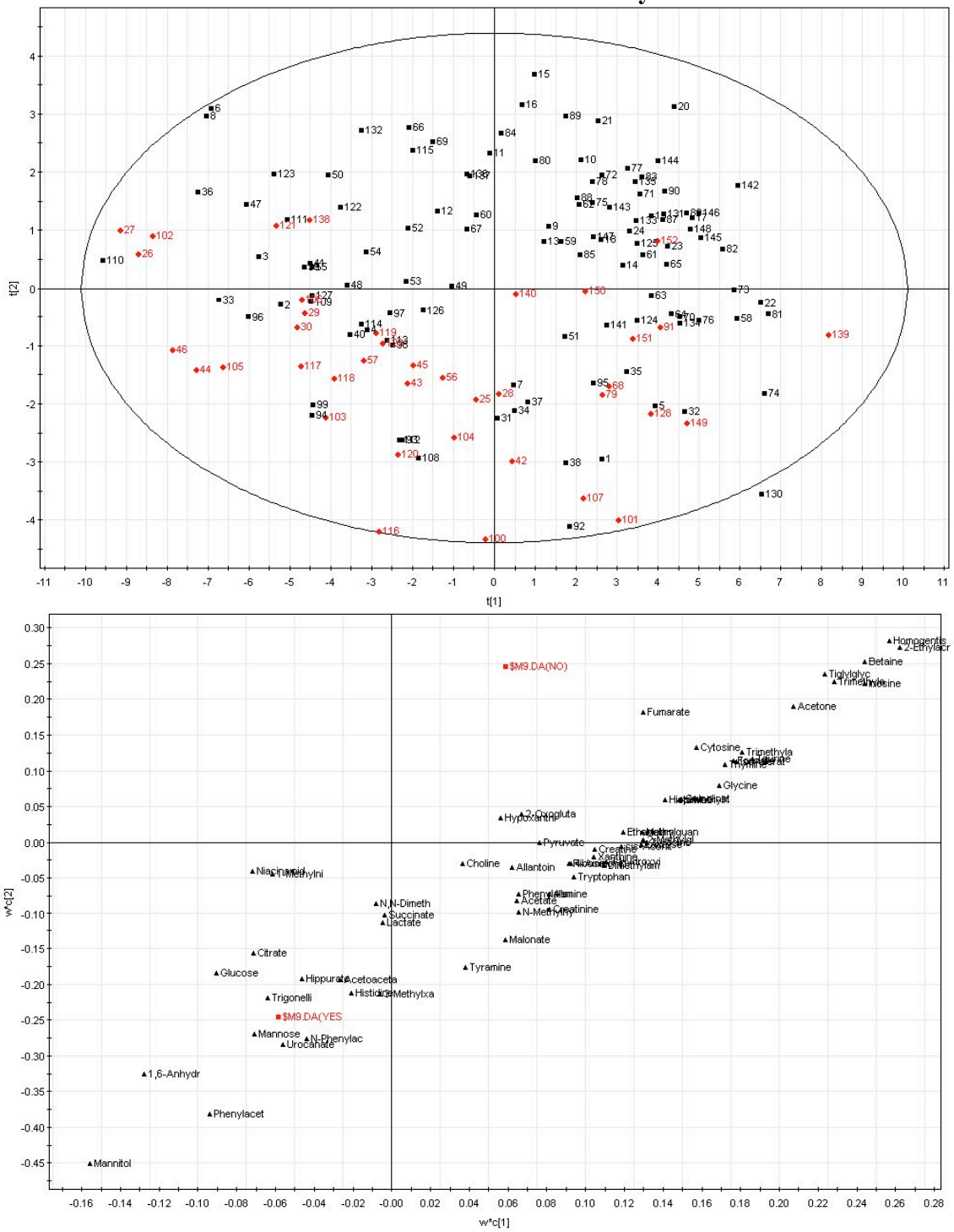

Model B: PLS-DA model of the full data set by survival (Black=Lived, Red=Died). This model has poor predictive value, as do all models that discriminate by survival (data not shown).

Model C: E1 vs. C1

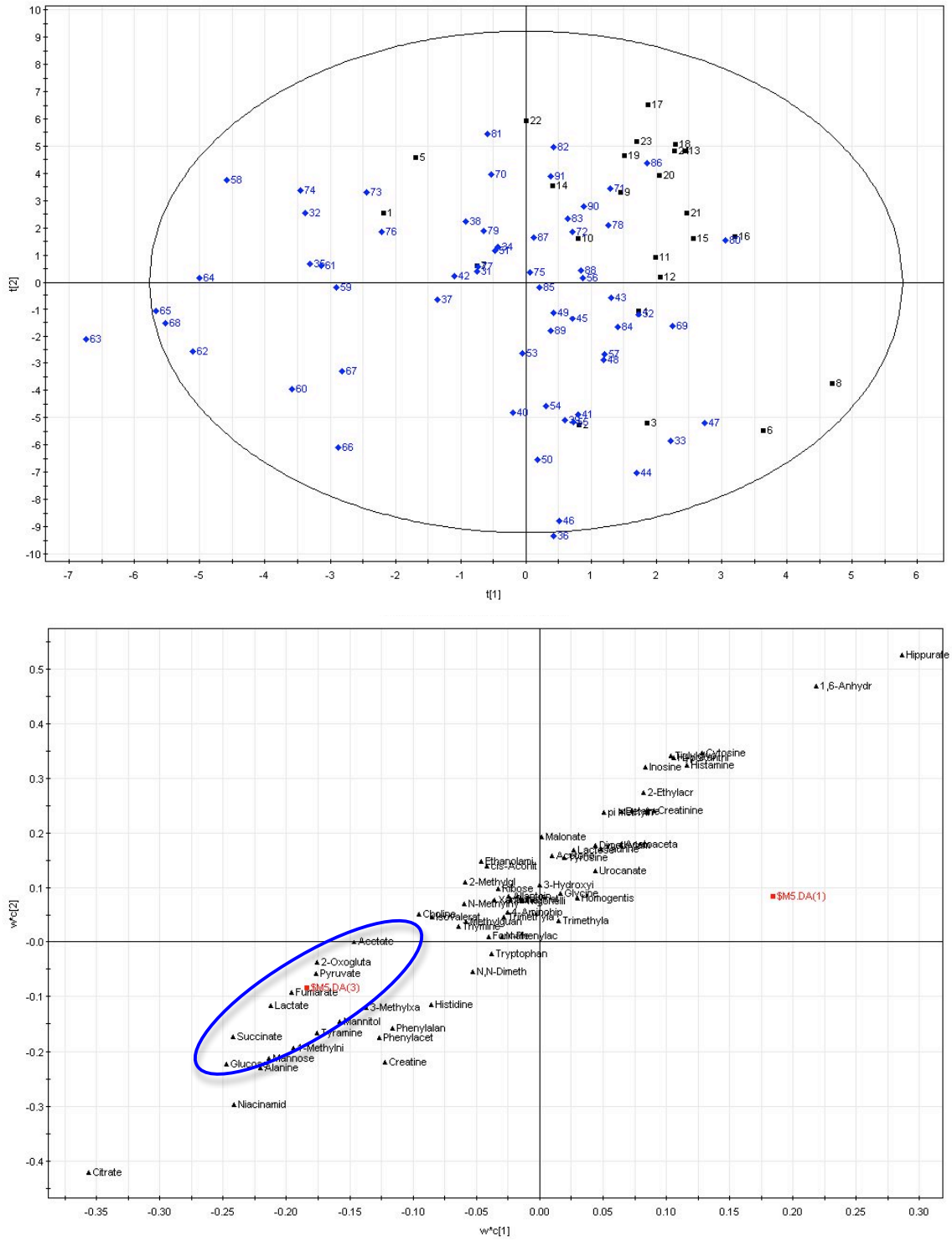

Model C: PLS-DA model of all E1 urine samples (blue) vs. all C1 urine samples (black). This model has poor predictive value, but E1 urine samples tend to cluster with metabolites associated with respiration (circled in blue). Other models were constructed to compare E1 to C1 at specific timepoints. None of these models had Q^2>0.5 save for E1 vs C1 at FR2. This is shown in Model M.

Model D: Full data set differentiated by group

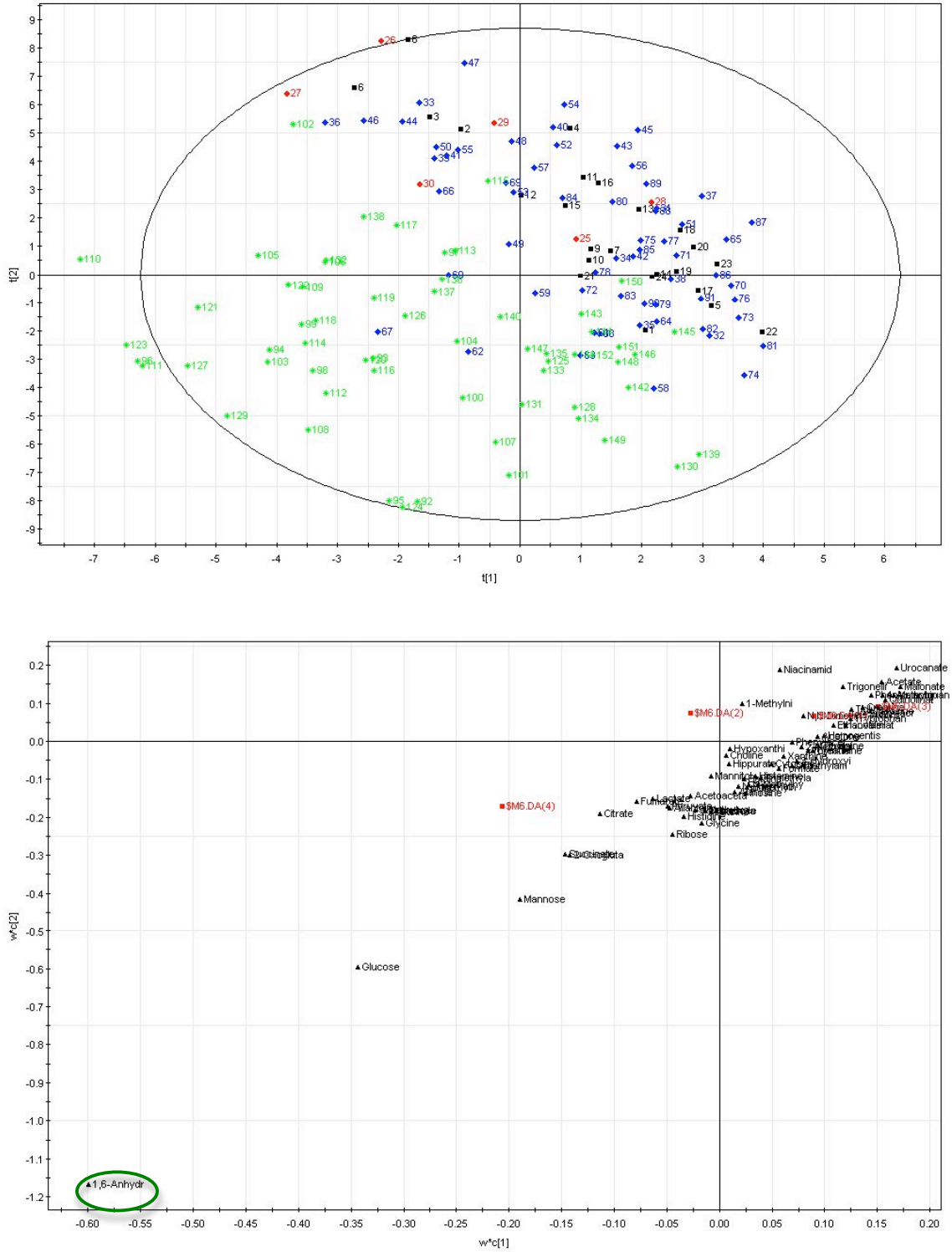

Model D: PLS-DA model of the full data set, differentiated by group (C1=black, C2=red, E1=blue, E2=green). This model has poor predictive power, but supports the mixed models result that urinary 1,6-Anhydro β-D-glucose (circled in green) is a marker of E2 animals.

Model E: E2 differentiated by timepoint

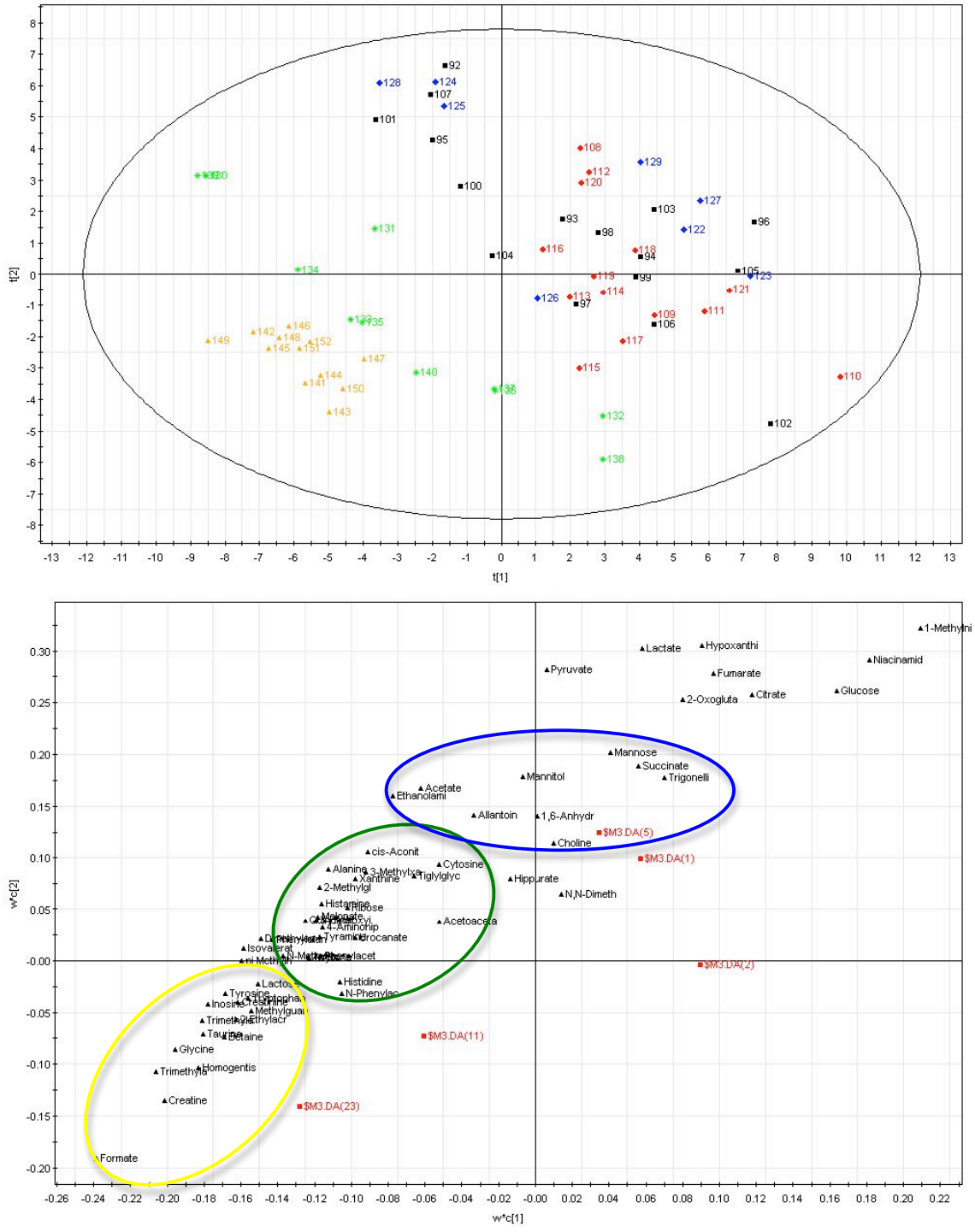

Model E: PLS-DA model of E2, separated by timepoint. Black=baseline; Red=S45; Blue=FR2; Green=FR8; Yellow=FR20. This model has moderate predictive value, and best separates late resuscitation timepoints from earlier timepoints. Early resuscitation (FR2) is associated with mannitol, acetate, ethanolamine, allantoin, 1,6-Anhydro β-D-glucose, choline, mannose, succinate, and trigonelline. FR8 is associated with cis-Aconitate, cytosine, alanine, 3-methylxanthine,tiglylglycine, xanthine, 2-

methylglutarate, histamine, ribose, acetoacetate, manolate, quinolinate, 4-aminohippurate, tyramine, urocanate, phenylalanine, dimethylamine, phenyacetylglycine, N-methylhydantoin, isovalerate, pi-methylhistidine, histidine, and N-phenylacetylglycine. FR20 is associated with formate, creatine, trimethylamine N-oxide, homogentisate, glycine, taurine, betaine, trimethylaime, 2-ethylacrylate, methylguanidine, inosine, creatinine, tryptophan, tyrosine, and lactose (ringed in green). There is little separation in the scores between B, S45, and FR2 timepoints. Unlike the FR2 timepoint in E1 models, FR2 is not directly grouped with metabolites associated with respiration (ringed in blue).

Model F: Full data set differentiated by timepoint

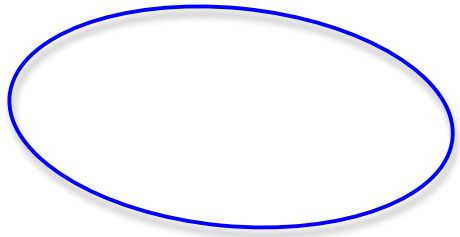

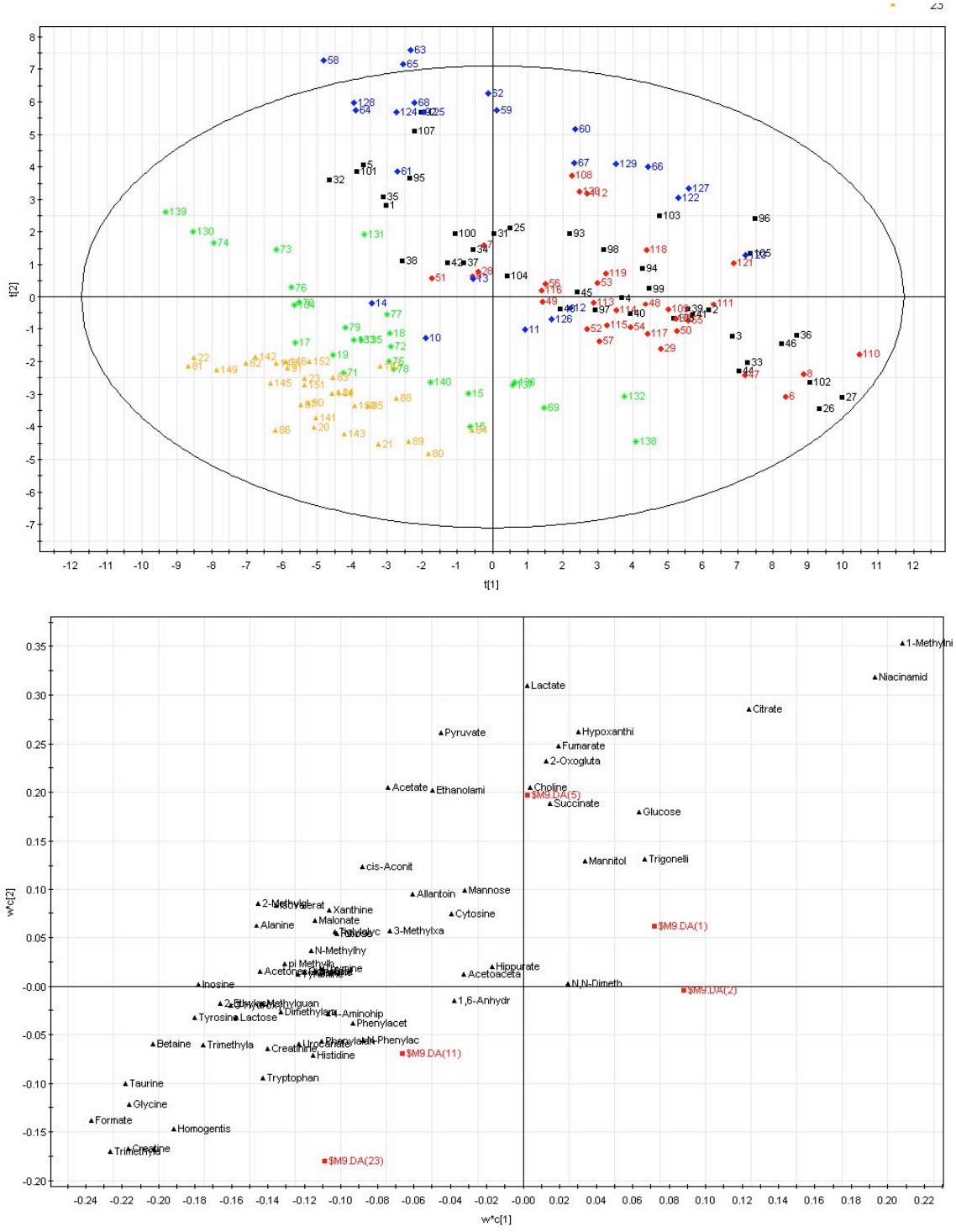

Model F: Scores plot (top) and loadings plot (bottom) for PLS-DA model of the full urine data set by timepoint. There is moderate separation between B/S45 data (black/red), FR2 data (blue), and FR8/FR20 data (green/yellow). Examination of the loadings plot shows that FR2 (blue) is strongly associated with choline and succinate. FR20 samples (yellow) are somewhat associated with taurine, glycine, formate, homogentisate, creatine, and trimethylamine N-oxide.

Model G: E1 differentiated by timepoint

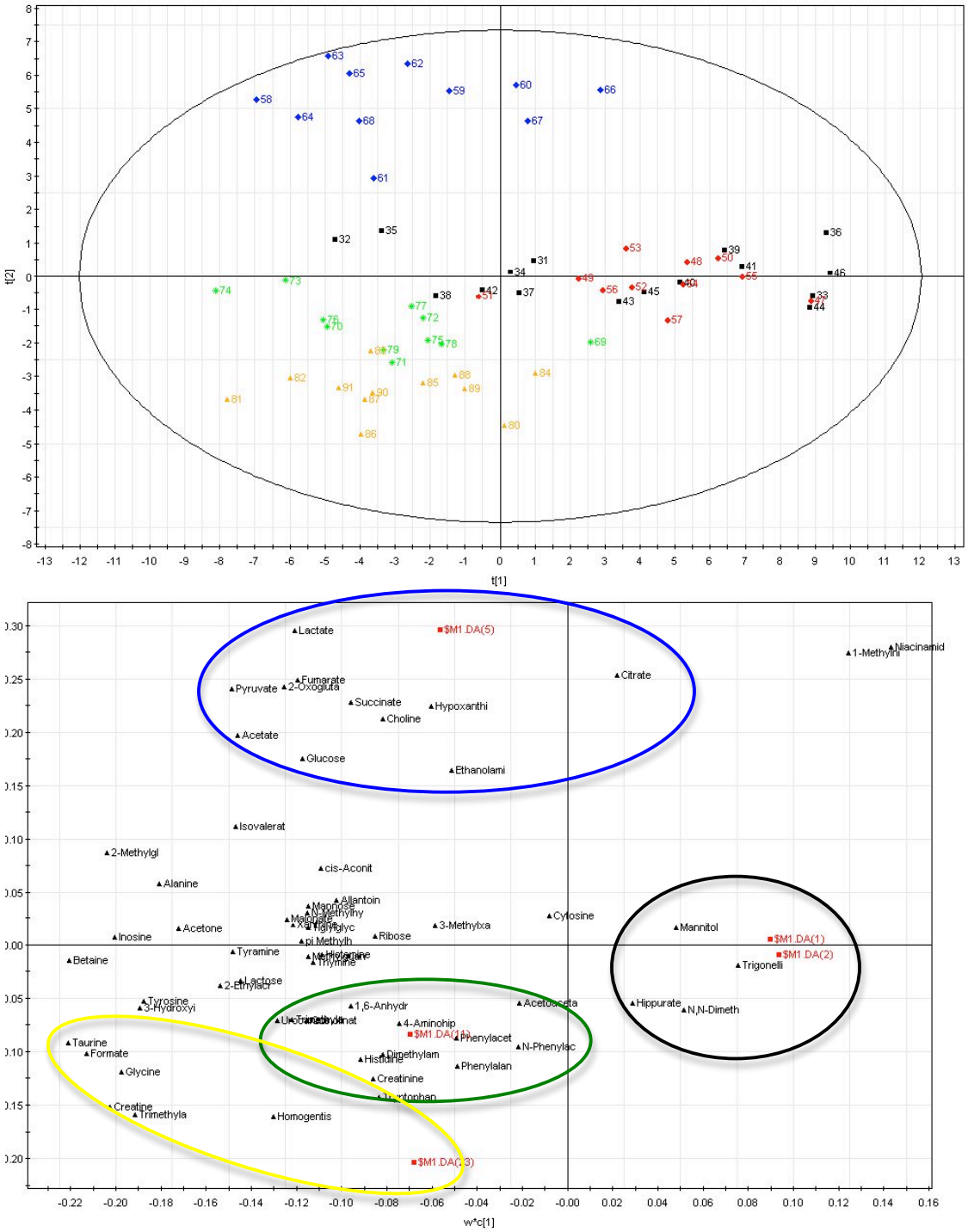

Model G: PLS-DA model of E1 urine samples by timepoint (black=B, red=S45, blue=FR2, green=FR8, yellow=FR20). This model has reasonably good predictive power (Q^2=0.55). FR2 loadings (blue) are clearly separated from the rest of the loadings, which show moderate separation from each other at best (green=FR8, yellow=FR20). Baseline and S45 samples are indistinguishable (ringed in black). Metabolites that are associated with FR2 are all involved in respiration, or are components of cellular

membranes, or are indicative of hypoxia. FR8 is associated with acetoacetate, 1,6 Anhydro β-D-glucose, trimethylamine, urocanate, 4-aminohippurate, phenylacetylglycine, N-phenylacetylglycine, phenylalanine, dimethylamine, histidine, tryptophan, and creatine. FR20 is associated with taurine, formate, glycine, creatine, trimthylamine N-oxide, and homogentisate.

Model H: E2 FR8 vs C1 FR8

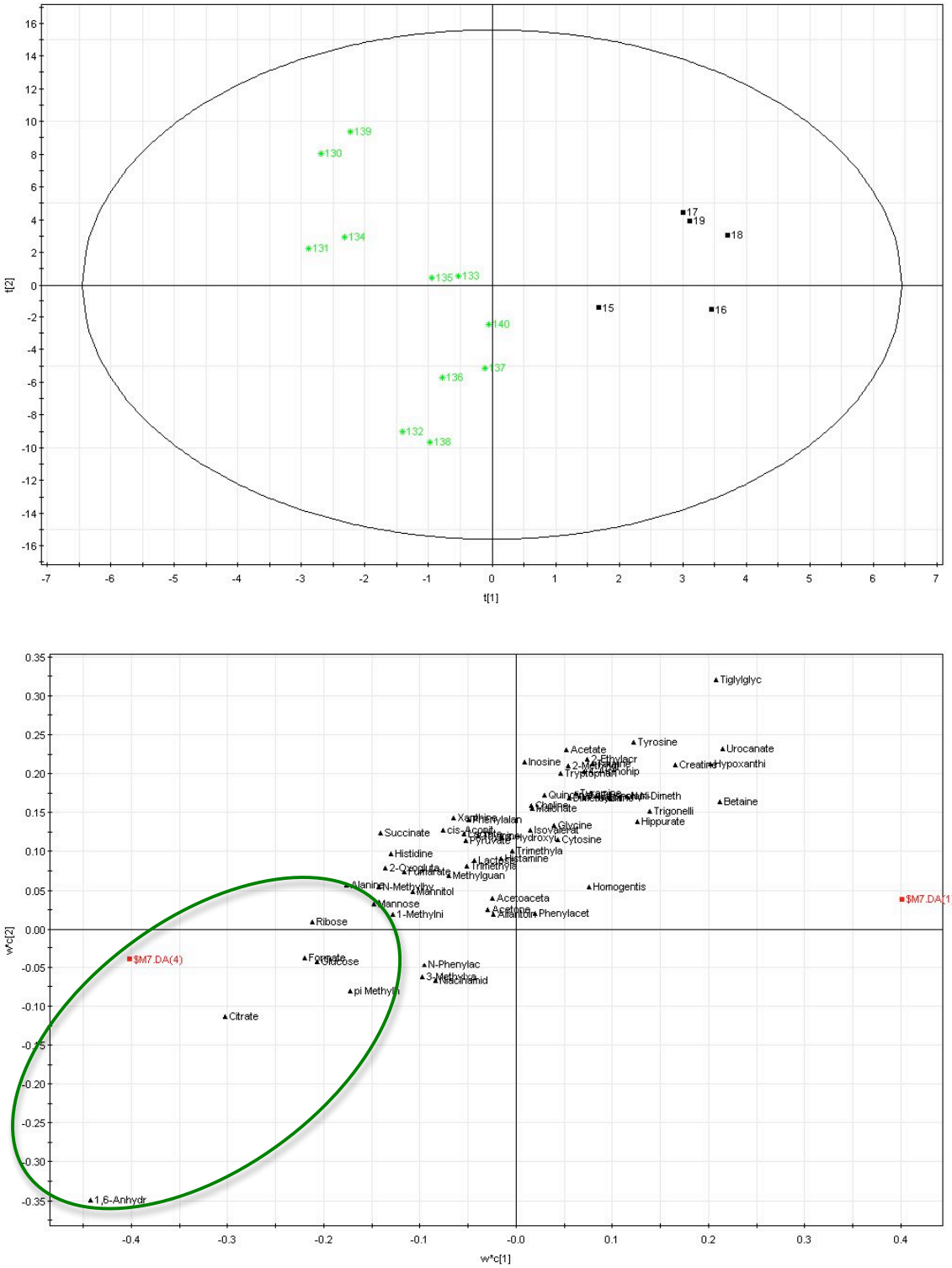

Model H: PLS-DA model of E2 (green) and C1 (black) urine samples at FR8. This model supports the mixed models result that 1,6-Anhydro β-D-glucose distinguishes E2 animals. Citrate and glucose implicate cellular respiration, formate is the simplest form of carboxyl in metabolism, and pi-methylhistidine is a

marker of trauma. Ribose is a component of DNA. These metabolites, which contribute to the separation of E2 urine samples from C1 urine samples at FR8, are ringed in green.

Model I: E2 FR2 vs C1 FR2

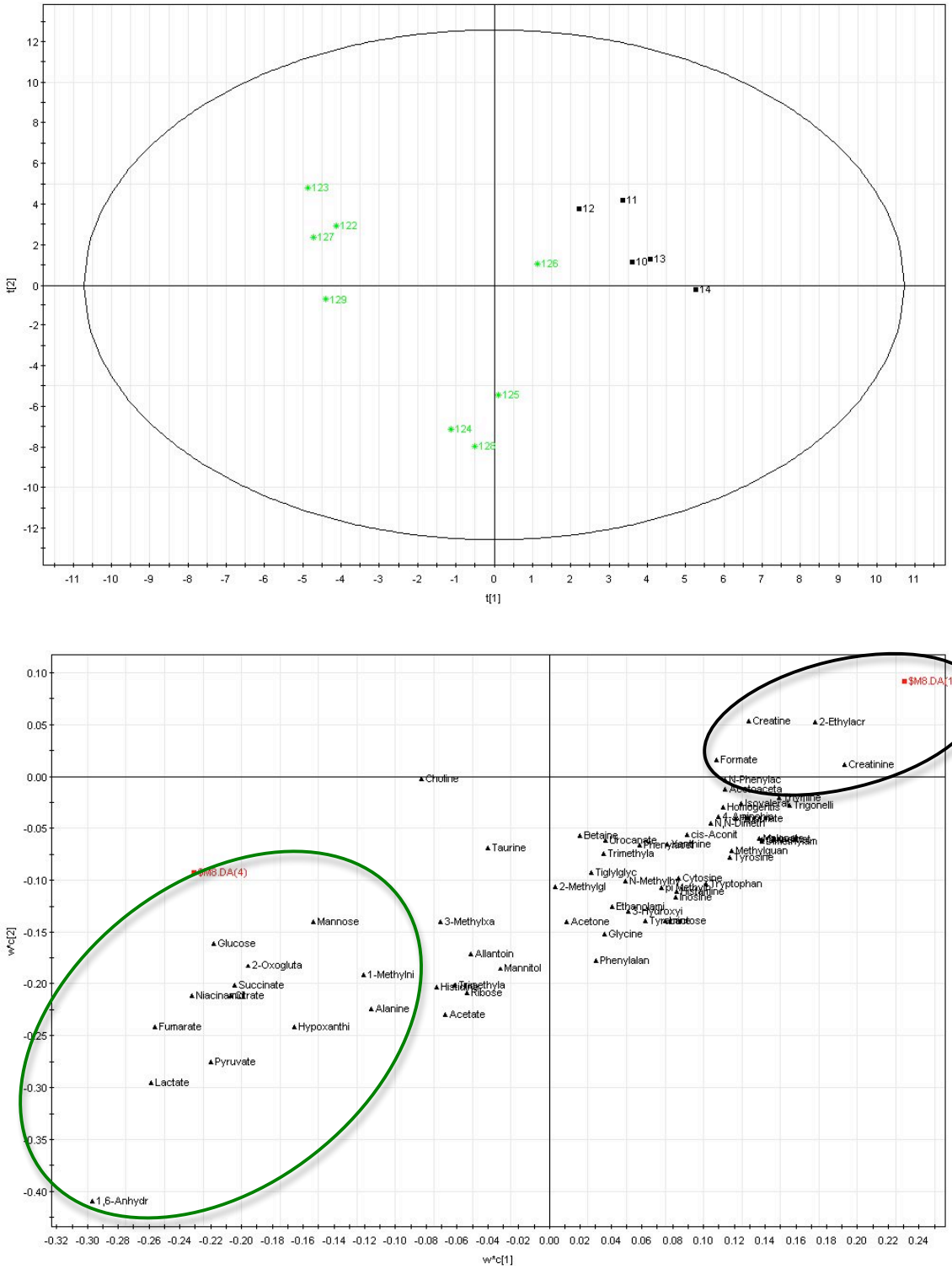

Model I: PLS-DA model of E2 (green) and C1 (black) urine samples taken at the FR2 timepoint. Loadings associate 1,6-Anhydro β-D-glucose, hypoxanthine, niacinamide, 1-methylnicotinamide, and respiratory metabolites with the E2 FR2 timepoints. C1 urine samples at FR2 are associated with creatine, creatinine,

formate, and 2-ethylacrylate.

Model J: E2 vs. C1

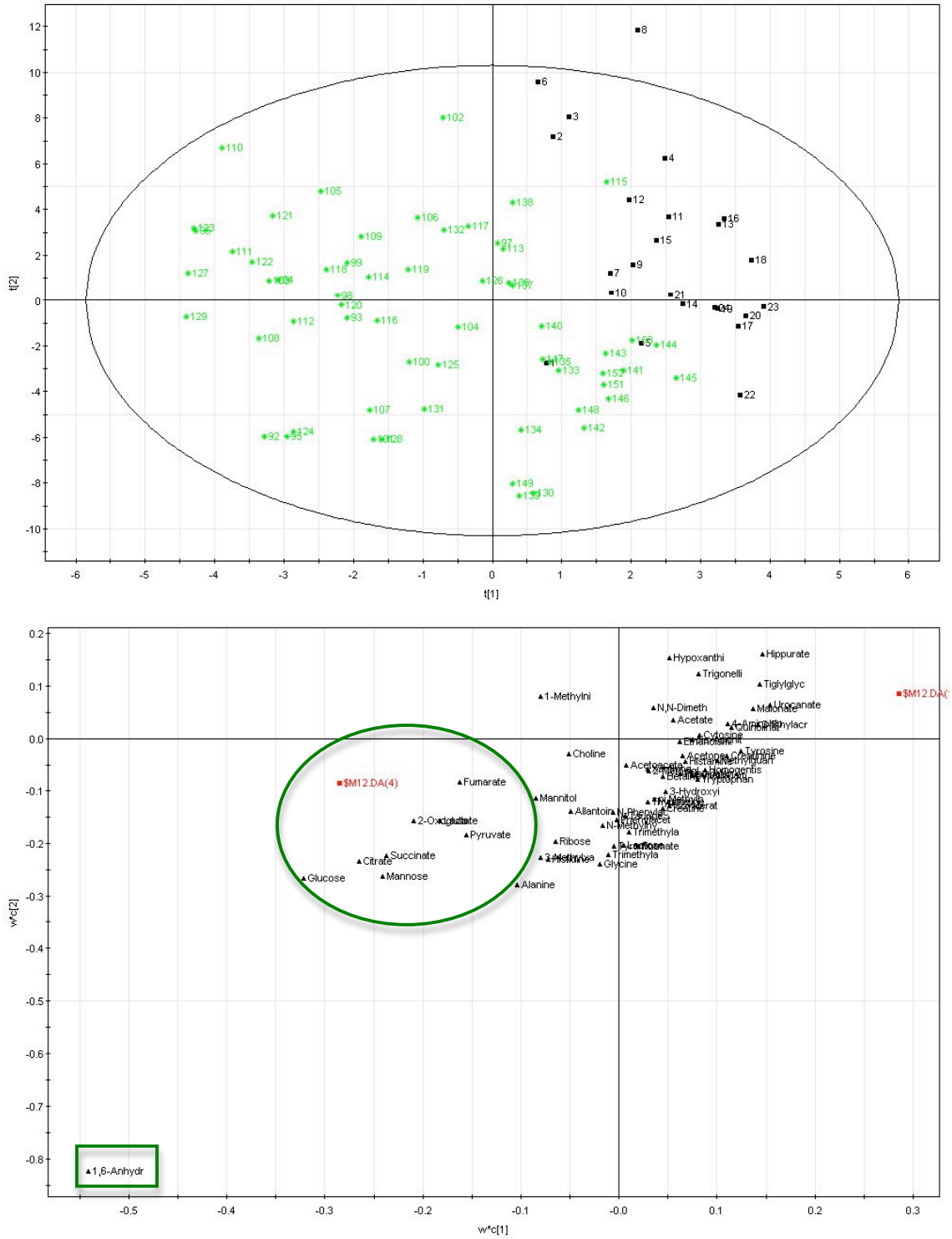

Model J: PLS-DA model of E2 (green) and C1 (black). According to the mixed models result in Chapter 6, the metabolite 1,6-Anhydro β-D-glucose (boxed in green) is the primary driver of separation between groups; this metabolite was present in E2 animals in much higher concentrations than in other animals. This is evidenced by the large negative loading shown in the figure above. It should also be noted that

metabolites related to respiration (circled in green) are more closely related to E2 urine samples than to C1 urine samples. Mannose, a metabolite related to inflammation in the lungs, is also identified here.

Model K: E1 B vs. E2 B

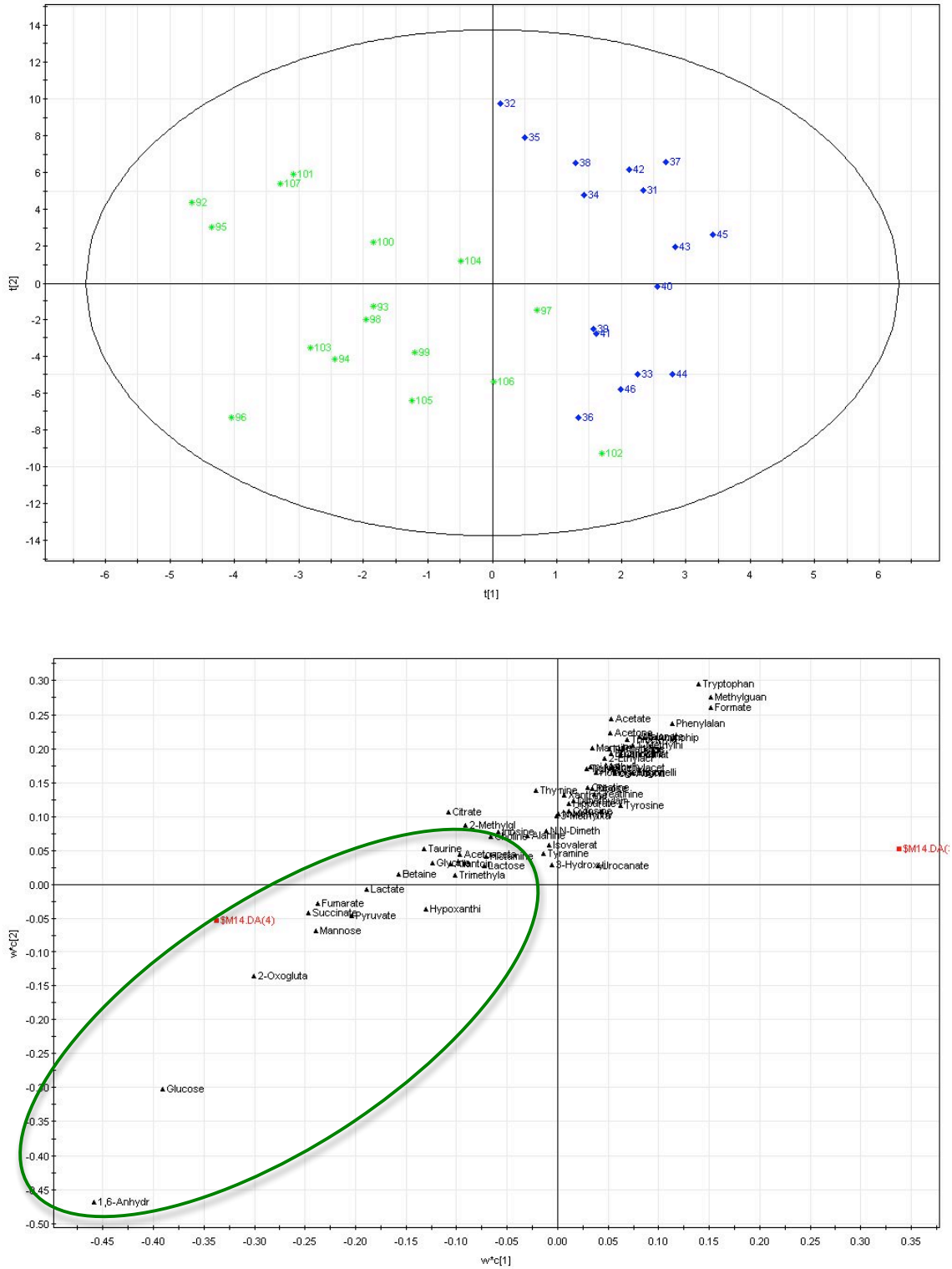

Model K: PLS-DA model of E1 baseline urine samples (blue) and E2 urine samples at baseline (green). No metabolites are clearly associated with E1 samples, though E2 samples are associated with 1,6-Anhydro

β-D-glucose, and metabolites associated with respiration. These samples are, to a lesser extent, also associated with taurine, mannose, acetoacetate, glycine, betaine, trimethylamine N-oxide, allantoin, acetoacetate, and lactose.

Model L: E1 vs. E2

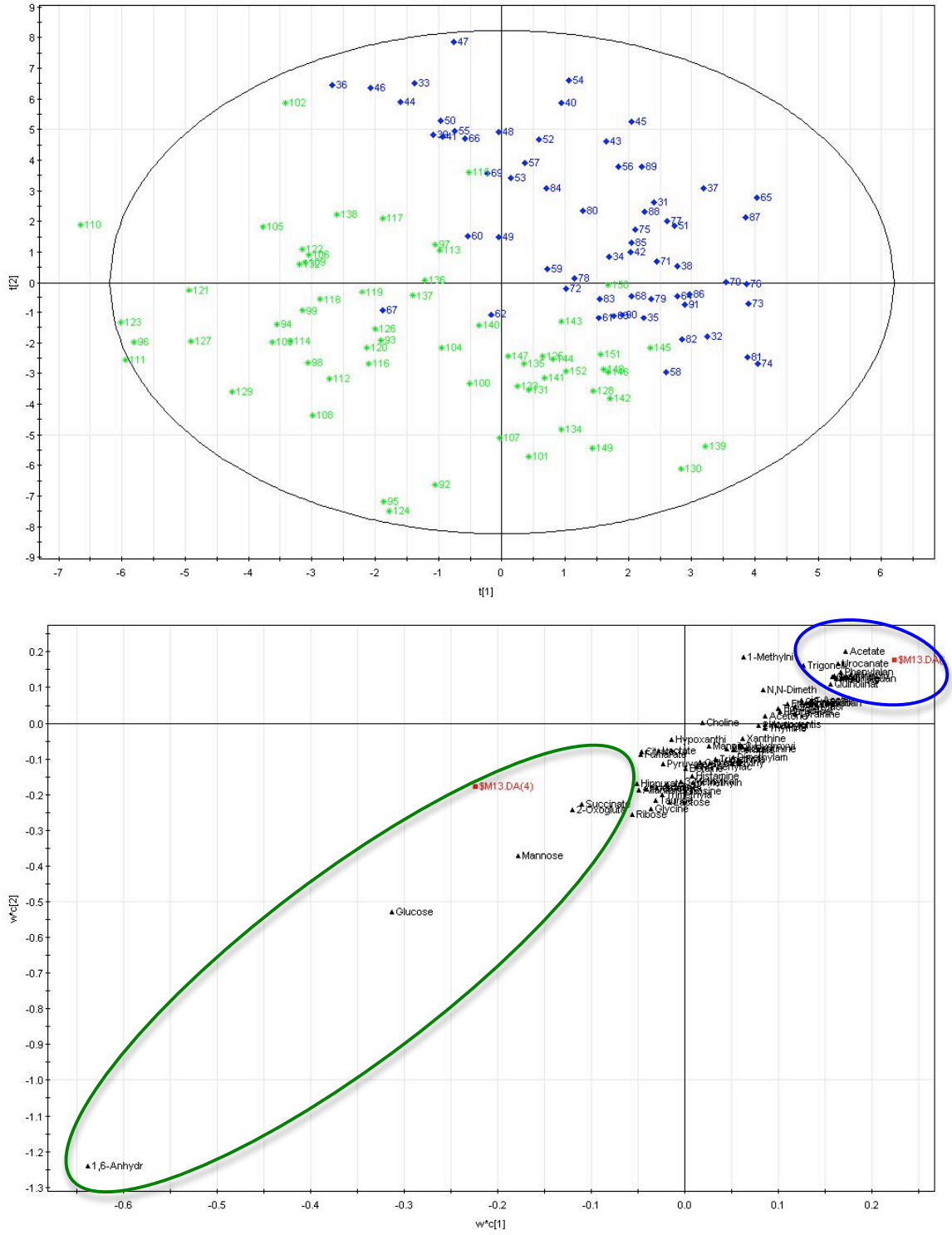

Model L: PLS-DA model of E1 urine samples vs. E2 urine samples. Again, 1,6-Anhydro β-D-glucose drives separation between the two groups. Mannose, glucose, succinate, and 2-oxoglutarate are also associated with E2 animals.

Model M: E1 FR2 vs. C1 FR2

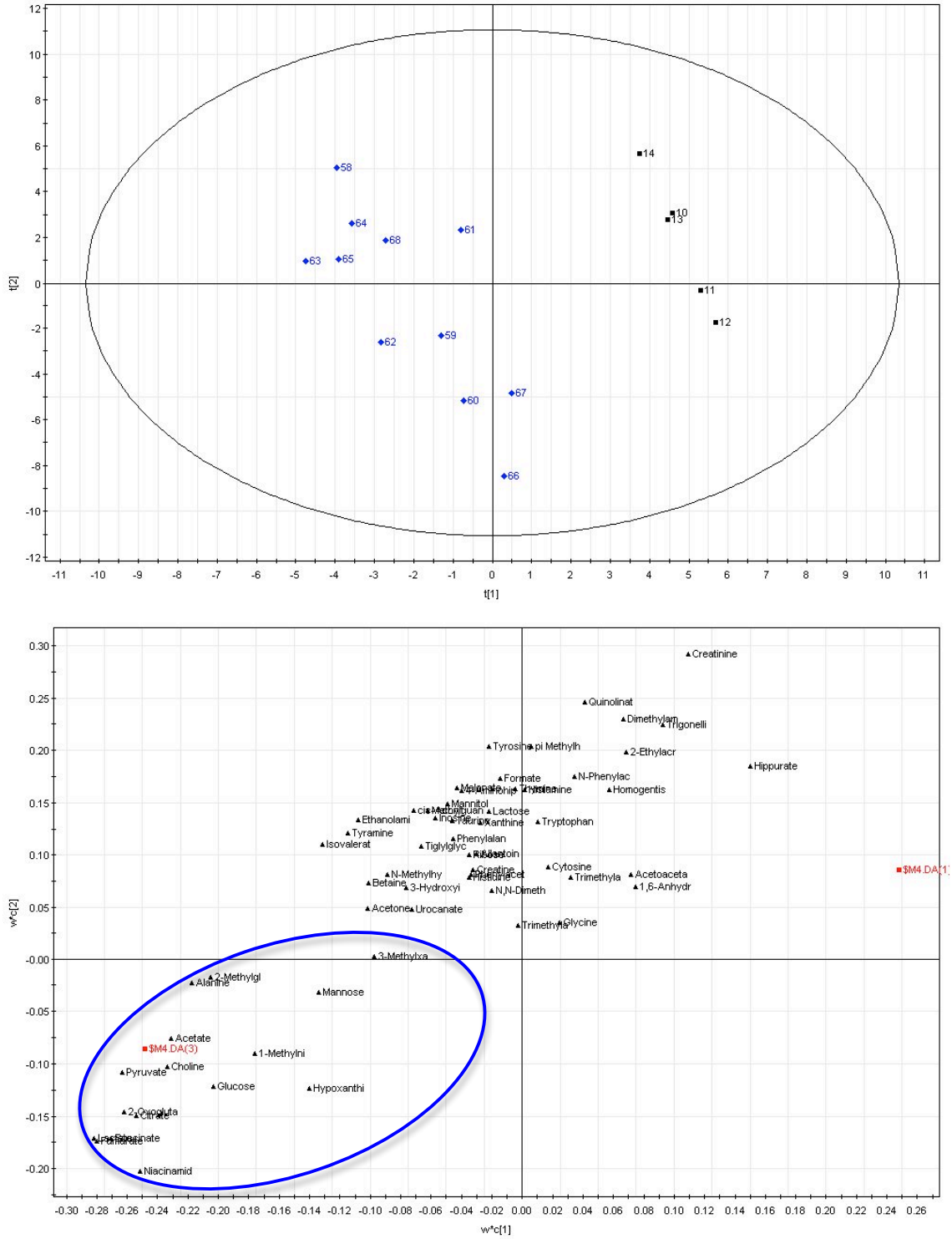

Model M: PLS-DA model of E1 urine samples at FR2 vs. C1 urine samples at FR2. This is the only timepoint at which the E1 and C1 urinary metabolomes differ. The respiratory metabolites, choline, hypoxanthine, 1-methylnicotinamide, niacinamide, mannose, alanine, 3-methylxanthine, and 2-

methylglutarate are associated with E1 urine samples at FR2. No metabolites are strongly associated with C1 urine samples at FR2.

Model N: Baseline vs. FR2

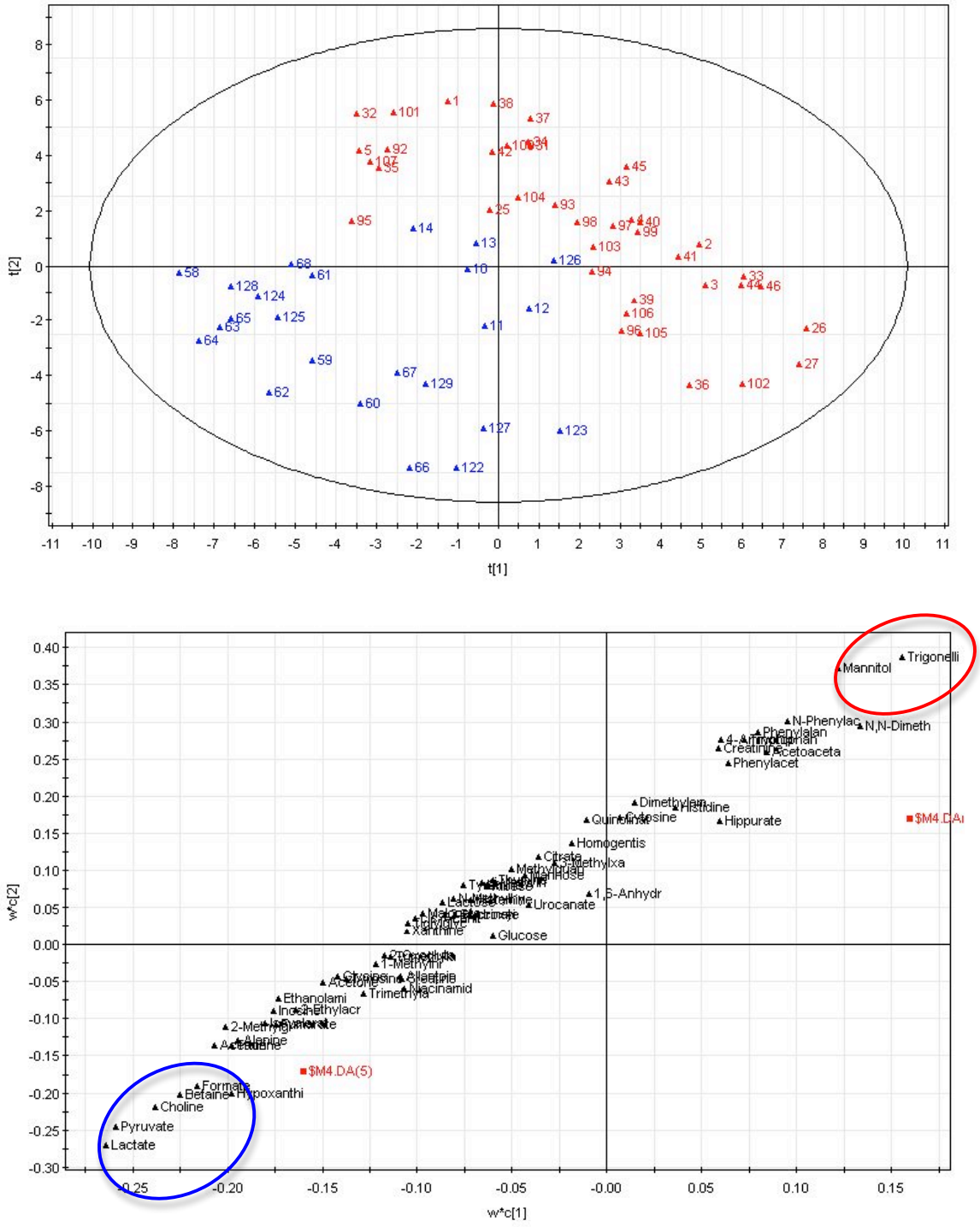

Model N: PLS-DA model of Baseline (red) and FR2 (blue). Loadings associate metabolites with the observation of experimental timepoint. Metabolites associated with baseline are ringed in red and those associated with FR2 are ringed in blue. Metabolites grouped with FR2 are associated with anaerobic respiration (lactate, pyruvate), ischemia/reperfusion injury (hypoxanthine), cellular damage (choline), osmotic stress (betaine) and catabolism (formate).

Model O: E1 FR8 vs. E2 FR8

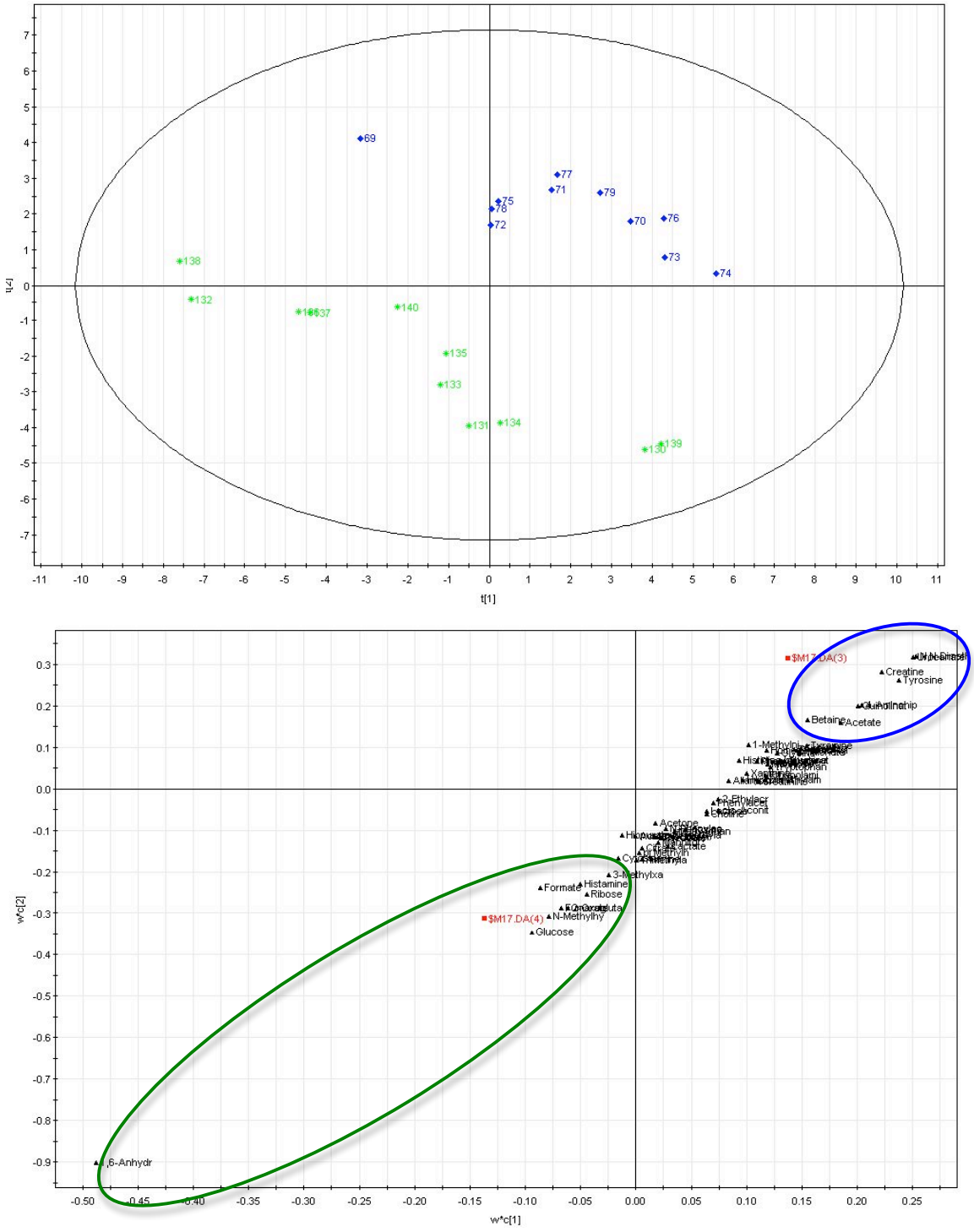

Model O: PLS-DA model of E1 FR8 urine samples (blue) and E2 FR8 urine samples (green). Again, separation is driven by the increased presence of the metabolite 1,6-Anhydro β-D-glucose in the urine of E2 animals. Metabolites associated with E1 urine samples at FR8 are betaine, acetate, quinolinate, 4-aminohippurate, creatine, tyrosine, N,N-dimethylglycine, and urocanate.

Model P: FR2/FR20

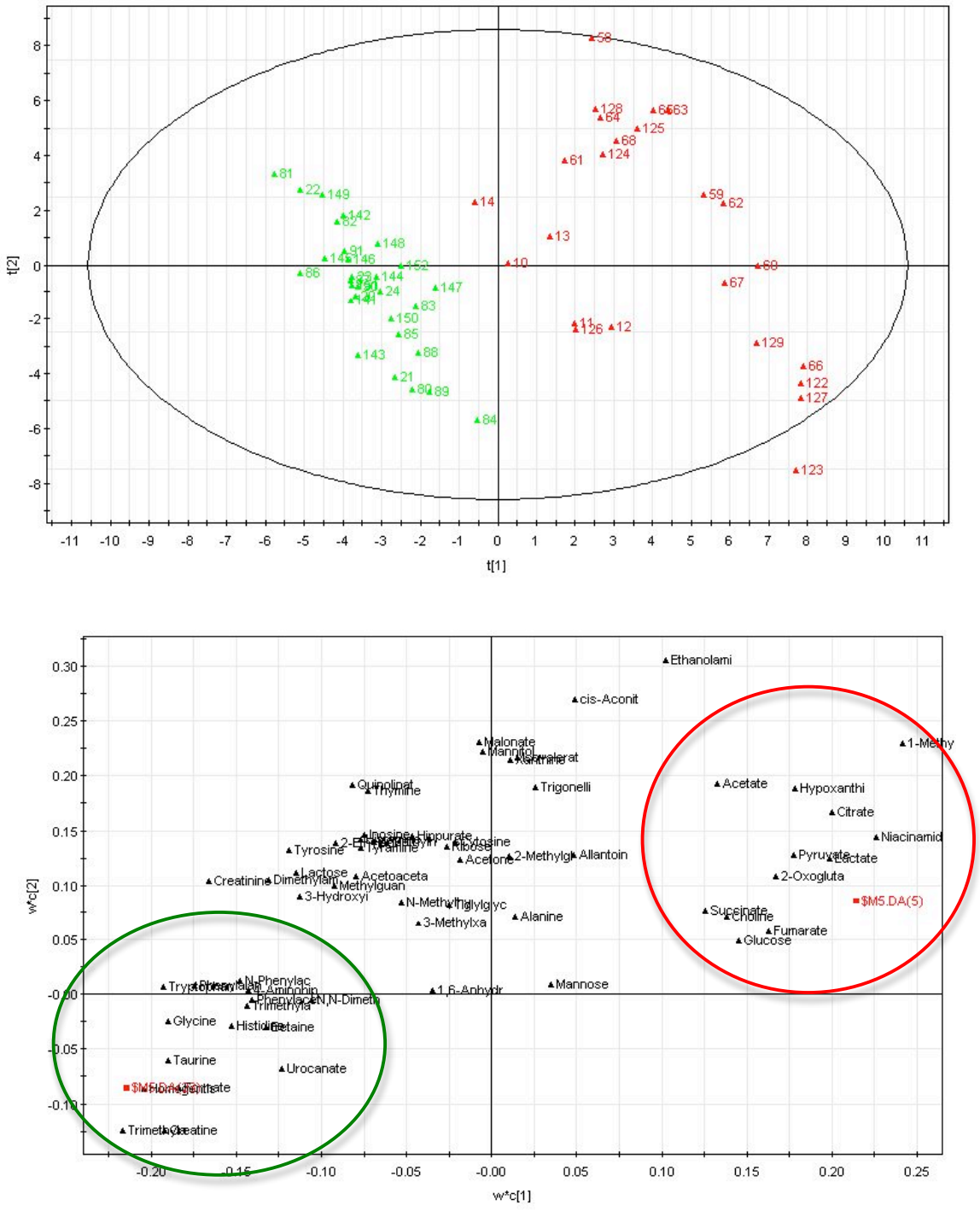

Model P: PLS-DA model of FR2 (red) and FR20 (green) timepoints. Metabolites associated with FR2 are largely associated with respiration, ischemia/reperfusion injury, and cell damage. Metabolites associated with FR20 are N-phenylacetylglycine, phenylalanine, tryptophan, 4-aminohippurate, phenylacetylglycine,

N,N-dimethylglycine, trimethylamine, glycine, histidine, betaine, taurine, urocanate, homogentisate, formate, trimethylamine N-oxide, and creatine.

Model Q: E1 B vs E1 FR2 vs E1 FR20

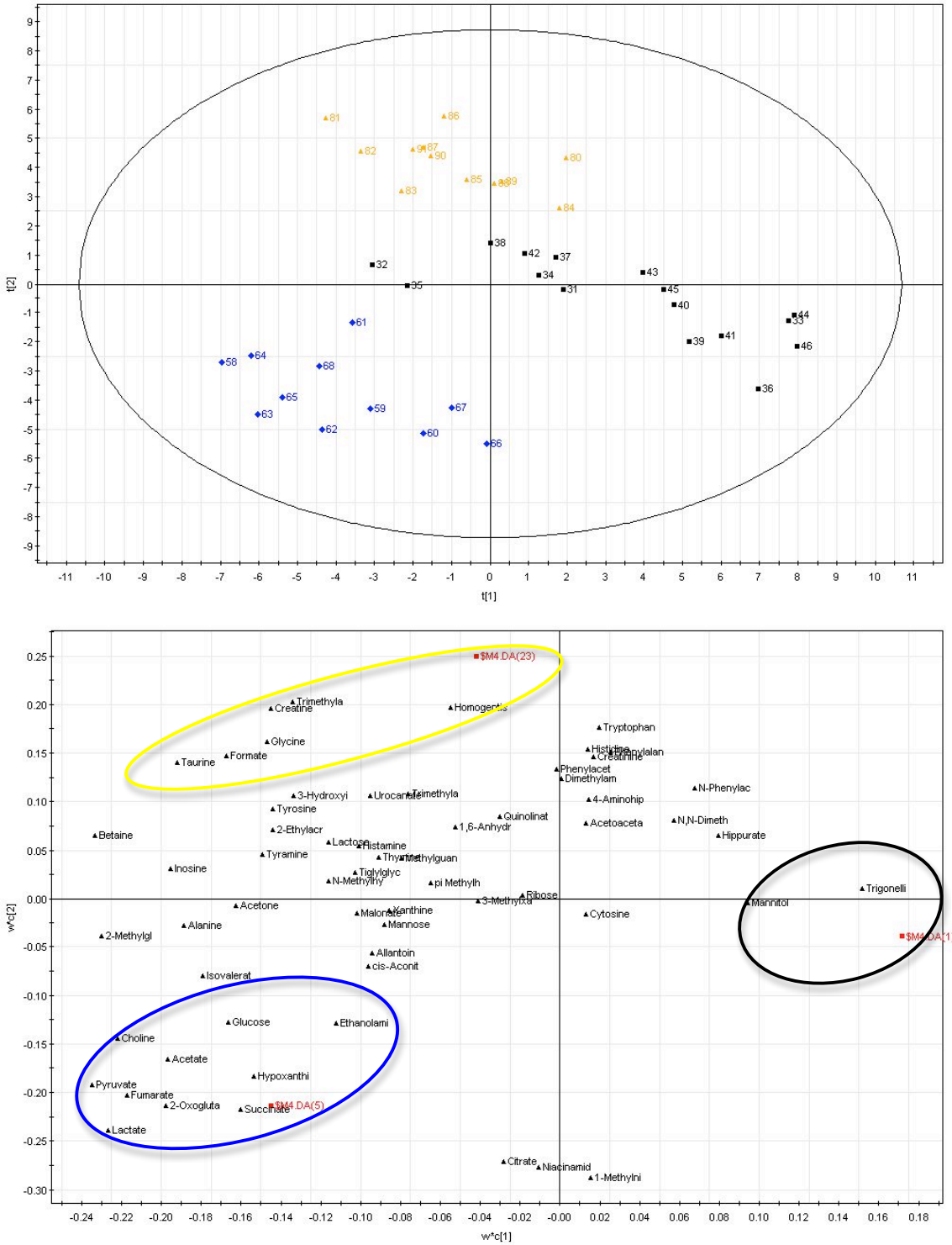

Model Q: PLS-DA model of E1 urine samples at baseline (black), FR2 (blue), and FR20 (green). The high Q^2 of this model indicates the predictive value of urine with respect to phase-of-care. Exogenous

metabolite mannitol and trigonelline are associated with baseline samples. The respiratory metabolites, choline, ethanolamine (cell damage), and hypoxanthine (I/R injury) are associated with FR2, and markers of injury and catabolism are associated with FR20.

Appendix C: Plots of important urinary metabolites

Boxplots of key urinary metabolites identified by PLS-DA analysis
The metabolites most commonly linked with an observable such as experimental timepoint or experimental group were identified in Table 6.7, along with known physiological properties. Boxplots of each of these metabolites are presented in this appendix, according to experimental group and experimental timepoint. The box covers the first (Q1) and third (Q3) quartile of the data. The line in the box represents the median value. The whiskers extend to ± 1.5*IQR, where IQR=Q3-Q1. Outliers are shown as points.

These boxplots were made with the urine output-normalized, log-transformed data with outliers removed. In the legends, Group 1=C1, Group 2=C2, Group 3=E1, and Group 4=E2.

Scatterplots of the metabolites associated with FR20 (creatine, formate, glycine, taurine, and trimethylamine N-oxide) are presented after the boxplots. The plots include data from a previous experiment done in the Beilman lab. Two animals from a previous study were minimally instrumented, sedated, and monitored. No laparotomy or splenectomy was performed on these animals. The data illustrates that little difference is seen between the five groups at FR20. This indicates that the observed levels of the metabolites are independent of trauma or hemorrhage. More than two animals are required to substantiate this claim.

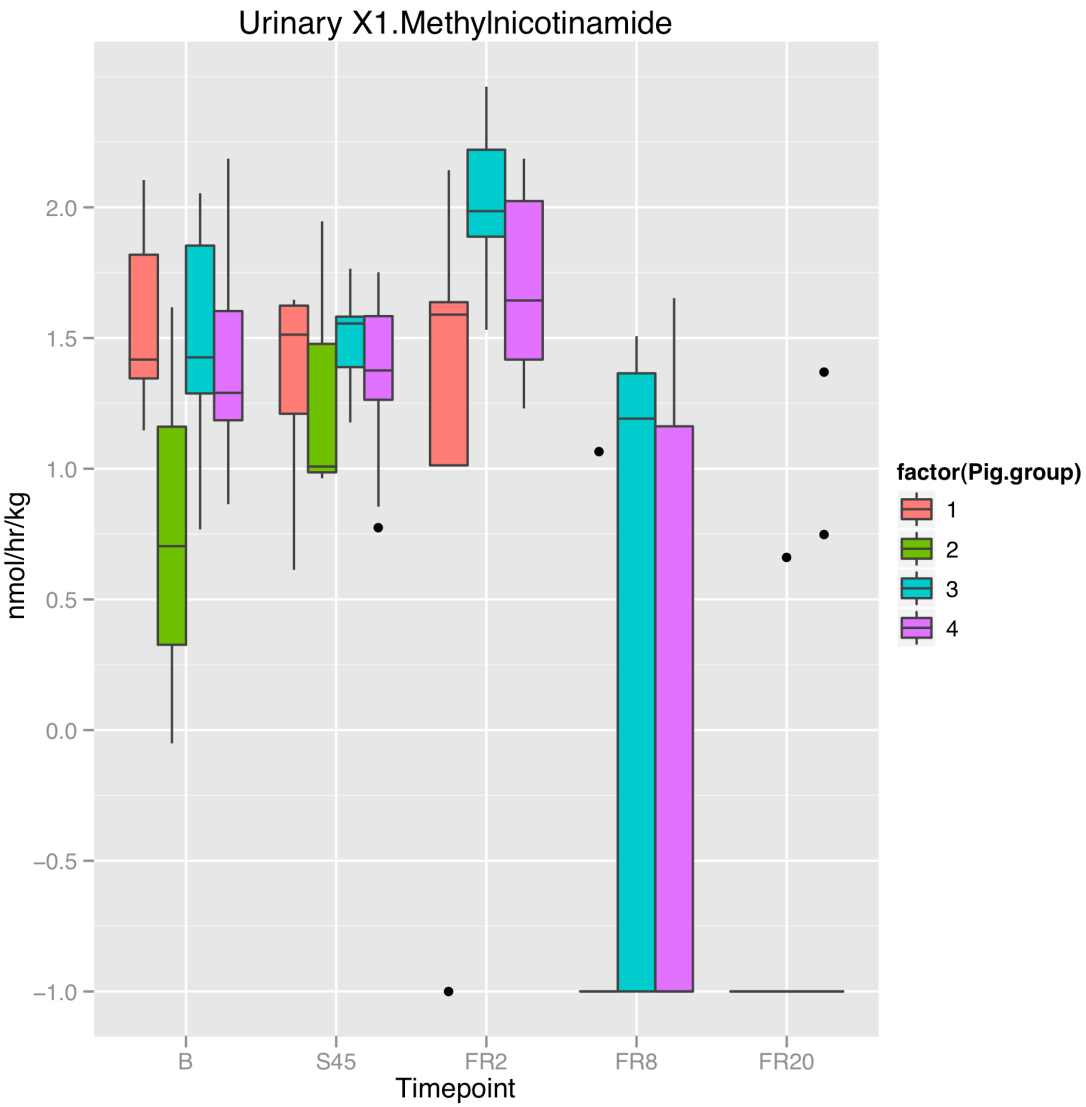
Urinary X1.MethylNicotinamide
nmol/hr/kg
2.0
1.5
1.0
0.5
0.0
−0.5
−1.0
B
S45
FR2
FR8
FR20
Timepoint
factor(Pig.group)
1
2
3
4

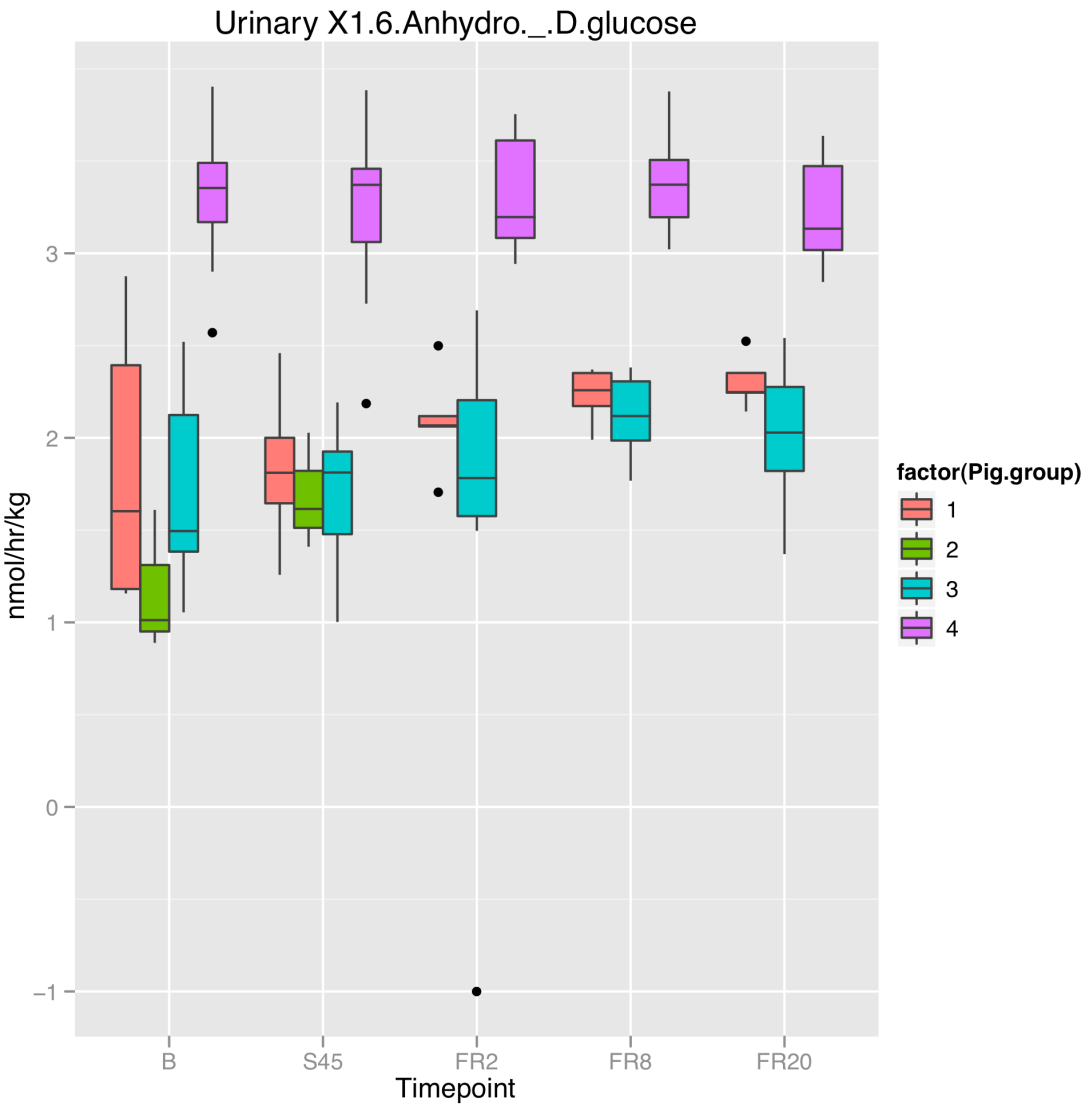
Urinary X1.6.Anhydro._.D.glucose
nmol/hr/kg
3
2
1
0
−1
B
S45
FR2
FR8
FR20
Timepoint
factor(Pig.group)
1
2
3
4

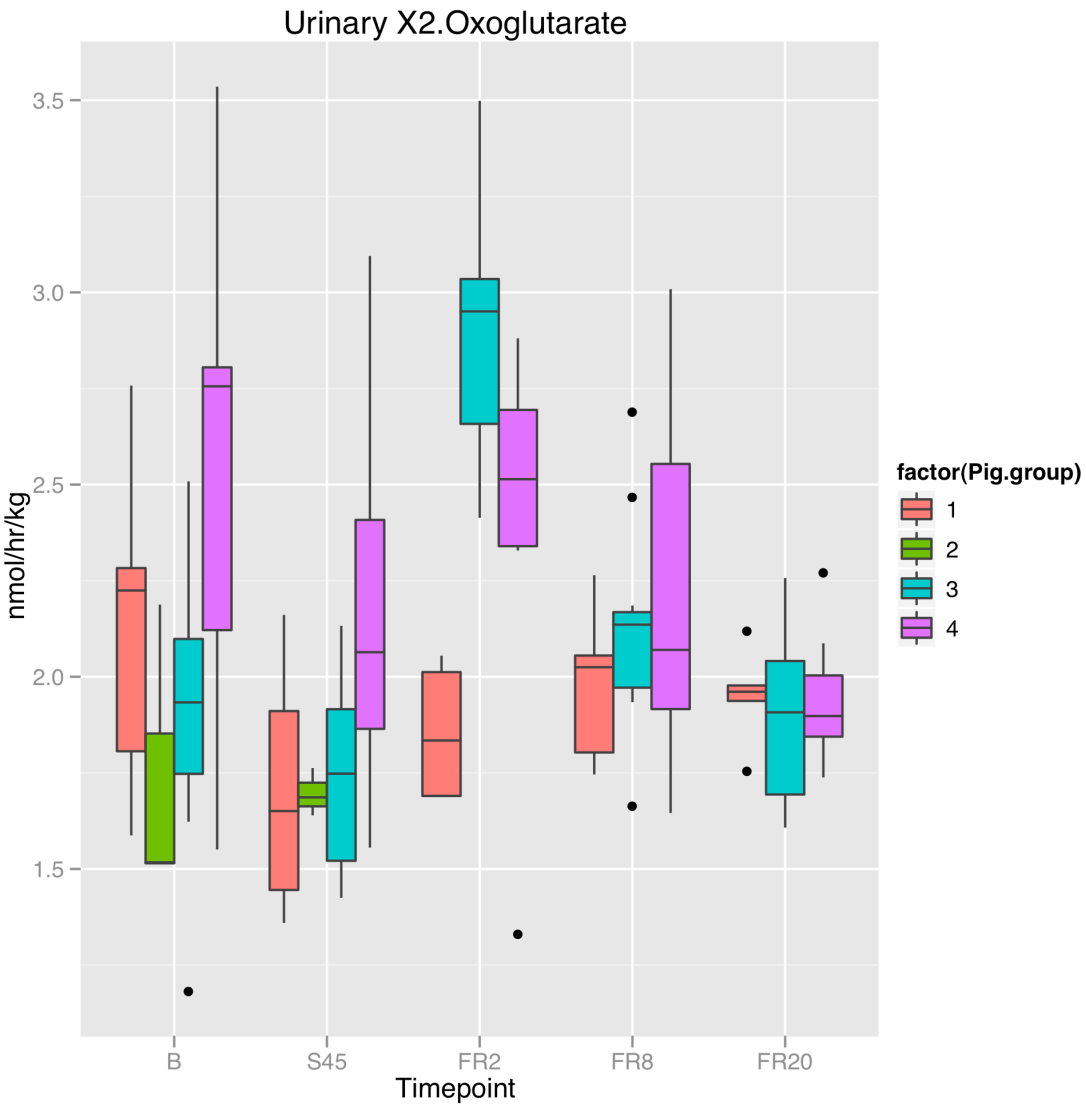
Urinary X2.Oxoglutarate
nmol/hr/kg
3.5
3.0
2.5
2.0
1.5
B
S45
FR2
FR8
FR20
Timepoint
factor(Pig.group)
1
2
3
4

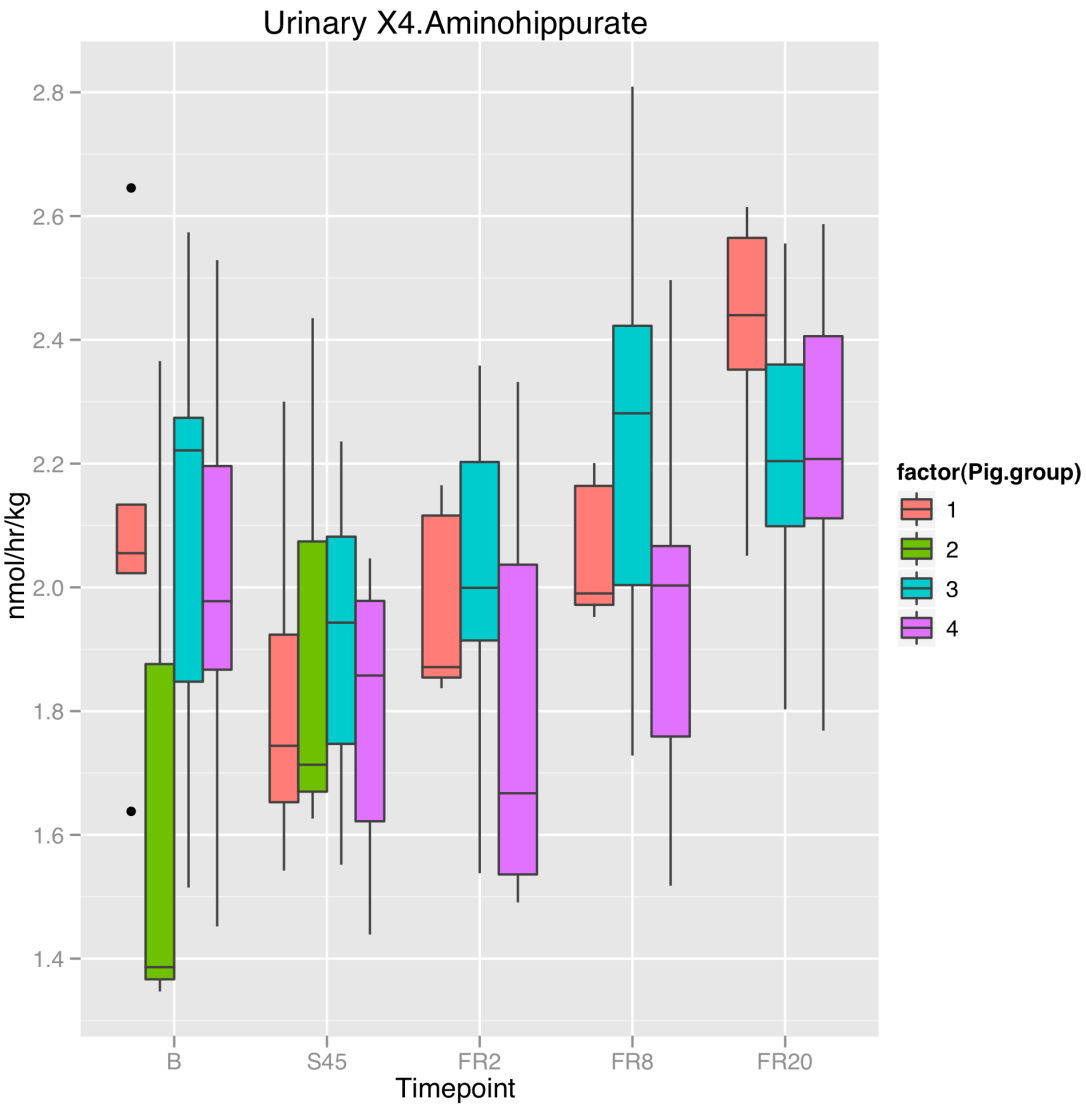
Urinary X4.Aminohippurate
nmol/hr/kg
2.8
2.6
2.4
2.2
2.0
1.8
1.6
1.4
B
S45
FR2
FR8
FR20
Timepoint
factor(Pig.group)
1
2
3
4

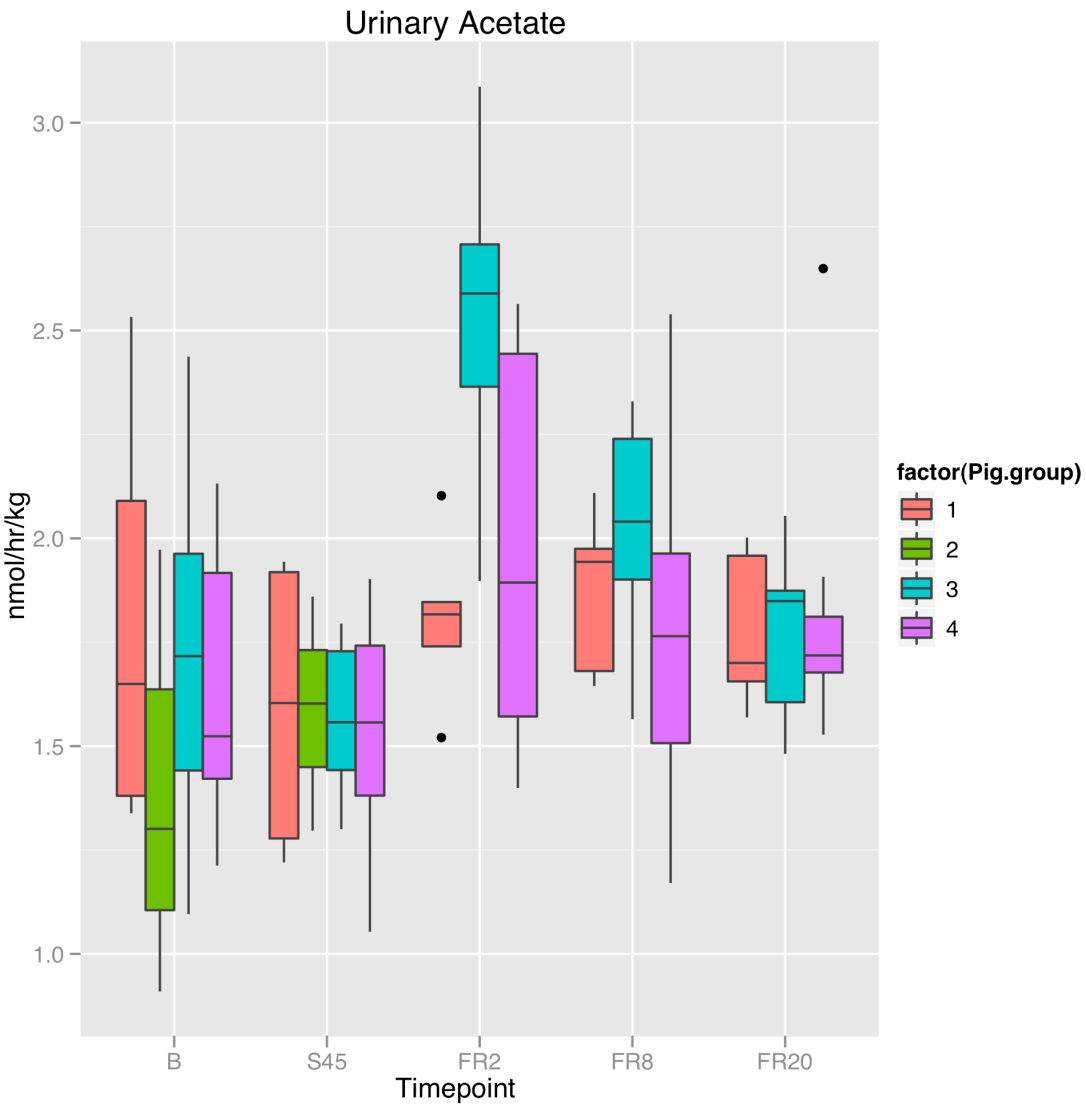
Urinary Acetate
3.0
2.5
2.0
1.5
1.0
nmol/hr/kg
B
S45
FR2
FR8
FR20
Timepoint
factor(Pig.group)
1
2
3
4

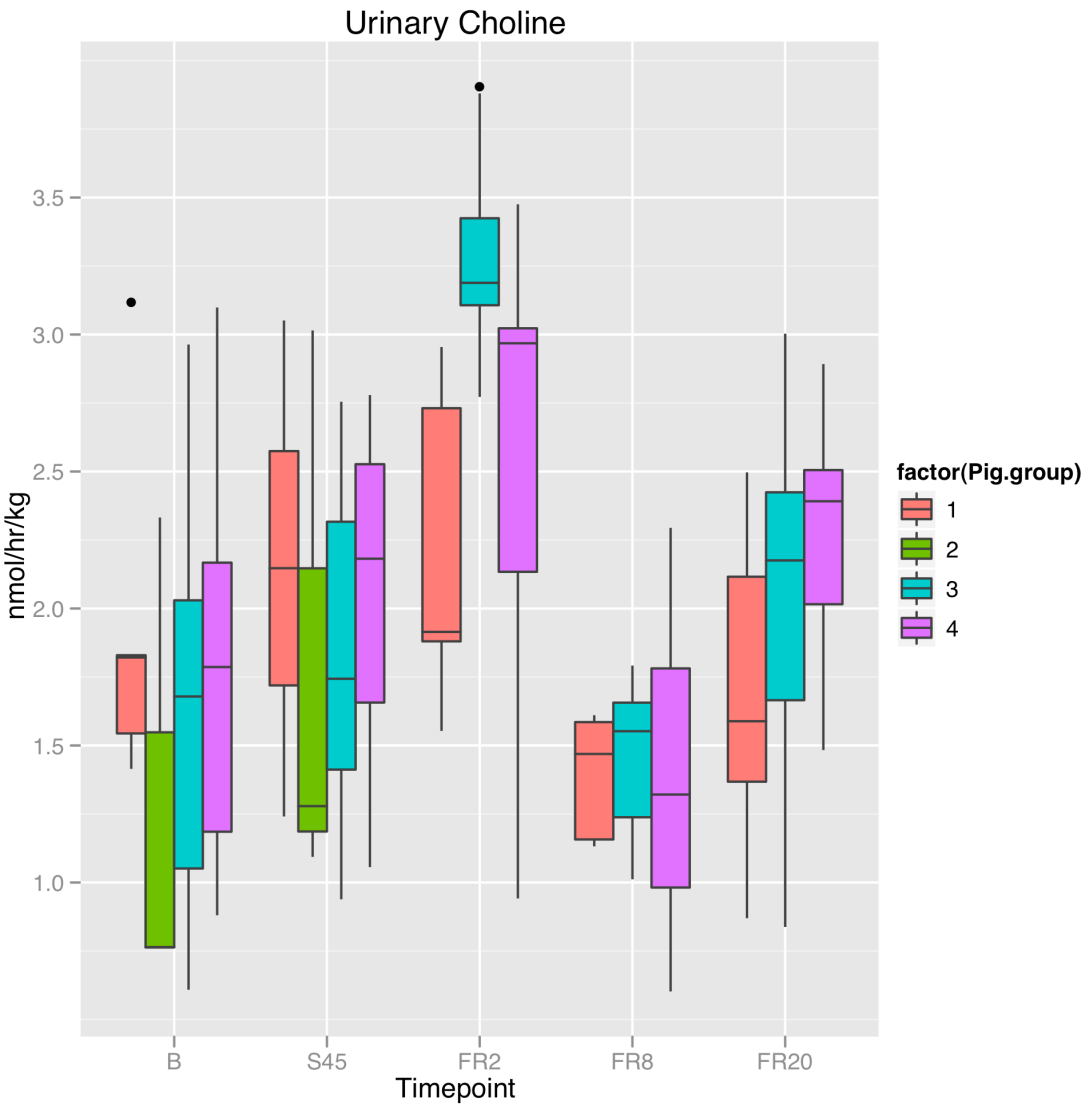
Urinary Choline
nmol/hr/kg
3.5
3.0
2.5
2.0
1.5
1.0
B
S45
FR2
FR8
FR20
Timepoint
factor(Pig.group)
1
2
3
4

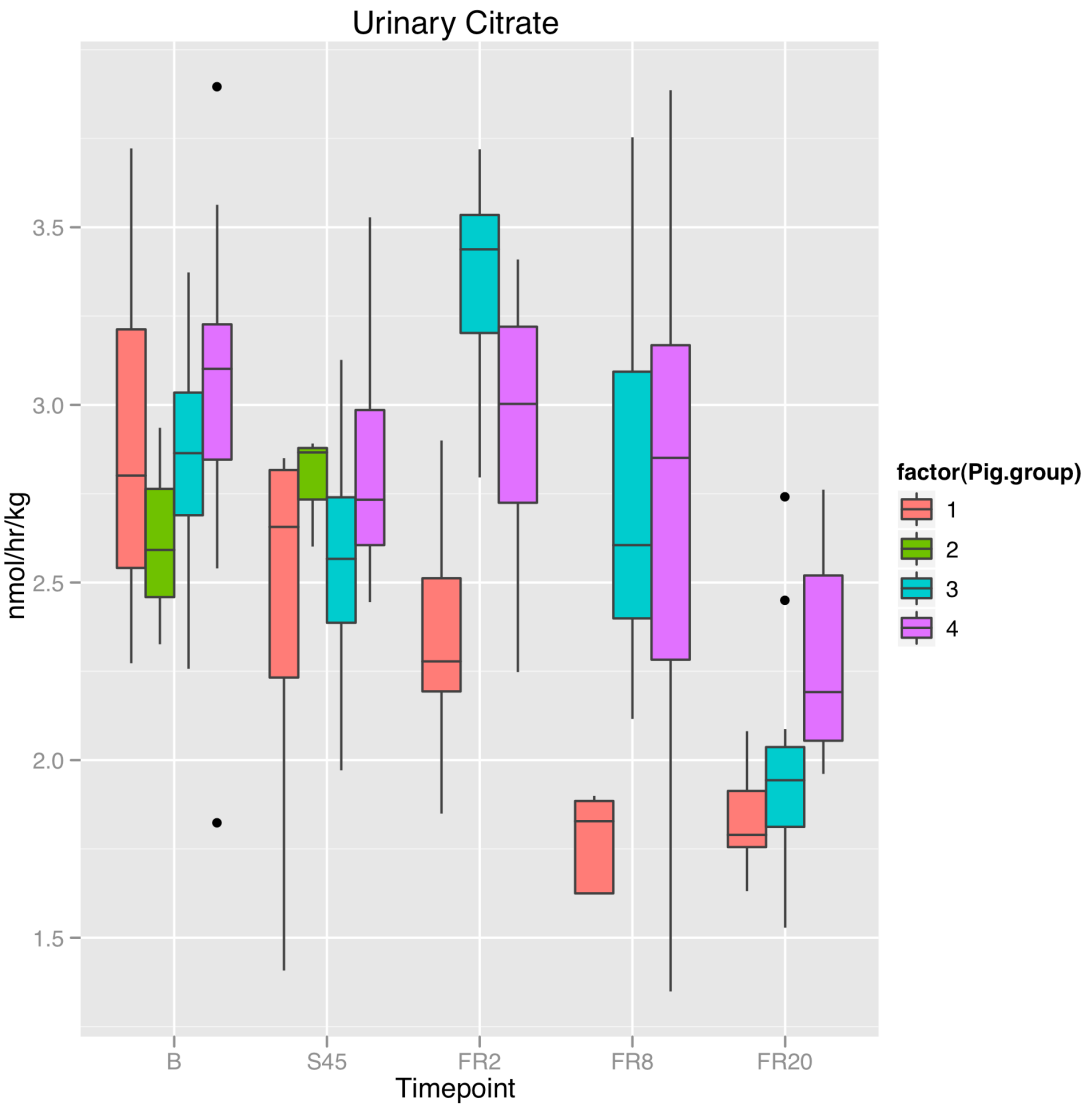
Urinary Citrate
nmol/hr/kg
3.5
3.0
2.5
2.0
1.5
B
S45
FR2
FR8
FR20
Timepoint
factor(Pig.group)
1
2
3
4

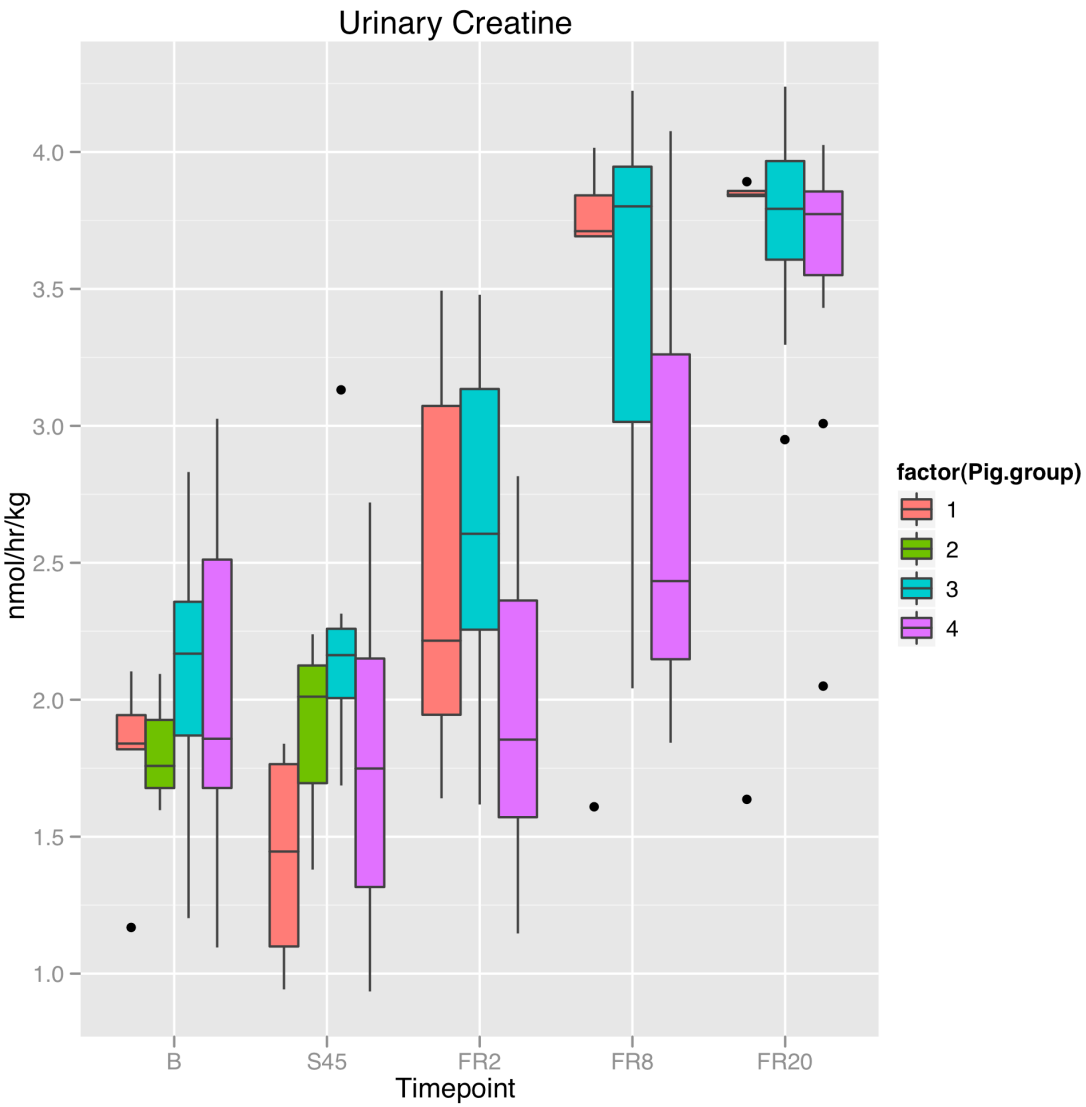
Urinary Creatine
nmol/hr/kg
4.0
3.5
3.0
2.5
2.0
1.5
1.0
B
S45
FR2
FR8
FR20
Timepoint
factor(Pig.group)
1
2
3
4

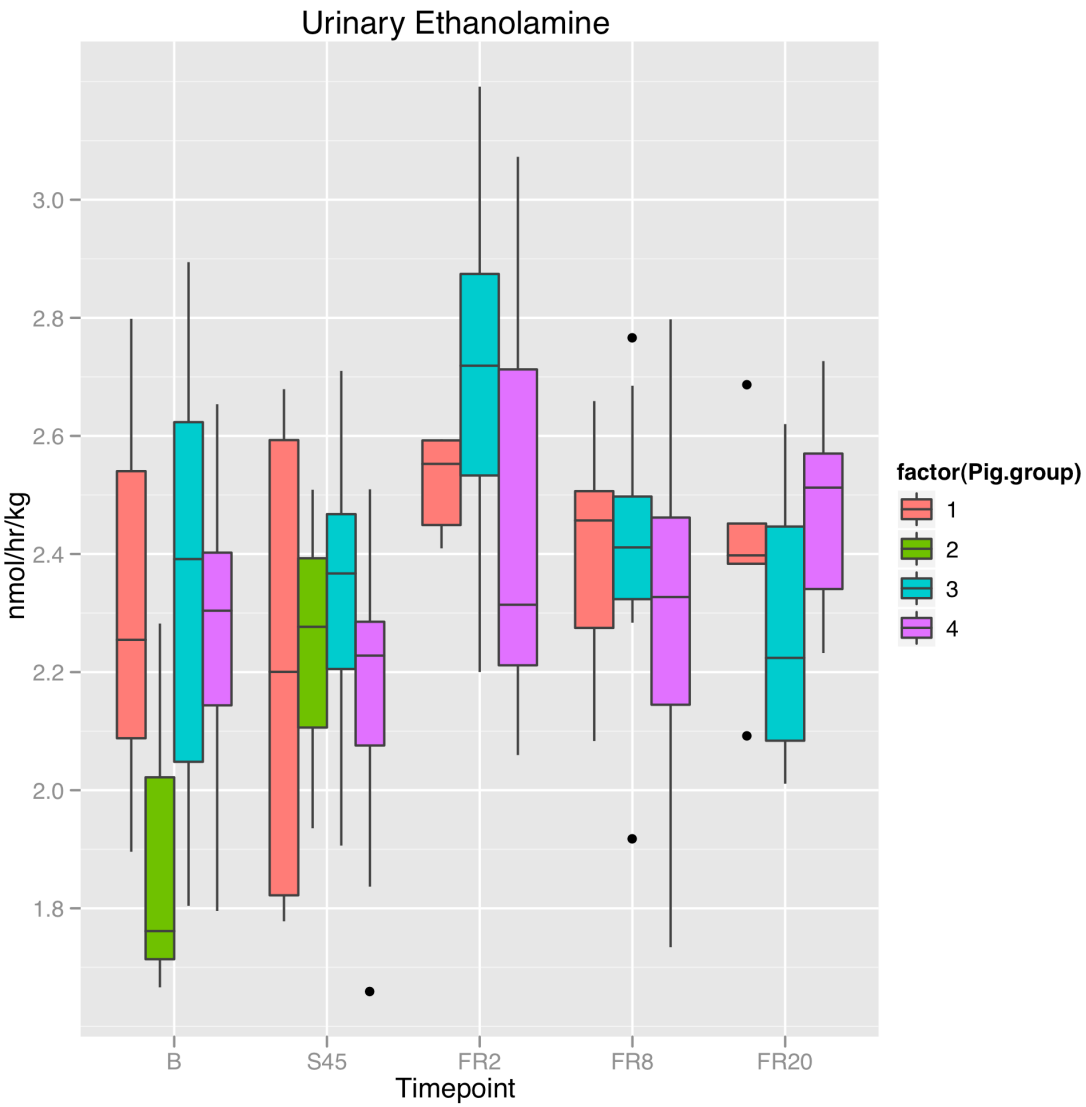
Urinary Ethanolamine
nmol/hr/kg
3.0
2.8
2.6
2.4
2.2
2.0
1.8
B
S45
FR2
FR8
FR20
Timepoint
factor(Pig.group)
1
2
3
4

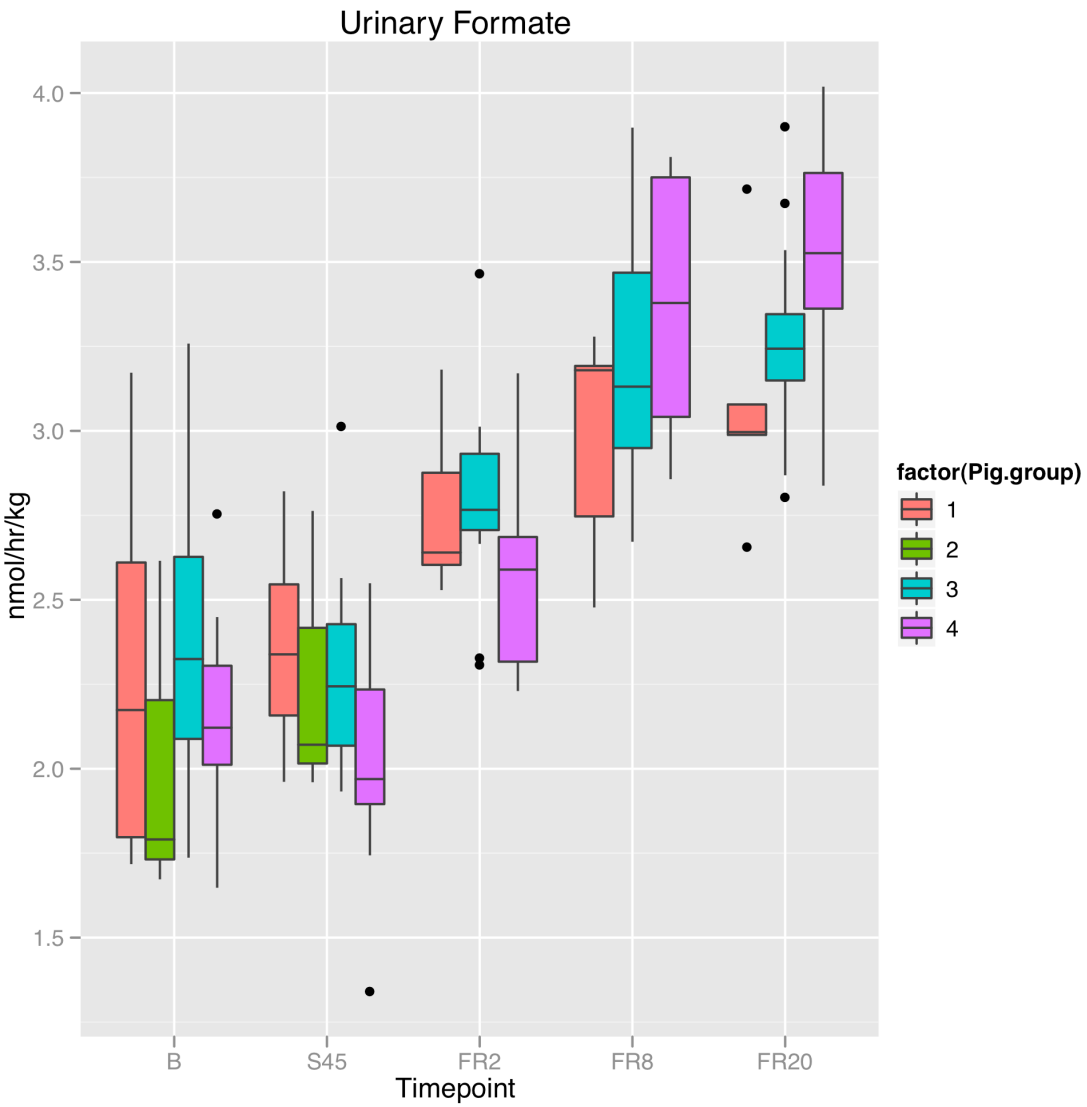
Urinary Formate
4.0
3.5
3.0
2.5
2.0
1.5
nmol/hr/kg
B
S45
FR2
FR8
FR20
Timepoint
factor(Pig.group)
1
2
3
4

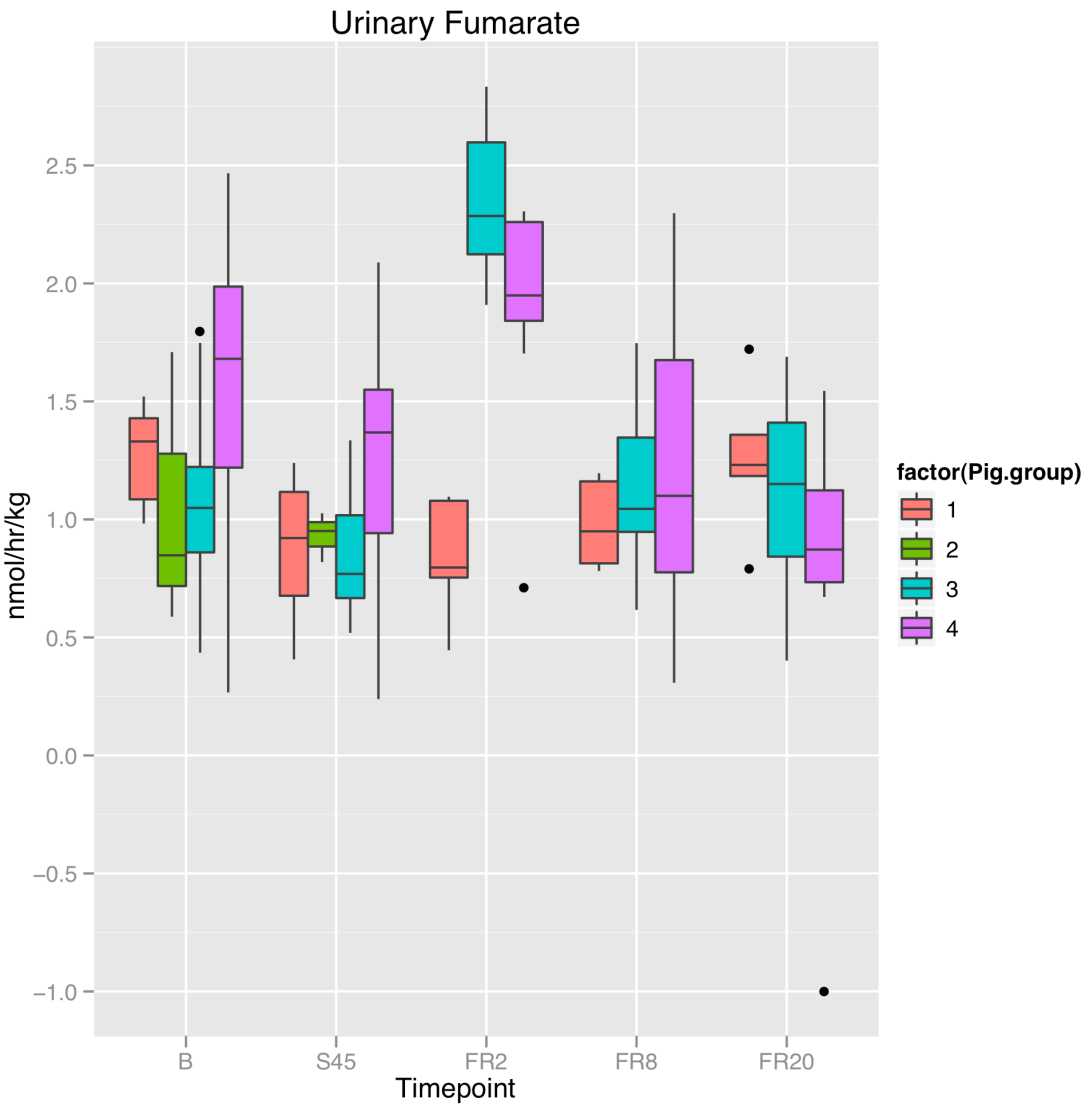
Urinary Fumarate
nmol/hr/kg
2.5
2.0
1.5
1.0
0.5
0.0
−0.5
−1.0
B
S45
FR2
FR8
FR20
Timepoint
factor(Pig.group)
1
2
3
4

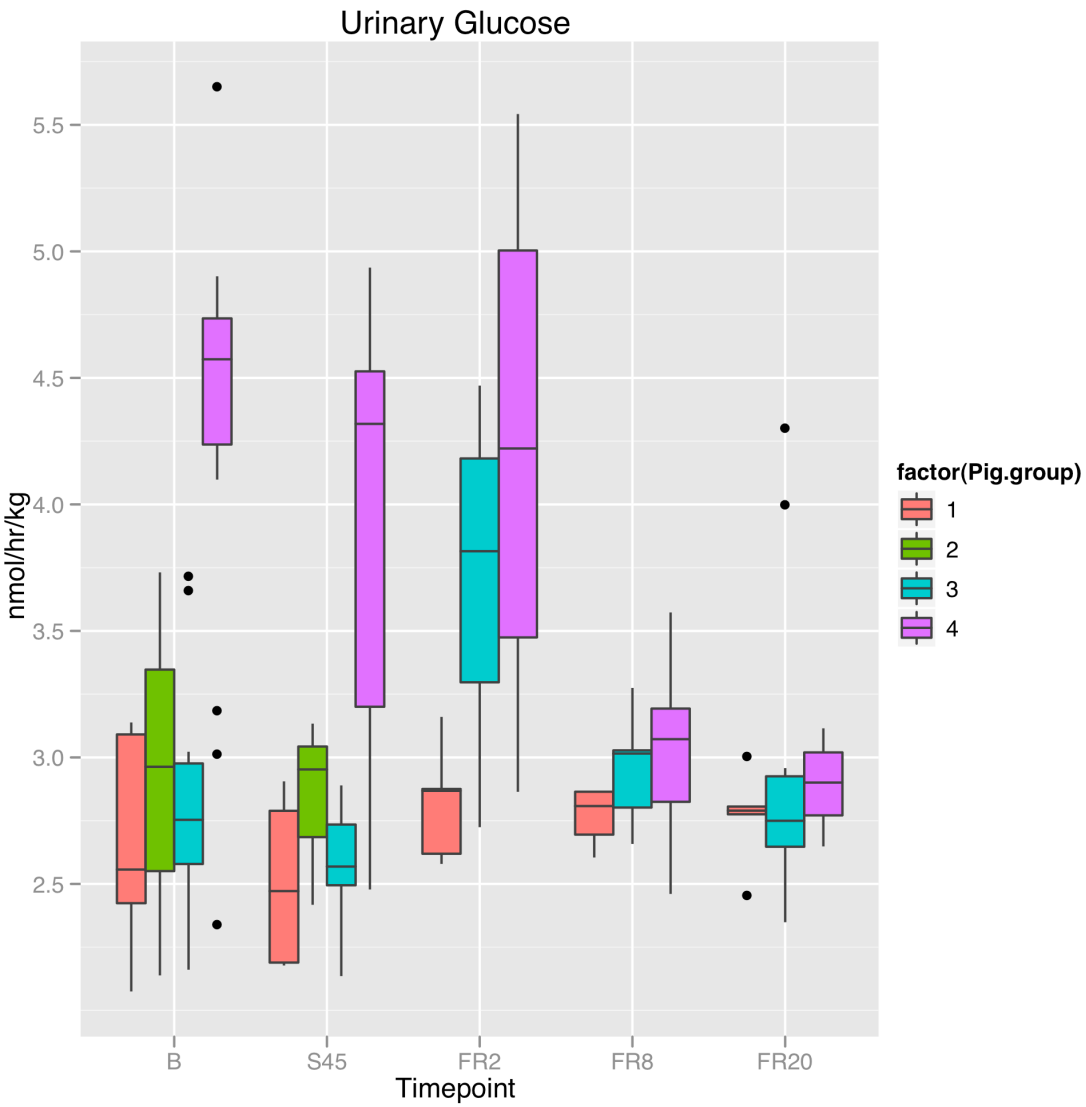
Urinary Glucose
nmol/hr/kg
5.5
5.0
4.5
4.0
3.5
3.0
2.5
B
S45
FR2
FR8
FR20
Timepoint
factor(Pig.group)
1
2
3
4

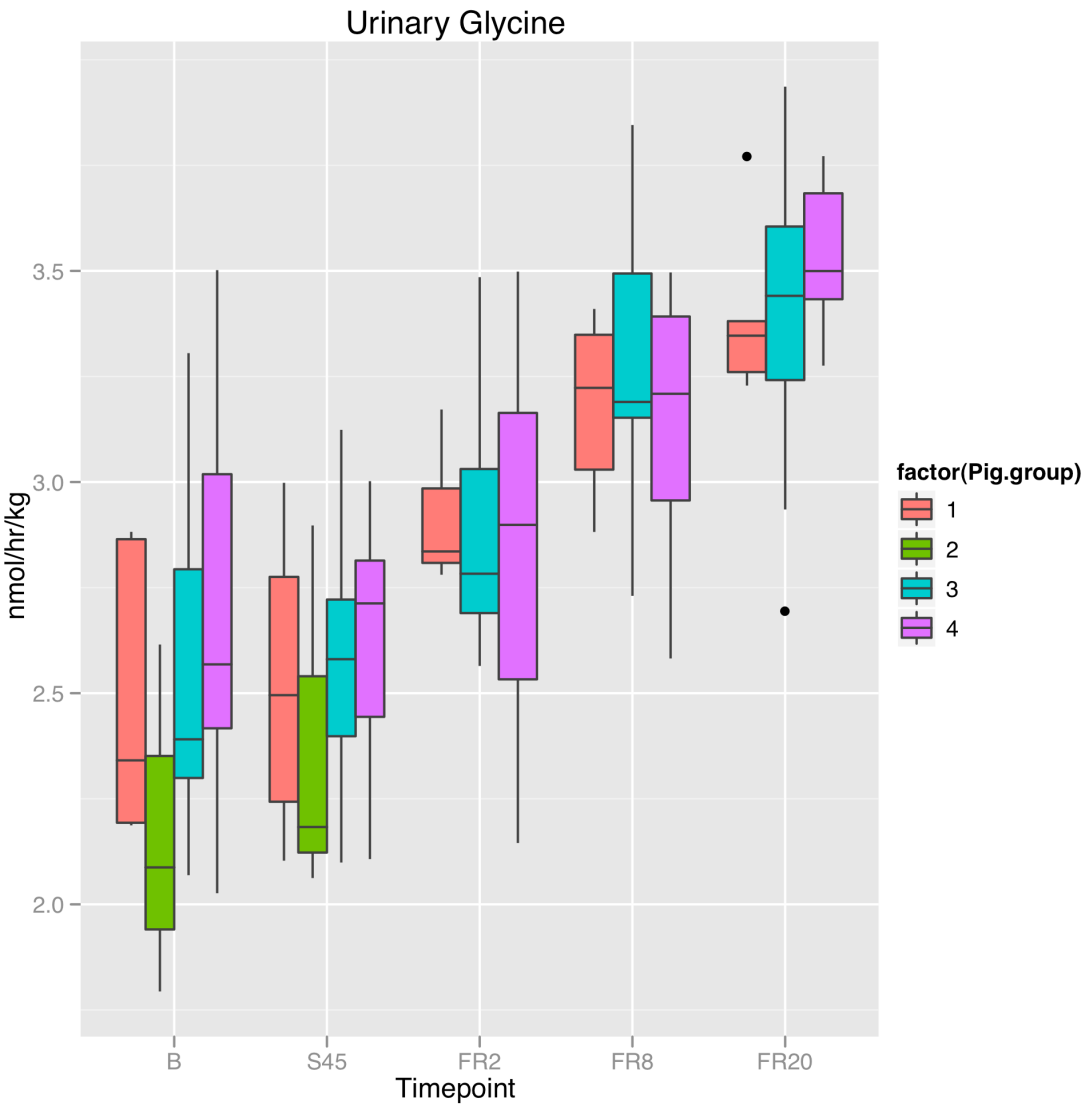
Urinary Glycine
nmol/hr/kg
3.5
3.0
2.5
2.0
B
S45
FR2
FR8
FR20
Timepoint
factor(Pig.group)
1
2
3
4

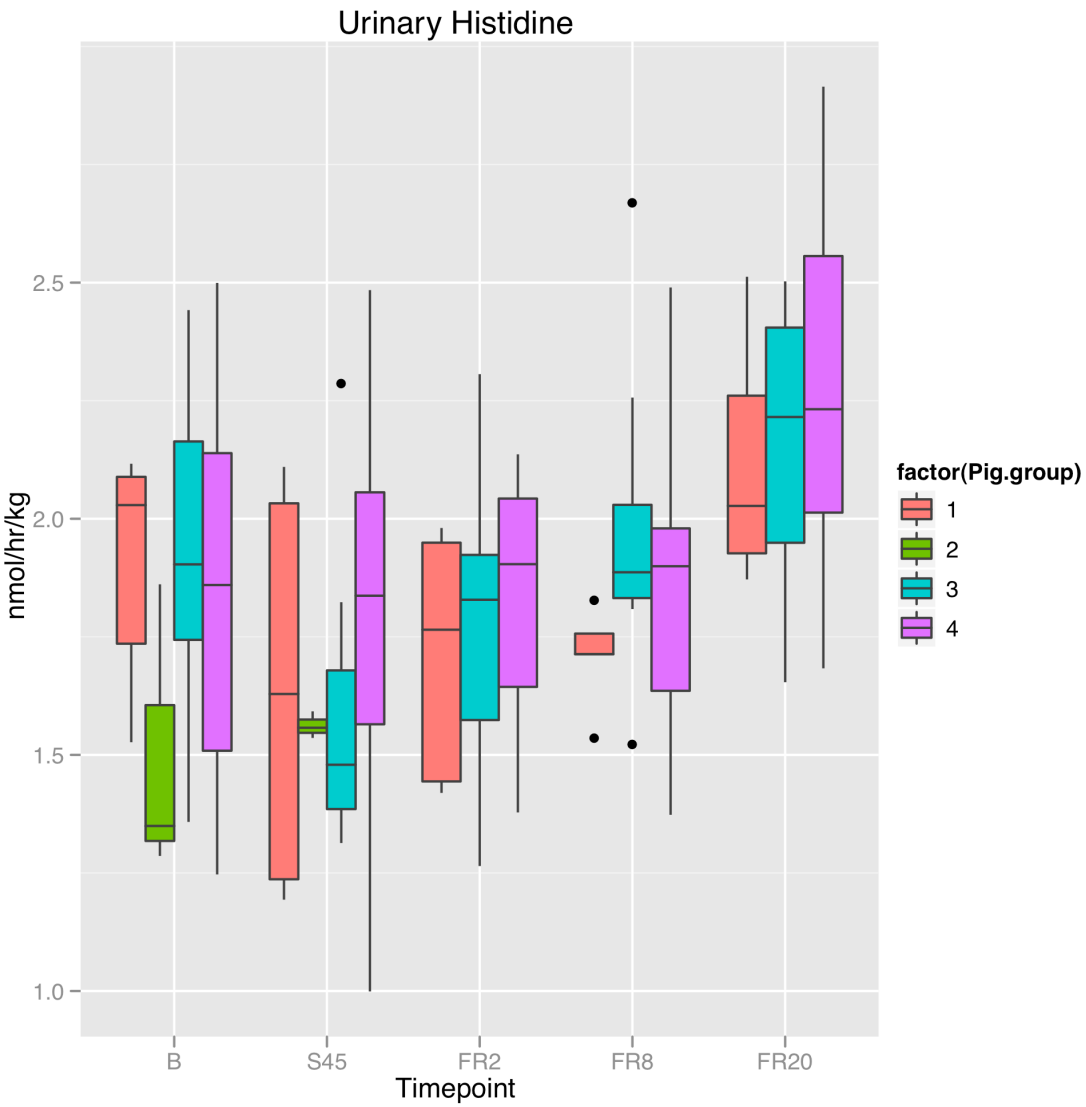
Urinary Histidine
nmol/hr/kg
2.5
2.0
1.5
1.0
B
S45
FR2
FR8
FR20
Timepoint
factor(Pig.group)
1
2
3
4

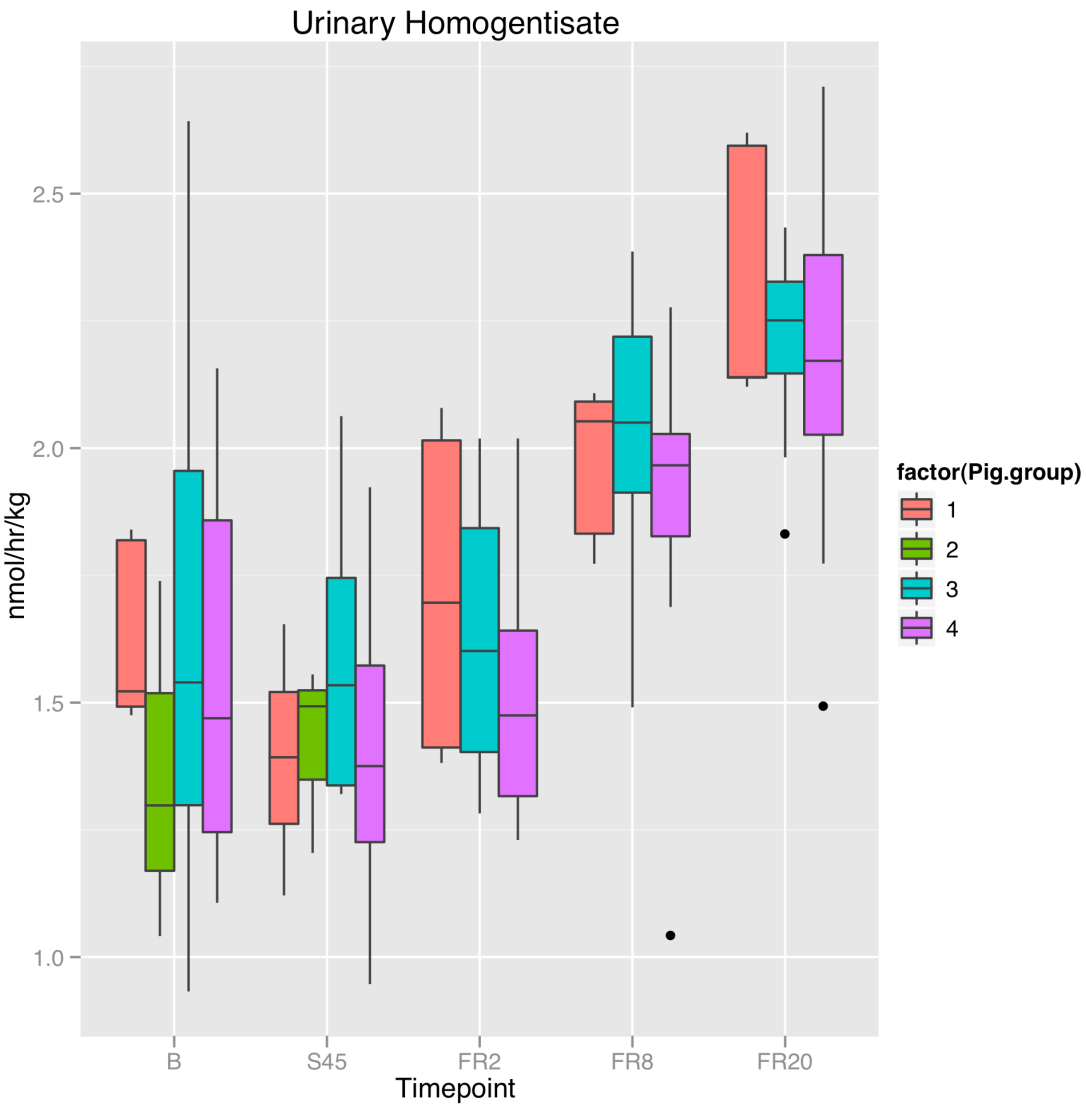
Urinary Homogentisate
nmol/hr/kg
2.5
2.0
1.5
1.0
B
S45
FR2
FR8
FR20
Timepoint
factor(Pig.group)
1
2
3
4

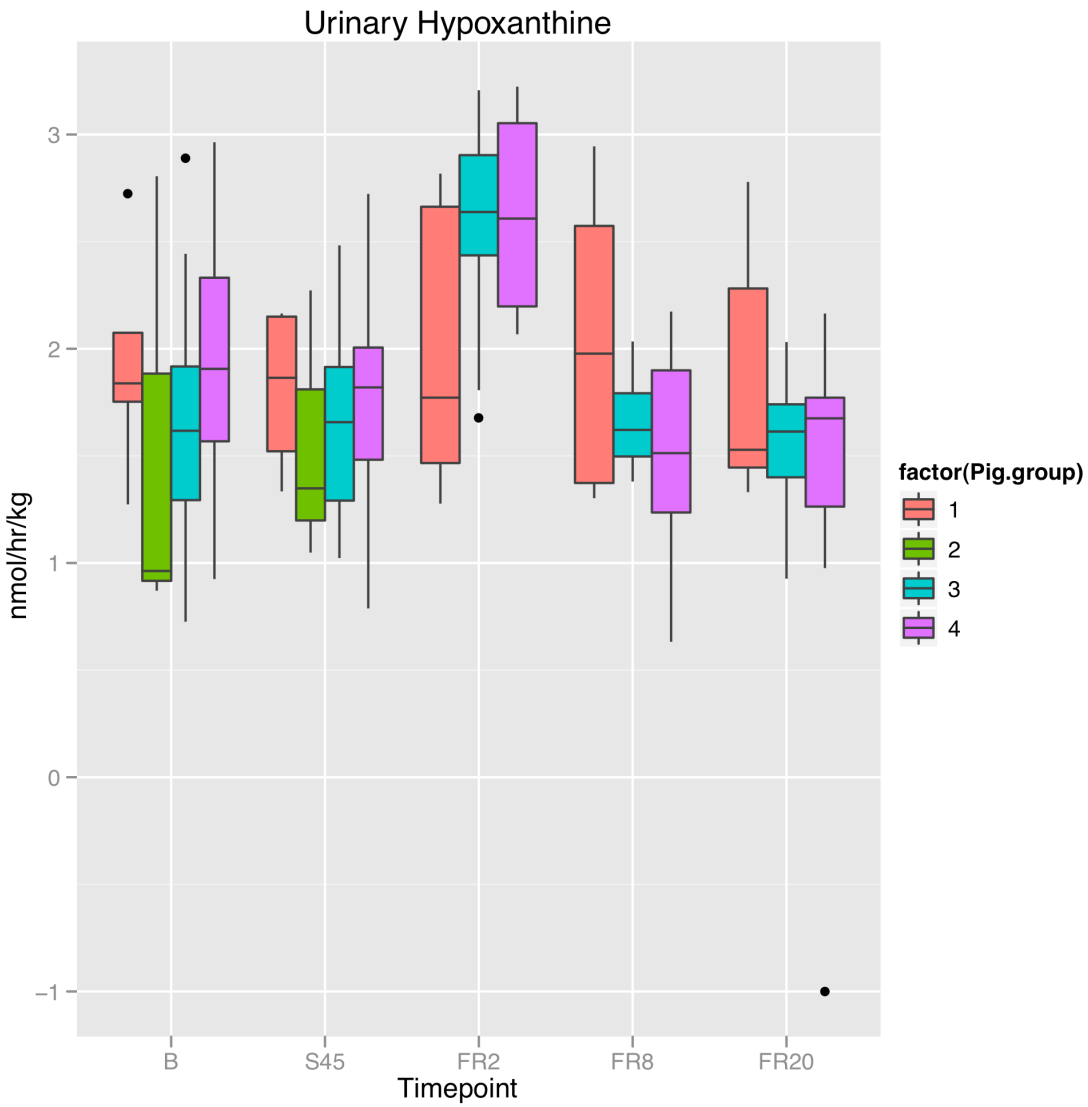
Urinary Hypoxanthine
nmol/hr/kg
3
2
1
0
−1
B
S45
FR2
FR8
FR20
Timepoint
factor(Pig.group)
1
2
3
4

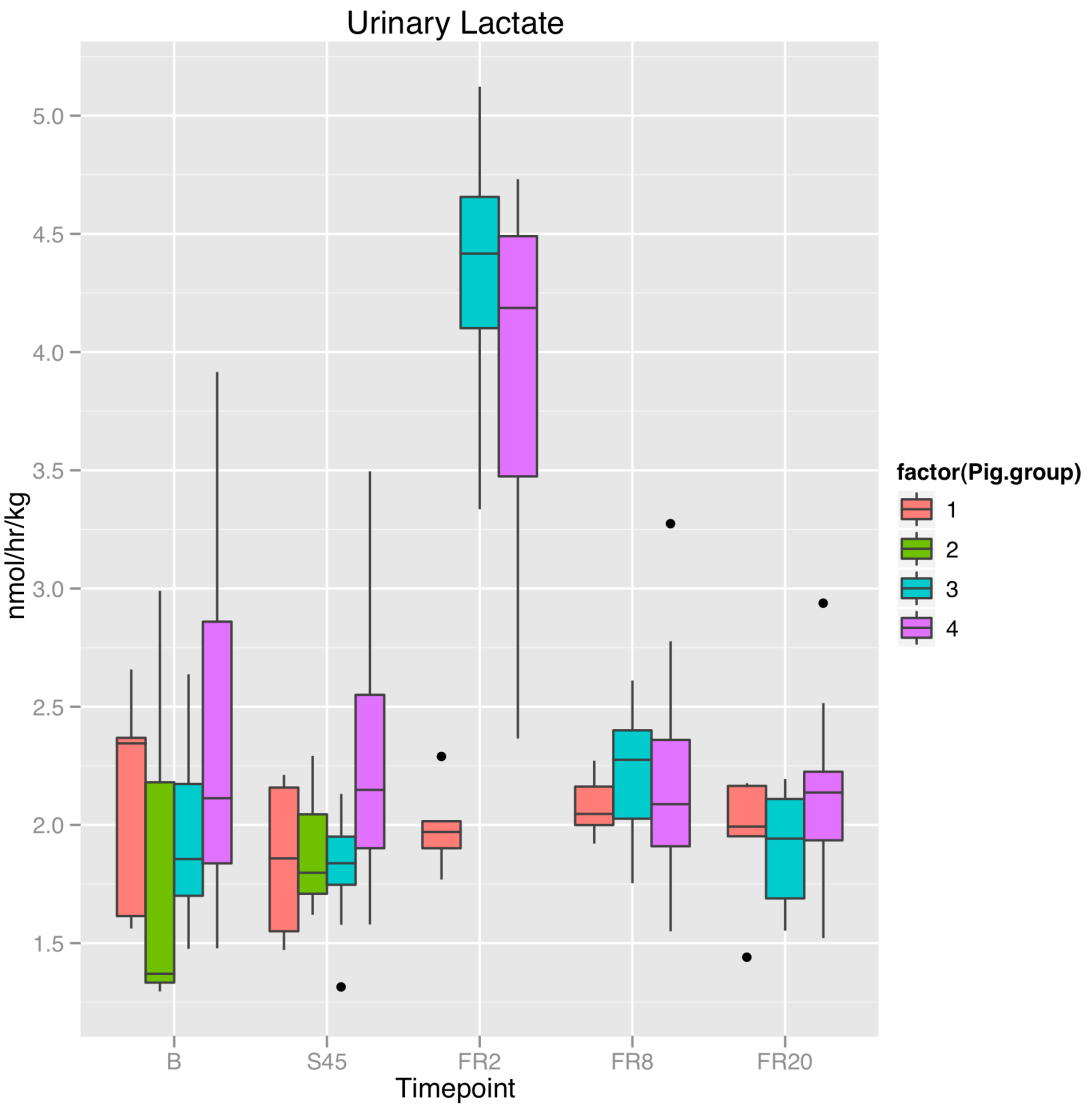
Urinary Lactate
nmol/hr/kg
5.0
4.5
4.0
3.5
3.0
2.5
2.0
1.5
B
S45
FR2
FR8
FR20
Timepoint
factor(Pig.group)
1
2
3
4

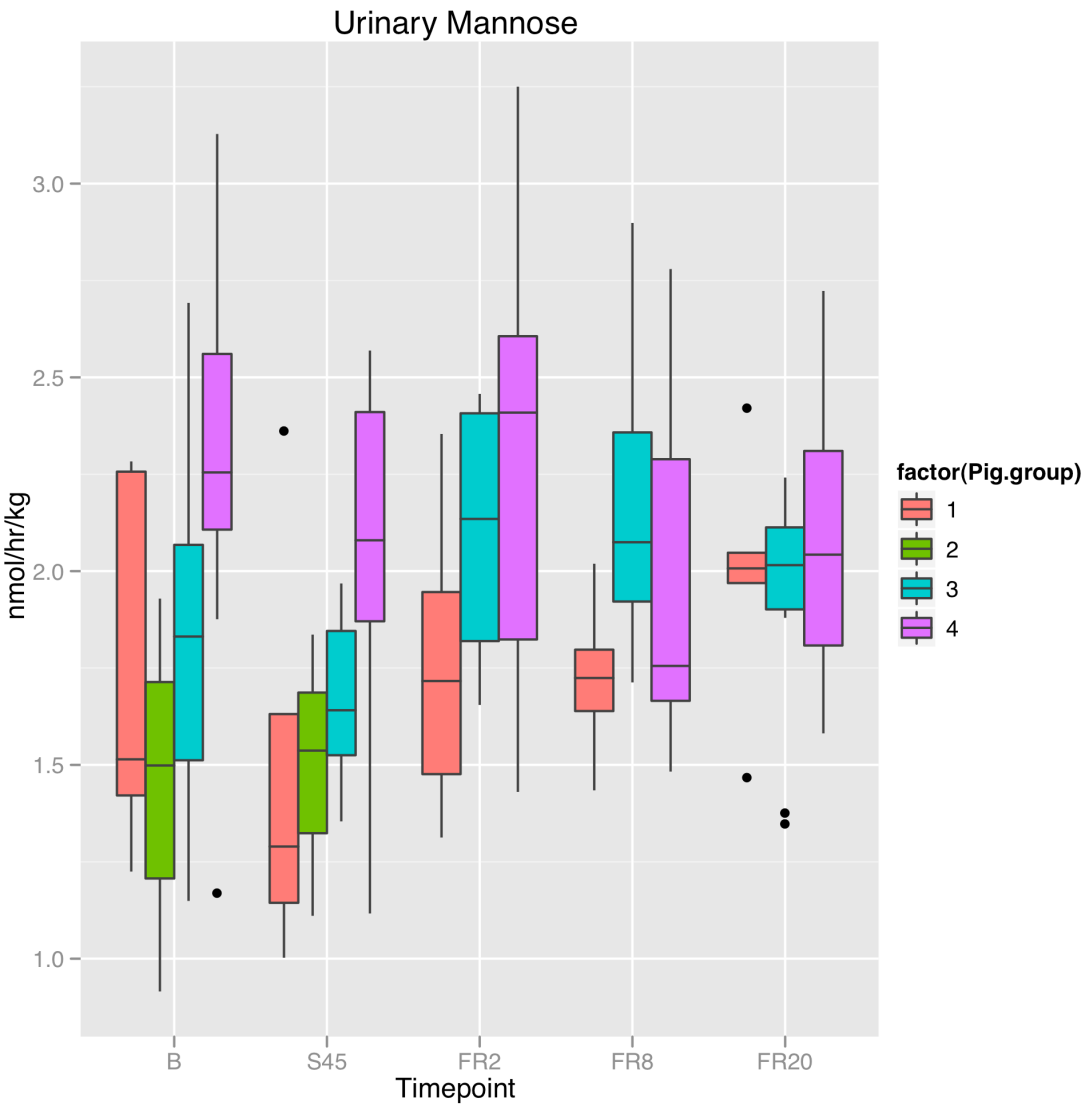
Urinary Mannose
nmol/hr/kg
3.0
2.5
2.0
1.5
1.0
B
S45
FR2
FR8
FR20
Timepoint
factor(Pig.group)
1
2
3
4

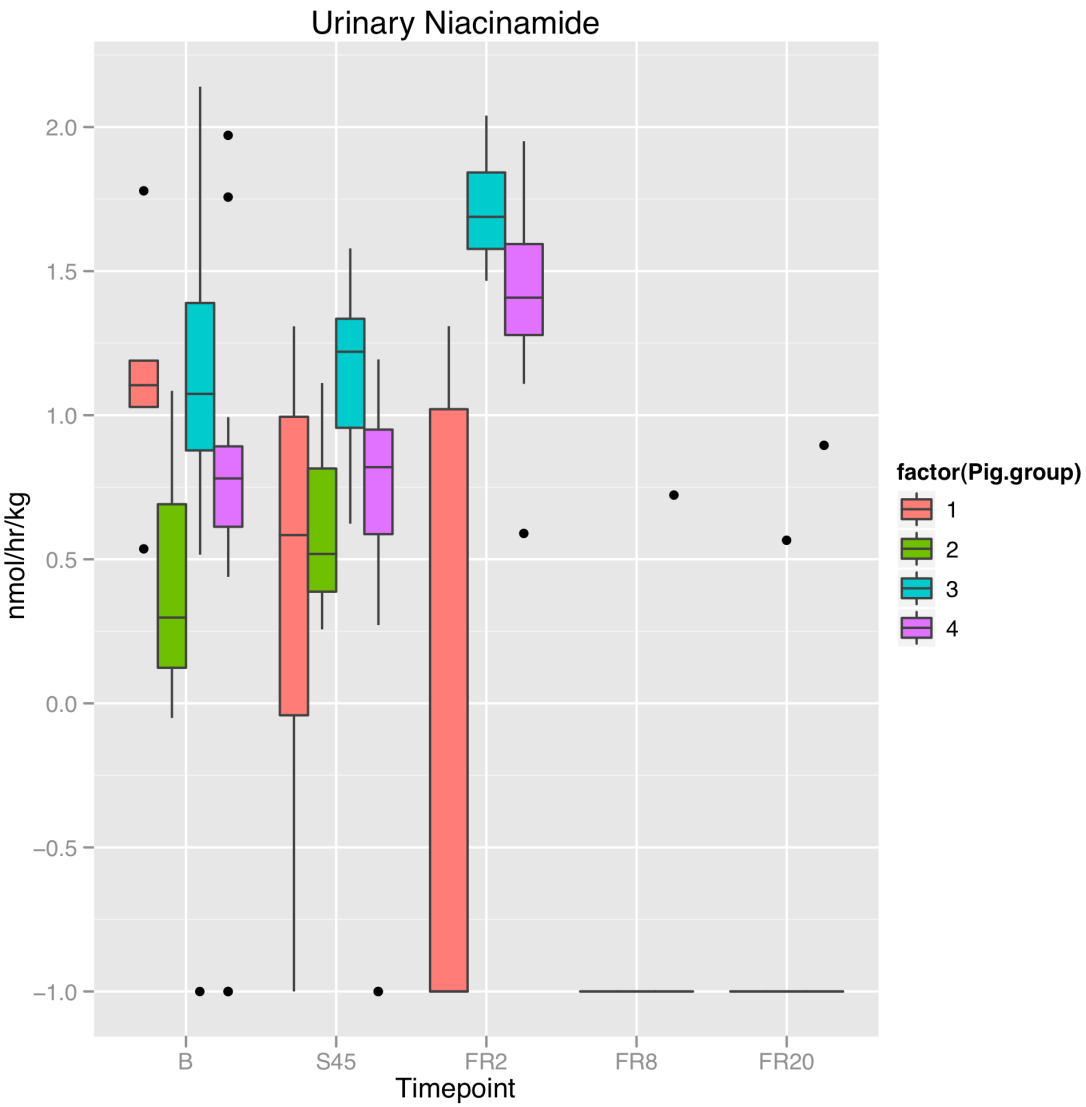
Urinary Niacinamide
nmol/hr/kg
2.0
1.5
1.0
0.5
0.0
−0.5
−1.0
B
S45
FR2
FR8
FR20
Timepoint
factor(Pig.group)
1
2
3
4

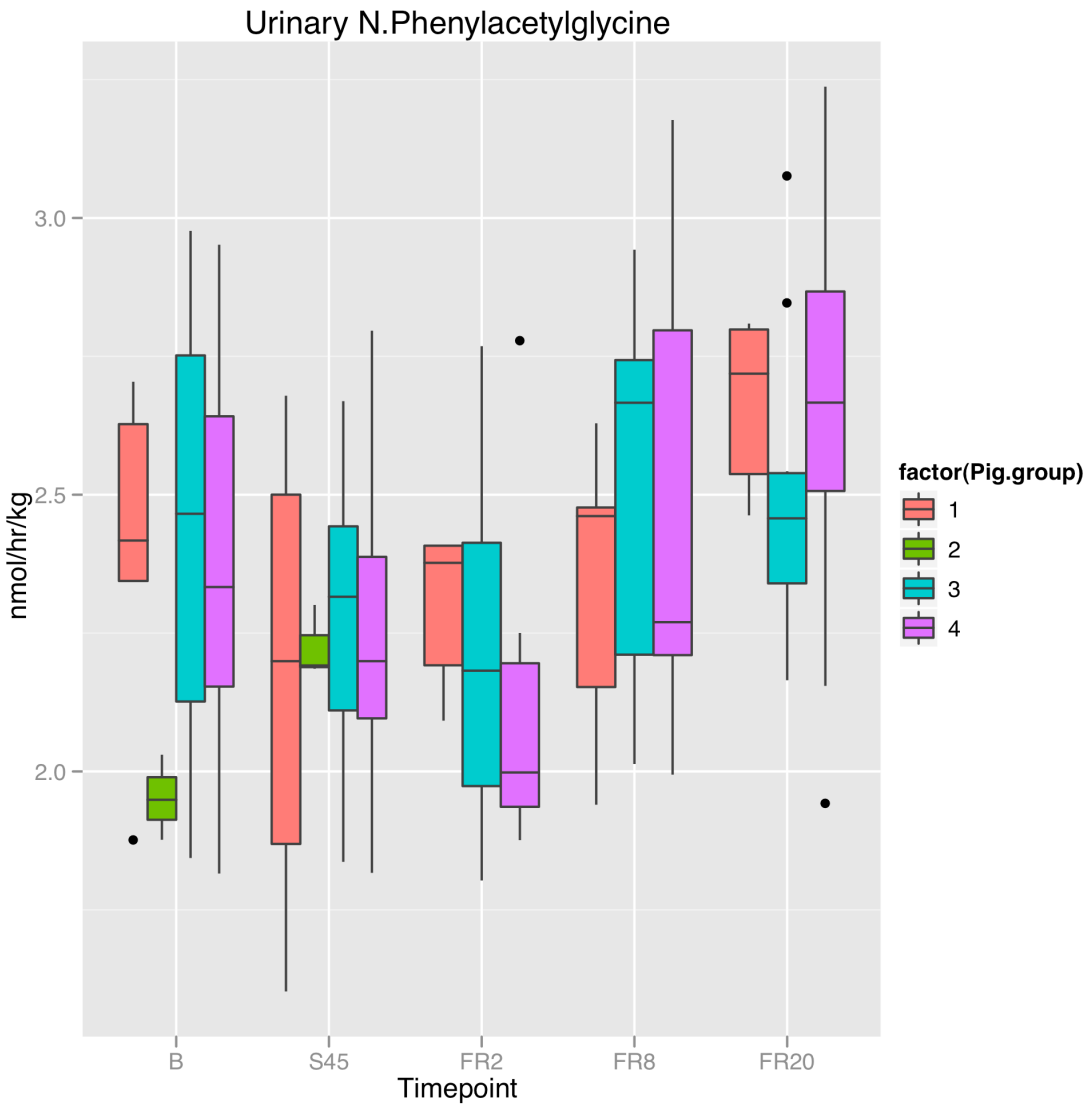
Urinary N.Phenylacetylglycine
nmol/hr/kg
3.0
2.5
2.0
B
S45
FR2
FR8
FR20
Timepoint
factor(Pig.group)
1
2
3
4

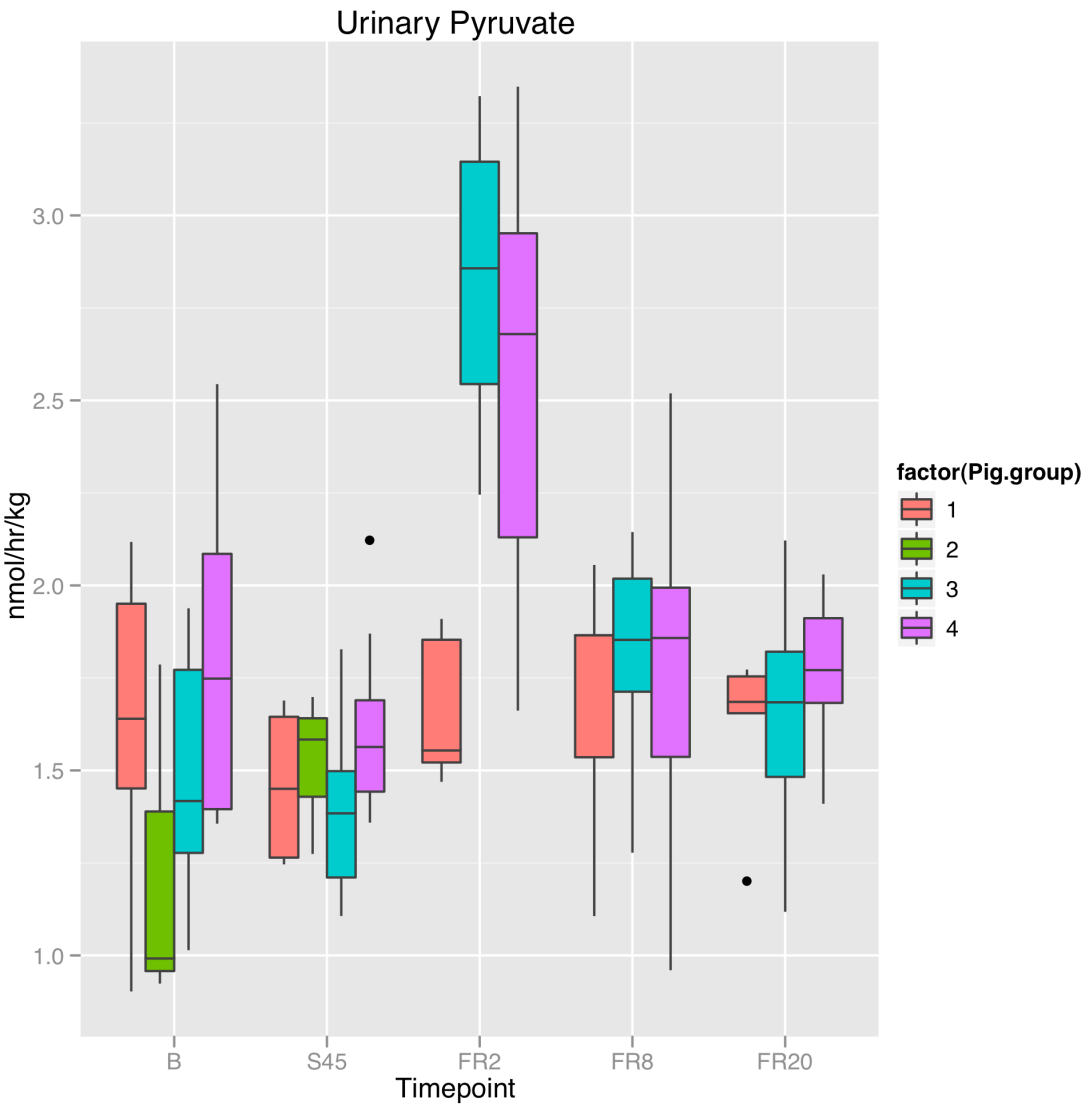
Urinary Pyruvate
nmol/hr/kg
3.0
2.5
2.0
1.5
1.0
B
S45
FR2
FR8
FR20
Timepoint
factor(Pig.group)
1
2
3
4

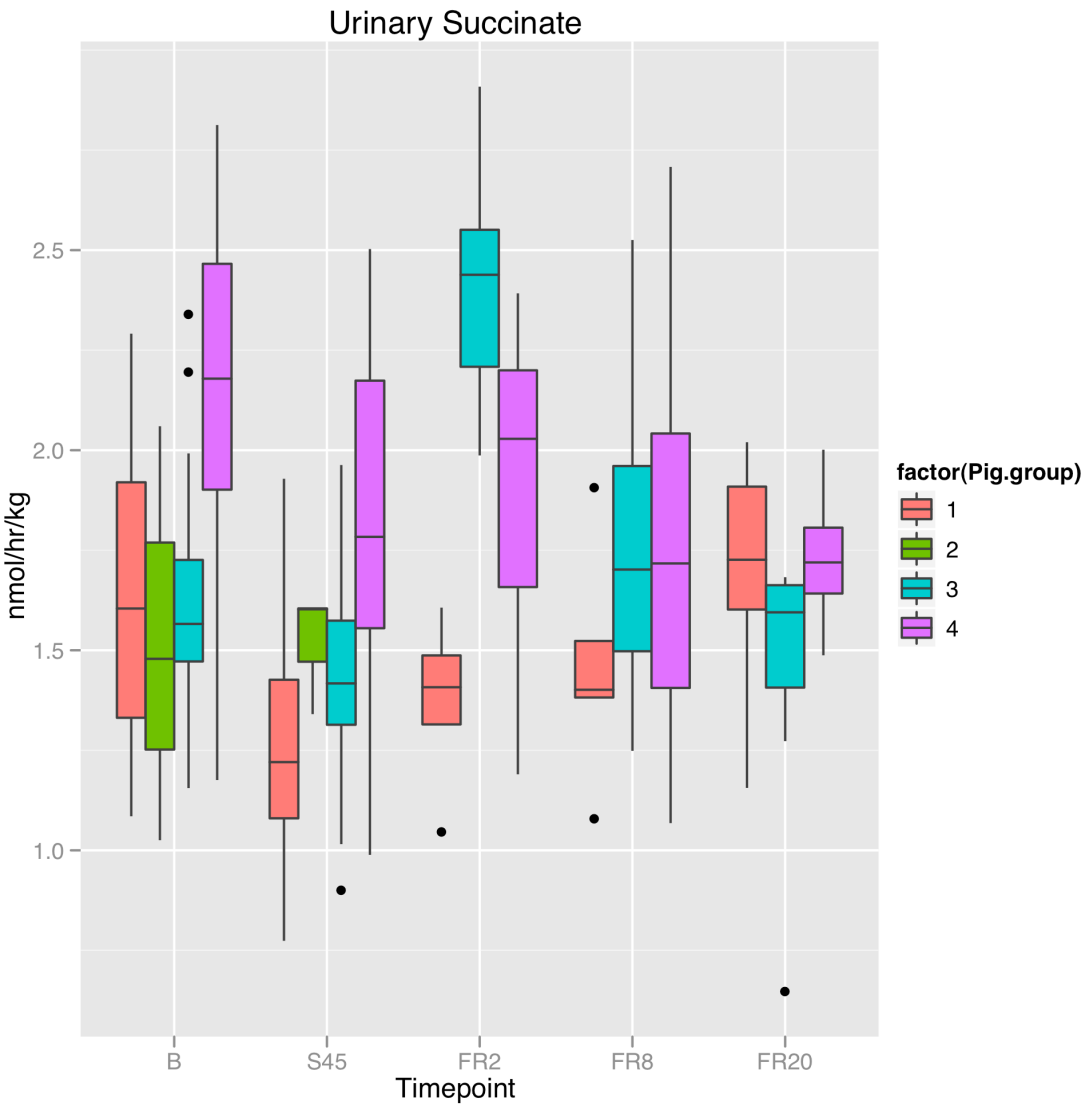
Urinary Succinate
nmol/hr/kg
2.5
2.0
1.5
1.0
B
S45
FR2
FR8
FR20
Timepoint
factor(Pig.group)
1
2
3
4

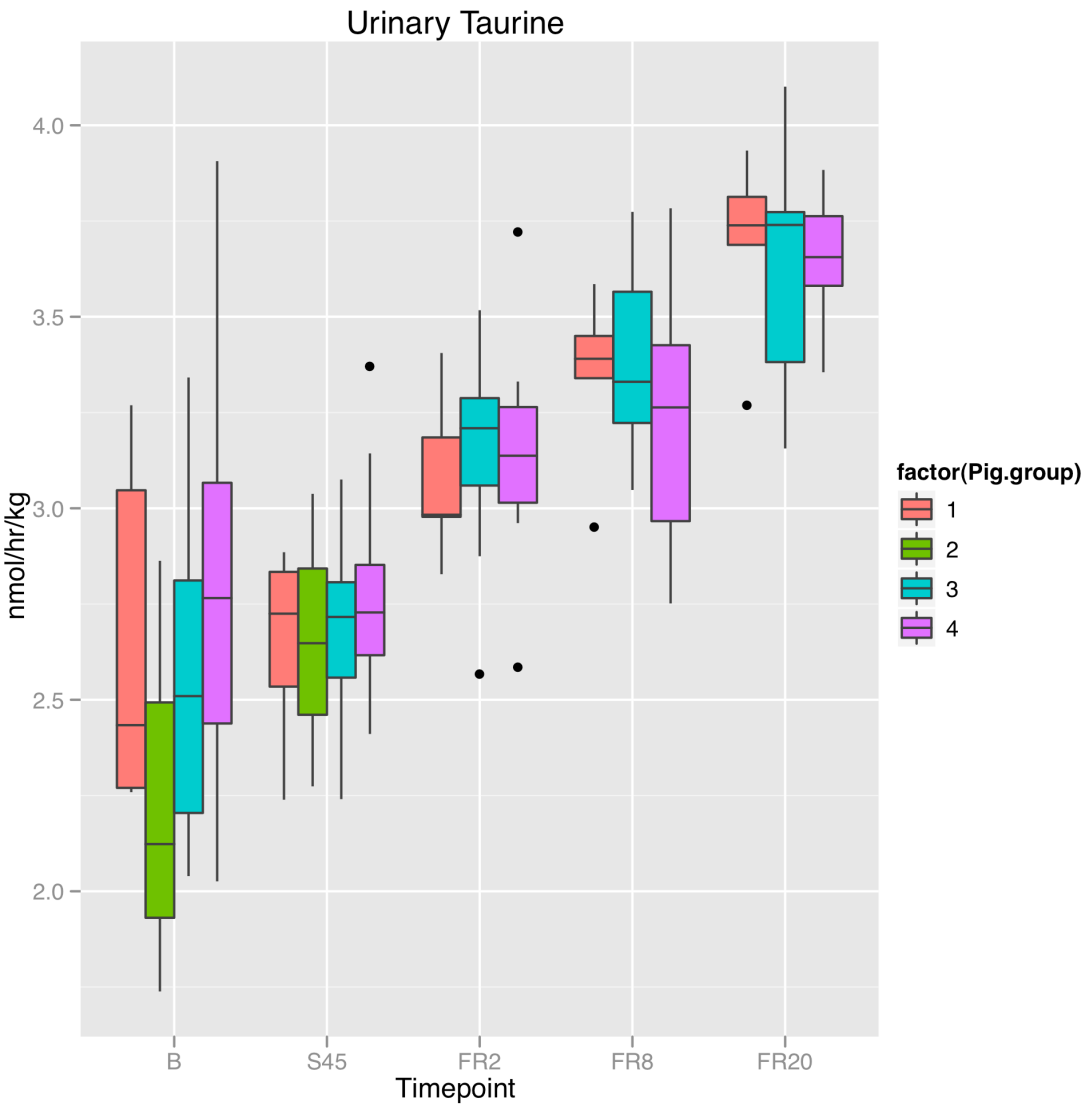
Urinary Taurine
4.0
3.5
3.0
2.5
2.0
nmol/hr/kg
B
S45
FR2
FR8
FR20
Timepoint
factor(Pig.group)
1
2
3
4

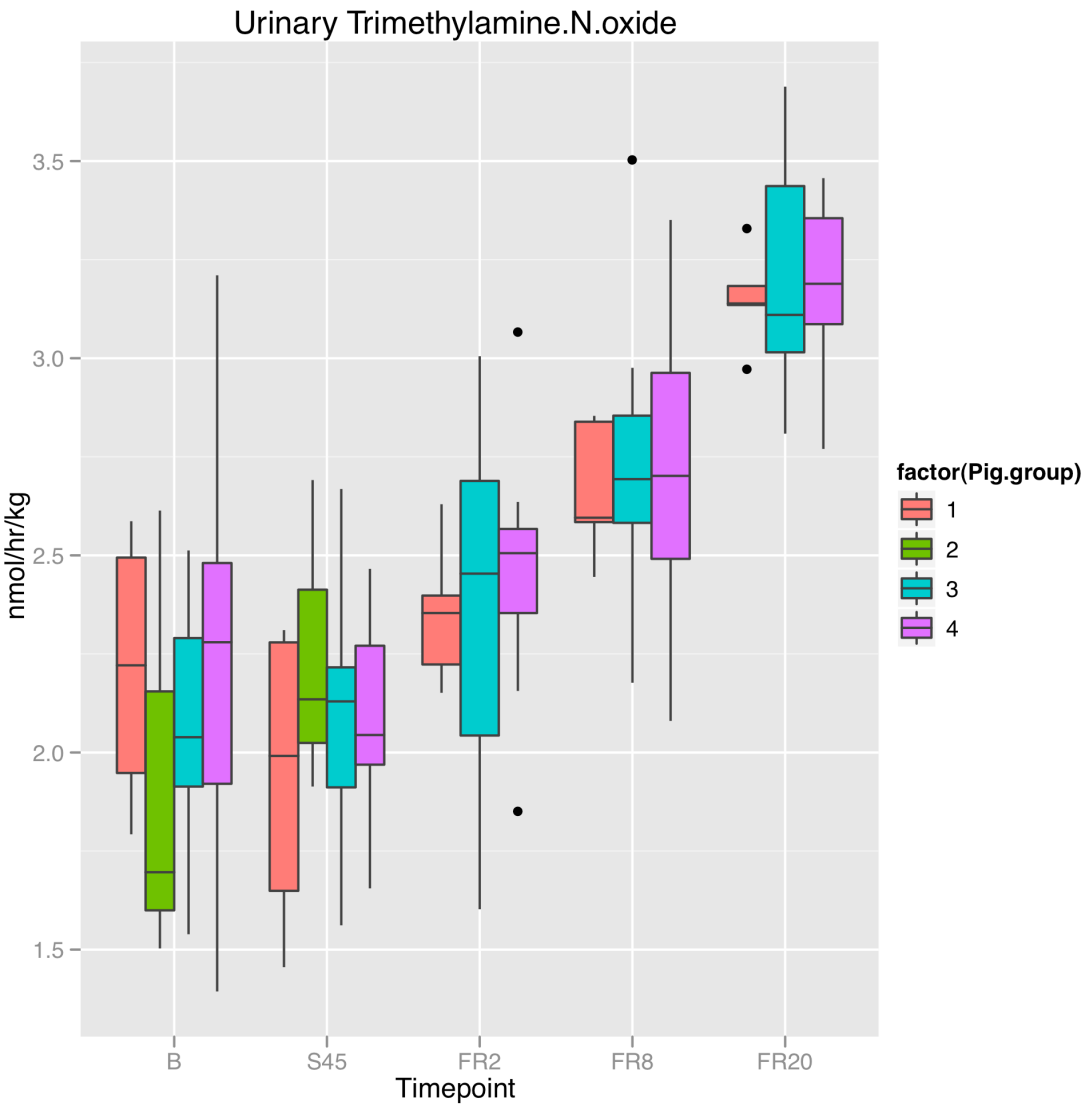
Urinary Trimethylamine.N.oxide
nmol/hr/kg
3.5
3.0
2.5
2.0
1.5
B
S45
FR2
FR8
FR20
Timepoint
factor(Pig.group)
1
2
3
4

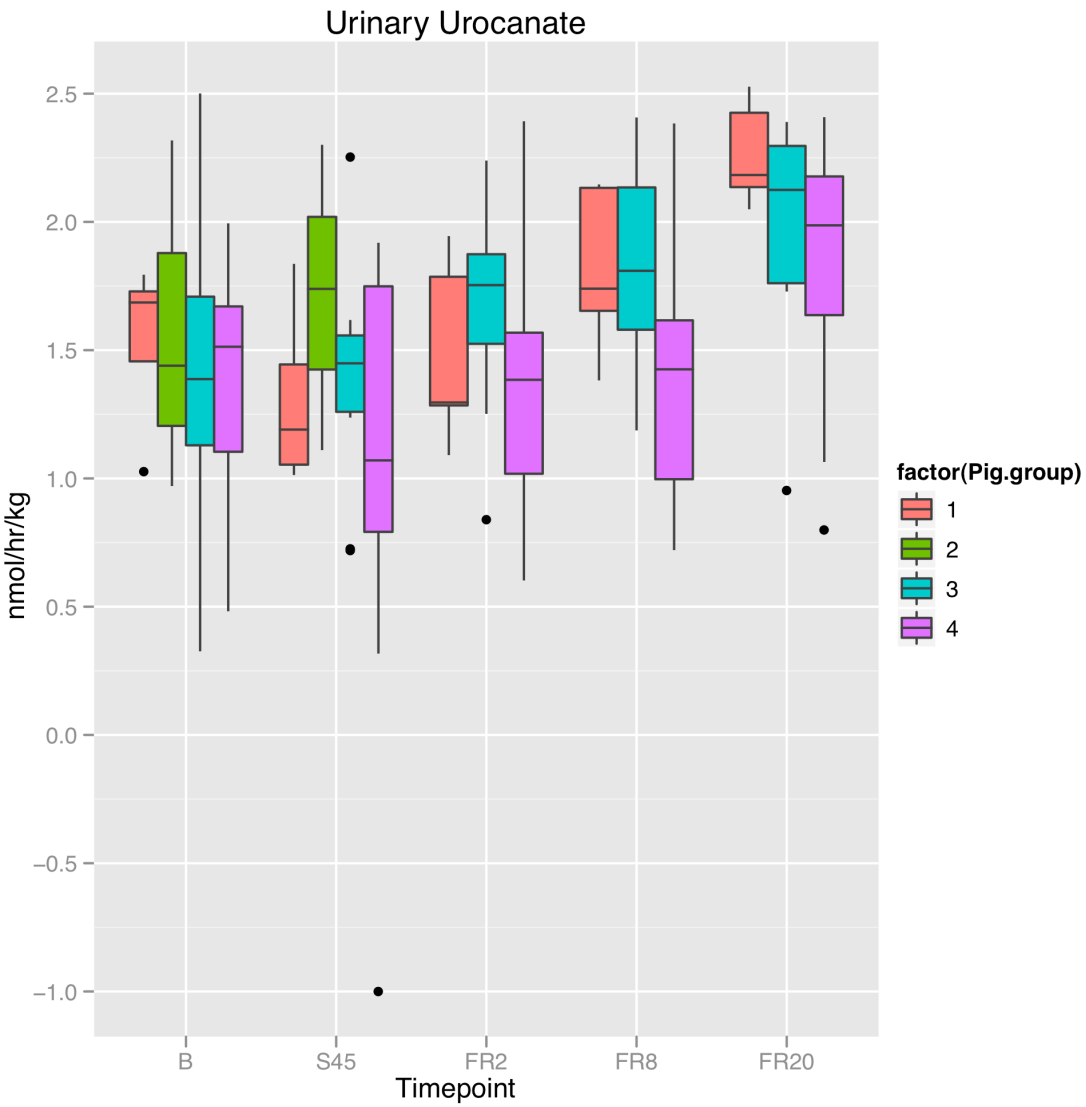
Urinary Urocanate
2.5
2.0
1.5
1.0
0.5
0.0
−0.5
−1.0
nmol/hr/kg
B
S45
FR2
FR8
FR20
Timepoint
factor(Pig.group)
1
2
3
4

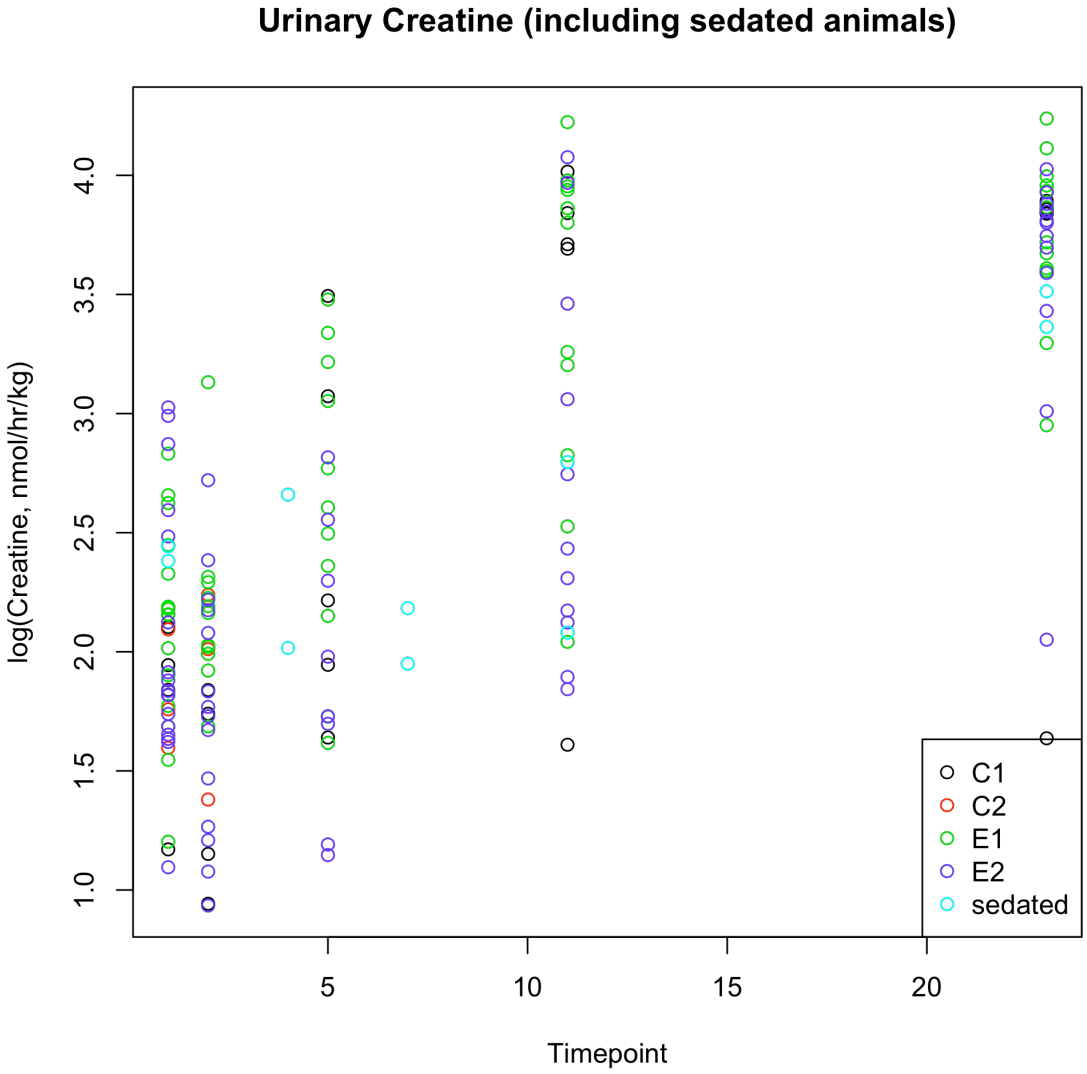
Urinary Creatine (including sedated animals)
log(Creatine, nmol/hr/kg)
1.0
1.5
2.0
2.5
3.0
3.5
4.0
5
10
15
20
Timepoint
C1
C2
E1
E2
sedated

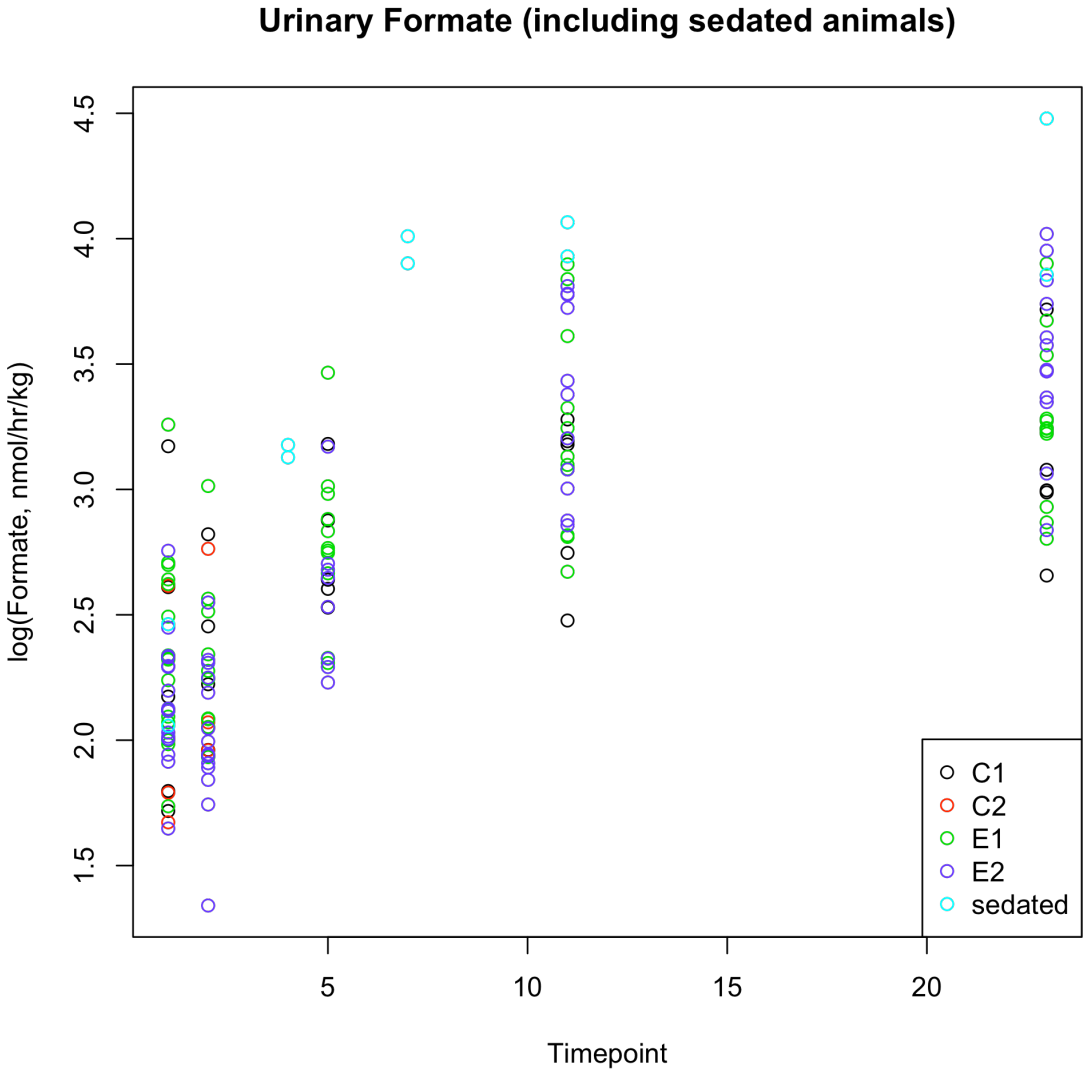
Urinary Formate (including sedated animals)
log(Formate, nmol/hr/kg)
1.5
2.0
2.5
3.0
3.5
4.0
4.5
5
10
15
20
Timepoint
C1
C2
E1
E2
sedated

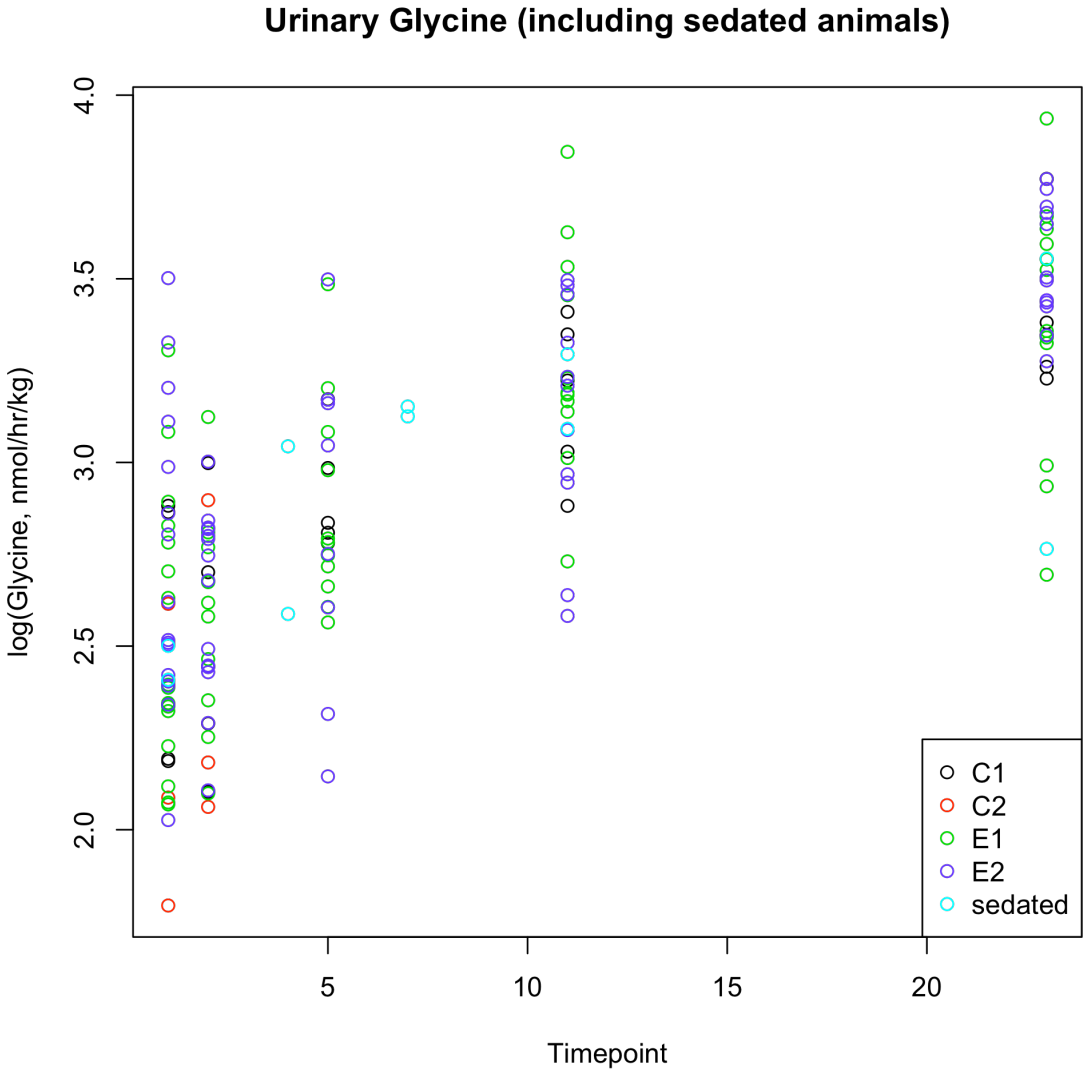
Urinary Glycine (including sedated animals)
log(Glycine, nmol/hr/kg)
2.0
2.5
3.0
3.5
4.0
5
10
15
20
Timepoint
C1
C2
E1
E2
sedated

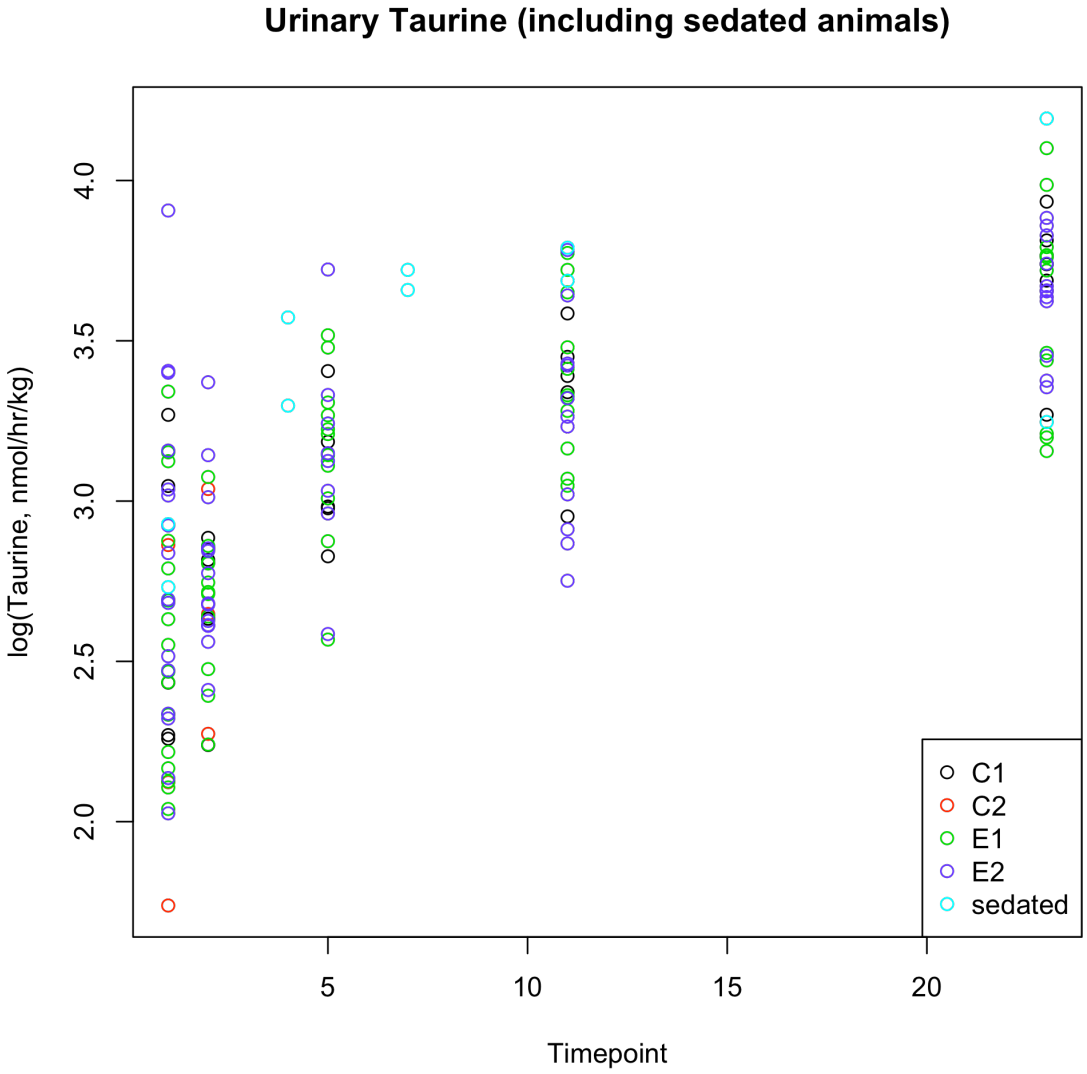
Urinary Taurine (including sedated animals)
log(Taurine, nmol/hr/kg)
2.0
2.5
3.0
3.5
4.0
5
10
15
20
Timepoint
C1
C2
E1
E2
sedated

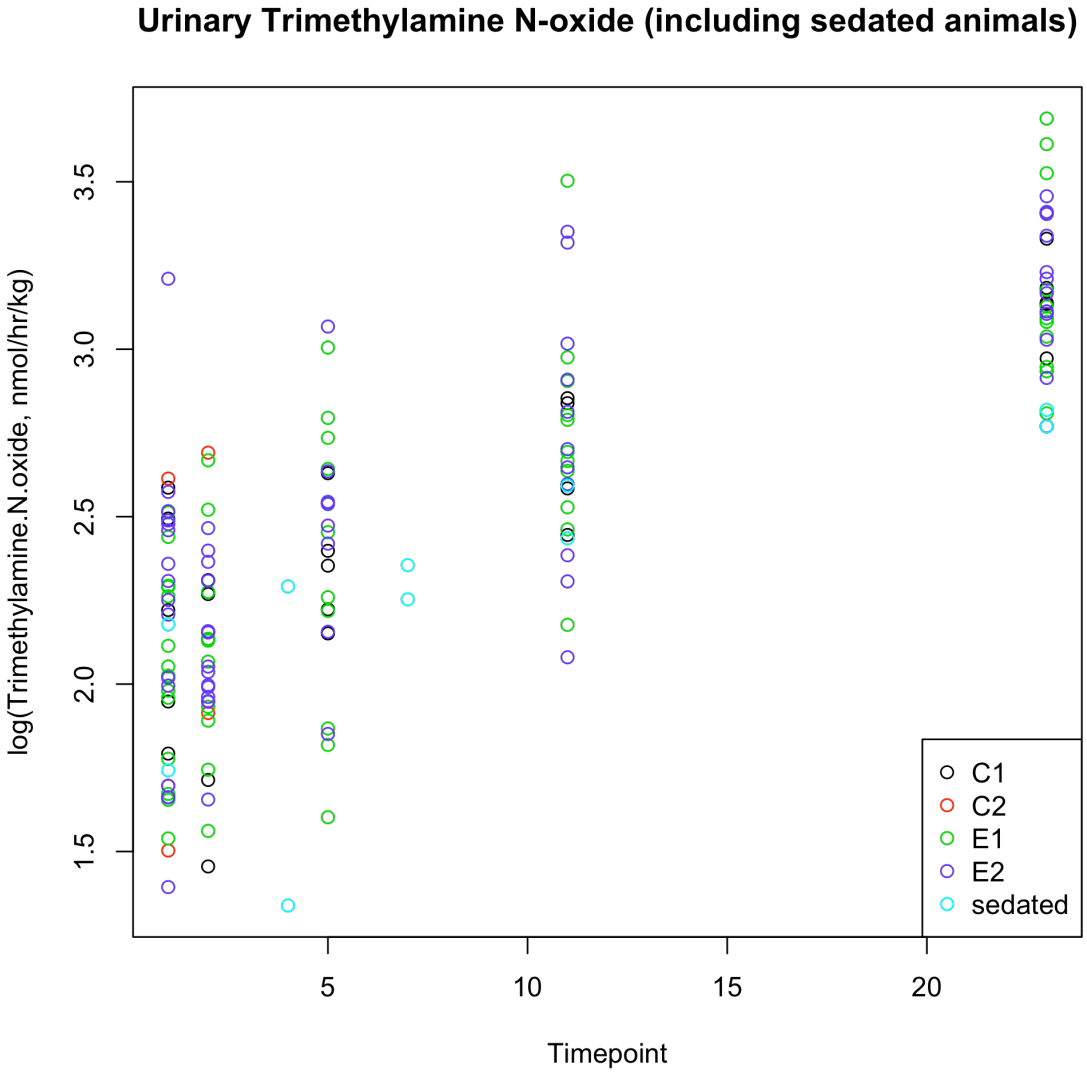
Urinary Trimethylamine N-oxide (including sedated animals)
log(Trimethylamine.N.oxide, nmol/hr/kg)
1.5
2.0
2.5
3.0
3.5
5
10
15
20
Timepoint
C1
C2
E1
E2
sedated